nanomaterials

MDPI

Review

A Comprehensive Review of Graphitic Carbon Nitride ($g\text{-}C_3N_4$)–Metal Oxide-Based Nanocomposites: Potential for Photocatalysis and Sensing

Amirhossein Alaghmandfard and Khashayar Ghandi *

Department of Chemistry, University of Guelph, Guelph, ON N1G 2W1, Canada; aalaghma@uoguelph.ca
* Correspondence: kghandi@uoguelph.ca

Abstract: $g\text{-}C_3N_4$ has drawn lots of attention due to its photocatalytic activity, low-cost and facile synthesis, and interesting layered structure. However, to improve some of the properties of $g\text{-}C_3N_4$, such as photochemical stability, electrical band structure, and to decrease charge recombination rate, and towards effective light-harvesting, $g\text{-}C_3N_4$–metal oxide-based heterojunctions have been introduced. In this review, we initially discussed the preparation, modification, and physical properties of the $g\text{-}C_3N_4$ and then, we discussed the combination of $g\text{-}C_3N_4$ with various metal oxides such as TiO_2, ZnO, FeO, Fe_2O_3, Fe_3O_4, WO_3, SnO, SnO_2, etc. We summarized some of their characteristic properties of these heterojunctions, their optical features, photocatalytic performance, and electrical band edge positions. This review covers recent advances, including applications in water splitting, CO_2 reduction, and photodegradation of organic pollutants, sensors, bacterial disinfection, and supercapacitors. We show that metal oxides can improve the efficiency of the bare $g\text{-}C_3N_4$ to make the composites suitable for a wide range of applications. Finally, this review provides some perspectives, limitations, and challenges in investigation of $g\text{-}C_3N_4$–metal-oxide-based heterojunctions.

Keywords: graphitic carbon nitride; $g\text{-}C_3N_4$; metal oxide; photocatalysts; sensors; bacterial disinfection; supercapacitors

Citation: Alaghmandfard, A.; Ghandi, K. A Comprehensive Review of Graphitic Carbon Nitride ($g\text{-}C_3N_4$)–Metal Oxide-Based Nanocomposites: Potential for Photocatalysis and Sensing. *Nanomaterials* **2022**, *12*, 294. https://doi.org/10.3390/nano12020294

Academic Editor: Detlef W. Bahnemann

Received: 10 December 2021
Accepted: 5 January 2022
Published: 17 January 2022

1. Introduction

Graphitic carbon nitride ($g\text{-}C_3N_4$) is a polymeric, visible-light-active photocatalyst with a bandgap of ~2.7 eV (~460 nm), that was introduced since 2006 [1]. $g\text{-}C_3N_4$ has become an important material in chemistry, physics and engineering because of its facile, low-cost, environmentally-friendly preparation methods with promising stability and good physicochemical properties for use in a wide range of applications [2]. Compared with other semiconductors, $g\text{-}C_3N_4$ can be easily synthesized by various methods with desirable electrical structures as well as morphologies, and high thermal stability up to 600 °C in the air [3,4].

The most common precursors used to prepare $g\text{-}C_3N_4$ are melamine, dicyandiamide, cyanamide, urea, thiourea, and ammonium thiocyanate. Among different types of carbon nitrides such as $\alpha\text{-}C_3N_4$, $\beta\text{-}C_3N_4$, cubic C_3N_4, pseudocubic C_3N_4, with bandgaps of around 5.49 eV, 4.85 eV, 4.30 eV, and 4.13 eV, respectively, $g\text{-}C_3N_4$ is the most stable phase under ambient conditions [2]. In order to enhance the performance and modulate the properties of $g\text{-}C_3N_4$, researchers have proposed different methods such as doping and making heterojunction with other materials. Examples of these materials are metal oxides, metal sulfides, noble metals, and carbonaceous nanomaterials [5–12]. Among them, metal oxides are the most common ones to improve the efficiency of $g\text{-}C_3N_4$, e.g., increasing the light absorption and reducing the recombination of electrons and holes by promoting the separation of charge carriers. This is mainly due to their suitable band structures [13–18].

The $g\text{-}C_3N_4$ structure has been widely used in many applications, in particular in energy-related applications. Energy consumption to provide electricity and heat will rise

to twice its current consumption by 2050, which is mainly due to industrialization, urbanization, and population growth [19,20]. The consumption of fossil fuels, such as natural gas, coal, and oil, should be decreased as their usage results in detrimental environmental impacts [2,19,20]. Two remedies are solar energy and photocatalysis [21–24]. Both require suitable semiconductors such as g-C_3N_4 with superior activities for different catalytic reactions, such as organic pollutants degradation, H_2, and O_2 generation by water splitting and CO_2 reduction to hydrocarbon fuels [14,25–29]. The g-C_3N_4 can also be used for water disinfection and bacterial control [25,30].

It is evident from Figure 1 that the number of publications, collected from the Scopus database, has been growing fast from 2012 in the field of g-C_3N_4 and g-C_3N_4–metal oxide-based heterojunctions. Figure 1a shows the number of all publications on g-C_3N_4 since 2012, showing that this topic is among the hot research areas. It is therefore important to provide a comprehensive review of the g-C_3N_4–metal oxide composites. To the best of our knowledge, no publication reviews a wide range of papers to explain the applications and structure of these heterojunctions comprehensively.

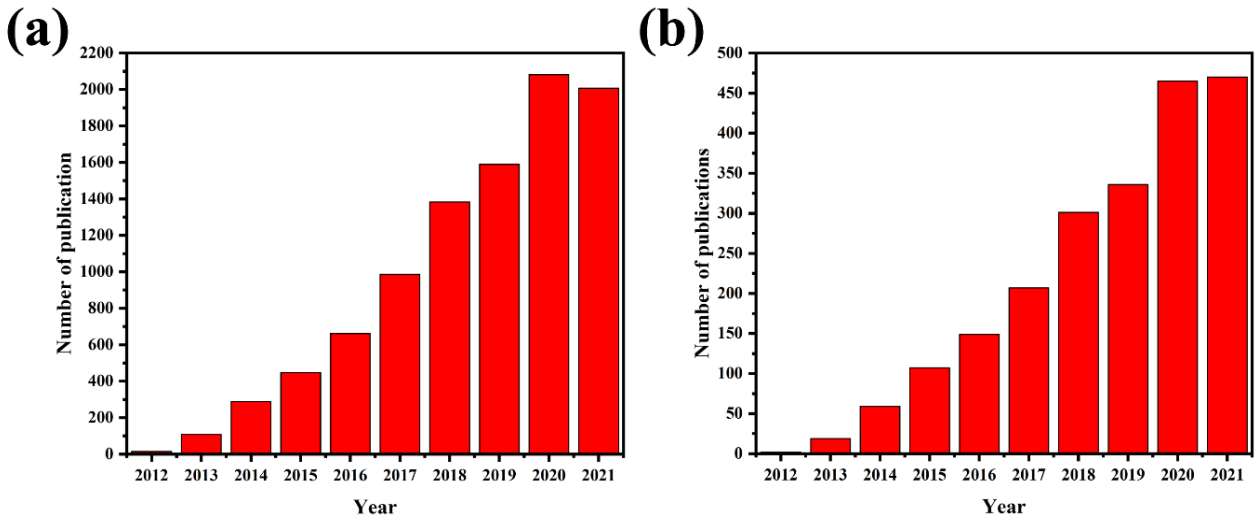

Figure 1. Number of annual publications (**a**) using "g-C_3N_4*" as a keyword since 2012, (**b**) using "g-C_3N_4*" with metal oxides ("TiO_2", "ZnO", "WO_3", "Iron Oxide", "Tin Oxide", and other metal oxides) as keywords since 2012. Adapted from Scopus database, dated 1 October 2021.

This review covers the research up to 1 October 2021. We highlighted some general information about the structure and characterization of the bare g-C_3N_4. We also discussed some modifications such as doping to improve the g-C_3N_4 properties. As well, we have also summarized the research on modification of the structure and properties, to enhance the efficiency of g-C_3N_4 for different applications, via combining g-C_3N_4 with metal oxides such as TiO_2, ZnO, iron oxide, WO_3, and tin oxide. After reviewing g-C_3N_4–metal oxides, we focus on the applications of these kinds of heterojunctions. In the last part of this review article, we suggest some potential investigations for the future in this field that have not been conducted to this date to our knowledge. We also recommend some studies to better understand the nature of these heterojunctions. Most graphs in this review are reproduced by us from the data in original research papers cited, unless stated otherwise in the captions where the permission has been obtained.

2. Structure and Properties of g-C_3N_4

Melamine, melam, melem, and melon are recognized as heptazine- and triazine-based molecular compounds (coplanar tri-s-triazine unit as the elementary structural motif of g-C_3N_4 structure) to prepare g-C_3N_4. As illustrated in Figure 2, triazine (C_3N_3) and tri-s-triazine/heptazine (C_6N_7) rings are the basic tectonic units of g-C_3N_4.

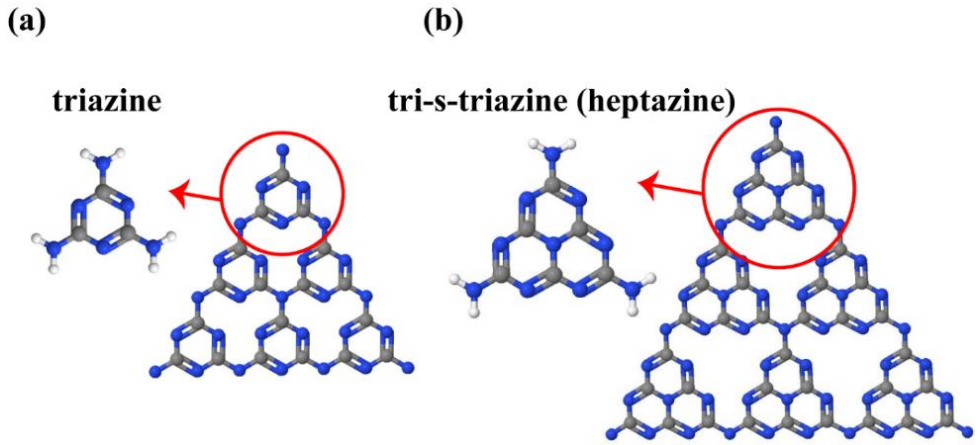

Figure 2. (**a**) Triazine and (**b**) tri-s-triazine (heptazine) structures of g-C_3N_4 (gray, blue, and white balls are carbon, nitrogen, and hydrogen, respectively).

Yan et al. properly studied the phase transition during heating of melamine from room temperature to 1000 °C with a heating rate of 10 °C/min [31]. Figure 3a shows that melamine sublimation and thermal condensation occur at 297 to 390 °C, observed from significant endothermic differential scanning calorimetry (DSC) peak and drastic thermogravimetric analysis (TGA) weight loss. Other endothermic peaks at 545 and 630 °C are attributed to the materials' deamination and decomposition, respectively.

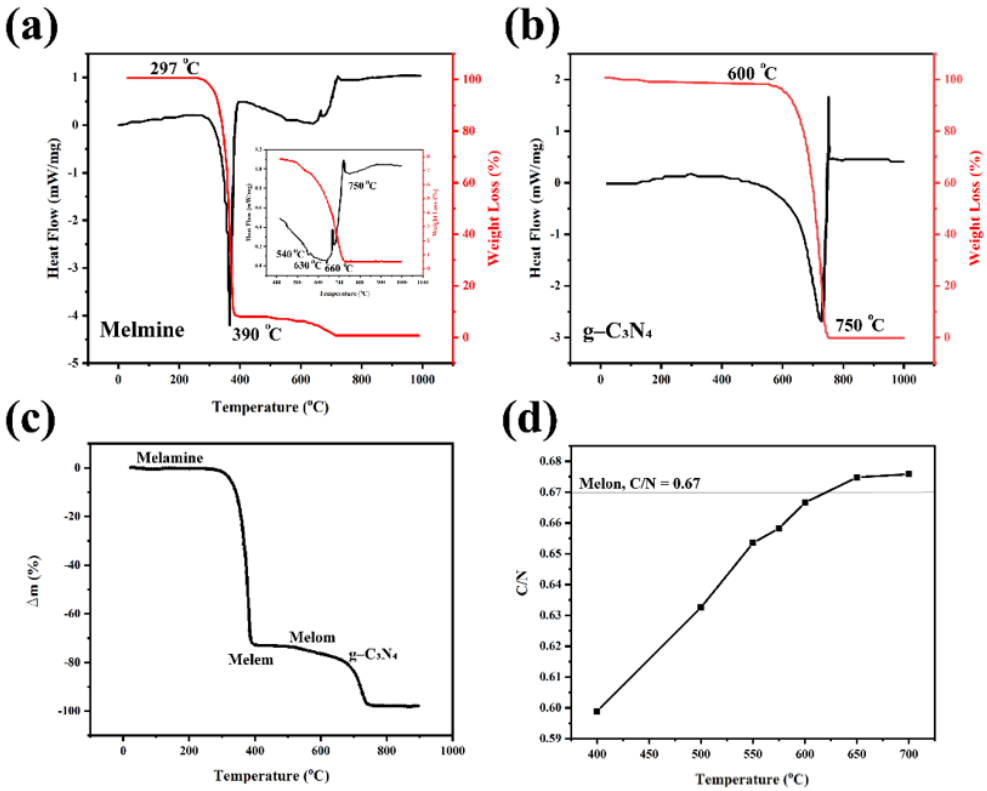

Figure 3. (**a**) Melamine and (**b**) g-C_3N_4 thermal analyses, Copyright © 2022 American Chemical society [31]; (**c**) thermogravimetric curve of annealing of melamine; (**d**) C/N values of melamine products at different temperatures, Copyright © 2022 Elsevier [32].

Figure 3b shows the g-C_3N_4 thermal stability and phase transitions in an open system. This figure shows that g-C_3N_4 has high stability below 600 °C, which is 30 °C lower than

the melamine decomposition temperature (630 °C). Beyond this temperature, g-C_3N_4 starts to decompose into small molecules (e.g., CO_2 and NH_3) [31]. The stability of g-C_3N_4 is higher in the semiclosed ammonia atmosphere than in the open system, mainly due to the inhibition of deamination under ammonia atmosphere. The TGA result illustrated that there is no residue at 750 °C [31]. The annealing temperature is a vital factor in the preparation and properties of the final g-C_3N_4 structure. Praus et al. used melamine as a precursor to synthesize g-C_3N_4 in an air atmosphere [32]. The TGA results, illustrated in Figure 3c, demonstrates that by heating the melamine to 400 °C melen is formed. The main reason for the weight loss at this temperature range is the elimination of ammonium. By further heating up to 600 °C, melon is obtained by melem polymerization [33]. In other words, at higher temperatures, the g-$C_6N_9H_2$ or g-$C_3N_{4.5}H$ is more stable than g-C_3N_4. Figure 3d illustrates that the C/N molar ratio is temperature dependent. The main difference in the C/N value of the synthesized g-C_3N_4 compared to the theoretical value of 0.75 for g-C_3N_4 is due to the incomplete condensation of the amino groups of melon and the low degree of polymerization. Reaction atmosphere is another factor affecting the g-C_3N_4 by providing defects and disordered structures. For instance, in the H_2 atmosphere, by dicyanamide thermal condensation, more nitrogen vacancies were formed [34].

3. g-C_3N_4 Characterizations

The presence of X-ray diffraction (XRD) peaks at about 13 and 27° is an indication of the formation of g-C_3N_4, corresponding to the (002) and (100) diffraction patterns, respectively [35–37]. Paul et al. showed the effects of calcination temperature on the naked g-C_3N_4 using XRD data, Fourier transform infrared spectra (FT-IR), bandgap structure, Brunauer–Emmett–Teller (BET), and photocatalytic recyclability data [36]. Due to the polycondensation of melamine at lower than 400 °C, the crystallinity of the g-C_3N_4 structure is detected (Figure 4a). In contrast, Figure 4b demonstrates that no significant differences are revealed in FTIR spectra at different calcination temperatures. In the FTIR spectra, the characteristic bands with high intensity at the wavenumber about 1640, 1569, 1412, 1328, and 1240 cm^{-1} are related to the stretching modes of C=N and C–N heterocycles. Besides, the strong peaks at 815 cm^{-1} are attributed to the s-triazine units. The broad range peak between 3000 cm^{-1} and 3500 cm^{-1}, is due to the N-H stretching and the remaining water molecules in the structure [35–39]. The BET specific surface areas were estimated to be 37.8, 73.7 and 65.6 $m^2 \cdot g^{-1}$ for g-C_3N_4 synthesized at the calcination temperature of 450, 550 and 650 °C, respectively. Calcination temperature also affects the g-C_3N_4 bandgap. The bandgap when calcinated at 550 °C is narrower than when calcinated at 450 and 650 °C (Figure 4c) [36,38,40]. When the temperature increases to 700 °C, a higher bandgap is observed. In other words, the higher the degree of g-C_3N_4 polymerization, the larger the π-plane conjugation degree of heptazine rings via N_2 atoms, at the higher temperature.

To assess the catalytic activity, ultraviolet-visible (UV-vis) diffuse reflectance spectrums (DRS) of the materials were determined at different temperatures [36]. As discussed earlier the results show that the bandgap of g-C_3N_4 prepared at 550 °C is narrower than those formed at 450 and 650 °C, so the structure prepared at the 550 °C absorbs more visible light, which can lead to the more appealing photoactivity. Moreover, the adsorption and degradation efficiencies for methylene blue dye by g-C_3N_4 prepared at 500 °C is 34.4% and 62.6%, which is higher than those synthesized at 450, 550, 600, and 650 °C [36]. Figure 4d reveals that the prepared g-C_3N_4 at a calcination temperature of 550 °C also showed good stability even after four cyclic runs. The pH, and catalyst loading are also important factors in the adsorption and degradation efficiency [36].

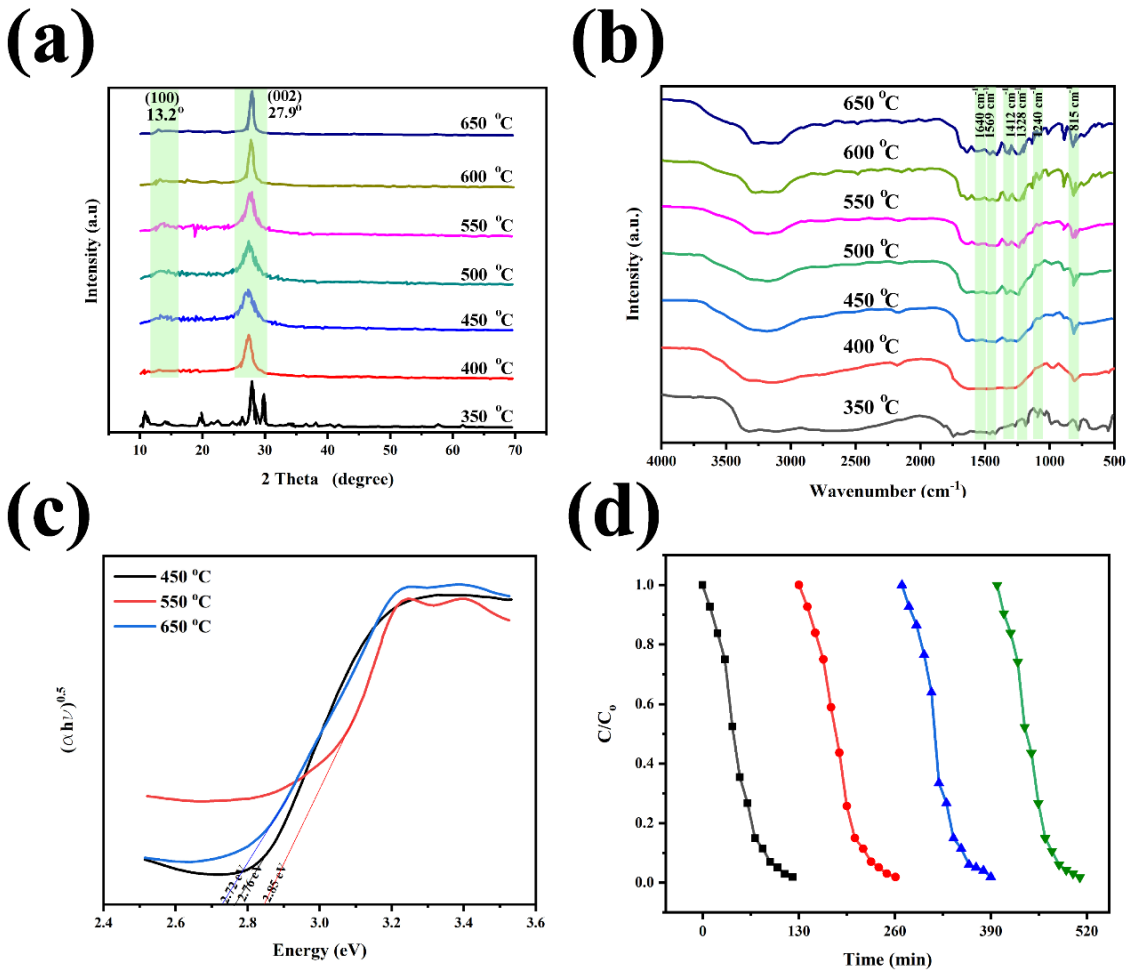

Figure 4. (**a**) XRD, (**b**) FTIR, (**c**) bandgaps of g-C_3N_4 prepared at different calcination temperatures, and (**d**) the photocatalytic recyclability degradation of dyes using prepared g-C_3N_4 at 550 °C [36].

Chen and coworkers illustrated that the PL depends on the condensation temperature (Figure 5a), showing the strong and stable emission in the range of 450–510 nm, mainly due to the π*–π, and π*–LP transitions [41]. The increase in the amount of the tri-s-triazine content at high temperature leads to the higher π states and cause orbital overlap and reduces the PL intensity. The UV-Vis spectra of the g-C_3N_4 at different synthesis temperatures are illustrated in Figure 5b. Like the PL emission peak, the strong absorption peaks at 450 nm and 500 nm are due to the π*–π and π*–LP transitions. Another study, conducted by Dias et al., concluded that during thermal treatment of g-C_3N_4, the enhanced porosity is mainly due to the creation of N vacancies and defects/holes within the nanosheets, resulting in the improvement of optoelectrical properties. Not only the treatment leads to the appearance of n $\rightarrow$ $\pi*$ transitions, but we can also observe red shift in the absorption spectra. Moreover, it can enhance the photocatalytic activities by improving the carrier separation, reducing charge recombination, which is mainly due to the presence of trap states [42]. Furthermore, researchers also investigated the effect of the different dopants on the absorption properties of g-C_3N_4 [43]. These results showed the effect of temperature and dopants on the optical properties of g-C_3N_4. Yuan et al. showed the photograph of the melamine and g-C_3N_4 synthesized at different temperatures, graphically showing the color variation in the deionized water under UV light (365 nm) (Figure 5c) [44]. By increasing the synthesis temperature, the emitted color varied from blue–violet to green, and the intensity went through a maximum at 550 °C. The impact of the temperature on the PL spectra was demonstrated by the 5–10 nm blue-shift at lower temperatures, due to a less delocalized orbital resulting in a larger bandgap. Figure 5d also reveals strong PL emission spectra

with a much smaller blue-shift. This research is among the rare studies investigating the effect of the environment on PL emission spectra. The g-C_3N_4 time-resolved PL spectra shows 5 ns electron-hole recombination at 25 °C [45].

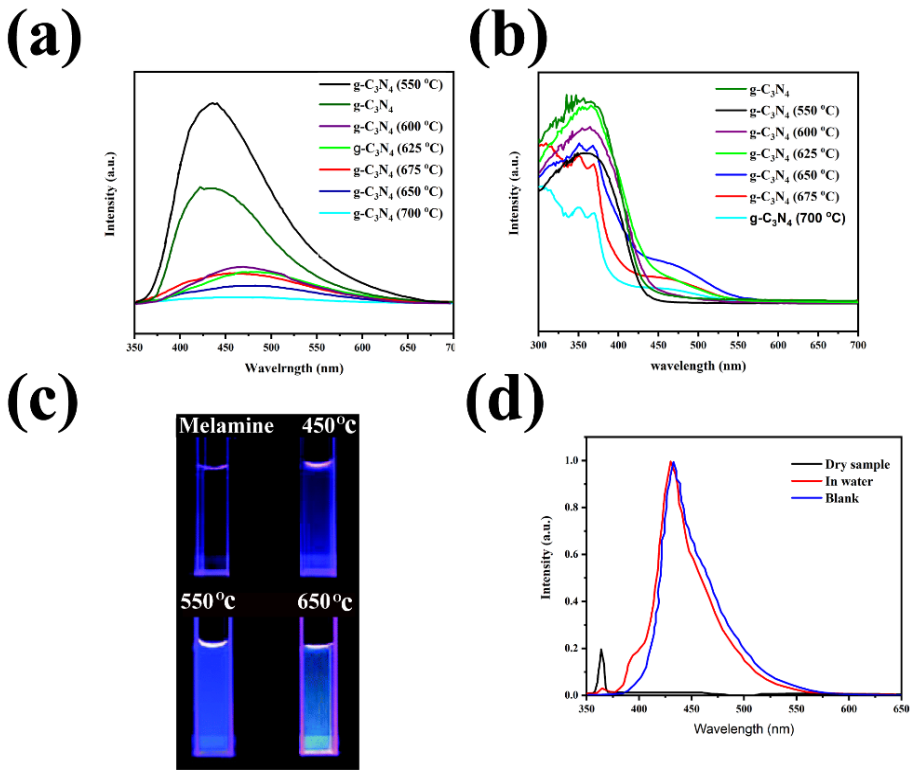

Figure 5. (**a**) The PL spectra under 325 nm excitation (**b**) UV-Vis spectra of g-C_3N_4, prepared at different temperatures, Copyright © 2022 American Chemical Society [41]; (**c**) The g-C_3N_4 in deionized water under 365 nm light; (**d**) the PL spectra of the g-C_3N_4, g-C_3N_4 in water and in the DI water [44].

4. g-C_3N_4 Preparation

Synthetic techniques for graphitic carbon nitride (g-C_3N_4) were first reviewed by Thomas et al. in 2008 [26]. g-C_3N_4 can be synthesized with various techniques such as chemical vapor deposition (CVD), solvothermal, and plasma sputtering deposition. Chemical vapor deposition to deposit g-C_3N_4 thin film on indium-tin-oxide (ITO), was performed by Ye et al. [27]. In this method, the mixture of thiourea and melamine was put at the bottom of a crucible with ITO substrate above it and finally transferred to the muffle furnace. CVD has several advantages and disadvantages. To be more specific, thin films prepared by CVD are cohesive in all dimensions, which is suitable for elaborately shaped pieces and helps users to fill the insides, undersides, high aspect ratio holes, etc. CVD does not require high vacuum and can deposit a wide variety of materials to prepare high purity composites. In contrast, physical vapor deposition (PVD) such as sputtering requires a high vacuum atmosphere. The drawback of CVD is that some CVD precursors are costly, and can be highly toxic, explosive, or corrosive, such as $Ni(CO)_4$, B_2H_6, and $SiCl_4$, respectively. The by-product of this method, including CO, or HF, can also be hazardous. The substrates are limited since they should tolerate high temperatures [46].

The graphitic carbon nitride nanocone arrays were grown onto the Ni-coated Si (100) substrate, using plasma sputtering deposition [47]. This method requires a vacuum chamber and a plasma source with a discharge cavity. Thermal condensation is an economical, energy-efficient approach, which has a higher chance for scaleup for commercialization. The solvothermal methods have some drawbacks such as more synthetic steps compared

to the thermal condensation method; however, they can be cost-effective, low energy consumption methods with more controllable size and morphology [48–50].

Several C−N precursors such as urea, thiourea, melamine, cyanamide, and dicyanamide are used for g-C_3N_4 synthesis (Figure 6a). The procedure is depicted in Figure 6b [51–55]. Among them, cyanamide and its derivates such as dicyanamide suffer from low solubility and high cost [56]. Pham and Shin showed that urea and melamine cause poor interconnection of g-C_3N_4 to $NiTiO_3$ since melamine provides a segregated g-C_3N_4 structure with no connection to the $NiTiO_3$ phase, and urea makes a condensed g-C_3N_4 structure by releasing oxygen-containing gas during the thermal condensation [56]. Dicyandiamide and thiourea with higher reactivity towards a polymerization reaction create strong Ti−N bonds in the composite, and allow for charge carrier formation, which is important for degradation of organic contaminants [57]. The order of photodegradation ability of bisphenol A (BPA) is g-C_3N_4-Melamine in N_2 atmosphere ≈ g-C_3N_4-dicyandiamide > g-C_3N_4-dicyandiamide in N_2 atmosphere > g-C_3N_4-Melamine > g-C_3N_4-Urea ≈ g-C_3N_4-Urea in N_2 atmosphere [58]. The differences between the catalytic activities are mainly due to the different preparation procedures, which can change the type, the density of active sites, the network of sp2 hybridized carbon, nitrogen, and oxygen-containing functional groups [58]. Jung et al. showed that the precursor could affect the morphology of the g-C_3N_4-based systems [59]. The good binding of dicyandiamide (DCDA) to ZnO nanoparticles, lead to the formation of the core-shell morphology DCDA-CNZ composite, resulting in improving the degradation of methylene blue by charge transfer [59]. In contrast, due to the weak interaction of thio and urea with ZnO, thio and urea-CNZ have a porous and segregated morphology and produce gases during the polymerization [59].

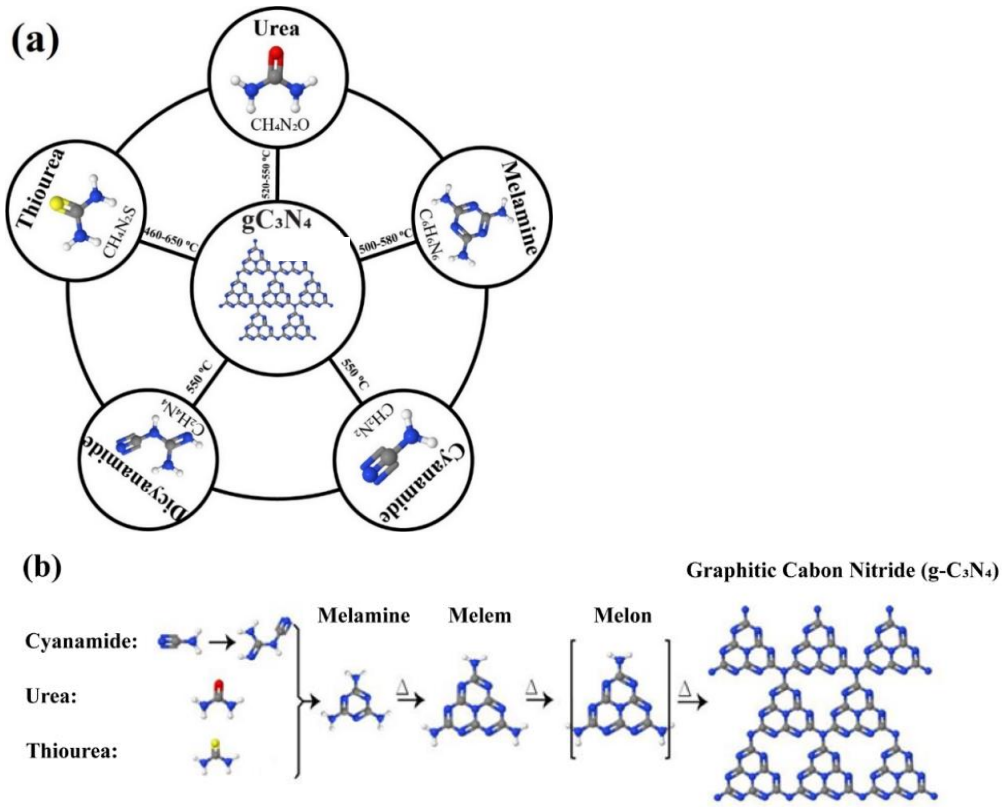

Figure 6. (**a**) Synthesis precursors and calcination temperature for g-C_3N_4 preparation; (**b**) synthesis procedure using cyanamide (dicyanamide), urea, thiourea, and melamine for g-C_3N_4 synthesis (gray, blue, red, yellow, and white balls are carbon, nitrogen, oxygen, sulfur, and hydrogen atoms, respectively).

As shown in Figure 6b, melamine can form from urea, thiourea, and cyanamide (dicyanamide), and then converted to tri-s-triazine (and melam) rings at ~335 and ~390 °C, respectively, and subsequently, g-C_3N_4 discovered from tri-s-triazine polymerization, by heating to 520 °C. Besides, the skeleton becomes prepared over 600 °C, and then beyond 700 °C, g-C_3N_4 is entirely decomposed into small molecules (e.g., NH_3). Figure 7a,b shows the urea and thiourea conversion mechanism into melamine. In this reaction, oxygen atoms in the urea structure help to facilitate g-C_3N_4 condensation and improve stability [60]. CO_2 and NH_3 are the by-products of the reaction of the melamine formation from urea, which can be recycled again to urea. In the formation of the g-C_3N_4, the presence of a crucible lid is so important since not only it prevents the gasses from escaping, but it also provides high pressure in the synthesis atmosphere, which is necessary for the preparation of g-C_3N_4. In other words, a covered alumina crucible should be used during thermal analysis to avoid melamine sublimation.

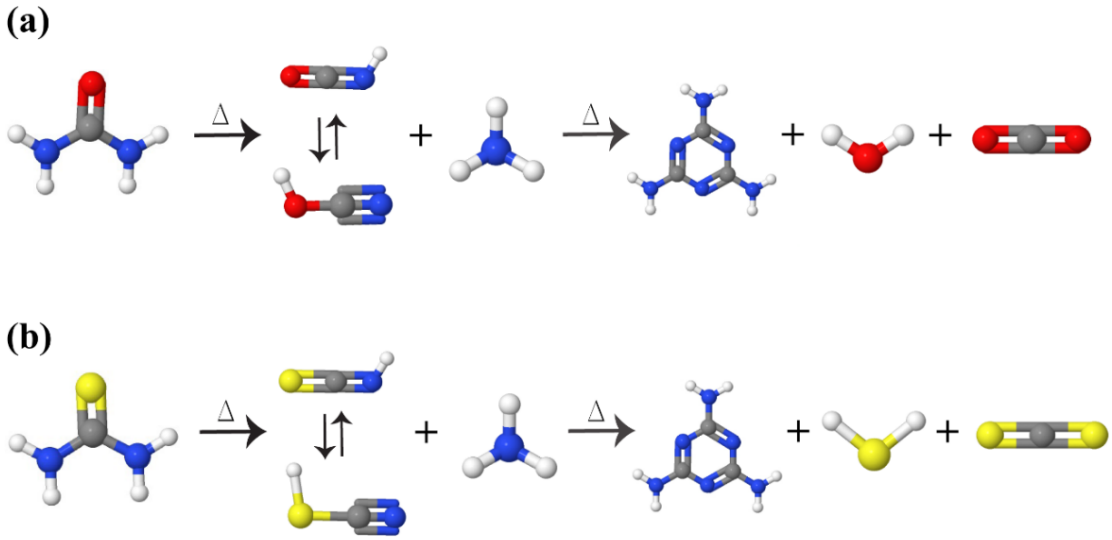

Figure 7. Polymerization of (**a**) urea and (**b**) thiourea into a g-C_3N_4 at high temperatures (gray, blue, red, yellow, and white balls are carbon, nitrogen, oxygen, sulfur, and hydrogen atoms, respectively).

During the heating reaction, the created gas bubbles act as soft templates to produce 24 nm pores in the yellow-colored graphitic carbon nitride [61]. Thiourea is used as another precursor for the g-C_3N_4 formation, and sulfur content improves the connectivity and packing of g-C_3N_4 sheets [60]. The overall conversion of urea and thiourea to melamine is endothermic. The first endothermic reaction of changing urea and thiourea to melamine is at temperatures higher than their melting temperatures, which are ~133 and ~180 °C, respectively, while at the higher temperature, melamine and heptazine were prepared in low pressure at, e.g., atmospheric pressure. To be more specific, the second reaction requires preheating to 260–280 °C to decompose urea in the presence of ammonia, passed over the activated alumina, silica gel, silica-alumina gel, or alumina gel. In order to completely form melamine, the vapors obtained from the first reaction should be maintained at ~400 °C [62]. It should also be noted that the g-C_3N_4 can be prepared by cyanamide and dicyanamide. Specifically, by polycondensation of cyanamide molecules and dicyandiamide, melamine was prepared at ~203 and ~234 °C, respectively [2].

5. g-C_3N_4 Modifications

5.1. Doping

The presence of heptazine ring in the g-C_3N_4 affects electronic structure, toxicity, and density, and is important for applications, especially as biosensors, for photocatalytic hydrogen evolution, and CO_2 conversion. The density-functional theory (DFT) showed that the bandgap of the fully condensed g-C_3N_4 is lower than melem, and polymeric melon, which

are 2.1 eV, 3.5 eV, and 2.6 eV, respectively [63–65]. As previously reported, the polymeric melon has a bandgap close to the defect containing bulk g-C_3N_4 [64]. There are mainly two types of experimental results to calculate the semiconductor bandgap. Specifically, the position of the conductive band (CB) and valance band (VB) can be measured by electrochemical impedance spectra (EIS), and Mott–Schottky (M–S) curve [63]. The result of both methods showed that the position of the conduction band (CB) and valance band (VB) of the g-C_3N_4 is about −1.3 eV and 1.4 eV, respectively [3,66]. The semiconductors' band edges can be tuned by functionalizing, doping, compositing with other materials. Liu et al. reviewed element-doped carbonized nitrogen in detail and investigated their organic pollutants degradation applications [3]. Ai et al. showed that the bandgap value of the phosphate doped g-C_3N_4 decreased from 2.57 eV to 2.49 eV, 2.43 eV, and 2.41 eV by increasing the content of the P element [67]. Other researchers demonstrated that the higher O, Na, Ag, and Co content doped to the g-C_3N_4 structure leads to the lower bandgap value [68–71]. Li et al. investigated the effect of different ratios of Sm to g-C_3N_4. They illustrated that by varying the percentile molar ratios of $Sm(NO_3)_3{\cdot}5H_2O$ with melamine from zero to 0.01%, 0.025% and 0.05%, the bandgap decreased from 2.63 eV to 2.57 eV, 2.50 eV, and 2.44 eV, respectively, so Sm narrowed the g-C_3N_4 bandgap [72]. Table 1 is illustrated the effect of different dopants on the band edge position. We will further discuss and analyze the properties and applications of different g-C_3N_4–metal oxides. g-C_3N_4 is a metal-free semiconductor, which possesses a narrow bandgap suited for visible light absorption (45% of solar energy output) [66]. To have an in-depth investigation of the optical properties of the g-C_3N_4, we will investigate some characteristics of the synthesized g-C_3N_4 such as photoluminescence (PL) and UV-vis spectra. The origin and nature of the PL emission come from three different transition pathway including π*–π, σ*—the nitride atom bridge's lone pair (LP), and the π*–LP transition.

5.2. Metal Oxide-Based g-C_3N_4 Nanocomposite

Different types of metal oxides, such as TiO_2, ZnO, WO_3, iron oxide, tin oxide, etc., can improve the photocatalytic efficiency of the g-C_3N_4 by reducing the electrons-holes recombination and promoting the charge carriers' separation. Consequently, metal oxide-based g-C_3N_4 nanocomposites can be used in different applications with enhanced electric, magnetic, and photocatalytic properties, such as H_2 generation, CO_2 reduction, NO oxidation, degradation of organic and inorganic dyes and other organic material, removal of toxic metal species, especially Cr (VI) from water, antibodies decontamination, solar cells, sensing, etc. [100–104]. In this part of the review, some metal oxide-based g-C_3N_4 heterojunction structures are compared with the g-C_3N_4.

There are five types of charge carrier separation for g-C_3N_4–metal oxide photocatalysts:

(1) Type I heterojunction,
(2) Type II heterojunction,
(3) Z-scheme heterojunction,
(4) p-n heterojunction,
(5) Schottky junction.

Most g-C_3N_4–metal oxide photocatalysts show type II and Z-scheme mechanisms for charge carrier separation. In this section, we will discuss these two heterojunction types.

In type II heterojunctions, two semiconductors are bound to form a stable heterojunction, and the position of the VB of semiconductor A is higher than that of semiconductor B. In this case, because of the difference in voltages, the photoinduced hole migrated from the VB of semiconductor B to that of semiconductor A (Figure 8a). On the other side, electrons are transferred from CB of semiconductor A to that of semiconductor B. The enhanced electrons and holes separation will reduce the rate of the recombination and promote the electrons' lifetime. The construction of type II systems is highly desired for photocatalysis for different applications [7].

Table 1. The electrical properties and application of doped g-C_3N_4.

Doping Element	E_c	E_g	E_v	Application	Further Explanation	Ref
Phosphorus	−1.11 eV	2.55 eV	1.44 eV	Catalytic aromatic alcohols	The presence of P enhances the aldehyde selectivity.	[73]
	−0.33 eV	2.58 eV	2.25 eV	Photocatalytic hydrogen evolution	The g-C_3N_4 tube doped with P improves light absorption. The quantum efficiency of the P-doped g-C_3N_4 tube is 4.7 and 22.4 times higher than that of the g-C_3N_4 tube and bulk g-C_3N_4.	[74]
	−1.34 eV	2.79 eV	1.44 eV	Photocatalytic CO_2 conversion	The P-modified g-C_3N_4 demonstrates the highest photocatalytic efficiency.	[75]
	−1.17 eV	2.69 eV	1.52 eV	Photocatalytic hydrogen evolution	The P-doped structure has a high efficiency in accordance with the recombination, migration, and separation of electron-hole pairs.	[76]
Sulfur	−1.04 eV	2.92 eV	1.88 eV	Photocatalytic nitrogen fixation	Sulfur enhances the adsorption and activation of N_2 molecules of g-C_3N_4 porous nanosheets and uses for photocatalytic nitrogen fixation.	[77]
	−1.23 eV	2.80 eV	1.57 eV	Photocatalytic hydrogen evolution	The H_2 generation rate of N-doped MoS_2 and S-doped g-C_3N_4 is about 23 and 38 times higher than that of pure SCN and NMS with 28.8 μmol/g/h and 17.4 μmol/g/h, respectively.	[78]
	−1.3 eV	2.67 eV	1.34 eV	Photocatalytic hydrogen evolution	The $BiPO_4$/S-C_3N_4 improves photocatalytic activity by facilitating carrier transportation.	[79]
	−1.3 eV	2.69 eV	1.39 eV	Photocatalytic bisphenol degradation	Ag–S-C_3N_4 enhanced the photocatalytic activity since Ag has a great electron storage ability.	[80]
	−1.32 eV	2.66 eV	1.34 eV	Photocatalytic hydrogen evolution	Sulfur promotes the photocatalytic ability of hydrogen evolution about four times higher than the bulk g-C_3N_4.	[81]
	−0.88 eV	2.61 eV	1.73 eV	Photocatalytic CO_2 reduction	The porous O-doped graphitic carbon nitride reveals enhanced photocatalytic activity.	[82]
	−0.76 eV	2.57 eV	1.84 eV	Photocatalytic hydrogen evolution	This result of the band edge value is related to the 1.1% oxygen content mass percentage.	[83]
	−0.37 eV	2.53 eV	2.15 eV		This result of the band edge value is related to the 2.3% oxygen content mass percentage.	
Oxygen	−1.08 eV	2.93 eV	1.85 eV	Photocatalytic hydrogen evolution and 2,4-dinitrophenol	The oxygen dopant with Pt exhibits excellent photocatalytic hydrogen evolution in overall water splitting with 29.6 μmol/(g·h), and O-g-C_3N_4 NR reached up to approximately 100% removal efficiency of 2,4-dinitrophenol within 75 min.	[84]
	1.51 eV	2.70 eV	−1.19 eV	photocatalytic water splitting	This band edge value is related to CN-x = 0 (*x* refers to the quantity of citric acid (gr)).	[85]
	1.50 eV	2.62 eV	−1.16 eV		This band edge value is related to CN-0.2.	
	1.46 eV	2.52 eV	−1.06 eV		This band edge value is related to CN-0.4.	
	1.46 eV	2.49 eV	−1.03 eV		This band edge value is related to CN-0.6.	
Carbon	−1.13 eV	2.54 eV	1.41 eV	Thermal oxidation etching process	C-doped g-C_3N_4 improves the catalytic activity by extending the visible light absorption.	[86]
Boron	−0.8 eV	2.8 eV	2 eV	Photocatalytic Oxygen evolution, Cr(VI) reduction	This structure is used for Cr(VI) reduction and O_2 generation simultaneously.	[87]
Nitrogen	−0.5 eV	2.4 eV	1.9 eV	Photocatalytic tetracycline degradation	This band edge value is related to the nitrogen-doped g-C_3N_4 used for Photocatalytic tetracycline degradation.	[88]
	−0.6 eV	2.5 eV	1.9eV		This band edge value is related to the nitrogen-doped g-C_3N_4 nanosheets.	
	−0.33 eV	1.82 eV	1.49 eV	Photocatalytic phenol degradation	N-doped g-C_3N_4 possesses a narrow bandgap since the N atom introduced an inter-bandgap, resulting in the redshift in the absorption UV-vis peak.	[89]

Table 1. *Cont.*

Doping Element		E_c	E_g	E_v	Application	Further Explanation	Ref
Metal	Na	−1.16 eV	2.77 eV	1.36 eV	17α-ethynylestradiol mineralization	The photostable Na doped g-C_3N_4 content causes the photoabsorption enhancement.	[70]
	K	−1.08 eV	2.72 eV	1.64 eV	Photocatalytic CO_2 reduction	K content causes defects leading to improving catalytic activity by reducing the electron-hole recombination.	[90]
	Ti	−1.02 eV	2.5 eV	1.48 eV	Photocatalytic enhancement	Ti-doped g-C_3N_4 caused narrower bandgap and reduced carrier recombination resulting in higher absorption.	[91]
	Mn	−0.59 eV	2.56 eV	1.97 eV	Photocatalytic methylene blue degradation	The Mn-doped g-C_3N_4 nanoribbon reveals a great potential photocatalytic agent for water splitting coupling with MB degradation.	[92]
	Ag	-	2.60 eV	-	Photocatalytic oxidation of methylene blue	The higher Ag content leads to the lower bandgap of the structure, and a lower recombination rate is observed in the Ag-doped g-C_3N_4.	[93]
	Fe	−1.10 eV	2.50 eV	1.40 eV	Environmental pollution control	Fe^{3+} with nitrogen in heptazine forms a σ-π bond and can accelerate the electron-hole separation.	[94]
	Co	−0.36 eV	2.62 eV	2.26 eV	Photo-electrochemical water oxidation	Co-doped g-C_3N_4 reduces the electron-hole recombination rate and demonstrates promising photocurrent and electrical conductivity.	[95]
Co-doped	P, O	−0.80 eV	2.30 eV	1.50 eV	Photocatalytic fluoroquinolone antibiotics degradation	The degradation rate of enrofloxacin was 6.2 times higher for phosphorus and oxygen co-doped graphitic carbon nitride (POCN) than g-C_3N_4.	[96]
	P, S	-	2.6 eV	-	Photocatalytic hydrogen evolution	The high photocatalytic activity can be observed because of the synergic impact of P and S co-doping.	[97]
	B, F	-	2.72 eV	-	Photocatalytic hydrogen evolution	B, F co-doped g-C_3N_4 improves the charge generation and the separation efficiency.	[98]
	Na, O	-	2.72 eV	-	Photocatalytic hydrogen evolution	Na, O co-doped g-C_3N_4 reveals that photocatalytic H_2 production activity was seven-fold improved by enhancing absorption of UV-vis spectra.	[99]

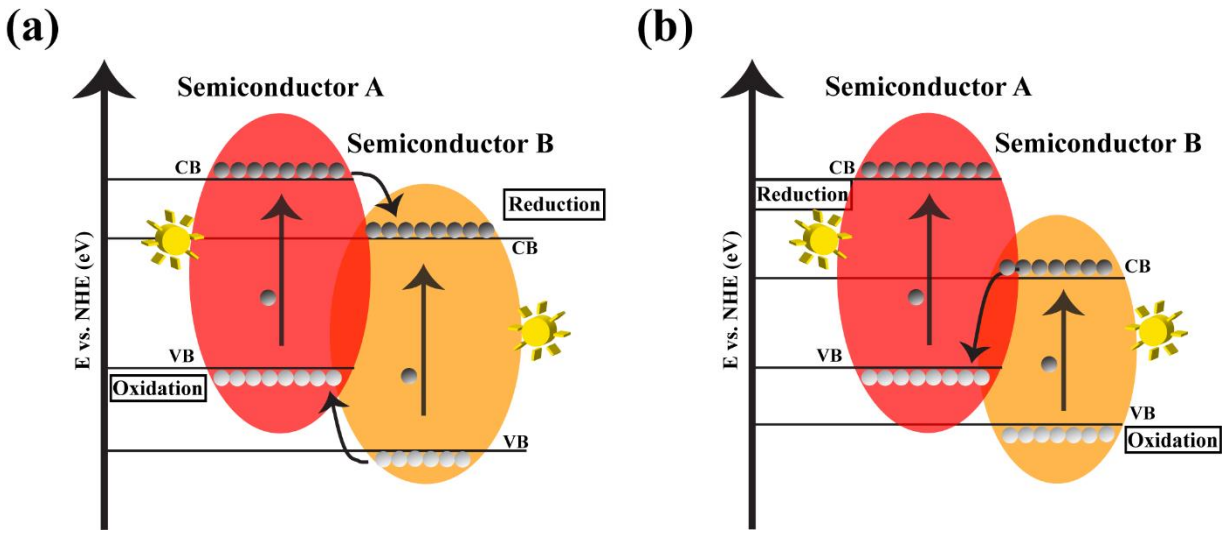

Figure 8. The two most common heterojunction types in g-C_3N_4–metal oxide photocatalysts: (**a**) type II heterojunction, (**b**) Z-scheme heterojunction (white and dark balls are holes and electrons, respectively).

The other heterojunction type is the direct Z-scheme photocatalytic system, which was initially suggested by Bard et al. in 1995 [105]. As shown in Figure 8b, in this heterojunction type, the generated electrons on the CB of semiconductor B transfer to the VB of semiconductor A and combines with the photogenerated holes. This type of photocatalysts can be helpful for both reducing the recombination by an increase of the electrons and holes separation and improving the redox ability [7]. Even if the electrons, and holes combine and generate hν in these heterojunctions, other photogenerated carriers can replace them.

Different patterns of the migration of electrons and holes are due to the driving force of the electric field, formed by the band edge positions of different semiconductors. Depending on the electrical field direction, charge carriers start moving to reduce the energy of the system. Thus, different systems are defined based on the migration of electrons and holes in the heterojunction. The difference in each type is mainly due to the movement of electrons and holes. All types can be used in different photocatalytic activities.

5.2.1. TiO_2-g-C_3N_4

Among the investigated semiconductor photocatalysts, TiO_2 has a suitable conduction band position, excellent stability, cost-effective preparation approach and is one of the most promising catalytic materials [106]. Fujishima and Honda were pioneers who researched using TiO_2 photocatalytic behavior in 1972 [107]. To improve TiO_2's photocatalytic efficiency, researchers would like to reduce the bandgap of the system by doping with other elements and compositing with other compounds to absorb visible light energy [108]. To deal with TiO_2's limitations, researchers have been using doping elements and compositing with organic material, such as conjugated polymers and g-C_3N_4, since they have a narrow bandgap [108]. Boron is an effective dopant, which can improve the photocatalytic applications of TiO_2 coupled with carbon nitride, as shown by Christoforidis and coworkers [109]. In another study conducted by this research group, TiO_2 and carbon nitride nanosheets were synthesized by hydrothermal in-situ approach, improving the catalytic application. The mentioned materials have high porosity to ensure a high concentration of reactants in the vicinity of catalytic sites, used for CO_2 reduction [110].

Various synthetic methods such as co-calcination, hydrothermal treatment, solvothermal, and microwave-assisted to prepare the g-C_3N_4-TiO_2 heterojunction [111–113]. The preparation of g-C_3N_4-TiO_2 heterojunction widely includes the hydrothermal and calcination method [114]. Figure 9 illustrates the schematic of the TiO_2/g-C_3N_4 preparation route.

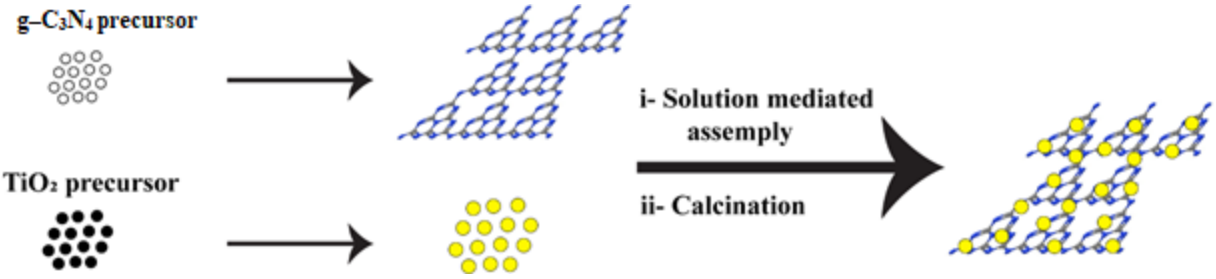

Figure 9. Schematic illustration of TiO_2/ g-C_3N_4 heterojunctions synthesis approach.

The conductive band of g-C_3N_4 (E_{CB} = −1.4 eV) is higher than those of anatase TiO_2 (E_{CB} = −0.5 eV), so the proper bandgap alignment helps to reduce the electron-hole recombination by increasing their separation and boost the space charge accumulation at the interface. Recombination is defined as a process of electrons and holes annihilation. The most common type of recombination is known as radiative recombination, which occurs when electrons and holes in a conductive and valance band, respectively, recombine and emit a photon. As discussed in the following sections, the presence of electrons and holes will assist us in different stages of photocatalytic activities. So, suppressing the charge recombination is crucial in the photocatalytic applications of semiconductors and heterojunctions. At the end of section three, we talked about how g-C_3N_4-based heterojunction separates the position of the electrons and holes. The charge carrier separation makes electron-holes recombination less favorable, so we can use these heterojunctions for photocatalytic activities.

Figure 10a illustrates the conduction, valance, and bandgap position of the g-C_3N_4 and TiO_2 and reveals that the g-C_3N_4-TiO_2 structure improves the photo-induced electrons flow from the g-C_3N_4 conductive band to that of TiO_2, which promotes the photoelectrical ability of the final composite. Thus, the photogenerated electrons tend to accumulate in the TiO_2 conductive band since the conductive band of TiO_2 is more positive than that of g-C_3N_4, (Figure 10a). In contrast, the holes transfer in an inverse way, which can provide type II heterojunction [112,115]. Due to the high recombination barrier, the heterojunction provides a high interfacial area for facilitating carrier transformation and separation to suppress the electron-hole recombination to improve the photocatalytic activity.

Kočí et al. successfully deposited TiO_2 on the g-C_3N_4 surface by hydrothermal approach followed by calcination processing [116]. In this research, the mixture of TiO_2 and g-C_3N_4, prepared by thermal hydrolysis and polycondensation from melamine, respectively, should be mixed in distilled water for 16 h in an air atmosphere dried at 60 °C. Finally, the dried sample should be maintained at 450 °C in a covered crucible with a heating ramp of 15 °C/min in the air in a muffle furnace. The highest photocatalytic performance was obtained under UVA (λ = 365 nm) irradiation compared to other types of ultraviolet (UV) rays (UVB, and UVC), which is attributed to the high separated charge carrier. The low rate of recombination leads to the great photocurrent stability. In another work on g-C_3N_4-TiO_2 heterojunction structure, Alcudia-Ramos et al. demonstrated that the prepared heterojunction has a higher photocatalytic efficiency than the individual g-C_3N_4 and TiO_2 [112]. The researcher also showed that solvothermal synthesis enhances tri-s-triazine's carbonization [117]. Miranda et al. used an impregnation method to prepare g-C_3N_4-TiO_2 [118]. The presence of the g-C_3N_4 in the heterojunction endows the high specific area to the structure. The researchers also used the photochemical reduction method to prepared g-C_3N_4-TiO_2 based nanocomposite. They also demonstrated that in the TiO_2/g-C_3N_4/G composite, TiO_2 was a semiconductor to capture visible light and also prevents g-C_3N_4/G stacking [119].

Several parameters affect the g-C_3N_4-TiO_2 heterojunction structure. Various research works have been investigated the effect of the g-C_3N_4's ratio. Wang et al. prepared this microstructure with 10%, 30%, 50%, 70% of g-C_3N_4, which are labeled with (x = 10, 30,

50, and 70) [110]. All the XRD results from different publications have shown the same diffraction pattern. As a case in point, the XRD pattern of g-C_3N_4-TiO_2 is illustrated in Figure 10b. In the TiO_2 diffraction pattern, the peaks at 25.5, 37.7, 48.2 and 54.1 °C are related to the (101), (004), (200) and (105) planes, respectively. Furthermore, there is no g-C_3N_4 characteristic peak at 13.1 °C in the g-C_3N_4-TiO_2 hybrid sample, which may be attributed to the low crystallinity of g-C_3N_4 compared to the TiO_2 in the microstructure. However, the peak at 27.5 is obviously observed in all samples. The more g-C_3N_4 ratio in the structure leads to the higher XRD intensity at 27.5 °C and the lower peak intensity at 25.5 °C [120]. TiO_2 possesses a high crystallinity so the characteristic peak at 25.5 °C is higher than 27.5 °C. There are no obvious changes in other characteristic peaks in the composite XRD patterns. The FT-IR spectra of the g-C_3N_4-TiO_2 structures are demonstrated in Figure 10c [120]. In all FT-IR analyses, stretching vibration of the Ti–O and Ti–O–Ti is observed at about 475 cm^{-1}. Additionally, peaks at 3419 cm^{-1} are attributed to the absorbed moisture and hydroxyl group in the structure. The peak at 2360 cm^{-1} that appeared in all samples is mainly due to the adsorbed CO_2. All the characteristic peaks at TiO_2 and g-C_3N_4 are observed in the composite samples. The pore size distribution of the g-C_3N_4, TiO_2, g-C_3N_4-TiO_2 is illustrated in Figure 10d [120]. The pore size at ~3.5 nm, 10 nm, and 3.8 nm, 32 nm is due to the presence of TiO_2, and g-C_3N_4, respectively. Additionally, the BET specific area of the g-C_3N_4-TiO_2 hybrid structure was increased at the higher g-C_3N_4 content. Finally, the higher the bandgap of TiO_2, the lesser the absorption wavelength at higher than 400 nm (Figure 10e). The g-C_3N_4 revealed the absorption band extending to about 430 nm, which is mainly due to the low bandgap [120]. The blue shift in the absorption spectra was also demonstrated at a higher g-C_3N_4 ratio in the structure. It was shown bandgaps calculation of the g-C_3N_4, TiO_2, g-C_3N_4-TiO_2. The results revealed that the bandgap of CNT50 samples is 2.92 eV, which is like the bulk g-C_3N_4 with the bandgap of 2.9 eV and narrower than the bandgap of TiO_2 (3.20 eV). Due to the narrow bandgap and heterojunction formation, the hybrid composite not only suggested the higher generation of the electron and hole but also improved photocatalytic activity [120,121]. Li et al. synthesized g-C_3N_4@TiO_2 hollow sphere nanostructure with high crystallinity [122]. In this work, researchers used the different ratios of TiO_2 hollow sphere and melamine (1:2, 1:4, and 1:8) in the solution, which are called HS-CNTO1, HS-CNTO2, and HS-CNTO3, respectively. They demonstrated that the recombination rate of the photogenerated electron-holes decreased by introducing the TiO_2 in the g-C_3N_4 structure. In all samples, the sharp PL emission peak at 455 nm can be observed. The intensity of the PL peak reduced as the g-C_3N_4 content ratio decreased [122]. In addition, as can be seen in Figure 10f, the electron resistance decreased when g-C_3N_4-TiO_2 heterojunction was used. Additionally, stability is another vitally important factor in determining the photocatalytic activities, and it is shown that the g-C_3N_4-TiO_2 heterojunction demonstrates excellent stability after three to five cycles under different circumstances [117,120,122,123].

Many factors may affect the g-C_3N_4-TiO_2 heterojunction productivity and improve the photocatalytic activity by enhancing the charge carrier separation and prevent recombination [124–126]. Rathi and coworkers showed that the CuNi@g-C_3N_4-TiO_2 nanocatalyst had a 3-fold and 5-fold higher photocatalytic activity than bare g-C_3N_4 and TiO_2 nanorod for Rhodamine B degradation. Besides, the photocurrent density of the TiO_2 nanorod, bare g-C_3N_4, Cu@g-C_3N_4, Ni@g-C_3N_4, and TiO_2/CuNi@g-C_3N_4 is 0.108 mA/cm^2, 0.377 mA/cm^2, 0.530 mA/cm^2, 0.6012 mA/cm^2, and 0.890 mA/cm^2, respectively. It should also be mentioned that the charge separation was promoted since the presence of Cu and Ni species [126]. In another work, researchers also prepared Ti^{3+}-TiO_2/O-g-C_3N_4 heterojunctions via a hydrothermal approach [125]. In this synthesis approach, 1 g g-C_3N_4 should disperse with titanium oxohydrides sol precursor at room temperature for 20 min, ultrasonically. The collected sample should transfer into the Teflon-lined autoclave at 160 °C for 27 h and then be washed and dried at 60 °C for 3 h. This method was used to prevent the g-C_3N_4 aggregation and fabricate exfoliated g-C_3N_4 nanosheets. The synthesized heterojunction significantly decreased the regenerated electron-hole pairs' recombination. Additionally,

the conductivity is greatly enhanced and widens the light absorption range by adding the Ti^{3+}, and O. P is another element used to improve the heterojunction connection and promote photocatalytic activity by facilitating the carriers' transfer and separation [127,128].

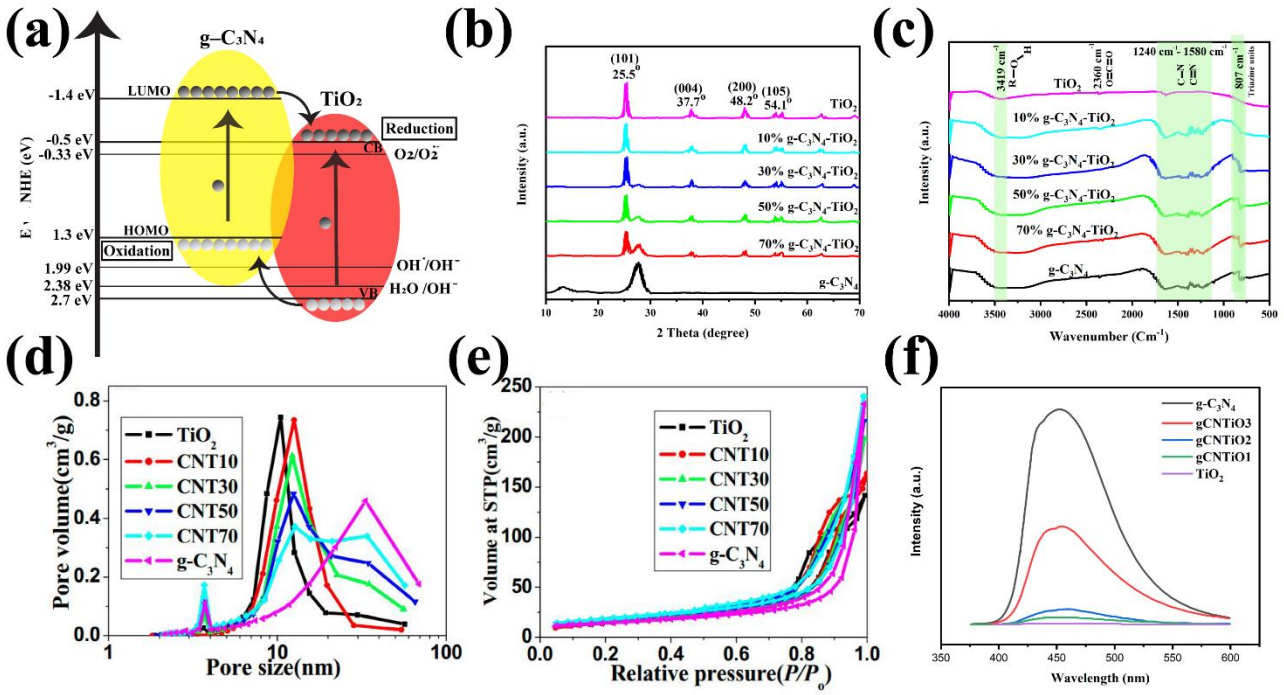

Figure 10. (**a**) Proposed mechanism for charge transfer of type II of the g-C_3N_4-TiO_2 heterojunction interface under visible light irradiation; (**b**) XRD patterns; (**c**) FT-IR spectra of the g-C_3N_4-TiO_2 heterojunction; (**d**) the pore size distribution curves; (**e**) UV-vis spectra of the prepared TiO_2, g-C_3N_4, and TiO_2- g-C_3N_4 composites, Copyright © 2022 Elsevier [120]; (**f**) PL emission spectrum of TiO_2, g-C_3N_4 -TiO_2, and g-C_3N_4 products, Copyright 2019 © American Chemical Society [122].

Various novel metal nanoparticles are leading to the improvement of photoexcited semiconductors because the surface plasmonic effect is beneficial to reduce the photogenerated electron-hole recombination, improve the efficiency of visible light absorption and photocatalytic activity. Silver, and gold nanoparticles, for instance, have high stability and good conductivity. Au nanoparticles can increase the electron concentration onto their surface and enhance and extended adsorption for catalytic activity by its surface π bond [129–131]. Ag nanoparticles (AgNPs) are also used to modify the g-C_3N_4-TiO_2 heterojunction [132–135]. The presence of AgNPs not only promotes the visible light response due to the surface plasmon resonance (SPR) effect, but also, they can result in capturing the electrons, to separate them, and transfer them more easily. These electrons react with the absorbed O_2 on the AgNPs modified TiO_2@g-C_3N_4 to form $O^{-}{}_2$. With reference to the high specific area, electrical conductivity, and mobility, different graphene-based materials such as reduced graphene oxide [119,136]. Other materials can also be used to modified g-C_3N_4-TiO_2 heterojunction to increase the specific area and separate the photo-induced electron-hole pairs to enhance photocatalytic efficiency [137–139].

The structure and morphological evaluation of the prepared g-C_3N_4–metal oxide-based heterojunctions have been investigated in different research works [140–143]. Jo et al. revealed structural properties of g-C_3N_3-TiO_2 heterojunctions, which are consistent with other similar composites [144]. Figure 11a showed the transmission electron microscope (TEM) micrograph and the selected area electron diffraction (SAED) pattern of 5%-g-C_3N_4/TiO_2 nanoparticles. Researchers observed that g-C_3N_4 nanolayer uniformly is covered with TiO_2 nanoparticles, which suggested an intimate interface between them. Besides, the inset Figure 11a showed that the circular rings corresponded to the (101), (004),

(200), and (105) planes of the polycrystalline TiO_2 nanoparticles anatase phase. A TEM image showed that the TiO_2 nanoparticles are deposited onto the layered structure on g-C_3N_4. Moreover, the high-resolution transmission electron microscope (HR-TEM) images of the 5%-g-C_3N_4/TiO_2 nanotube indicates the interplanar distance of 0.350 nm, attributed to the (101) plane of anatase phase of TiO_2 (Figure 11b,c). In addition, elemental mapping analysis of the 10%-CN/TNP (Figure 11d) suggested that TiO_2 is uniformly present onto the g-C_3N_4 surface. Figure 11d also revealed the presence of Ti, O, C, and N, which suggested the co-existence of both layered g-C_3N_4 and TiO_2 nanotube [144].

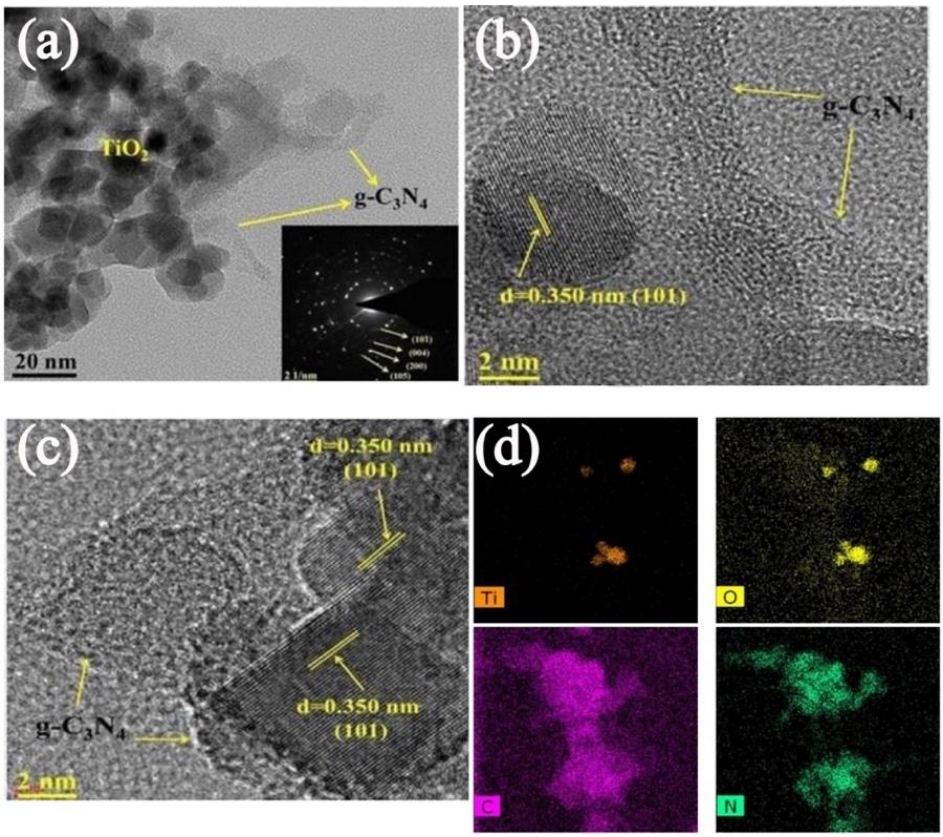

Figure 11. (**a**) TEM images of 5%-g-C_3N_4/TiO_2 nanoparticles (inset SAED pattern); (**b**,**c**) HRTEM images of 5%-g-C_3N_4; (**d**) elemental mapping image of Ti, O, C, N elements of the 10%-g-C_3N_4 /TiO_2 composite, Copyright © 2022 Elsevier [144].

5.2.2. ZnO-g-C_3N_4

ZnO nanostructures such as nanosheets, nanoplates, and nanorods are semiconductors that have been used for preparing of g-C_3N_4-based heterojunctions. Like the TiO_2, the ZnO bandgap is about ~3.2 eV with E_{CB} and E_{VB} of about 2.7 eV and −0.5 eV, respectively [145]. We showed that the ZnO nanostructure's size, shape, and order could be tuned by an interplay of magnetic and gravity forces [146]. We also demonstrated the enhanced microbial detection capability when the synthesis was conducted under these external forces by changing the materials' electrical resistance based on surface interactions. Because of low-cost of the preparation, having a large surface area, high aspect ratio, proper bandgap energy, minimal toxicity, and good stability, ZnO nanostructures have captured considerable researchers' attention [147,148]. However, ZnO suffers from minimal light absorption (5% of the ultraviolet spectrum of the sun energy). Additionally, a high electron-hole recombination rate is another undesirable factor of ZnO for photocatalytic applications.

To deal with these problems the heterojunction of ZnO with g-C_3N_4 might be an option for different photocatalytic applications because, coupling g-C_3N_4 with ZnO nanostructures can improve charge migration, separation and prevent electron-hole recombination.

Researchers have reported various methods for preparing the g-C_3N_4-ZnO structure, such as hydrothermal, solvothermal, atomic layer deposition, etc. [149–153]. Jung et al. synthesized g-C_3N_4-ZnO with various thermal treatment and condensation temperatures (T = 350, 400, 450, 500 °C). The BET specific area and ZnO crystallite size of the prepared Z-scheme g-C_3N_4-ZnO structure is decreased by increasing the thermal treatment temperature [154]. Other researchers who designed g-C_3N_4-ZnO via thermal treatment announced that the optimal amount of the g-C_3N_4 content in the composite is 5.0 wt.% [155]. Melamine and $ZnCl_2$ should be vigorously stirred for 20 min in a 250 mL beaker, then, Na_2CO_3 is added dropwise into the suspension and stirred magnetically for 30 min, and finally, dried at 60 °C for 30 min. The product was placed into a crucible with a cover to prevent from the volatilization of melamine and heated at 500 °C for 2 h at a rate of 10 °C/min. The g-C_3N_4/ZnO photocatalysts were obtained after deamination treatment at 520 °C for 2 h. The effect of different g-C_3N_4 precursors such as dicyandiamide (DCDA), urea, and thiourea on the g-C_3N_4 and ZnO interaction and structural morphology was investigated in another work [156]. The excellent interaction of the DCDA-ZnO results in the perfect Z-scheme charge transfer core-shell structure with the ZnO core and shell of the g-C_3N_4, and the low electron density of the PL emission resulting in promoting the efficiency of the Methylene Blue (MB) photocatalytic degradation. If the interaction between the precursors, such as urea and thiol, and ZnO is weak, the porous, segregated morphology is obtained. Hydrothermal method to prepare g-C_3N_4-ZnO heterojunction [149] not only is a low-cost preparation but also Zhang et al. revealed that it could detect nine pesticide residues in four different samples simultaneously. The solvothermal synthesis method of the preparation of the g-C_3N_4-ZnO modified the TiO_2 nanotube arrays by using the ethylene glycol solution is reported by Mohammadi et al. [150]. Zhang and coworkers synthesized the g-C_3N_4-ZnO heterojunction composite in the metal ion-containing ionic liquid's presence by the solvothermal method [156]. g-C_3N_4 was added to the $ZnCl_4$ in an ethanol solution, sonicated, and mixed with NaOH. Then, the mixture should be placed in a 25 mL Teflon-sealed autoclave and maintained at 160 °C for 24 h. After washing with distilled water and absolute ethanol, the dried g-C_3N_4-ZnO powder was provided. The strong interaction between g-C_3N_4 and ZnO result in the higher migration of the generated electrons and slower recombination rate was prepared. They revealed that the power conversion of the structure composed by the solvothermal approach compared to the pure TiO_2 nanotube arrays increases from 1.04% to 2.45%. Besides, the uniform type II heterojunction between g-C_3N_4 and ZnO can also be synthesized by atomic layer deposition (ALD) [151]. The mentioned heterojunction composite, synthesized by the ALD method, possessed a stable dispersion of g-C_3N_4 powder in the reactor, which prevented the charge carrier recombination. Mechanochemistry (mechanical milling) is also employed to prepare g-C_3N_4-ZnO composite [157]. This method provided significant photocatalytic stability and enhanced the composite's photocatalytic activity, which was 3-fold higher than the bulk g-C_3N_4 because of the strong interaction with ZnO. Figure 12 illustrates the schematic of the ZnO/g-C_3N_4 preparation method.

Introducing the ZnO to the g-C_3N_4 is proved that this structure can enhance photocatalytic performance such as charge transfer and separation and decrease the photogenerated carriers' recombination (Figure 13a) [159–163]. In recent years, several types of research have been worked on the characterization of these heterojunctions. For example, Wang et al. demonstrated the eight XRD characteristic peaks for the pure Zn in the g-C_3N_4-ZnO sample, shown in Figure 13b [164]. The reduction in the g-C_3N_4 content results in a decrease in the intensity of its two prominent characteristic peaks. Besides, they also revealed the FTIR analysis of the synthesized composites. The g-C_3N_4-ZnO composites' FTIR peaks show the main peaks of the bulk g-C_3N_4, which are shifted to the lower wavenumber, and this is because of the low strength of the characteristic bonds. The FTIR peaks of the g-C_3N_4-ZnO heterojunction are also similar to those of the main peaks of the g-C_3N_4 wavenumber. The indication announces a chemical bond in the heterojunction between g-C_3N_4 and ZnO so that this structure will improve the charge transfer and photocatalytic efficiency. Moreover,

the UV-vis DRS spectra of the g-C_3N_4, ZnO, and g-C_3N_4-ZnO heterojunction with the different g-C_3N_4 ratio is illustrated in Figure 13c [164]. The absorption edge of the g-C_3N_4 is about 460 nm, attributed to the bandgap of 2.69 eV. Besides, the absorption wavelength of the pure ZnO appeared at 396 nm showing the bandgap of 3.13 eV. Finally, the g-C_3N_4-ZnO revealed the redshift for the higher g-C_3N_4 content, which is extended to the visible-light region. The intense visible light absorption is another significant indication of the strong chemical interaction and more electron-hole generation leading to the photocatalytic activity's improvement [164]. The high photocatalytic activity of the mentioned structure is mainly used to degrade of dyes such as malachite green (MG). After the reaction of the photocatalyst with MG, the photocatalytic rate in 0, 5, 10, 15, 20, 25, 30, 35 and 45 min was measured (Figure 13d) [165]. A similar analysis was conducted on other dye types, such as Rhodamine-B (Rh–B), Congo red (Con-R), and Red ink (RI) solution. The results show the degradation efficiency after 45 min in the presence of the g-C_3N_4 was determined ~97.24%, 82.37%, 70.05% and 46.99% for MG, Rh-B, Con-R, and RI's degradation, respectively [165]. Figure 13e demonstrated the photoinduced charge transfer capability of g-C_3N_4-ZnO nanorod arrays. The photocurrent density of the prepared materials was generated and increased under visible light irradiation. However, the photocurrent density decreased as the illumination was stopped. It was also revealed that the g-C_3N_4-ZnO produced the most photocurrent density compared to the bare ZnO and g-C_3N_4, showing excellent charge transfer and separation. The charge transfer resistance is depicted in Figure 13f, shown impedance spectroscopy (EIS) Nyquist plots [160]. The arc radius in EIS spectra corresponds to the resistance of the interface layer at the photocatalyst surface. As observed in Figure 13f, the smaller arc radius is shown for g-C_3N_4-ZnO than that of g-C_3N_4 and ZnO. To be more specific, the smaller arc radius leads to the lower charge transfer resistance, resulting in the improved photogenerated transformation at the interface. PL spectra announce the photocurrent recombination, separation, and migration rate [160]. The ZnO PL emission wavelengths under the excitation wavelength of 350 nm were low-intensity emissions at 445 nm and 600 nm with low intensity. Besides, the emission spectra of the g-C_3N_4 and g-C_3N_4-ZnO heterojunction under the same excitation wavelength are 452 nm and 506 nm, respectively. Moreover, the higher PL intensity of the composite than that of g-C_3N_4 and ZnO reveals a more recombination rate of photogenerated charge carriers via the Z-scheme pathway. One of the most critical factors in photocatalytic efficiency is the catalyst's lifetime. Recyclability of g-C_3N_4-ZnO is obviously illustrated by the negligible loss of the photocatalytic activity after the five cycles resulting in good stability of the g-C_3N_4-ZnO photocatalyst [166–168].

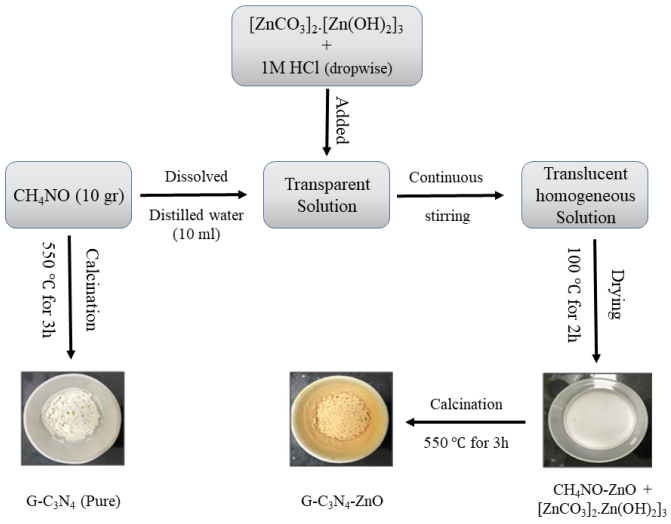

Figure 12. Schematic of the g-C_3N_4−ZnO heterojunction synthesis approach, reproduced from Reference [158].

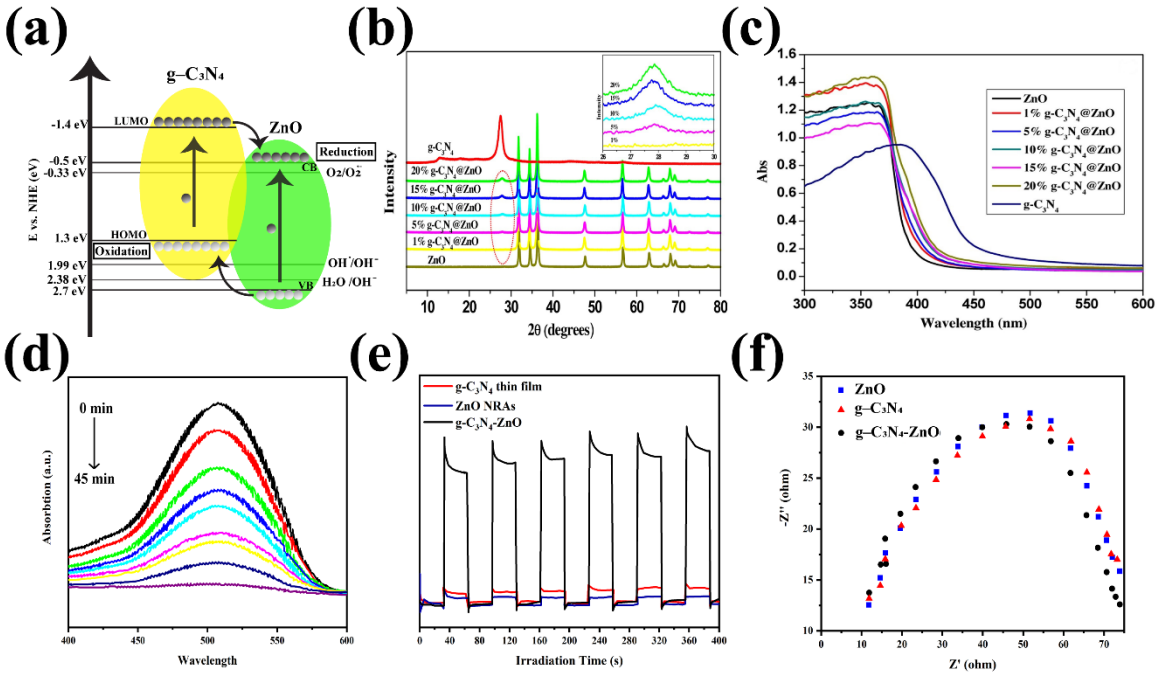

Figure 13. (**a**) Proposed mechanism for charge transfer of type II of the g-C_3N_4-ZnO heterojunction interface under visible light irradiation; (**b**) XRD patterns of ZnO, g-C_3N_4, and g-C_3N_4@ZnO samples; (**c**) UV-vis absorption spectra of ZnO, g-C_3N_4, and g-C_3N_4@ZnO composites, Copyright © 2022 Elsevier [164]; (**d**) Malachite Green (MG) photocatalytic activity of the g-C_3N_4/ZnO photocatalyst, Copyright © 2022 Elsevier [165]; (**e**) the pure ZnO NRAs, g-C_3N_4 thin film, and g-C_3N_4/ZnO heterostructure photocurrent response to a light on-off under visible light illumination (≥420 nm), Copyright © 2022 Elsevier [159]; (**f**) Nyquist plots of the ZnO, g-C_3N_4, and g-C_3N_4/ZnO catalysts. Reproduced from Reference [160].

The doping of the heterojunction is a method to change and tune the properties of the bare g-C_3N_4-ZnO heterojunction. The metal elements are one of the excellent candidates used as dopants in the g-C_3N_4-ZnO structure. Ahmad et al. illustrated the effect of different metal dopants on photocatalytic efficiencies [169]. Ag-doped g-C_3N_4-ZnO showed the highest specific area compared to the pure ZnO, g-C_3N_4, and Al, Mg, Ni, Cu-doped heterojunctions. The redshift is observed for UV-vis absorption for the metal-doped g-C_3N_4-ZnO composite compared to the pure ZnO, revealing the more visible light absorption, and inducing a higher charge carrier generation rate [169]. The bandgap of the ZnO, g-C_3N_4, Al, Mg, Ni, Cu, and Ag-doped g-C_3N_4-ZnO, which is determined by the Tauc's plots, is 3.23 eV, 2.66 eV, 3.15 eV, 3.08 eV, 3.06 eV, 3.0 eV and 3.05 eV, respectively. The PL spectra of these doped composites demonstrated the three emissions at 391 nm, 456–466 nm, and 550 nm, which are attributed to the free exciton transition or recombination process, bandgap recombination of photoinduced charge carriers, and oxygen vacancies [169]. The photocurrent of the metal-doped structure is higher than that of the pure ZnO and g-C_3N_4. The Cu-doped composite showed the lower electron transition resistance among all composites. It was concluded that the synergistic impact of Cu-doped g-C_3N_4-ZnO, promotes electron mobility and separation efficiency [169]. Photocatalytic activity of the Mg-doped composite is higher than that of ZnO, g-C_3N_4, and g-C_3N_4-ZnO structure. Mg is one of the ideal candidates for charge separation in the composite structure [170]. Other kinds of metal-based materials such as K, Cr, Co, and Fe have shown excellent light absorption, increased photo-induced electron-hole generation and separation, and migration for improved photocatalytic activities [171–174]. ZnO/K@g-C_3N_4 had higher stability after five cycles (84%) for tetracycline removal. Doping the Cr into the g-C_3N_4-ZnO structure promoted photocatalytic performance [172]. 60% g-C_3N_4 /Cr-ZnO photocatalyst had 93% degradation rate in

1.5 h, which is 3.5, 2.5, and 2-fold higher than that of 5% Cr-ZnO, bulk g-C_3N_4, and 60% g-C_3N_4-ZnO, respectively. Nitrogen is another widely important element used as a dopant for the g-C_3N_4-based heterojunctions [147,175–177]. g-C_3N_4 with 7 wt % of N-ZnO showed the highest photocatalytic RhB degradation with 5 and 4 times higher than those of N-ZnO, and g-C_3N_4, respectively [175]. g-C_3N_4-ZnO with N doping exhibited a 77% higher H_2 evolution rate than that of pure carbon nitride and showed a great charge carrier transfer [147,176]. The N-doped heterojunction revealed the high photocatalytic activities for methylene blue degradation since it shows the narrower bandgap [178]. Other researchers showed the impact of carbon doping in the ZnO-g-C_3N_4 composites [177,179–181]. The Z-scheme heterojunction system containing C-doped g-C_3N_4 grafted on the C, N co-doped ZnO was used to improve the optical properties for enhancing the BPA organic pollutants photodegradation and hydrogen evolution reaction [177]. Oxygen and sulfur are also used to improve the efficiency of the composites [181,182].

Different g-C_3N_4-ZnO heterojunction-based ternary composites have been constructed by various researchers worldwide [183–187]. The surface plasmon resonance (SPR) effect of Ag and Au nanoparticles (NPs), resulting in the improved photocatalytic activities improve by increasing the electron-hole generation and separation, so many researchers tend to use Ag NPs in the heterojunction structures [188–192]. Ag NPs facilitate the migration and improve the photoinduced electron-hole pairs separation by creating close interfaces between g-C_3N_4 and ZnO. Besides, Ag NPs reduce the energy barrier for CO_2 to increase the intermediate radicals on the surface of the nanocomposites [191,193]. It is also revealed that the reaction constant rate for Ag (5 mol%)/ZnO/ g-C_3N_4 is 2.4 times higher than ZnO/ g-C_3N_4. Ag (5 mol%)/ZnO/ g-C_3N_4 composite extends its surface, leading to promoting the photogenerated electron-holes pairs and increasing the lifetime and stability of the charge carrier [194,195]. To show the improved photocatalytic performance with high stability, different Ag-based compounds between g-C_3N_4 and ZnO have been investigated [188,196–199]. In another research, the hydrothermally synthesized Ag-ZnO/S-g-C_3N_4, comprising ZnO NPs doped with 7% Ag with 25% Sulfurized-g-C_3N_4, exhibited outstanding MB photodegradation (97% in 40 min) with excellent recyclability [200]. Carbon-based materials are also used beside the g-C_3N_4-ZnO structure [199,201,202]. Graphene oxide (GO) is carbon-based material commonly used in the g-C_3N_4-ZnO heterojunction [199,203,204]. GO is a two-dimensional platform, providing a promising electron conductivity, high specific surface area, and Young's modulus, which are useful for improving photocatalytic activities. The RhB dye degradation is about 99% for ZnO-g-C_3N_4-GO nanocomposites in 14 min [199]. The trinary nanocomposites provide high stability, which can be used for a wide range of environmental applications [203]. Other forms of carbon-based nanomaterials such as carbon dots (C Dots) are also used to improve the heterojunction structures' efficiency [201,205]. The C Dots provide the facile photoinduced electrons transfer from the ZnO's CB to the g-C_3N_4's VB. The Z-scheme heterojunction structure can be used in biomedical applications for bacteria-killing and acceleration of wound healing system [201].

5.2.3. Iron Oxide-g-C_3N_4

Fe_xO_y such as FeO, Fe_3O_4, and Fe_2O_3, not only can improve the photocatalytic performance of the g-C_3N_4structure due to some unique characteristics but they can also be vastly used for contaminant removal in various media [206–209]. Compared to the combination of g-C_3N_4 with TiO_2 or ZnO, fewer papers have been focused on the g-C_3N_4-FeO_x heterojunctions. Xu et al. announced that the CB and VB of Fe_2O_3 are 0.3 eV and 2.4 eV, respectively [210]. FeO_x failed to show any appreciable photocatalytic activity since the improper, more positive CB edge position (Figure 14a). It is confirmed that g-C_3N_4/α-Fe_2O_3 nanocomposites obey a Z-scheme mechanism for photogenerated charge separation. Working on the g-C_3N_4-FeO_x composite was ignited by the pioneering study authored by Ye et al. [211]. They demonstrated that the efficiency of the Fe_2O_3/g-C_3N_4 photocatalysts was increased up to 1.8 times than the bulk C_3N_4 for the RhB degradation under visible light irradiation.

One of the most common synthetic methods to make iron oxides, especially superparamagnetic iron oxides (SPIONs), which show the highest saturation magnetization among all iron oxides while having a low magnetic coercivity, is co-precipitation method [212]. The effect of different parameters such as solution temperature, alkalinity, and stirring rate were investigated by Hosseini's group on the suspension properties for MRI applications [213]. Iron oxides have many applications in different area such as biomedical applications, environmental application, etc. [214,215]. Wang et al. prepared g-C_3N_4-Fe_2O_3 nanocomposite via chemical co-precipitation approach [209]. They also evaluate the adsorption and desorption of seven polycyclic aromatic hydrocarbons (PAHs). Low limits of detection (LOD), excellent linearity, and recovery of the g-C_3N_4/Fe_3O_4 nanocomposites revealing their ideal candidacy for environmental applications, especially PAHs removal from water samples. In another research, the Fe_2O_3-g-C_3N_4 heterojunction was synthesized by thermal treatment in a hypoxia environment [216]. The presence of Fe_2O_3 in the structure will reduce the recombination rate and promote N_2 adsorption. Some other researchers used in-situ thermal condensation to prepared g-C_3N_4 with iron oxides, which can be used in ciprofloxacin (CIP) degradation [217]. CIP is an antibiotic for bacteria sterilization by inhibiting the bacterial DNA. Besides, it is demonstrated that the remnant CIP in the soil can be absorbed by plants and transfer to the human body by consumption. The long-term CIP intake leads to some serious health issues [218]. The hydrothermal method is another method for preparing this composite [219]. In this method, researchers used the solution containing colloidal of the mixture of both Fe_2O_3 and g-C_3N_4. Fe_2O_3 could not cause the methanol yield since the low conduction band of the Fe_2O_3. To be more specific, Fe_2O_3 (5, 10, 15, 20 wt %) was added to 500 mg of g-C_3N_4 (in 25 mL of water), prepared by direct solid-state reaction of dicyandiamide and thiourea, to form a homogeneous mixture. The solution was transferred into the Teflon-lined stainless-steel autoclave at 150 °C for 4 h, and then washed and dried at 60 °C overnight. As a result, Duan and Mei revealed that the g-C_3N_4-Fe_2O_3 heterojunction significantly improved methanol yield from the CO_2 photoreduction.

As mentioned above, Fe_2O_3 has a narrow bandgap of about 2.1 eV, making the iron oxides an excellent candidate for broad visible light absorption. Some factors, such as the high recombination rate of electron-holes, the short diffusion length of holes, and lack of sufficient conductivity, improve the need to constructing a FeO_x-based composite, which will increase the applications of this composite. One of the most well-known FeO_x-based composites is the g-C_3N_4-Fe_2O_3, which can adequately promote photocatalytic activities. Geng et al. illustrated the XRD and FTIR pattern of the g-C_3N_4-Fe_2O_3 composites, which are similar to the results of other publications [220]. Any significant peak shift is observed in the XRD pattern of the composites, which are indicated in Figure 14b. Additionally, the intensity of the peaks related to the (104) and (110) of α-Fe_2O_3 are strengthened by increasing the α-Fe_2O_3 content in the structure [220]. They also investigated that the FTIR characteristic peaks of the g-C_3N_4-Fe_2O_3 composites are not significantly change compared to the bare g-C_3N_4 and Fe_2O_3 (Figure 14c). As mentioned previously, the broad peak around 3500 cm^{-1} is due to the presence of moisture in the samples. The characteristic peaks at the bare Fe_2O_3 and g-C_3N_4 comprising 3000–3400 cm^{-1} and unresolved peaks from 1237 to 1640 cm^{-1} indicating N–H, C–N, and C=N in the g-C_3N_4, respectively [220]. Besides, the sharp peak at 811 cm^{-1} is related to the stretching vibration of the triazine units. At the same time, the peaks at 543 cm^{-1} and 469 cm^{-1} directly correspond to the Fe-O stretching vibrations. The optical studies are also depicted in Figure 14d,e, which not only showed absorption and emission of this composite but also revealed the effect composition on these characteristics features. All samples showed a promising UV absorption above 450 nm compared to the g-C_3N_4, helping the photocatalytic characteristics improvements (Figure 14d) [221]. The PL emission spectra showing in Figure 14e will aid us in a clearer understanding of the photophysical behavior of the prepared materials. The results showed a broad peak at the range of 440–463 nm, while the PL intensity of the Fe_xO_y showed a high decrease. The decrease in the PL intensity may be due to the reduction in the luminous recombination probability, resulting in enhancing the charge

separation and photocatalytic reactions. Cheng et al. also demonstrated the insignificant deactivation in about 16 h during 4 cycles showing high stability of this composition. In order to improve the photocatalytic activities, Wang and his coworkers used Al–O bridged g-C_3N_4-α-Fe_2O_3 z-scheme nanocomposites [222]. In this work, the photocurrent density with 450 nm excitation wavelength increased when researchers used the Al–O bridged 15 g-C_3N_4-α-Fe_2O_3, containing 15 mass percentage of g-C_3N_4 and 6 mole percent of Al to Fe. This analysis indicated in Figure 14f showed that Al–O bridged g-C_3N_4 facilitated the photo-generated charge transfer and separation [222].

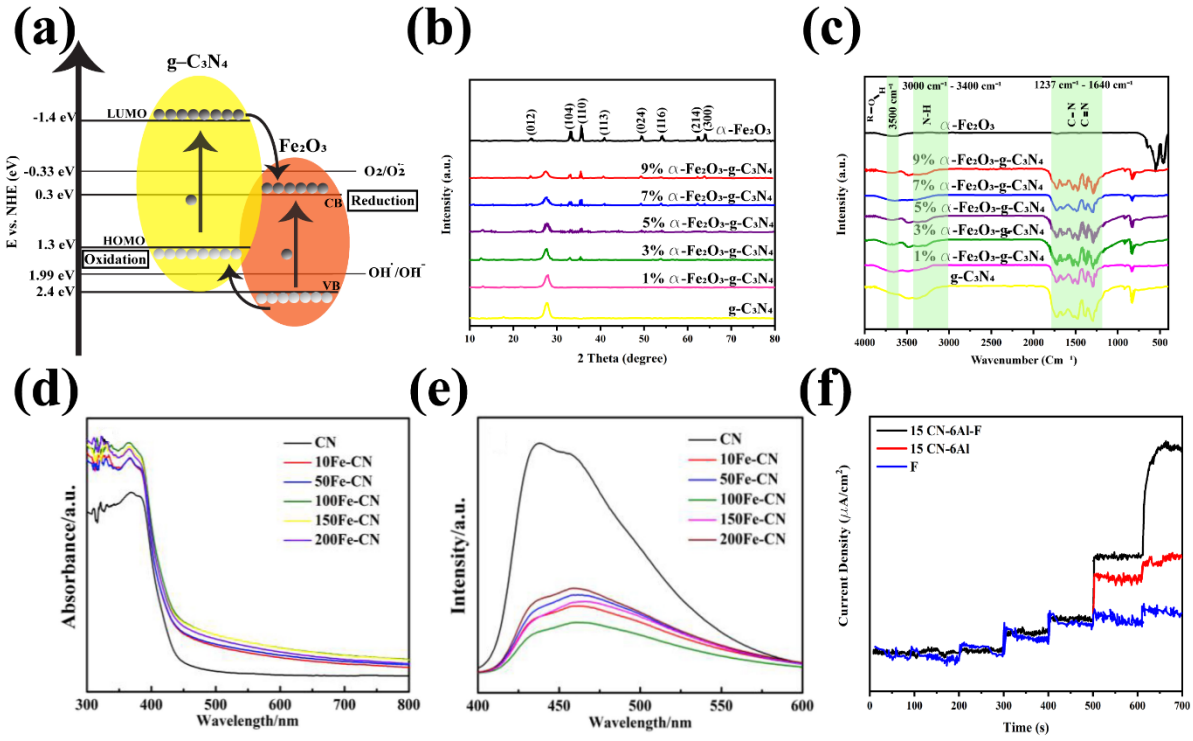

Figure 14. (**a**) Proposed structure of g-C_3N_4-FeO_x heterojunction interface; (**b**) XRD patterns and (**c**) FT-IR spectra of g-C_3N_4, α-Fe_2O_3, and α-Fe_2O_3/ g-C_3N_4 composites, Copyright © 2022 Elsevier [220]; (**d**) UV-Vis diffuse reflection absorption spectra; (**e**) PL spectra of CN and xFe-CN samples with an excitation wavelength of 380 nm, Copyright © 2022 Elsevier [221]; (**f**) single-wavelength photocurrent response of F, 15CN-F and 15CN-6Al-F, Copyright © 2022 Elsevier [222].

Metastable materials that transform from one to another state over a long period of time have superior properties. Bibyite phase of iron(III) oxide (β-Fe_2O_3) act as its α-phase (hematite) iron(III) oxide. However, it shows a more desirable bandgap (1.8 eV) for photocatalysis. Christoforidis et al. prepared metastable β-phase Fe_2O_3 nanoparticles on the g-C_3N_4 surface by a solid-state, in-situ growth method, without the need of specialized equipment, surfactants, stabilization, or precipitating agents [223]. In this research, the β-Fe_2O_3 improve the photocatalytic activities by increasing the ability of light absorption in the visible region, and enhanced carriers' separation. The hybrid β-Fe_2O_3/g-C_3N_4 nanomaterials are an excellent candidate for photodegradation since they showed higher photocatalytic activity and a promising stability [223].

There are several g-C_3N_4-FeO_x-based composites with promising photocatalytic activities. The g-C_3N_4 coated with the Fe_xO_y covered by metals will enhance the photocatalytic properties by ameliorating the photo-induced charge generation and separation. The promising LSPR effect of the Au and active sites of Pt convinced researchers to use Fe_2O_3/Pt/Au nanocomposite immobilized on the g-C_3N_4 surface as an excellent composite for hydrogen evolution [224]. As discussed in our previous papers, Au nanoparticles with strong LSPR can participate in catalytic reactions (for an example see [225]). Au NPs with a

strong LSPR effect enlarge the photo-electron conversion efficiency of the photocatalyst. The researcher also investigates the CO_2 photoreduction of g-C_3N_4 quantum dots-Au NPs co-modified CeO_2/Fe_3O_4 micro-flowers (MFs). They showed that Au NPs promote photocatalytic activities by generating the electrons and holes and enhance carriers' separation in CeO_2 MFs and CN QDs in the photocatalyst [226]. Copper is another metal used in the g-C_3N_4-FeO_x-based composite. Liu et al. fabricated g-C_3N_4/Fe_2O_3-Cu for electrochemical detection of glucose [227]. g-C_3N_4/Fe_2O_3-Cu composites improved the electrochemical performance for glucose detection with a LOD of 0.3 mM. They also confirmed that g-C_3N_4-Fe_xO_y composite can be used as an electrode in sensors to measure other compounds. The effect of a multi-walled carbon nanotube was investigated by Zhang et al. [228]. They demonstrated that due to the large specific area, hydrogen bonds, π-π, and electrostatic interactions of the MWNTs@g-C_3N_4@Fe_2O_3, these 3D structures were novel magnetic solid-phase extraction sorbents for PAH with the LOD of 0.001–0.5 mgr·L^{-1}. Besides, the 3D structure has a good repeatedly and recovery for 16 PAHs in the water samples. Graphene, as other carbon-based materials also used to improve the efficiency of Fe_3O_4/g-C_3N_4 composites. Wng et al. showed that the Fe_3O_4/graphene/S doped g-C_3N_4 dose of 1.0 g/L comprising 20% Fe_3O_4 mass fraction could completely remove Ranitidine ($\leq$2 mg/L) in 60 min, an initial pH of 7.0 [229].

The other ternary composite used for the water splitting is g-$C_3N_4/CeO_2/Fe_3O_4$ [230]. The composites showed enhanced oxygen and hydrogen evolution reaction with high current density (40 mA·cm^{-2}) at the potential of 327 mV, which was greater than the bare Fe_3O_4 and bulk g-C_3N_4. The ternary composites showed excellent stability and negligible activity loss up to 14 h. the Z-scheme g-C_3N_4/Fe_3O_4 can be coupled with the CdS and was used for different antibiotics degradation [231]. The results showed the improved degradation rate to 45 times of CdS, 26 times of pure g-C_3N_4, and 9.5 times of CdS/g-C_3N_4 for the tetracycline removal. The presence of the Fe_3O_4 improves the photocatalytic performance and stability by an increase in the inducing and separation of the electron-hole pairs and generating more $\cdot O_2^-$ for organic pollutant degradation [231].

Other Fe_xO_y compounds are also used to improve the UV-visible light absorption for different applications. $NaFe_2O_4$ is one of the most well-known FeO_x structures, using in the g-C_3N_4-based composites [232–234]. The Fe_3O_4@$NiFe_2O_4$-g-C_3N_4 improves photocatalytic activity up to 90% of CIP degradation by reducing the electron-hole recombination [232]. In all superparamagnetic samples, the high M_s assists in improvig of the recyclability and stability of the photocatalyst. The more magnetite content in the sample leads to a higher probability in the particle agglomeration, resulting in the decrease in the active sites of the and the reduction in the photocatalytic efficiencies. The fabricated g-$C_3N_4/NiFe_2O_4$ can also be used to degrade MB and RhB by activating H_2O_2 to produce the oxidizing reagent [233,234]. The magnetic properties of the $NiFe_2O_4$ (M_s= 45 emu/g) were induced to the whole composite (M_s= 40 emu/g) to promote repeatability and improve the photodegradation rate [233]. The other most popular compound captured researchers' attentions are $ZnFe_2O_4$ and $LaFeO_3$ [235–237].

5.2.4. WO_3-g-C_3N_4

Figure 15a demonstrated the band edge position of the WO_3 compared to the g-C_3N_4. This Figure illustrated that the bandgap of the WO_3 is 2.6 eV with VB and CB of 2.9 eV and 0.3 eV, respectively, which are more positive than that of g-C_3N_4 and the O_2/O_2^- potential [238–240]. Thus, it is approximately impossible to produce $\cdot O_2$ by using the traditional type-II mechanism. Many researchers showed that the charge migration almost occurred by the Z-scheme mechanism in the binary g-C_3N_4-WO_3 composite [241–243]. Various methods have been fabricated this binary composite. The hydrothermal approach is one of the main routes to prepare the g-C_3N_4-WO_3 composite [244,245]. Zhang et al. prepared WO_3/g-C_3N_4 by dissolving the WCl_6 and ascorbic acid in ethanol and g-C_3N_4 followed by 5 min sonication and stirred for 20 min [244]. The uniform suspension was heat-treated at 220 °C for 12 h, and then washed several times using ethanol. The other

way for the preparation of the heterojunction is the microwave irradiation technique with the direct calcining of the WO_3 and g-C_3N_4 combination at 400 °C for 2 h [246]. In this method, to prepare WO_3 by simple household microwave irradiation, tungstic acid in NaOH solution was mixed and stirred for 30 min to form a tungstic hydroxyl group [246]. Afterward, the pH of the prepared mixture was reduced to 1 by adding HCl solution, and the gel should be put into the Teflon-lined household microwave oven (2.45 GHz) for 10 min to prepared WO_3. Finally, the mixture should be placed in an alumina crucible with a cover in a muffle furnace and heated at 400 °C for 4 h. A wet chemical process, sonochemical, in situ self-assembly, etc., are other ways to synthesize the g-C_3N_4- WO_3 heterojunction [247–249].

g-C_3N_4-WO_3 composites were characterized by various techniques. In most research papers, XRD and FTIR are the prime characteristic methods to evaluate the formation of g-C_3N_4-WO_3. Researchers announced that the WO_3/CN wt % = 10% provides the best characteristics compare to the balk g-C_3N_4 and WO_3 [250]. Figure 15b shows the XRD patterns of the bulk g-C_3N_4, WO_3, and g-C_3N_4-WO_3, perfectly showing the impact of WO_3 content on this characterization. There are nine distinct peaks for the as-prepared WO_3 [247,251]. Additionally, the binary composites revealed the combination peaks of the WO_3 and g-C_3N_4. The higher WO_3 content leads to the lower peak's intensity of the g-C_3N_4, corresponding to the expansion of the interlayers and g-C_3N_4 coverage with a WO_3. The low intensity of the peaks at 23.5° and 36.6°, which is detectible in the sample with a high WO_3 to g-C_3N_4 ratio, is related to the hexagonal-phase WO_3 and illustrated the formation of the composite successfully. They also characterized the g-C_3N_4-WO_3 composite with the FTIR spectra analysis [251]. Like other materials' FTIR spectra, the wide peak at the range of 3000–3500 cm^{-1} in all samples is attributed to the N-H and O-H stretching vibration, and the adsorbed water molecules' bending vibration stands at about 1630 cm^{-1} for samples (Figure 15c). The broad peak at the 750–1000 cm^{-1} corresponds to the O-W-O stretching vibrations of WO_3 [252,253]. As a result, although the g-C_3N_4 characteristic FTIR peaks can be observed in the composite FTIR spectra, WO_3 peaks are not significantly detected in the hybrid composite, which can be ascribed to the vacancies between the g-C_3N_4 clusters or band overlapping. Optical studies were carried out by Chai et al. on the g-C_3N_4 with WO_3 structure [254]. The UV-vis DRS of the WO_3, g-C_3N_4, and WO_3-g-C_3N_4 composites with the WO_3 contents is depicted in Figure 15d. The obvious absorption edges at ~470 nm and 455 nm are detected for WO_3, g-C_3N_4, respectively, corresponding to the 2.64 eV and 2.73 eV. The g-C_3N_4-WO_3 composites present the combination absorption features of g-C_3N_4 and WO_3 [254]. Figure 15e displays the PL emission peak of the bulk g-C_3N_4 and 18.6 wt % WO_3/g-C_3N_4 hybrid composite [254]. The result demonstrates that the intensity of the composites' PL peak at ~440 nm is lower than that of the pure g-C_3N_4 [255–257]. The PL spectra revealed that WO_3 apparently suppresses the photoinduced electron-hole recombination in the WO_3/g-C_3N_4 composites and confirms the Z-scheme interface contact [258]. They are also revealed that the OH^- generating during the photocatalytic reaction leads to the higher PL intensity increases the irradiation time. Besides, the transient PL decay trace of the bare g-C_3N_4, WO_3, and g-C_3N_4-WO_3 composite hollow microsphere are ~ 4.46 ns, 1.62 ns, 2.23 ns, respectively [259]. The zeta potential values of the WO_3, g-C_3N_4 and their binary composites announce the negatively charged surface of the samples [260]. The presence of WO_3 in the composite changes the zeta potential from −5.7 mV to −33.1 mV, while it decreases the BET specific area from 100.97 $m^2 \cdot g^{-1}$ to 47.88 $m^2 \cdot g^{-1}$, which are high enough for promising adsorption ability and photocatalytic activities. g-C_3N_4-WO_3 reveals high stability and repeatability after 4 cycles with a slight efficiency decrease for the degradation of RhB [261–263].

There are also some dopants and compounds used to improve the photocatalytic efficiency of the binary composites. In the z-scheme C or Pt-g-C_3N_4 with hydrogen treated WO_3, the electrons from g-C_3N_4 and holes from WO_3 facilitate the photogenerated charge carries generation, which will enhance the photocatalytic activities [254,264]. In other words, the C or Pt dopants help the composite to improve the light absorption and charge

separation. This structure also enhances stability and repeatability. O-doped g-C_3N_4-WO_3 has 4.7 times higher H_2 performance than the bare composite [265]. The carbon vacancies and g-C_3N_4 oxidization resulted in the formation of the porous composites and a decrease in the composite's surface area. The effective Si-O bridge between g-C_3N_4 and WO_3 significantly promotes charge transfer and separation [266].

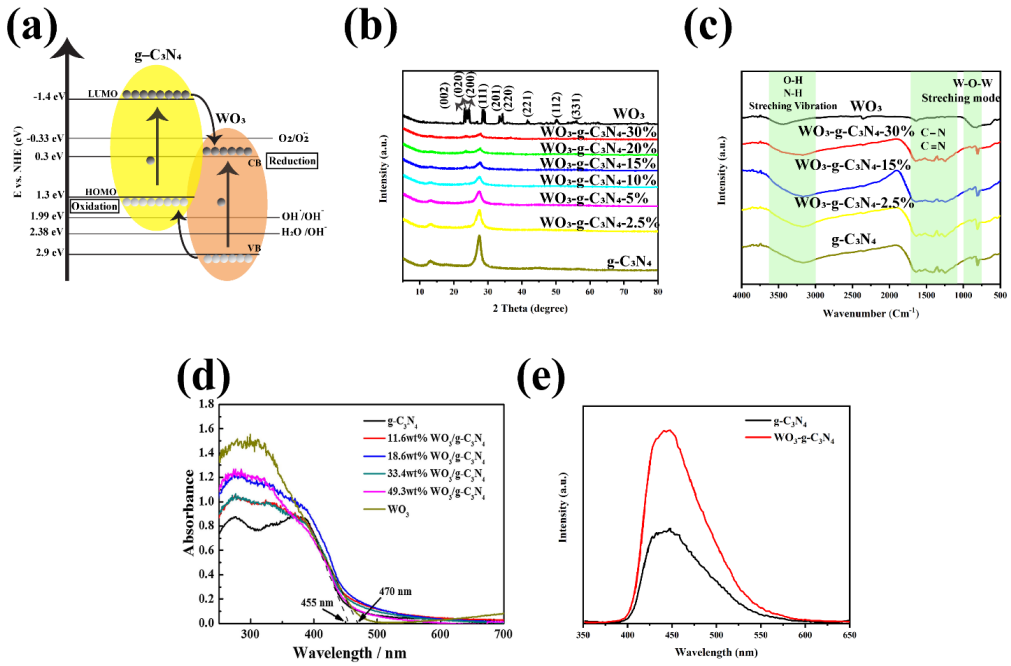

Figure 15. (**a**) Proposed structure of g-C_3N_4-WO_3 heterojunction interface; (**b**) XRD patterns and (**c**) FT-IR spectra of obtained samples (x in WO_3/g-C_3N_4 refer to the mass ratio of WO_3 to g-C_3N_4), Copyright © 2022 Elsevier [251]; (**d**) UV-DRS spectra of pure g-C_3N_4, WO_3 and WO_3/ g-C_3N_4 heterojunctionp; (**e**) PL emission spectra of g–C_3N_4 and 18.6 wt % WO_3/ g-C_3N_4 composite, Copyright © 2022 Elseviers [254].

In addition to the doped binary composites, adding other compounds to form the ternary structure is a practical way to boost the composite characteristics. Mediators and co-catalyst such as metals (such as Ag, Au, Cu, Pt, and Sn) are currently used to improve the Z-scheme composites by facilitating the transporting and carrier capturing during the photocatalyst process [267–272]. Li et al. demonstrated the charge carrier migration between various WO_3-Metal (Cu, Ag, Au)-g-C_3N_4. They showed that Cu plays the ideal candidate for photocurrent enhancement and improves the photocatalytic performance in the Z-scheme g-C_3N_4-WO_3 heterojunction among different metals used in the research. In other words, the Cu-g-C_3N_4 and WO_3-Cu are favorable for electron migration since they have the matched Fermi level of energy [267]. In other research, the developed WO_3/Ag/g-C_3N_4 ternary composite was used for the RhB and tetracycline (TC) degradation. The results demonstrated that the improved photocatalytic activity of WO_3/Ag/g-C_3N_4 is obtained due to the large contact region between g-C_3N_4 nanosheets and WO_3 nanoplates. Besides, the presence of the Ag NPs in the composite with SPR effect accelerates the charges to transfer, improves the photocatalytic activity, and enhances the stability and repeatability [268,269].

Researchers also worked on the Ag/g-C_3N_4/WO_3 to degrade oxytetracycline hydrochloride under visible light [273]. The 0.4 g/L of Ag/g-C_3N_4/WO_3 composite demonstrated the highest photocatalytic activity, which could degrade 97.74% of oxytetracycline (10 mg/L) in 60 min. In another research, Qin et al. showed that the presence of Pt in the WO_3-g-C_3N_4 composites possesses excellent photocatalytic H_2 evolution with 1299.4 µmol under visible light, which is higher than that of WO_3/g-C_3N_4/Pt and pure CN with

1119.4 µmol, and 113.2 µmol, respectively [274]. As mentioned above, g-C_3N_4/Au/WO_3 as Z-scheme heterojunction displayed excellent photocurrent that can be used in photoelectrochemical immunosensing of Aflatoxin B1 in food, which can be dangerous for humans [275]. The methane formation over the WO_3-Bt-g-C_3N_4 composite was 5.98, 6.74, and 25.19 times higher than that of WO_3-g-C_3N_4, Bt-g-C_3N_4, and g-C_3N_4 samples, respectively [272].

Some promising properties of tungsten-based materials such as electrical, optical, magnetic, and photocatalytic activities, low-cost preparation persuade researchers to use these materials such as $NiWO_4$, $BaWO_4$, $CuWO_4$, and $BiWO_6$ [270,276–278]. The band structures of these compounds with g-C_3N_4 and WO_3 make the CB and VB positions match each other, leading to the prolonged charge carriers' lifetime in the form of a double Z-scheme system. The photoelectrochemical (PEC) of a double Z-scheme g-C_3N_4-WO_3-Bi_2WO_6 system reveals the enhanced photocurrent density, reduced electron-hole recombination, resulting in the promotion of photocatalytic efficiency [276]. Other materials have been anchored in the g-C_3N_4-WO_3 to form an excellent composite for different applications [279,280]. Bi-based materials are among the prime and important materials used to construct the composites for photocatalytic activities [281–283]. MoS_2 and MoO_3 are other compounds to be utilized as materials for this ternary composite [284,285]. g-C_3N_4/WO_3 with TiO_2 can also be useful for the methylene blue dye degradation, which its efficiency is about 3.1 folds higher than that of the binary counterparts of TiO_2/WO_3 (0.00691 min^{-1}) in 120 min. The kinetic constant for different composition of this composite are in order of TWG-15% (which 15% is the g-C_3N_4 wt %) > TWG-10% > TWG-5% > TWG-20% > TW [286].

5.2.5. Tin Oxide-g-C_3N_4

Other metal oxides widely used in g-C_3N_4 binary heterojunction are tin oxides. SnO (stannous oxide) and SnO_2 (stannic oxide) are two forms of tin oxide. Figure 16a shows the band edges' position in the tin oxide and compares it to the CB and VB of the g-C_3N_4. He et al. showed that the SnO_2 has a large bandgap of about 3.6 eV, and its CB level is lower than that of g-C_3N_4 [287]. It is also demonstrated that these tin oxide-g-C_3N_4 composites mostly form the Z-scheme heterojunction [288,289]. Tin oxide can be designed with various shapes by wet and dry methods. The heterojunction is synthesized by different synthetic methods, including hydrothermal and thermal treatment [78,290–292]. Sadrnezhad and coworkers prepared g-C_3N_4-SnO_2 with the pyrolysis of urea under microwave irradiation [293]. In this work, tin, ammonium, and urea were put into the beaker and placed in a microwave oven operating at 2.45 GHz and 900 W for 30 min. Finally, the product was washed and dried in the oven. In another work, the mesoporous SnO_2 decorated with g-C_3N_4 was prepared via pulsed electrophoresis and facile water-crystallization [293]. With pulsing electrophoresis optimized parameter, the 0D g-C_3N_4 can be homogeneously and completely distributed inside the 1D SnO_2. Sol-gel is also used to fabricate an efficient g-C_3N_4-SnO_2 photocatalyst [294].

Several techniques have been used to confirm the formation of this composite. The XRD pattern and FTIR spectra of g-C_3N_4, SnO_2, and SnO_2-g-C_3N_4, are depicted in Figure 16b,c [295]. SnO_2 does not change during the preparation of the final structure, which can be seen from the insignificant differences between the pure SnO_2 and the SnO_2-g-C_3N_4 XRD pattern in Figure 16b. The characteristic peaks in SnO_2 revealed the (110), (101), (200), and (211) planes of a tetragonal rutile-like structure. Other small peaks, which are not mentioned in Figure 16b, are related to the (220), (310), (301), (202), and (321). As shown in Figure 16b, the (002) crystal plane peak of g-C_3N_4 overlapped with the (110) crystal plane peak of SnO_2. Additionally, the Sn–O–Sn anti-symmetric stretching vibration between 400 cm^{-1} and 700 cm^{-1} was demonstrated in Reference [295] (Figure 16c). The red-shift peak at 597 cm^{-1} was a good indication of the formation of SnO_2-g-C_3N_4 heterojunction [296,297]. The presence of SnO_2 in the structure suppresses the electron-hole recombination rate. Peng et al. demonstrated the negligible differences and slight blue shift of g-C_3N_4-muscovite sheet/SnO_2 structure, compared to the absorption edges of g-C_3N_4 (Figure 16d) [298]. Introducing the muscovite sheets does not affect the composites'

absorption, and g-C_3N_4-muscovite sheet/SnO_2 absorption spectra reveal the potential photocatalytic applications under visible light. They also showed that the g-C_3N_4-muscovite sheet/SnO_2 Cement has an excellent photocatalytic activity for RhB stains and isopropyl alcohol photodegradation. Due to the low electron-hole recombination probability of the SnO_2-g-C_3N_4, the intensive PL intensity was observed in Figure 16e [298,299]. The faster interfacial charge-transfer and lower resistance, results in the Nyquist plot diameter decrease compared to SnO_2 and g-C_3N_4, shown in Figure 16f [300]. This is therefore a promising photocatalyst. The properties and morphology of this composite change when the relative content of g-C_3N_4 varies in the heterojunction [301,302]. Chen et al. showed that the g-C_3N_4 mass ratio of 72% provides the highest photocatalytic performance, which is 17 times higher than bulk g-C_3N_4 [303]. SnO_2-g-C_3N_4 heterojunction reveals notable stability and recyclability [18]. In addition to robust photocatalytic activities, this composite has a noticeable photoelectrochemical performance under visible light. Doping different elements, such as Sb, S, B, and P, is one of the main approaches to improve the performance of the SnO_2-g-C_3N_4, which can modify the band edges [304–306].

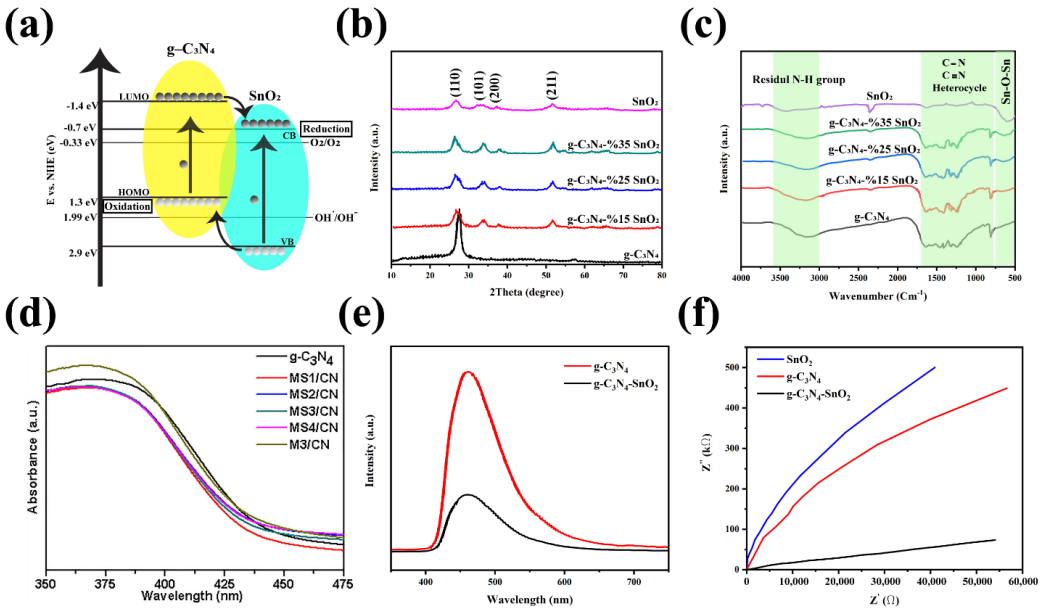

Figure 16. (**a**) Proposed structure of g-C_3N_4-SnO_2 heterojunction interface; (**b**) XRD patterns and (**c**) FT-IR spectra of SnO_2, graphene-like C_3N_4, SnO_2/g-C_3N_4 composites (reproduce from Reference [295]); (**d**) UV-vis absorption spectra of g-C_3N_4-based samples (muscovite sheet(x)/SnO_2/g-C_3N_4 (MSx/CN), which x refers to the mass of MS powder), Copyright © 2022 Elsevier [298]; (**e**) PL spectra of g-C_3N_4 and SnO_2 quantum dots-g-C_3N_4 nanocomposite, Copyright © 2022 Elsevier [299]; (**f**) EIS Nyquist plots of the bare SnO_2, g-C_3N_4, and SnO_2-g-C_3N_4 structure, Copyright © 2022 Elsevier [300].

Doping is a method to improve the efficiency of SnO_x-g-C_3N_4 heterojunctions, which are used in different applications. SnO_2/g-C_3N_4 sensor doped with Ni shows LOD about 1.38 ppb and has high stability, promising selectivity, rapid response and recovery time, and great resistivity against humidity [307]. Besides, researchers used made Ce doped SnO_2/g-C_3N_4 to make capacitors with a specific capacity of <274 F/g. A supercapacitor with energy and power densities of 39.3 W h kg^{-1} and 7425 W kg^{-1}, respectively, was made by using Ce-SnO_2/g-C_3N_4/Activated Carbon. The supercapacitor device exhibited retention of 84.2% after completing 5000 cycles [308].

Additionally, several researchers used the SnO_2-g-C_3N_4 based ternary composites to increase the applications of these kinds of composites [309,310]. The plasmonic Au-SnO_2-g-C_3N_4 photocatalyst was fabricated for H_2 evolution and degradation of the organic pollutant, which is commonly used due to the outstanding photocatalytic activities and

significant stability (remain unchanged after 5 h in 5 cycles) [309,311]. In this ternary heterojunction, the presence of the plasmonic Au and g-C_3N_4 offer enhanced photogenerated electrons to the structure. SiO_2 is another compound used besides the SnO_2-g-C_3N_4 system for pollution treatment applications [312]. As mentioned above, TiO_2 has promising properties that aid us in promoting the properties of this composite [313,314]. This ternary composite also demonstrated the perfect antibacterial activity for the degradation of *E. coli* bacteria, probably due to the interface between g-C_3N_4-SnO_2 and TiO_2 and lower charge recombination rate [314]. SnO_2/chitosan/g-C_3N_4 nanocomposite has been used as an Electrochemiluminescence aptasensor to improve lincomycin detection [315]. Ali et al. also showed the cost-effective prepared g-C_3N_4/rGO/SnO_2 nanocomposite for RhB degradation. The optimal amount of this nanocomposite reveals an increased RhB degradation efficiency [316].

As a result, the SnO_2-g-C_3N_4 structure can be used in a wide range of applications. The exploitation of new clean energy instead of fossil fuels is of great interest to many since the fossil energy is exhausted. As a case in point, water splitting is a perfect example of this clean energy generation, which is widely applied by the g-C_3N_4-SnO_2 [317,318]. Besides, in order to reduce environmental pollution, the demand for electric transports has been increased. Thus, it is essential to use the rechargeable batteries such as lithium-ion batteries (LIBs) and improve lithium storage capacity. Specifically, g-C_3N_4 enables SnO_2 anode to enhance the Li storage in these batteries [319,320]. This heterojunction is also used to detect different compounds. Cao et al. showed that SnO_2/g-C_3N_4 composite promoted the sensitivity and selectivity in ethanol gas-sensing applications [321]. The degradation of the inorganic pollutant is another application of this heterojunction [322,323]. The emission of nitrogen dioxide (NO_2) and nitric oxide (NO) causing some environmental issues is one of the biggest challenges among several researchers, solved by Zou and coworkers by using SnO_2-g-C_3N_4 photocatalysts using visible-light irradiation under 30 min [287]. SnO_2-g-C_3N_4 is also used to decomposed Ammonium Perchlorate (AP), a toxic inorganic material [324].

5.2.6. Other Metal Oxides

Other kinds of metal oxides such as V_2O_5, NiO, MoO_3, Cu_2O, Co_3O_4, CeO_2, Bi_2O_3, Al_2O_3, etc., are also used to improve the performance of the bulk g-C_3N_4 [325–345]. The g-C_3N_4-based heterojunctions can be modified by combining with several metals or doping with various agents [346–348]. Cu is a conventional metal using for the improvement of photocatalytic performance. Zhou et al. used Cu/Al_2O_3/g-C_3N_4 for Rhodamine B degradation by H_2O_2 [349]. The Cu immobilized Al_2O_3/g-C_3N_4 also showed promising stability for the treatment of water pollution. Besides, copper is used as a charge separation center for hydrogen evolution, MO, and phenol solution degradation under visible light [350,351]. In addition to Cu, the noble metal Ag and Au is another metal catalyst used besides the g-C_3N_4-based composite [347,352–356]. The Ag and Au can prevent rapid recombination probability, improve the transfer of a generated electron, and enhance the visible light absorption by the surface plasmon resonance, and can be used for a wide range of applications, especially decontamination of organic pollutants. Bi, Pd, Pt, Ni, and Cd are other metal photocatalysts used for improved photocatalytic activities [357–363]. Some semiconductors are also used besides the metal oxide-g-C_3N_4 based composites. Carbon-based nanomaterials provide excellent stability, cost-effective synthesis, enhanced photogenerated electron reservoirs used in bioimaging and sensing, photocatalysis, electrocatalysis [214,336,364–367]. Xie et al. fabricated the carbon quantum dots modified with MoO_3-g-C_3N_4 and demonstrated that this structure showed outstanding visible-light absorption used to degrade tetracycline (TC) from the environment [364]. Besides, among all carbon-based nanomaterials, reduced graphene oxide (rGO) has captured intensive attention [368,369]. Gong and coworkers illustrated that the charges transfer between g-C_3N_4 and $Bi_2Fe_4O_9$ (BFO) was improved by using rGO. The presence of the rGO causes the separation of electrons and holes in the CB of g-C_3N_4 and the VB of BFO, respectively [354].

In addition to the mentioned metals and semiconductors, metal-organic frameworks (MOFs) are a novel class of porous and crystalline materials with a large surface area-to-volume ratio, high porosity, and tunable pore size that might improve the biosensor sensitivity. Since these structures are made from metal ions, clusters, and organic ligands, these materials can promote the separation and transfer of photoinduced electrons, making them a promising candidate for photocatalytic activities, such as organic pollutants degradation, water splitting, and CO_2 reduction [370]. Cui et al. utilized the Fe-based MOFs, MIL-53(Fe), with Bi_2O_3 and g-C_3N_4 for the degradation of amino black 10B since this structure can enhance the visible light absorption range [371]. Like other heterojunctions, doping is another element to improve the performance of these composites and widen their applications [372–376].

Some g-C_3N_4-based ternary composites comprising the metal oxide compounds can promote photocatalytic activities [103,377–380]. Bismuth complex oxides are among the most efficient catalysts with layered structures beside the g-C_3N_4-based composites. Among various Bi-based compounds, Bi_2O_3 based catalysts have drawn significant attention in the different areas [381,382]. It illustrated that CuO_2/Bi_2O_3/g-C_3N_4 nanocomposite reveals improved photocatalytic activities for decomposing of 2,4-dichlorophenol under visible light [381]. In another research work, Vattikuti et al. prepared Bi_2O_3/V_2O_5 photocatalysts anchored on the g-C_3N_4 nanostructure, which can be used for the phenol red (PR) pollutant degradation [383]. They also demonstrated that the efficiency of hybrid composites for the PR removal under the simulation solar light irradiation was higher than that of fabricated materials. Bi_2O_3/g-C_3N_4 heterojunctions were also conjugated with the $BiPO_4$ [15]. g-$C_3N_4/Bi_2O_3/BiPO_4$ hybrid exhibited the perfect photoelectric performance, which is mainly due to the high separation and photogeneration charges and can increment the oxidation/reduction rate. $Bi_2O_2CO_3$ is another Bi contained material that shows promising photocatalytic activities [384,385]. Kumar and coworkers suggested novel magnetic g-$C_3N_4/Bi_2O_2CO_3/CoFe_2O_4$ heterojunction with high visible light absorption for reduction of 4-nitrophenol into 4-aminophenol [386]. TiO_2-g-C_3N_4 based ternary composites are widely used for photodegradation. Min et al. fabricated the Cu_2O-TiO_2/g-C_3N_4 hybrid composite for the organic dyes' discolorations. Besides, this nanocomposite can also illustrate good performance for discolorations of RhB, MB, and MO within 3, 10, and 15 min, respectively [387]. TiO_2-g-C_3N_4 composites are also anchored with CeO_2 and metal to form g-C_3N_4-Me^{n+1}/CeO_2-TiO_2 for photooxidation of toluene [388].

6. Application of Metal Oxide-Based g-C_3N_4 Nanocomposites

6.1. Photocatalysts

6.1.1. H_2 Generation via Water Splitting

These days, the demand for safe, efficient, and renewable energy resources instead of limited fossil fuel sources has increased among more and more people [14,184,389–391]. This replacement is an efficient remedy for global warming and greenhouse gases emission. The hydrogen energy content is in the range of 120 to 142 MJ kg^{-1}, which is higher than that of hydrocarbon fuels. Thus, it is estimated that hydrogen will be responsible for 90% of energy production by 2080. As a result, H_2 generation is a novel and environmentally-friendly research topic among many researchers [8,13,392–395]. One of the most recent hydrogen production techniques is the photocatalytic water splitting method via metal oxide-g-C_3N_4 heterojunctions by using prolific light sources [365,390,396–400]. For water splitting, the band position of the photocatalysts should be modified to provide the CB position more negative than the H_2O reduction potential (0 eV vs. Normal Hydrogen Electrode (NHE)) for H_2 generation and more positive than the H_2O oxidation potential (1.23 eV vs. NHE) for O_2 generation. To be more specific, the generated electrons are used for the hydrogen evolution reaction (HER) and oxygen evolution reaction (OER)

via Equations (1) and (2), respectively, and the final water-splitting reaction is shown in Equation (3) [111].

$$\text{Hydrogen evolution reaction (HER): } 2H^+ + 2e^- \rightarrow H_2,\ E^\circ = 0.00 \text{ eV vs. NHE} \quad (1)$$

$$\text{Oxygen evolution reaction (OER): } H_2O \rightarrow 1/2O_2 + 2H^+ + 2e^-,\ E^\circ = -1.23 \text{ eV vs NHE} \quad (2)$$

$$\text{Overall water splitting: } H_2O \rightarrow H_2 + 1/2O_2,\ \Delta G^\circ = -1.23 \text{ kJ mol}^{-1} \quad (3)$$

where NHE is the normal hydrogen electrode.

Generally, there are three steps for each photocatalytic reaction; initially, the semiconductor absorbs light with energy equal to or higher than the bandgap to generate the electrons and holes in the valance and conductive band, respectively. Then, the photoinduced electrons and holes are moved to the surface of the semiconductor to start the reaction. Finally, the charge carriers participate in the reduction and oxidation reactions on the surface of the photocatalysts.

Considering the band edges position of some of the metal oxide-g-C_3N_4 composites, which were noted previously, some heterojunctions are more anodic than that of H_2O reduction potential to show excellent performance under visible light irradiation [111,401]. As a case in point, TiO_2-g-C_3N_4 heterojunctions are widely used as an excellent photocatalytic for H_2 evolution. Yan et al. demonstrated that the efficiency of the visible-light-induced H_2 evolution of the binary composite comprising anatase TiO_2 and g-C_3N_4 was enhanced, and this is due to the desirable photoinduced carriers' separation [402]. In order to raise the heterojunction efficiency, other kinds of materials with various effective characteristics are also used. These materials (metals) or cocatalysts such as Ag, Au, Pt, etc., can host active sites for H^+ reduction [403,404]. The loading Au and Ag would be significantly beneficial for this application because of their plasmonic characteristic. Marchal et al. illustrated that the optimized components ratios and contact quality in Au/(TiO_2–g-C_3N_4) lead to the enhanced visible light absorption with the proper band positions for photogenerated charge carriers [403]. Besides, the presence of Au and Ag will promote the water splitting for H_2 production by the improved charge separation rate. The H_2 generation rate under sunlight irradiation as a function of the relative ratio of methanol as a sacrificial agent and TiO_2/g-C_3N_4 is depicted in Figure 17a. It was mentioned that no H_2 generation was observed for the Au-free g-C_3N_4 and TiO_2. Furthermore, the best photocatalytic H_2 production was observed for the 0.5 wt % Au/(TiO_2–g-C_3N_4) (95/5) structure, using 1 vol% of CH_3OH as a sacrificial agent (Figure 17a). Carbon quantum dots (CQDs) can also improve photocatalytic performance to effectively decompose H_2O_2 to H_2O and O_2. CQDs possess up-conversion fluorescence spectra, which could convert visible light to ultraviolet or near-ultraviolet light, resulting in excellent photocatalysis. Consequently, it is proven that the combination of C_3N_4, TiO_2, CQDs is a great candidate for water splitting [405]. Other metal oxide-g-C_3N_4 based composites such as WO_3-g-C_3N_4 and ZnO-g-C_3N_4 are used for H_2 generation. Mahala et al. demonstrated that the prepared ZnO nanosheets decorated with g-C_3N_4 quantum dots composites on the fluorine-doped tin oxide (FTO) coated glass slide could be utilized as a photoanode for water splitting via PEC (Figure 17b) [406]. In another work, the effect of boron addition and carbon nitride content did increase the H_2 evolution up to 85% compared to the bare TiO_2, which is mainly due to charge carriers' generation and separation [109]. It was also shown that the photoconversion efficiency of the low charge-transfer resistance of ZnO decorated with g-C_3N_4 is 2.3 times higher than that of pure ZnO [406]. As discussed previously, this composite had a high specific surface area, promising electronic conductivity, and excellent charge transfer interfaces and would be excellent candidates for the water splitting and H_2 evolution [407]. Other materials with suitable properties can also be used to improve the H_2 generation of g-C_3N_4–metal oxide-based composites [141,283].

In a plasmonic photocatalyst, a metal nanostructure with a size less than the wavelengths of the light, is embedded onto dielectric or semiconductor materials [408]. In such systems, the light can lead to a local electromagnetic field by generating localized surface

plasmon resonance (LSPR) and hot carriers. The hot carriers move to conductive and valance bands and this phenomenon is called the LSPR sensitization [409,410]. The hot carriers can be useful for direct oxidation or reduction of chemical species. Some of the metals that showed plasmonic effects are gold (Au), silver (Ag), copper (Co), and platinum. Zhao et al. state that the LSPR of Au can enhance the light absorption and increase the number of photogenerated carriers in the Au/g-C_3N_4/CeO_2 plasmonic heterojunction. The heterojunction was employed for Cr^{6+} reduction and oxytetracycline hydrochloride (OTH) catalytic degradation [411].

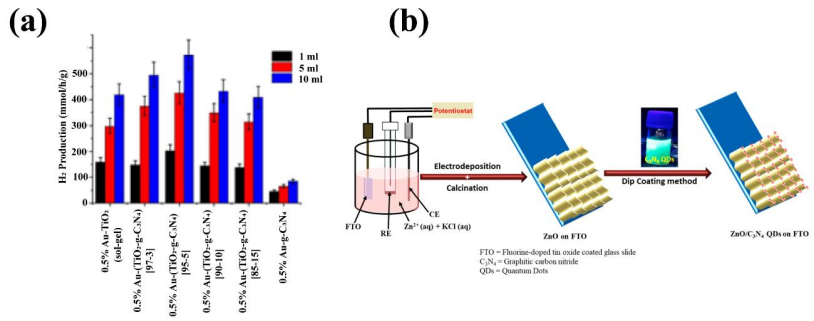

Figure 17. (**a**) Hydrogen production rate of different samples as a function of the amount of methanol added as a sacrificial agent under solar light irradiation, Reproduced from Reference [403]; (**b**) schematic image of the ZnO/C_3N_4 QDs synthesis on FTO using electrodeposition and a dip-coating method, Copyright © 2022 Elsevier [406].

Metal oxide-g-C_3N_4 based ternary composites capture lots of attention among researchers [412]. For example, g-C_3N_4 (CN)/TiO_2 (TO)/$PbTiO_3$ (PTO) films were prepared by the sol-gel followed by the CVD method and were investigated for PEC water splitting [413]. Wang et al. showed the decreased resistance of the interface (R_{CT}) of CN0.10/TO0.4/PTO compared to the pristine PTO and CN0.10/PTO, which facilitated the charge transfer and reduced electron-hole recombination [413]. The incident photo-to-current conversion efficiency (IPCE) was calculated to measure the PEC performance. The pristine PTO has a lower IPCE than CN0.10/PTO, which is mainly due to the higher charge recombination rate. After the TO buffer layer's insertion, the IPCE value was drastically increased to 14.2% at 380 nm [413]. The inserted compact TiO_2 buffer layer provided the type II and Z-scheme interfaces between PTO, TO, and CN and promoted the PEC performance with an improved current density of -68.5 μA cm^{-2} at 0 V versus Ag/Ag-Cl electrode. The high performance is mainly due to the high photogenerated ability of g-C_3N_4/TiO_2 heterojunction. $BiVO_4$ is another cost-effective compound with a proper bandgap (2.4 eV) to enhance the PEC water splitting [184]. Like $PbTiO_3$, $BiVO_4$ can also improve the photocurrent density of the g-C_3N_4@ZnO/$BiVO_4$ heterojunction to the 0.65 mA cm^{-2} at 1.23 V versus Ag/Ag-Cl electrode.

Table 2 provides some other research activities on the water-splitting application of the g-C_3N_4–metal oxide-based composites.

6.1.2. CO_2 Reduction

CO_2 emission is one of the leading environmental problems causing by fossil fuel consumption and results in a temperature rise of the earth's surface. Photocatalytic CO_2 reduction is a green method to deal with this problem for two reasons [111]. Not only CO_2 reduction reduces the CO_2 emission, but it also solves the future energy demands by producing energy fuels such as CH_4, CH_3OH, etc. Photocatalytic CO_2 conversion is largely achieved by different metal oxide-g-C_3N_4 based systems, as they have desirable band edges positions. Equations (4)–(7) are chemical reactions for CO_2 conversion to other solar fuels.

$$CO_2\ (g) + 2\ H^+ + 2\ e^- \rightarrow CO + H_2O \qquad E^\circ = -0.53\ \text{eV vs. NHE at pH 7} \qquad (4)$$

$$CO_2\ (g) + 2\ H^+ + 2\ e^- \rightarrow HCOOH \qquad E^\circ = -0.61\ eV\ vs.\ NHE\ at\ pH\ 7 \quad (5)$$

$$CO_2\ (g) + 6\ H^+ + 6\ e^- \rightarrow CH_3OH + H_2O \qquad E^\circ = -0.38\ eV\ vs.\ NHE\ at\ pH\ 7 \quad (6)$$

$$CO_2\ (g) + 4\ H^+ + 4\ e^- \rightarrow HCHO + H_2O \qquad E^\circ = -0.48\ eV\ vs.\ NHE\ at\ pH\ 7 \quad (7)$$

ZnO and TiO_2 are widely used as the g-C_3N_4-based composites for CO_2 conversion [429,430]. Wang et al. designed a photocatalyst comprising TiO_2 and g-C_3N_4 using ball milling and calcination. The heterostructure between TiO_2 and C_3N_4 leads to a low charge recombination rate, and high separation, resulting in the high CH_4 and CO evolution yields of 72.2 and 56.2 μmol g^{-1} are obtained [431]. In another research, Nb-TiO_2/g-C_3N_4 Z-scheme heterojunctions were investigated and showed that the 50Nb-TiO_2/50g-C_3N_4 composition was the best photocatalysts with high carrier separation ability for the reduction of CO_2 [432]. The existence of electrons and holes in the CB of the g-C_3N_4 and VB of Nb-TiO_2, respectively, makes the Nb-TiO_2/g-C_3N_4 system a potential candidate for reducing of CO_2 into CH_4 and CO and HCOOH. Guo and coworkers were thermally deposited g-C_3N_4 onto the porous ZnO nanosheets by two-step calcination and demonstrated that the ZnO porous nanosheets @ g-C_3N_4-0.4 showed the highest CO_2 conversion efficiency [433]. Not only this composite suppressed the photoinduced electron recombination and facilitated the carrier transfer, but also the CO_2 chemosorption increased in this composite since the increasing defect vacancies formed on the porous ZnO nanosheets. Shen et al. demonstrated 3-ZnO/g-C_3N_4 (3 is the mass ratio of ZnO) has a high photocatalytic activity for CO_2 reduction to CO and CH_4 [434]. This experiment showed an insignificant decrease in photocatalytic activities, which indicates ZnO-g-C_3N_4 had high photocatalytic stability. A similar analysis has been performed on the hydrocarbon generation rate with hollow g-C_3N_4, hollow CeO_2, which is shown in Figure 18a [435]. The fast kinetics of CO reduction results in a higher CO evolution rate compared to the CH_4 and CH_3OH. The highest yield obtains for g-C_3N_4@ 49.7 wt % CeO_2. Increasing amounts of CeO_2 in the g-C_3N_4@CeO_2 composites will decrease the PL intensity at about 460 nm, meaning that the lower electrons and holes recombination and enhanced charge separation (Figure 18b) [435].

Other researchers also work on the CO_2 reduction of g-C_3N_4–metal oxide-based photocatalysts, which is listed in Table 3.

6.1.3. Photodegradation of Organic Pollutants

The development of an increased number of dye-related industries such as textile, food, and furniture manufacturing leads to severe environmental problems [445,446]. In addition to the negative aesthetic impact on water sources, the chemical oxygen demand (COD) in wastewater will be increased in the presence of organic dyes. Various methods, such as coagulation, adsorption, and membrane separation, have been used to eliminate organic dye from effluents, which only reclaim organic dyes from the wastewater liquid phase to the solid phase, creating secondary pollutants in the environment. These techniques are also a significant threat to living organisms. As a result, a metal oxide semiconductor has been widely used for the degradation of organic dyes. Photocatalysis in which most of the metal oxide can eliminate organic dyes by degradation and transfection them into particles, using solar energy for activation of the reaction. The related equations for dye degradation of the metal oxide-g-C_3N_4 are shown in Equations (8)–(11) [447]:

$$(g\text{-}C_3N_4\text{+Metal Oxide}) + h\upsilon \rightarrow {e_{CB}}^- + {h_{VB}}^+ \quad (8)$$

$${O_2}^- + 2{e_{CB}}^- + 2H^+ \rightarrow OH^\bullet + OH^- \quad (9)$$

$${h_{VB}}^+ + H_2O \rightarrow H^+ + OH^\bullet \quad (10)$$

$$\text{Organic pollutant} + OH^\bullet \rightarrow CO_2 + H_2O \quad (11)$$

Table 2. A list of selected works on g-C_3N_4–metal oxide-based photocatalytic water splitting.

Photocatalyst	Type of Heterojunction	Source of Light	Highest Photocatalytic Rate	Ref
TiO_2-g-C_3N_4	Type II	Asahi Spectra Hal-320 (300 mW cm^{-2}) with a 420 nm cut off filter (λ > 420 nm)	3.6 μmol·h^{-1}	[115]
TiO_2-g-C_3N_4	Type II	Xenon lamp with a 320 nm cut off filter (λ > 320 nm)	76.25 μmol·h^{-1}	[414]
C-doped TiO_2-g-C_3N_4	Type II	300 W Xe lamp (PLS-SXE300) with a 420 nm cutoff filter (λ > 420 nm)	35.6 μmol·g^{-1}·h^{-1}	[128]
TiO_2-g-C_3N_4 decorated by Co-Pi	Type II	300 W Xe lamp coupled with a monochromator	-	
TiO_2 nanodots/g-C_3N_4	S-scheme	300 W Xe lamp (LANPU) with a 300 nm cutoff filter (λ > 300 nm)	The H_2 and O_2 evolution rate is 1318.3 and 638.7 μmol g^{-1}, respectively, (roughly as same as the stoichiometric ratio of evolved H_2 to O_2)	[415]
ZnO-g-C_3N_4	Type II	PLS-SXE-300C lamp with an UV light intensity of 34 mW/cm^2 and visible-light intensity of 158 mW/cm^2	-	[416]
N-doped ZnO-g-C_3N_4	Z-scheme	PLS-SXE-300C UV lamp with a 420 nm cut off filter (λ > 420 nm)	152.7 μmol·h^{-1}	[417]
g-C_3N_4-WO_3	-	300-W Xe lamp (PLS-SXE300) with a 420 nm cutoff filter (λ > 420 nm)	963 μmol·g^{-1}·h^{-1}	[141]
O-g-C_3N_4/WO_3	Z-scheme	300 W Xenon lamp with a 420 nm cutoff filter (λ > 420 nm)	15,142 μmol·g^{-1}	[265]
S-Cu_2O/g-C_3N_4	Z-scheme	300 W Xe lamp with a 420 nm cutoff filter (λ > 420 nm)	24.83 μmol·h^{-1}	[418]
BiO_2/g-C_3N_4	Type II Z-scheme	500 W Xe lamp with a 420 nm cutoff filter (λ > 420 nm)	8,542 μmol·g^{-1}	[419]
g-C_3N_4/ $BiYO_3$	Type II	-	37.6 μmol·g^{-1}·h^{-1}	[420]
g-C_3N_4/$La_xCo_{3-x}O_4$	-	300 W Xe lamp with a 420 nm cutoff filter (λ > 420 nm)	63.12 μmol·h^{-1}	[421]
Fe_2O_3/g-C_3N_4	Z-scheme	350 W Xe lamp with a 420 nm cutoff filter (λ > 420 nm)	398.0 μmol·g^{-1}·h^{-1}	[210]
Mn_3O_4/g-C_3N_4	p-n heterostructure	300 W Xenon lamp with a 420 nm cutoff filter (λ > 420 nm) (PLS-SXE300D/300DUV, Beijing Perfectlight)	The H_2 and O_2 evolution rate is 3300 and 654 μmol g^{-1}·h^{-1}, respectively.	[422]
g-C_3N_4/Nitrogen-Doped Carbon Dots/WO_3	-	300 W Xenon lamp with a 420 nm cutoff filter (λ > 420 nm) (CEL-HXF 300)	3.27 mmol g^{-1} h^{-1}	[423]
Mn_3O_4/g-C_3N_4	-	300 W Xenon lamp source (PLS-SXE300D/300DUV)	2700 mmol·g^{-1}·h^{-1}	[422]
NiO/g-C_3N_4	Type II	Xe lamp with a 420 nm cutoff filter (λ > 420 nm)	1.41 mmol·h^{-1}	[424]
In_2O_3/g-C_3N_4	Type II	300 W Xe lamp with a 420 nm cutoff filter (λ > 420 nm)	0.99 mmol·h^{-1}	[425]
MoO_{3-x}-g-C3N4	Z-scheme	300 W Xe lamp with a 420 nm cutoff filter (λ > 420 nm)	22.8 mmol·h^{-1}	[426]
ZnO/Au/g-C_3N_4	Z-scheme	150 W Xenon arc lamp with a 420 nm cutoff filter (λ > 420 nm)	3.69 μmol h^{-1} cm^{-2}	[397]
d-Ti_3C_2/TiO_2/g-C_3N_4	-	300 W Xe lamp with a 420 nm cutoff filter (λ > 420 nm)	1.62 mmol·$h^{-1}g^{-1}$	[396]
TiO_2/g-C_3N_4	Type II	450 W high-pressure mercury lamp	22.4 mol·h^{-1}	[402]
TiO_2-WO_3-g-C_3N_4	-	-	286.6 mmol·h^{-1}	[427]
TiO_2/Ti_3C_2/g-C_3N_4	-	300 W Xe lamp	2592 mmol·g^{-1}	[428]

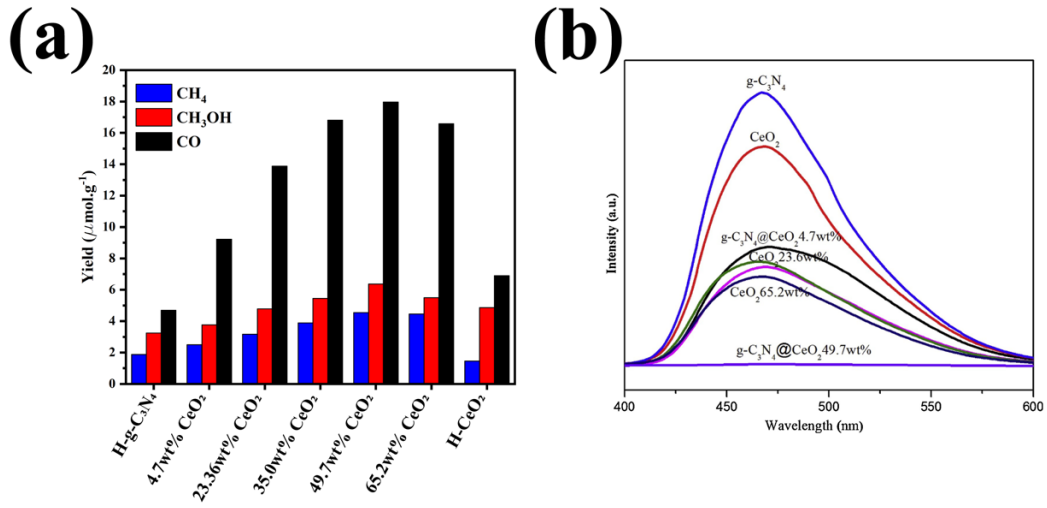

Figure 18. (**a**) Hydrocarbon generation of hollow g-C_3N_4 (H-g-C_3N_4), hollow CeO_2 (H-CeO_2), and g-C_3N_4@CeO_2 for 4 h illumination; (**b**) photoluminescence emission spectra of H-g-C_3N_4, H-CeO_2 references, and g-C_3N_4@CeO_2 heterojunction with different ratios. Copyright © 2022 Elsevier [435].

Researchers have suggested several metal oxide semiconductors that can be used in the g-C_3N_4-based heterojunctions. There are increasing numbers of studies showing the degradation capability of TiO_2, ZnO, WO_3, Bi_2O_3, CeO_2, etc. [100,101,113,116,448–451]. Zada et al. investigated the photodegrading of 2,4-dichlorophenol (2,4-DCP) and bisphenol A (BPA) over Au-(TiO_2/g-C_3N_4) nanocomposites. As mentioned above, the excellent photocatalytic of the nanocomposites containing Au is mainly due to the SPR of decorated Au [131]. The structure revealed 46% and 37% for 2,4-DCP and BPA degradation, which is 5.11 and 3.1 times larger than the bulk g-C_3N_4 in water under visible-light irradiation, respectively [131]. In another research, the synthesized ZnO@g-C_3N_4 exhibited an enhanced photocatalytic activity to degrade tetracycline (TC) under visible-light irradiation, which is 2.77 and 1.51 fold more than the photocatalytic ability of pure g-C_3N_4 and ZnO [452]. The improved degradation was due to the enhanced transference of charge carriers and reduced charge recombination in the presence of the generated reactive oxygen species (ROS). The pharmaceuticals contaminants have hazardous impacts on human health and environmental biodiversity. Zhu and coworkers fabricated WO_3-g-C_3N_4 composites for the photocatalytic degradation of one of the most well-known antibiotics, sulfamethoxazole (SMX), under visible light irradiation [453]. It is also revealed that the presence of RGO besides WO_3-g-C_3N_4 heterojunctions promoted the degradation rate of ciprofloxacin (CIP) nearly twice as compared to the WO_3-g-C_3N_4 structure [454]. In addition, H_2O_2 can raise the photocatalytic activities by the hydroxyl radicals' productions from the degradation of a natural organic matter up to 71% for 5 h [455]. Shafawi et al. prepared Bi_2O_3 particles decorated on porous g-C_3N_4 sheets by impregnation method [456]. 1 g/L of the composite containing g-C_3N_4 with 9 wt % Bi_2O_3 at 10 ppm reactive black 5 (RB 5) at pH = 5.7 demonstrated 84% degradation efficiency under UV-vis light for 120 min. The synergistic effects between g-C_3N_4 and CeO_2 provides higher catalytic activities compared to the bare ones [457–459]. The catalytic effects of the g-C_3N_4/CeO_2 composite, bare g-C_3N_4, and CeO_2 on the thermal decomposition of ammonium perchlorate (AP) were analyzed by using TGA and DTA characterization [460]. Two weight-loss regions from 25 °C to 500 °C, which were similar to the weight loss steps of AP in the absence of catalyst, were observed in Figure 19a,b. The weight loss decomposition temperatures of AP in the presence of the pure g-C_3N_4, CeO_2, and g-C_3N_4/CeO_2 were 53.6 °C, 47.6 °C and 74.6 °C, respectively (Figure 19a). It is also noticeable from Figure 19b that the AP thermal decomposition rate of g-C_3N_4/CeO_2 nanocomposites was higher than that of CeO_2 and g-C_3N_4. This heterojunction also shows a highly efficient for 2,4-dichlorophenol degradation [460].

Table 3. A list of CO_2 reduction applications of the g-C_3N_4–metal oxide-based photocatalytic.

Photocatalyst	Type of Heterojunction	Source of Light	Highest Photocatalytic Rate	Ref
NiO-g-C_3N_4	Type II	300 W Xenon-arc lamp	4.17 $\mu mol \cdot g^{-1} \cdot h^{-1}$	[436]
g-C_3N_4 foam-Cu_2O	Z-scheme	350–780 nm lamp	8.182 $\mu mol \cdot g^{-1} \cdot h^{-1}$ (CO revolution)	[437]
$NiMoO_4$-g-C_3N_4	Z-scheme	-	7238 $\mu mol \cdot g^{-1} \cdot h^{-1}$	[438]
CeO_2-g-C_3N_4	Type II	300 W of Xenon-arc lamp	0.590 $\mu mol \cdot h^{-1}$ (CO evolution)	[439]
ZnO/Au/g-C_3N_4	Z-scheme	300 W UV-Vis lamp	689.7 $\mu mol/m^2$ (CO evolution)	[440]
ZnO/g-C_3N_4	Z-scheme	300 W xenon light source with a 420 nm cutoff filter ($\lambda > 420$ nm)	~72.24 $\mu mol \cdot g^{-1}$	[435]
TiO_2/g-C_3N_4	Type II	8 W UV lamp	The highest CH_4 and CO yields of 72.2 and 56.2 $\mu mol\ g^{-1}$	[431]
Nb doped TiO_2/g-C_3N_4	Z-scheme	1000 W Xe lamp	The CH_4, CO, O_2, HCOOH generation rate in the presence of 50Nb-TiO_2/50 g-C_3N_4 is 562, 420, 1702, 698 $\mu mol\ h^{-1}\ g^{-1}$, respectively.	[432]
ZnO/g-C_3N_4	Z-scheme	350 W Xe lamp	The CH_3OH production rate was 1.32 $\mu mol\ h^{-1}\ g^{-1}$	[429]
ZnO/g-C_3N_4	Type II	300 W xenon lamp with a 420 nm cutoff filter ($\lambda > 420$ nm)	H_2, CH_4, and CO production rates of 22.7 $\mu mol \cdot g\text{-}C_{at}{}^{-1} \cdot h^{-1}$, 30.5 $\mu mol \cdot g\text{-}C_{at}{}^{-1} \cdot h^{-1}$, and 16.8 $\mu mol \cdot g\text{-}C_{at}{}^{-1} \cdot h^{-1}$	[433]
ZnO/g-C_3N_4	Type II	350 W Xe arc lamp	45.6 $mol \cdot g\text{-}C_{at}{}^{-1} \cdot h^{-1}$	[441]
TiO_2/g-C_3N_4	Type II	450 W Xe lamp	22.5 $\mu mol \cdot g^{-1}$ and 70 $\mu mol \cdot g^{-1}$ for CO and CH_4 yield, respectively	[442]
g-C_3N_4/ 3D ordered microporous (3DOM)-WO_3	Z-scheme	visible light ($\lambda \geq 420$ nm)	48.7 $\mu mol\ g^{-1}\ h^{-1}$	[443]
$NiTO_3$/g-C_3N_4	Z-scheme	300 W xenon lamp with a 420 nm cutoff filter ($\lambda > 420$ nm)	The highest yield of CH_3OH production is 13.74 $\mu mol \cdot g^{-1} \cdot h^{-1}$	[444]

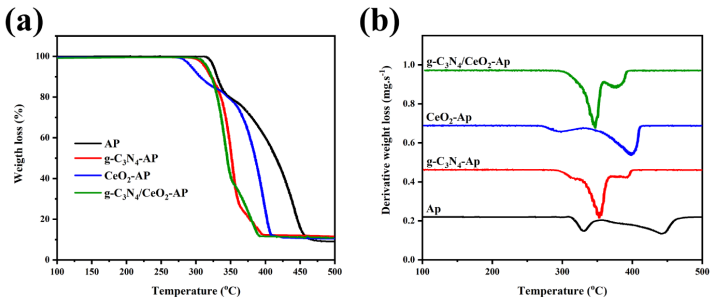

Figure 19. (**a**) TG and (**b**) DTG curves of pure ammonium perchlorate (AP), AP coupled with g-C_3N_4, CeO_2, and g-C_3N_4/CeO_2 heterojunction, Copyright © 2022 Elsevier [460].

Methylene Blue (MB), Methylene Orange (MO), and Rhodamine B (RhB) are the most commonly stable dyes in water at room temperature [461–468]. MB and RhB are toxic dyes that their high concentration can be so harmful to human and marine animal health. In accordance with the high resistivity of the MB and RhB in different environmental conditions, wastewater treatment is an urgent issue. Therefore, it is crucial to provide an effective and low-cost system to eliminate MB and RhB from sewage. As mentioned above, 2D/1D g-C_3N_4/ZnO nanocomposites reveal high stability, which retains the initial activity after repeated cycles [469]. The enhanced photocatalytic activity of g-C_3N_4-ZnO is likely due to the synergistic effects of photon acquisition and direct contact between organic dyes and photocatalyst [470]. To be more specific, the RhB dye degradation efficiency of this composite is 99% and 95% after one and three cycles under sunlight irradiation, respectively [471]. It is reported that the highest degradation efficiency for MB is obtained for the 30 wt % few-layer g-C_3N_4-ZnO nanocomposites is the best composition [472]. The higher amount of g-C_3N_4 can increase the electrons and holes recombination, leading to the decrease of photocatalytic activity. It is also noticeable that RhB degradation efficiency for this composite is about 2.1 times higher than that of pristine ZnO [473]. Apart from g-C_3N_4-ZnO heterojunction, g-C_3N_4-TiO_2 heterojunction has high capability in the RhB degradation [474–477]. In these composites, $^{\bullet}O_2^-$ played a major role while h^+ played a minor role [478–480]. Li et al. prepared Ti^{3+} self-doped TiO_2 nanoparticles/g-C_3N_4 heterojunctions and demonstrated that the Ti^{3+} and O defects improve the conductivity and light absorption range to the visible wavelength region. Besides, the photocatalytic activities for environmental purification of organic compounds (MB) of the Ti^{3+} self-doped TiO_2/g-C_3N_4 nanostructures were improved under visible light irradiation remarkably [481]. It is proven that the photocatalytic activity of 2 wt % g-C_3N_4-TiO_2 improved by 70% compared to the bare TiO_2 [118]. The RhB degradation kinetic constant of g-C_3N_4-TiO_2 heterojunction is 9 times and 25 times higher than g-C_3N_4 and TiO_2, respectively [482]. The $AgPO_4$/g-C_3N_4 was used for the degradation of organic pollutants. Z-scheme carbon nitride with $AgPO_4$ and Ag nanoparticles was used for the degradation of RhB. The presence of Ag can improve visible light absorption. The prepared hybrid structure can improve the electrons holes separation and efficiency [483]. Other metal oxides can also be used in the g-C_3N_4 based heterojunction for organic dye degradation [398,484–487]. Bi_2O_3/g-C_3N_4 heterojunctions are the most commonly used composites for organic dye degradation [488,489]. Fan et al. mentioned that the $^{\bullet}OH$ radicals played the crucial roles during photocatalytic degradation of MB in 0.5- Bi_2O_3/g-C_3N_4 (0.5 is the mass of Bi_2O_3 in the synthetic process) Z-scheme heterojunction, while $^{\bullet}O_2^-$, h^+, e^- radicals have less contribution to this activity [490]. Compared to the pure Bi_2O_3 and bare g-C_3N_4, the Bi_2O_3/g-C_3N_4 heterojunctions showed better catalytic activity with 100% MB degradation ability in 90 min [490]. The 2% Bi_2O_3/g-C_3N_4 composites showed a degradation rate constant of 0.040 min^{-1}, which is 2.5 and 1.9 fold higher than that found for bulk and nitrogen vacant 2D g-C_3N_4 nanosheet, respectively [491]. This composition showed excellent photocatalytic activity with a methylene green degradation efficiency of 98.7% under visible light irradiation [448]. At 30 °C, 5% CeO_2/g-C_3N_4 (5% is the molar ratios of the CeO_2/g-C_3N_4 samples) photocatalyst showed

the best efficiency for MB degrading under visible light irradiation with the constant rate of 1.2686 min^{-1}, which is 7.8-fold higher than pure g-C_3N_4 [492]. Some ternary composites are also used for RhB and MB dye degradation [493]. SnO_2-ZnO quantum dots anchored on g-C_3N_4 nanosheets were demonstrated as a promising candidate for RhB degradation, which is 99% in 60 min under visible-light irradiation [494]. This hybrid also showed a promising potential for hydrogen production with the photocatalytic rate of 13.61 μmol g^{-1}, which is 1.06 and 2.27 times higher than that of the binary ZnO/g-C_3N_4 hybrid and pristine g-C_3N_4. In similar work, ZnS quantum dots (ZNS)/SnO_2/g-C_3N_4 ternary nanocomposites were synthesized via solid-state calcination [495]. The high bandgap of SnO_2 and ZnS QDs leads to the reduction of the recombination rate and increases the separation of the generated carriers in the g-C_3N_4 [495]. The lower conduction band edge position of the SnO_2, which is lower than others compel electrons to accumulate in this state. The position of the electrons and holes helped in improving the photocatalytic performance and enhancing stability. As a result, the transferred electrons can act as a suitable reductant and react with adsorbed O_2 to produce superoxide radicals (O_2^-). On the other side, the holes in the valence band of g-C_3N_4 can directly oxidize the pollutants to degraded products since these holes have strong oxidizing power [495]. g-C_3N_4–metal oxide heterojunction is used to degrade different elements such as Hg, Cr (VI) [136,496,497], and different toxic and harmful materials such as atrazine (ATZ), chloramphenicol, ciprofloxacin (CIP), and etc. [197,454,498–502]. There are several research activities on the photodegradation applications of g-C_3N_4–metal oxide-based heterojunctions which are listed in Table 4.

6.2. Sensors

Some benefits, such as high sensitivity to analytes, rapid response to external stimulations, excellent fluorescence quenching abilities, light and electricity conversion properties, biocompatibility, and high stability make g-C_3N_4 nanosheet a promising candidate as a modified electrode for sensors to detect different analytes such as glucose, hydrogen peroxide, dopamine, etc. [6,549–554]. Metal oxide semiconductors/g-C_3N_4 composites are widely used as gas sensors [555]. As a result, the g-C_3N_4 loaded with metal oxides has also revealed new types of sensors to detect different kinds of materials [556]. General schematic description in Figure 20, shows different types of g-C_3N_4–metal oxide sensors.

Like other applications, g-C_3N_4–TiO_2 based structures are one of the most used composites for sensing applications. Li et al. demonstrated that the photoelectrochemical TiO_2/g-C_3N_4/CdS platform could be employed for the ultrasensitive determination of T4 polynucleotide kinase (T4 PNK) because this composite showed significant stability and reproducibility with high selectivity [557]. The photocurrent response is demonstrated in Figure 21A. To be more specific, "trace a" shows a low photocurrent at a bare electrode. The rapidly increased photocurrent is detected in "trace b" (from 10 to 30 s) due to decrease in the rate of electron-hole recombination and the high-efficiency absorption. In the TiO_2/g-C_3N_4 modified-FTO in "trace c", the photocurrent increases to 30.7 μA since the bandgap of the g-C_3N_4 reduces the charge carrier recombination and facilitates the electron transmission [557]. The photocurrent increases in "trace d" (TiO_2/g-C_3N_4/CdS nanocomposite-modified electrode). The photocurrent increased to 80.0 μA after attaching DNA_3, which can capture ssDNA$_2$ to the electrode and then blocking 6-mercaptohexanol (MCH) ("trace e"). For comparison, the photocurrent of CdSe QDs with or without the bio-functionalization of DNA_2 on the electrode matrix is 180 and 78 μA, respectively [557]. In addition, "trace f" shows that DNA_2-CdSe QDs hybridized onto the surface, the photocurrent density increases to 180.0 μA since the presence of CdSe QDs improve the light absorption efficiency. To compare, CdSe QDs also functionalized the electrode matrix without DNA_2, and the result showed that the photocurrent density is about 78.0 μA which is similar to the "trace e" and highly lower than "trace f". As a result, the constructed platform shows a promising candidate for ultrasensitive detection of T4 PNK activity [557]. TiO_2 with g-C_3N_4 is also used for sensitive detection of protein kinase A (PKA), which is an enzyme that covalently decorates proteins with phosphate groups [558].

Table 4. the photodegradation application of g-C_3N_4–metal oxide-based heterojunctions.

Photocatalyst	Type of Heterojunction	Source of Light	Application	Highest Photocatalytic Rate	Stability	Ref
TiO_2-g-C_3N_4	Z-scheme	300 W Xenon arc lamp with a 420 nm cutoff filter (λ > 420 nm)	Degradation of Rhodamine B and tetracycline hydrochloride	The RhB removal rates for 5 layer TiO_2, 3, 5, 7 layers g-C_3N_4 (0.5)/TiO_2 were 5.1%, 17.9%, 31.2%, and 22.6%, respectively	-	[503]
P/O co-doped g-C_3N_4/anatase TiO_2	Z-scheme	350 W Xenon-arc lamp as a light source with a 420 nm cutoff filter (λ > 420 nm)	Degradation of enrofloxacin	~98.5%	1 h	[504]
TiO_2@ g-C_3N_4	Z-scheme	100-W xenon lamp with a 420 nm cutoff filter (λ > 420 nm)	Degradation of RhB	95.68%		[505]
MoS_2-g-C_3N_4@TiO_2	-	350 W Xenon lamp	Degrdation of Methylene Blue	97.55	1 h	[506]
g-C_3N_4 and polyaniline-co-modified TiO_2	-	xenon lamp containing an optical filter	Degradation of tetrabromobisphenol A	92.42%	16 h	[507]
N-TiO_2/O-doped N vacancy g-C_3N_4	Type II Z-scheme	Lamp with a 420 nm cutoff filter (λ > 420 nm)	Degradation of tetracycline hydrochloride and Cr(VI)	TC-HCl and Cr(VI) removal efficiency is 79.9% and 89.5%, respectively	-	[508]
TiO_2@g-C_3N_4	Type II	300 W xenon lamp	Degradation of tetracycline antibiotic	TiO_2@g-C_3N_4 photocatalyst shows the The highest tetracycline degradation rate is 2.2 mg/min, which is 2 times higher than that of TiO_2 and 2.3 times higher than that of bulk g-C_3N_4.	-	[509]
TiO_2/g-C_3N_4/ persulfate (PS)	Type II	300 W xenon lamp with a 420 nm cutoff filter (λ > 420 nm)	Degradation of micropollutant (phenol, bisphenol A and carbamazepine	99.3%.		[510]
TiO_2 nanowire/g-C_3N_4 nanosheet/graphene (G) heterostructures	-	300 W xenon lamp	Degradation of nitrobenzene	97%	4 h	[119]
Ti^{3+} and O doped TiO_2/g-C_3N_4	Type II	30 W cold visible light-emitting diode	Degradation of Rhodamine B	The photodegradation reaction rate constant based on this heterojunction is 0.0356 min^{-1}, which is 3.87 and 4.56 times higher than those of pristine Ti^{3+}-TiO_2 and g-C_3N_4, respectively.	-	[125]
TiO_2/g-C_3N_4	Type II	-	Degrdation of ciprofloxacin (CIP)	68.1%	3 h	[511]
ZnO-g-C_3N_4	Z scheme	500 W Xe lamp, with a 420 nm cutoff filter (λ > 420 nm)	Degradation of Methylene Blue (MB)	75%	3 h	[512]
ZnO-g-C_3N_4	Z scheme	300 W xenon lamp	Degradation of cephalexin oxidation	98.9%	1 h	[513]

Table 4. *Cont.*

Photocatalyst	Type of Heterojunction	Source of Light	Application	Highest Photocatalytic Rate	Stability	Ref
djembe-like ZnO-g-C_3N_4	-	150 W Xenon light sources	Degradation of MB and RhB	MB and RhB degradation efficiency are ~95% and ~97%, respectively.	50 min	[514]
WO_3-g-C_3N_4		300 W Xenon lamp with a 420 nm cutoff filter (λ > 420 nm)	Degradation of tetracycline	90.54%	1 h	[515]
WO_3-g-C_3N_4	Z-scheme	450 W xenon lamps	Degradation of AO7	100%	75 min	[516]
WO_3-g-C_3N_4	Z-scheme	35-W Xe lamp with a radiation intensity of 1380 μW·cm^2	Degradation of orange G	98%	1 h	[517]
Ag-WO_3/g-C_3N_4	Z-scheme	500 W Xe lamp (Beijing Bofei Technology. Co. Ltd., Beijing, China)	degradation of oxytetracycline hydrochloride	97.74	1 h	[273]
WO_3@g-C_3N_4@MWCNT	Z-scheme	5 mW cm^{-2} Xe lamp (SANEI electronics-JAPAN)	Degradation of tetracycline	79.54%	2 h	[518]
g-C_3N_4/WO_3	Z-scheme	-	Degradation of nitenpyram	The photocatalyst rate constant is 0.036 min^{-1} which is about 1.7 and 25 times higher than that of pure g-C_3N_4 and WO_3, respectively.	-	[519]
Bi_2O_3- g-C_3N_4	Z-scheme	350 W xenon lamp with a 420 nm cutoff filter (λ > 420 nm)	Degradation of Rhodamine B	98%	80 min	[520]
Bi_2O_3- g-C_3N_4	Z-scheme	250 W Xenon lamp with a 420 nm cutoff filter (λ > 420 nm)	Degradation of tetracycline	80.2%	50 min	[521]
g-C_3N_4-CeO_2	Type II	300W Xe arc lamp	Degradation of antibiotic doxycycline hydrochloride	84%	1 h	[522]
Shuttle-like g-C_3N_4-CeO_2	-	300 W Xe arc lamp	Degradation of norfloxacin	88.6%	1 h	[523]
Kaolin/CeO_2/g-C_3N_4	-	500 W Xenon lamp with a 420 nm cutoff filter (λ > 420 nm)	Removal of ciprofloxacin	90%	150 min	[524]
Fe_3O_4/CeO_2/g-C_3N_4	-	300 W Xe lamp with a 420 nm cutoff filter (λ > 420 nm)	Degradation of tetracycline hydrochloride	96.63%	3 h	[525]
Au/g-C_3N_4 nanosheets/CeO_2	Z-scheme	500 W Xe lamp with a 400 nm cutoff filter (λ > 400 nm)	Reduction of hexavalent chromium Oxidation of oxytetracycline hydrochloride	88.2% 95.1%	150 min	[411]
Co_3O_4-g-C_3N_4	-	250 W Xe lamp with a 420 nm cutoff filter (λ > 420 nm)	Degradation of Methyl Orange	100%	3 h	[526]

Table 4. *Cont.*

Photocatalyst	Type of Heterojunction	Source of Light	Application	Highest Photocatalytic Rate	Stability	Ref
NiO-g-C_3N_4	Type II	500 W Xe-lamp with a 420 nm cutoff filter (λ > 420 nm)	Degradation of Methylene Blue	6.3 wt. % NiO loading shows a 2.3 times higher MB degradation rate than that of the pristine g-C_3N_4.	80 min	[527]
V_2O_5-g-C_3N_4	Z-scheme	500 W Xenon lamp with a 420 nm cutoff filter (λ > 420 nm)	Degradation of Congo Red and Cr (VI) reduction	-.	90 min	[528]
MoO_3-g-C_3N_4	Z-scheme	150 W-Xe lamp having 1.5 AM filter which allows wavelength larger than 400 nm for the visible light-based catalytic reaction	Degradation of Rhodamine B	93%	3 h	[529]
MoO_3-g-C_3N_4	Z-scheme	500W Xenon lamp	Degradation of Rhodamine B	100%	10–15 min	[530]
MoO_3-g-C_3N_4	Z-scheme	visible light (λ > 420 nm)	Degradtion of tetracycline	85.9%	100 min	[531]
$BiMoO_6$-g-C_3N_4	Z-scheme	300 W Xe lamp	Degradation of ciprofloxacin	~100	30 min	[532]
g-C_3N_4/SnO_2	S-scheme	A 300 W Osram, 230 V with a 420 nm cut-off filter as used as the visible light source.	Degradation of NO	44.17%	30 min	[533]
g-C_3N_4-NiO	Z-scheme	30 W LED-light source	Degradation of Methyl Orange (MO)	96.8%	2 h	[461]
ZnO/g-C_3N_4	Type II	150 W Xe lamp	Degradation of MB and RhB	The MB and RhB degradation was ~95% and ~97%, respectively.	50 min	[514]
g-C_3N_4/CuO_x	-	350W Xe lamp	Degradation of Methyl Orange (MO)	~62.5%.	70 min	[534]
WO_3/g-C_3N_4	Z-scheme	300 W Xe arc lamp	Degradation of sulfamethoxazole	91.7%	4 h	[453]
g-C_3N_4 Nanosheets/ZnO	-	500 W Xe lamp	Photocatalytic reduction of aqueous chromium(VI)	70%	4 h	[535]
ZnO/g-C_3N_4	-	500 W xenon lamp	Photodegradation of Direct Blue 199 (DB)	99%	100 min	[536]
ZnO/g-C_3N_4	-	A 150 W xenon lamp	Degradation of tetracycline hydrochloride	97%	30 min	[452]
MoS_2/Al_2O_3/g-C_3N_4	-	150 W tungsten halogen lamp with a 420 nm cutoff filter (λ > 420 nm)	Degradation of crystal violet (CV)	97.3%.	90 min	[537]
g-C_3N_4/ZnO	Z-scheme	300 W Xenon lamp cutoff filter with a 420 nm cutoff filter (λ > 420 nm	Degradation of 4-chlorophenol	~ 95%	1 h	[538]

Table 4. *Cont.*

Photocatalyst	Type of Heterojunction	Source of Light	Application	Highest Photocatalytic Rate	Stability	Ref
Gd_2O_3 NPs@g-C_3N_4	-	300 W Xe lamp with a 420 nm cutoff filter (λ > 420 nm) (PLS-SXE300, Beijing Perfectlight Technology Co., Ltd., Beijing, China)	Degradation of Methyl Orange (MO) Methyl Blue (MB) Rhodamine B	72.4% 95.5% 100%	2 h	[539]
MoO_3/g-C_3N_4/peroxydisulfate (PDS)	Z-scheme	350 W Xenon lamp with a 420 nm cutoff filter (λ > 420 nm)	degradation of ofloxacin (OFLX)	94.4%	2 h	[540]
ZnO/g-C_3N_4	Z-scheme	300 W Xe lamp	Degradation of cephalexin	98.9%	1 h	[513]
Ce_2O/Bi_2O_3/g-C_3N_4	Z-scheme	75 W halogen lamp	Degradation of Malachite green and Rose Bengal	-	1 h	[541]
CuO/ZnO/g-C_3N_4	Z-scheme	400 W hallow lamp	Degradation of Methylene Blue and ammonia-nitrogen	The MB and ammonia-nitrogen degradation efficiency are ~98% in 45 min and 91% in 6 h.	45 min, and 6 h	[542]
Fe_3O_4/ZnO/g-C_3N_4	Type II	23 W white LED	Degradation of pantoprazole	97.09%.	90 min	[543]
Fe_3O_4/TiO_2/g-C_3N_4	-	500 W Xenon Lamp with a 420 nm cutoff filter (λ > 420 nm	Degradation of Rhodamine B (RhB) and Methylene Orange (MO)	The photocatalyst shows the RhB, and MO degradation efficiency is ~96.4% in 80 min and 90% in120 min.	8 min and 120 min	[544]
g-C_3N_4/ZnO/TiO_2	-	1000 W xenon lamp irradiation system equipped with a 410 nm cutoff filter under room temperature.	Degradation of p-toluenesulfonicacid (p-TSA)	100%	60 min	[545]
ZnO/Ag_2O/g-C_3N_4	-	high pressure xenon short arc lamp with the light intensity of 100 mW cm^{-2}	Degradation of ciprofloxacin	97.4%	48 min	[196]
WO_3/TiO_2@g-C_3N_4	-	500 W metal halide lamp	Removal of acetylsalicylate (aspirin) and methyl-theobromine (caffeine)	98%	90 min	[546]
TiO_2@g-C_3N_4/Co_3O_4	-	300 W xenon lamp	Degradation of tetracycline (TC) and Methylene Orange (MO)	The TC (10 mg/L) and MO (25 mg/L) degradation efficiency are 91.6% and 97.8%, respectively.	1 h	[547]
g-C_3N_4/Bi_2O_3/TiO_2	-	Xe-lamp light source with a 420 nm cutoff filter (λ > 420 nm	Degradation of Methylene Blue (MB)	The MB removal efficiency is 77.5%.	3 h	[548]
SnO_2/ZnO@g-C_3N_4	-	300 W xenon lamp	Degradation of Rhodamine B dye and H_2 production	99%	1 h	[494]
g-C_3N_4/NiO/ZnO/Fe_3O_4	-	-	removal of esomeprazole	95.05 ± 1.72%	70 min	[513]

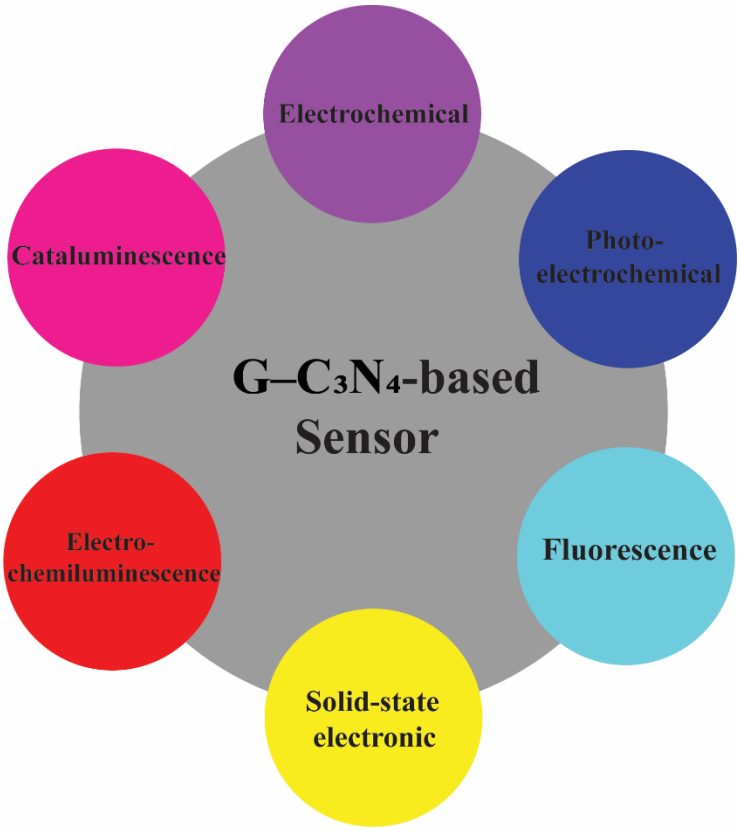

Figure 20. Different kinds of g-C_3N_4–metal oxide-based sensors for materials detection.

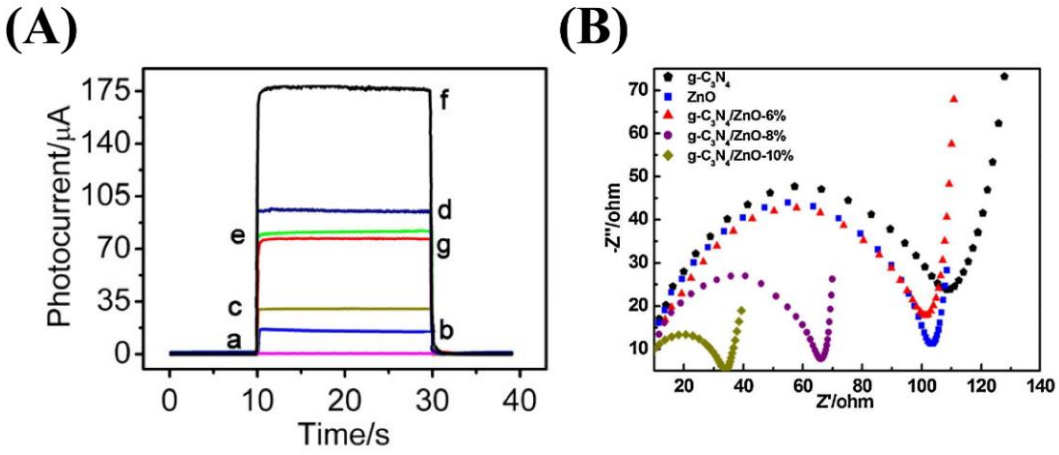

Figure 21. (**A**) Photocurrent responses of (a) FTO, (b) FTO/TiO_2, (c) FTO/TiO_2/g-C_3N_4, (d) FTO/TiO_2/g-C_3N_4/CdS, (e) FTO/TiO_2/g-C_3N_4/CdS/capture-DNA_3/MCH, (f), FTO/TiO_2/g-C_3N_4/CdS/capture-DNA_3/MCH/DNA_2-CdSe, (g) FTO/TiO_2/g-C_3N_4/CdS/capture-DNA_3/MCH/CdSe, Copyright © 2022 American Chemical Society [557]; (**B**) Nyquist plots of ZnO, g-C_3N_4/ZnO composites and g-C_3N_4 nanosheets electrodes, Copyright © 2022 American Chemical Society [559].

ZnO-g-C_3N_4 is another heterojunction used as an agent as UV-assisted gas sensors. It is shown that the ethanol (C_2H_5OH) sensing capability of ZnO-g-C_3N_4 is much higher when compared to the bare ZnO and g-C_3N_4. The ZnO with 8% g-C_3N_4 showed the best sensing performance than the others, which attributes to effective electrons and holes separation between g-C_3N_4 and ZnO and the UV-light catalytic effect in the room temperature [559]. The structure showed an excellent response of ethanol at room temperature, which was

higher than the pure ZnO at the same condition. The arc radius of ZnO and g-C_3N_4/ZnO is shown in Figure 21B. The results show that adding g-C_3N_4 nanosheets to ZnO improves the charge transfer and reduces the electrical resistivity [559].

Sensing of NO_2 and CH_4 by ZnO-g-C_3N_4 heterojunction have also been investigated [560,561]. Hydrogen sulfide (H_2S) is a corrosive and toxic gas, which can be generated from oil refining, mines, or petroleum fields, fuel cells, or food processing industries and may cause severe problems. As a result, eliminating H_2S has always been a serious research topic. Zeng et al. used α-Fe_2O_3/g-C_3N_4 for H_2S detection and showed that 5.97% α-Fe_2O_3 with g-C_3N_4 provides the best cataluminescence response [562]. The prepared α-Fe_2O_3/g-C_3N_4 composite can be used as an H_2S gas sensor in environmental monitoring, oil refining, food processing, and so forth. Researchers have shown that g-C_3N_4-SnO_2 composites can also be used as sensors for different kinds of compounds. Specifically, Zhang et al. proved that the presence of g-C_3N_4 beside SnO_2 enhances the gas sensitivity and selectivity of SnO_2 to acetic acid vapor with the reduced temperature from 230 °C to 185 °C [563]. The limit of acetic acid vapor detection is 0.1 ppm; however, the long-term stability of the prepared composite is low and should be improved. In-SnO_2 loaded cubic mesoporous g-C_3N_4 will be a new method and structure to design efficient humidity sensors for monitoring indoor climatic conditions [564]. Table 5 lists the applications of g-C_3N_4–metal oxide heterojunction used as sensor material.

6.3. Bacterial Disinfection

According to different sizes, shapes, and structures of bacteria, viruses, microbes, and microalgae, the g-C_3N_4 has the ability to eliminate them under ultraviolet or visible light irradiation changes. Fabricating the g-C_3N_4 with different metal oxides is important for effective composites for water antimicrobial disinfection and microbial control. Biohazards are widely present in wastewater and contaminated water containing a variety of viruses, bacteria, fungi, etc., causing health issues in humans [30]. The pioneering work by Matsunaga et al. showed that TiO_2 could help in inactivating bacteria such as *Escherichia coli,* Lactobacillus acidophilus, and *Saccharomyces cerevisiae* under UV light [580]. TiO_2 suffers from low absorption of solar energy and this is due to the wide bandgap of TiO_2, which is widely discussed in the previous parts. One method to increase TiO_2 performance is to combine it with different semiconductors. Li et al. prepared g-C_3N_4-TiO_2 using a facile hydrothermal-calcination approach with high photocatalytic bacterial inactivation ability [114]. They demonstrated that this composite could facilitate water disinfection, especially in hospital wastewaters with highly concentrated pathogenic microorganisms, using visible light. In another work, researchers investigated the excellent efficiency of this composite on the removal of the microcystis aeruginosa and Microcystin-LR [581].

In order to improve the photocatalytic activity, researchers are more likely to dope metal elements such as Ag and Cr in the g-C_3N_4–metal oxide structure, which can perform as an electron sink to separate the carriers. Doping these elements not only can modify the band edge positions of these structures but also, due to antimicrobial and bacterial properties of these materials, they are widely used in the g-C_3N_4–metal oxide-based photocatalysts [102,189]. g-C_3N_4/Cr-ZnO nanocomposites with superior antibacterial activity against Gram-negative (*Escherichia coli*) and Gram-positive (*Bacillus subtilis, Staphylococcus aureus*, and *Streptococcus salivarius*) were investigated [172]. In this research, the 60%g-C_3N_4/5%Cr-ZnO nanocomposite performs the highest antibacterial activity. Fe-SnO_2/g-C_3N_4 revealed a promising sterilization performance for *Escherichia coli* and *Staphylococcus aureus* under sunlight, near-ultraviolet light, and daylight lamp [582]. The sterilization performance of this structure is mostly deserved under a daylight lamp. The magnetic silver-iron oxide nanoparticles decorated graphitic carbon nitride nanosheets showed antibacterial performance against *E. coli* bacteria [583].

Table 5. The list of applications of g-C_3N_4–metal oxide heterojunction used for detection.

Photocatalyst	Application	Explanation	Ref
MoO_3-g-C_3N_4	Detection of Furazolidone	The high electroactive surface area (0.3788 cm^2), as well as enhanced heterogeneous electron transfer rate ($K°_{eff}$ = 4.91 × 10^{-2} cm·s^{-1} can detect Furazolidone with low limit of detection (LOD) (1.4 nM) with a working range of 0.01–228 µM.	[528]
Co_3O_4-g-C_3N_4	Detection of environmental phenolic hormones	This composite showed a wide detection range and a low limit of detection LOD (10^{-9} mol L^{-1})	[565]
g-C_3N_4-Fe_3O_4	Determination of Tramadol in Human Biological Fluids	LOD of this composite is ~0.1 µM	[566]
V_2O_5-g-C_3N_4	Detection of folic acid	The sensitivity, the LOD, and noise-to-signal ratio of the sensor is 19.02 µA mM^{-1} cm^{-2}, and 0.00174 µM, and 3 (S/N = 3), respectively	[567]
g-C_3N_4-NiO	Detection of quercetin	The dynamic range and LOD of g-C_3N_4-NiO for sensing quercetin is 10 nM to 250 and 0.002 µM, respectively	[568]
Cu_2O-g-C_3N_4	Humidity sensor	The response time and recovery time were 180–200 s and 5–10 s, respectively.	[569]
NiO-Co_3O_4-g-C_3N_4	Detection of tetrabromobisphenol-A	This structure showed a LOD of ~0.1 mmol L^{-1}	[570]
ZnO @ g-C_3N_4	Detection of CCRF-CEM cells	The LOD of this compsite is ~20 cell/mL	[571]
ZnO flower-rod/g-C_3N_4-gold nanoparticle	Detection of carcinoembryonic antigen (CEA)	The PEC aptasensor for CEA determination is from 0.01 to 2.5 ng·mL^{-1} with detection of 1.9 pg·mL^{-1}.	[572]
g-C_3N_4/ZnO	Ethanol sensing	Compared to the ZnO, the g-C_3N_4/ZnO-8% composites revealed an excellent response ~60 orders of magnitude at room temperature.	[559]
ZnO/g-C_3N_4	NO_2 sensing	The response, recovery time, and LOD of ZnO/g-C_3N_4-10 wt % are 142, 190 s, and 38 ppb, respectively.	[561]
SnO2/g-C_3N_4	Ethanol gas Sensing	The composite with 7 wt % g-C_3N_4 content exhibited a promising gas sensing property to ethanol, which has better response and selectivity than that of the pure SnO_2 based sensor.	[321]
g-C_3N_4/ZnO	CH_4 Sensing	The higher active sites can be obtained in this structure due to the larger specific surface area leading to the great response toward 1000 ppm CH_4.	[560]
g-C_3N_4-Mn_3O_4	H_2S sensor	The LOD (S/N = 3, LOD) is 0.13 µg mL^{-1}	[573]
α-Fe_2O_3/g-C_3N_4	H_2S sensor	The linear detection range and detection limit of the H_2S gas sensor were 0.88–7.01 µg mL^{-1}(r = 0.998) and 0.5 µg mL^{-1}(S/N = 3), respectively.	[562]
O vacancy $WO_{2.9}$/g-C_3N_4	4-nitrophenol Sensing	Compared to other research works, this heterojunction showed the linear range of 0.4–100 µmol/L and a lower detection limit of 0.133 µmol/L.	[574]
b-Bi_2O_3/g-C_3N_4	Detection of chlorpyrifos	The linear detection range and detection limit of this sensor were 0.1–80 ng mL^{-1} a03 µg mL^{-1}, respectively.	[575]
Fe_3O_4/Bi_2O_3/g-C_3N_4	Determination of Cd^{2+} and Pb^{2+}	The minimum quantity for Cd^{2+} and Pb^{2+} that can be detected is 3 × 10^{-9} and 1 × 10^{-9} mol/L, respectively.	[576]
WO_3/g-C_3N_4	Detection of phosmet	The limit of detection (LOD) and limit of quantification (LOQ) of this device was calculated 3.6 nM and 11.2 nM, respectively.	[577]
WO_3/g-C_3N_4/MnO_2	Detection of oxytetracycline cathodic	This sensor exhibited a wide detection range from 1 pM to 150 nM and a low detection limit of 0.1 pM.	[578]
CuO-g-C_3N_4	Aflatoxin B1 sensing	The limit of detection of 6.8 pg mL^{-1} for AFB1.	[579]

Zhao and coworkers illustrated that g-C_3N_4/ZnO/cellulose (CNZCel) shows the high thermal stability of the composite and photo-excited carriers separation efficiency and decreases the recombination rate [202]. Besides, the nanocomposite revealed excellent antibacterial activity against Escherichia coli (*E. coli*) and Gram-positive bacteria *Staphylococcus aureus* (*S. aureus*). The presence of ZnO in the structure can efficiently enhance the antibacterial activities against *E. coli* and *S. aureus*. Compared to the other materials, these ternary composites demonstrated better antibacterial performance (Figure 22a,b). The effect of the g-C_3N_4 content on the antibacterial property against *E. coli* and *S. aureus* in this composite is also investigated, which is shown in Figure 22c,d [202]. The mechanism of antibacterial activity generates electron-hole pairs under illumination, which can provide enormous reactive oxygen species (ROS), such as $^{\bullet}O_2^-$, $^{\bullet}OH_2$ and H_2O_2, needed for the inhibition of *E. coli* and *S. aureus* growth.

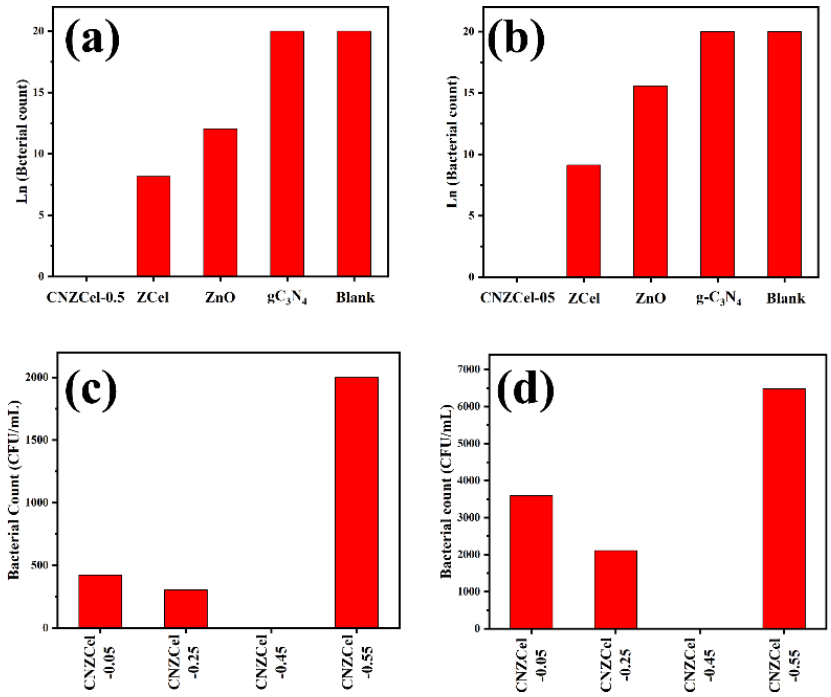

Figure 22. (**a**) Plots of bacterial counts of g-C_3N_4/ZnO/cellulose-0.45 (0.45 corresponds to the mass of g-C_3N_4 addition), ZnO/cellulose, ZnO, g-C_3N_4, and blank sample against *S. aureus* and (**b**) *E. coli*; (**c**) bacterial counts of g-C_3N_4/ZnO/cellulose composites against *S. aureus* and (**d**) *E. coli*. Reproduced from Reference [202].

Table 6 mentioned some additional studies on the disinfection ability of g-C_3N_4–metal oxide-based nanomaterials.

Table 6. Number of researches on the disinfection ability of the g-C_3N_4 metal oxide-based nanomaterials.

Photocatalyst	Source of Light	Application	Highest Photocatalytic Rate	Ref
g-C_3N_4/TiO_2/Ag	Xe lamp with a 420 nm cutoff filter (λ > 420 nm)	Bactericidal efficiency against *E. coli*	the optimal bacterial inhibition of g-C_3N_4/TiO_2/Ag was 84%	[102]
g-C_3N_4/Cu_2O	300 W xenon lamp with 400 nm cutoff filter (λ > 400 nm)	Inactivation efficiencies of *E. coli* as well as Fusarium graminearum	g-C_3N_4 with 45%Cu_2O composition revealed the inactivation efficiencies of ~7 log *E. coli*	[584]
TiO_2/g-C_3N_4/SnO_2	300 W xenon lamp with 420 nm cutoff filter (λ > 420 nm)	Bactericidal efficiency against *E. coli*	TiO_2/g-C_3N_4/SnO_2 structure showed a good *E. coli* disinfection efficiency under visible and UV irradiation, with ~−6.7 log *E. coli* and −8.2 log *E. coli*, respectively.	[314]
α-Fe_2O_3/CeO_2 decorated g-C_3N_4	500 W Xe light with the cut-off filter of ~420 nm (λ > 420 nm)	Antibacterial activities against *S. aureus* (G+) and *E. coli* (G−) bacteria	α-Fe_2O_3/CeO_2 decorated g-C_3N_4 exhibited perfect antibacterial to *E. coli* and *S.aureus* activity with the maximum zone of inhibition (ZOI) of 11 ± 0.5, 12 ± 0.	[585]
g-C_3N_4-m-Bi_2O_4	500 W halogen lamp with UV-cut off filter (λ > 420 nm)	Bactericidal efficiency *E. coli* and *S.aureus* bacteria	The ZOI value for E.coli and *S. aureus* bacterial strains was ~11±0.5 mm and 12–13 ± 0.5.	[586]
Ag/ZnO/g-C_3N_4	300 W xenon arc lamp	Bactericidal efficiency against *E. coli*	The *E. coli* disinfection efficiency of Ag/ZnO/g-C_3N_4 structure is ~7.4 log *E. coli*.	[190]
Ag/AgO-g-C_3N_4	100 W tungsten lamp	Bactericidal efficiency against *E. coli*	The 1, 2, 3, and 4 mg of catalyst showed low quantitative *E. coli* growth inhibition, which was ~17% and 65%, 97%, 99%, respectively.	[587]
Cu_2O-g-C_3N_4	36 W fluorescent lamp with the cut-off filter of ~400 nm (λ > 400 nm)	Bactericidal efficiency against *B. subtilis*, *E. coli*, *S. aureus* and *P. aeruginosa*	The maximum ZOI for Cu_2O-g-C_3N_4 to *B. subtilis* *E.coli*, *S. aureus* and *P. aeruginosa* is 22 ± 1.67, 15 ± 1.08, 11 ± 1.22, 6 ± 0.09, respectively.	[587]
g-C_3N_4 / TiO_2 Kaolinite	Xenon lamp with a 400 nm cut-off filter	Disinfection ability towards *S. aureus*	The disinfection efficiency of g-C_3N_4/TiO_2/kaolinite is ~4.3 log cfu/mL in 5 h.	[588]
TiO_2/g-C_3N_4	500 W xenon arc lamp with a 400 nm cut-off filter	Anti-fouling ability of *E. coli*	TiO_2/g-C_3N_4 showed an excellent *E. coli* removal with a permeate flux of 2 times higher than that of filtration alone.	[589]
TiO_2/g-C_3N_4	-	Bactericidal efficiency against *E. coli*	The bacterial survival rate for the TiO_2 nanotube/g-C_3N_4 nanofilms is ~16%.	[590]
g-C_3N_4/Ag-TiO_2	Xenon lamp	Bactericidal efficiency against both Gram-negative 18 Escherichia-coli and Gram-positive Staphylococcus-aureus	The presence of Ag in g-C_3N_4/Ag-TiO_2 structure could enhance water disinfection under visible light.	[591]
g-C_3N_4/MoS_2-Bi_2O_3	300 W xenon arc lamp	Bactericidal efficiency against *E. coli*	g-C_3N_4/Bi_2O_4 with the ratio of 1:0.5, could entirely inactivate 6-log10 cfu/mL *E. coli*.	[586]

6.4. Other Applications

Due to the specific properties of g-C_3N_4-based heterojunctions, these composites can be used in many other applications [150,247,585,592]. With reference to the high energy demand for electronic devices and vehicles, rechargeable lithium-ion batteries (LIBs) have captured enormous attention among many researchers [319,320,593–595]. Anode materials, which are a significant part of the LIBs, should have improved specific capacity, high stability. SnO_2 is a new type of lithiophilic material with high specific capacity (1494 mAh g^{-1}), low potential for Li^+ insertion, increased number of sources, and etc. [320,593,596–602]; however, it suffers from significant volume expansion (∼300%) during the charge-discharge cycling, leading to fast capacity fading. SnO_2 nanosheets with 20–25 nm thickness dispersed in the g-C_3N_4 showing the potential lithium storage for LIBs. SnO_2@C_3N_4 nanocomposites can also be prepared by a scalable solid-state reaction [319]. Tran et al. used the hydrothermal method to grow SnO_2 onto the graphite oxide/g-C_3N_4 [320]. This composite showed an excellent reversible capacity and cycling performance for lithium storage, which may attribute to the existence of g-C_3N_4 or graphite oxide-g-C_3N_4. SnO_2@g-C_3N_4 based nanocomposites provide a suitable substitute for next-generation high-power and low-cost LIBs [319]. Zn_2GeO_4 nanoparticles demonstrate high capacity and act as spacers to prevent the g-C_3N_4 sheets from stacking, leading to the expanded interlayer and exposed vacancies for higher Li-ion storage. Besides, g-C_3N_4 layers, in turn, reduce the expansion of the particles and provide more stable solid electrolyte interphase, results in highly reversible lithium storage capacity, which is 1370 mA h g^{-1} at 200 mA g^{-1} after 140 cycles with a significant rate capability of 950 mA h g^{-1} at 2000 mA g^{-1} [595]. The SnO_2 nanosheets with g-C_3N_4 can enhance lithium storage capabilities and cycling performance [593]. Other g-C_3N_4–metal oxide nanocomposites can also be used in the supercapacitor that can be used with batteries to mitigate the power delivery problems associated with batteries [596–598]. The bare g-C_3N_4, g-C_3N_4/CuO, g-C_3N_4/Co_3O_4 electrode-based device exhibited a specific capacitance of 72 F g^{-1}, 95 F g^{-1}, and 201 F g^{-1}, respectively [599]. Besides, the energy density of g-C_3N_4/CuO and g-C_3N_4/Co_3O_4 at the constant power density of 1 kW·kg^{-1} are 13.2 W·h·kg^{-1}, and 27.9 W·h·kg^{-1}, respectively. Moreover, the excellent theoretical capacities of V_2O_5 for the next generation supercapacitors makes the porous g-C_3N_4@V_2O_5 good candidate with a high specific capacity of about 457 Fg^{-1} at 0.5 Ag^{-1} with high cycling performance (~84% after 500 cycles) [600].

Photocatalytic nitrogen fixation, which is a clean and sustainable method for the production of NH_3, is another application of g-C_3N_4-based materials. However, insignificant surface-active sites, poor stability, and high recombination rate of carriers have restricted the efficiency of g-C_3N_4 for nitrogen fixation activities. The carrier separation should be enhanced by doping with other elements or compositing with various metal oxides. Finally, nitrogen gas should completely adsorb on the photocatalyst for the reduction steps [603]. It is shown that the cyano group (–C ≡NC) in cyano group modified g-C_3N_4 enhance the photocatalytic applications for N_2 fixation up to 128 times [604].

As we discussed earlier, iodine and sulfur are atoms that can improve the carriers' activities in the bulk g-C_3N_4 [605]. To be more specific, ultrathin sulfur-doped g-C_3N_4 porous nanosheets revealed a superior photocatalytic nitrogen fixation rate with 5.99 mM·h^{-1}·g^{-1} for 4 h under simulated sunlight irradiation [606]. Zhang et al. demonstrated that B atoms change the band structures and WO_3 enhances the photocatalytic activities. The quantum efficiency (QE) of the prepared composites is 0.71% for nitrogen fixation at 400 nm with a yield of 450.94 µmol g^{-1} h^{-1} under visible light [606]. In another work, Liu and coworkers mentioned that the phosphorus-doped 1 T-MoS_2 as co-catalyst decorated nitrogen-doped g-C_3N_4 nanosheets speed up the N_2 reduction rate to 689.76 µmol L^{-1} g^{-1}·h^{-1} in deionized water under simulated sunlight irradiation, which is 2.59, 1.65, 1.47, and 1.30 times higher than that of pure g-C_3N_4, 1 T-MoS_2@g-C_3N_4, 1 T-MoS2@N doped g-C_3N_4, and P doped 1 T-MoS_2@g-C_3N_4, respectively. It is noteworthy to note that MoS_2 mainly includes semiconductive 2H phase and metal octahedral 1 T phase with promising conductivity and suitable photocatalysis since this phase provides a large number of active

sites on the base and edge [607]. Researchers also used metal oxides with g-C_3N_4-based composites to improve nitrogen fixation productivity. TiO_2/$SrTiO_3$/g-C_3N_4 ternary heterojunction nanofibers demonstrated N_2 fixation value under-stimulated sunlight irradiation is 2192 μmol g^{-1} h^{-1} L^{-1}, which is 1.9 and 3.3 times better than those of TiO_2/g-C_3N_4 nanofibers and $SrTiO_3$/g-C_3N_4 nanofibers, respectively [605,608]. Oxidized g-C_3N_4 can also enhance the chemo selective and unselective oxidative processes, utilized in organic reactions to provide synthons required in several value-added preparations [609].

It is interesting to mention that g-C_3N_4–metal oxide-based heterojunction can be widely used to detect of different biological materials, gasses, heavy metals, organic and inorganic materials [547,610]. g-C_3N_4–metal oxide-based composites can also be widely used for other applications, especially supercapacitors and desulfurization [107,611–613].

7. Conclusions, Limitations and Challenges

To fix inadequate light-harvesting of the bare g-C_3N_4, many researchers used doping elements to improve the efficiency, while combining g-C_3N_4 with other materials, such as metal oxides are another approach to deal with this issue. The investigation of g-C_3N_4–metal oxide-based heterojunctions with engineered bandgaps, and modified surface to enhance the abortion spectrum towards the visible-light region, reduction of the charge carrier recombination, and increasing the surface adsorption and reaction are among the main scopes of investigations of g-C_3N_4 based materials. Among all types of heterojunctions mentioned in the review paper, almost all g-C_3N_4–metal oxide-based nanocomposites have a Type II or a Z-scheme system, which have been proven to be outstanding for different applications. The applications highlighted included water splitting, CO_2 reduction, photodegradation of organic pollutants, nitrogen fixation, catalysis, sensing, bacterial disinfection, energy storage, etc.

Several types of carbon-based nanomaterials such as carbon-based quantum dots (CDs) (carbon quantum dots (CQDs) and graphene quantum dots (GQDs)), which are discussed in our previous work, can be used as sensors [214]. One kind of carbon-based nanomaterials is g-C_3N_4, which is widely used to detect different cells in human biological fluids, gasses, humidity, heavy metals, etc. Nevertheless, these applications also can be enormously challenging and give plenty of room for research and development, and there are great demands for fast and accurate diagnostic methods for both clinical and commercial applications. As a result, it is suggested to develop systems for clinical use to detect different diseases outside the body, especially the newly emerging one, COVID- 19, mainly due to its high chemical stability and excellent efficiency in absorbing the light and promising photocatalytic performance. In addition, the detection of different heavy metals and ions is one of the most crucial factors for contaminant removal and water treatment. Since g-C_3N_4–metal oxide photocatalysts have exhibited the superior potential to detect different materials, it seems critical to extending investigations on the efficiency of these heterojunctions for detection of Cu^{2+}, Hg^{2+}, Cr (VI), and Ag^{+}.

The need for using solar energy has increased among many researchers, as energy resources are going to be depleted. Researchers require suitable semiconductors for different catalytic reactions, such as H_2 and O_2 generation by water splitting, CO_2 reduction to hydrocarbon fuels, etc. In order to have a future practical application in this area, we have to resolve some issues about the conversion of solar energy to fuel. The cocatalysis and quantum efficiency are among the most important properties for H_2O splitting and CO_2 reduction, which for the g-C_3N_4–metal oxide composites, researchers do not have enough knowledge. The enhanced photocatalytic activity of the mentioned nanocomposites in this review under visible light encourages researchers to use these heterojunctions in antibacterial and antiviral applications. Inactivation originates from direct hole oxidation and $^{\bullet}O_2^{-}$, $^{\bullet}OH$, and H_2O_2, which are produced in a reductive way, and dependent on the type of microorganisms. Because several research works have been conducted on water disinfection and microbial control in the laboratories, it is necessary to have more practical exploration on full-scale water treatment.

Author Contributions: A.A.: Investigation, Reviewing papers, Writing the first draft. K.G.: Conceptualization, Supervision, Writing-Reviewing and Editing, Funding acquisition. All authors have read and agreed to the published version of the manuscript.

Funding: This research received was funded by NSERC Discovery Grant of Dr. Ghandi to support the PhD of Amirhossein Alaghmandfard at University of Guelph.

Institutional Review Board Statement: Not applicable.

Informed Consent Statement: Not applicable.

Data Availability Statement: The data presented in this study are available on request from the corresponding author.

Conflicts of Interest: The authors declare no conflict of interest.

References

1. Goettmann, F.; Fischer, A.; Antonietti, M.; Thomas, A. Metal-Free Catalysis of Sustainable Friedel–Crafts Reactions: Direct Activation of Benzene by Carbon Nitrides to Avoid the Use of Metal Chlorides and Halogenated Compounds. *Chem. Commun.* **2006**, *43*, 4530–4532. [CrossRef] [PubMed]
2. Ong, W.-J.; Tan, L.-L.; Ng, Y.H.; Yong, S.-T.; Chai, S.-P. Graphitic Carbon Nitride ($g\text{-}C_3N_4$)-Based Photocatalysts for Artificial Photosynthesis and Environmental Remediation: Are We a Step Closer to Achieving Sustainability? *Chem. Rev.* **2016**, *116*, 7159–7329. [CrossRef] [PubMed]
3. Liu, X.; Ma, R.; Zhuang, L.; Hu, B.; Chen, J.; Liu, X.; Wang, X. Recent Developments of Doped $g\text{-}C_3N_4$ Photocatalysts for the Degradation of Organic Pollutants. *Crit. Rev. Environ. Sci. Technol.* **2020**, *51*, 751–790. [CrossRef]
4. Taha, M.M.; Ghanem, L.G.; Hamza, M.A.; Allam, N.K. Highly Stable Supercapacitor Devices Based on Three-Dimensional Bioderived Carbon Encapsulated $g\text{-}C_3N_4$ Nanosheets. *ACS Appl. Energy Mater.* **2021**, *4*, 10344–10355. [CrossRef]
5. Jiang, H.; Li, Y.; Wang, D.; Hong, X.; Liang, B. Recent Advances in Heteroatom Doped Graphitic Carbon Nitride ($g\text{-}C_3N_4$) and $g\text{-}C_3N_4$/Metal Oxide Composite Photocatalysts. *Curr. Org. Chem.* **2020**, *24*, 673–693. [CrossRef]
6. Wang, L.; Wang, C.; Hu, X.; Xue, H.; Pang, H. Metal/Graphitic Carbon Nitride Composites: Synthesis, Structures, and Applications. *Chem. Asian J.* **2016**, *11*, 3305–3328. [CrossRef] [PubMed]
7. Ren, Y.; Zeng, D.; Ong, W.-J. Interfacial Engineering of Graphitic Carbon Nitride ($g\text{-}C_3N_4$)-Based Metal Sulfide Heterojunction Photocatalysts for Energy Conversion: A Review. *Chin. J. Catal.* **2019**, *40*, 289–319. [CrossRef]
8. Ismael, M. A Review on Graphitic Carbon Nitride ($g\text{-}C_3N_4$) Based Nanocomposites: Synthesis, Categories, and Their Application in Photocatalysis. *J. Alloys Compd.* **2020**, *846*, 156446. [CrossRef]
9. Inagaki, M.; Tsumura, T.; Kinumoto, T.; Toyoda, M. Graphitic Carbon Nitrides ($g\text{-}C_3N_4$) with Comparative Discussion to Carbon Materials. *Carbon* **2019**, *141*, 580–607. [CrossRef]
10. Chu, Y.-C.; Lin, T.-J.; Lin, Y.-R.; Chiu, W.-L.; Nguyen, B.-S.; Hu, C. Influence of P, S, O-Doping on $g\text{-}C_3N_4$ for Hydrogel Formation and Photocatalysis: An Experimental and Theoretical Study. *Carbon* **2020**, *169*, 338–348. [CrossRef]
11. Wei, T.; Xu, J.; Kan, C.; Zhang, L.; Zhu, X. Au Tailored on $g\text{-}C_3N_4/TiO_2$ Heterostructure for Enhanced Photocatalytic Performance. *J. Alloys Compd.* **2022**, *894*, 162338. [CrossRef]
12. Gotipamul, P.P.; Vattikondala, G.; Rajan, K.D.; Khanna, S.; Rathinam, M.; Chidambaram, S. Impact of Piezoelectric Effect on the Heterogeneous Visible Photocatalysis of $g\text{-}C_3N_4$/Ag/ZnO Tricomponent. *Chemosphere* **2022**, *287*, 132298. [CrossRef]
13. Fu, J.; Yu, J.; Jiang, C.; Cheng, B. $g\text{-}C_3N_4$-Based Heterostructured Photocatalysts. *Adv. Energy Mater.* **2018**, *8*, 1701503. [CrossRef]
14. Zou, W.; Deng, B.; Hu, X.; Zhou, Y.; Pu, Y.; Yu, S.; Ma, K.; Sun, J.; Wan, H.; Dong, L. Crystal-Plane-Dependent Metal Oxide-Support Interaction in CeO_2/ $g\text{-}C_3N_4$ for Photocatalytic Hydrogen Evolution. *Appl. Catal. B Environ.* **2018**, *238*, 111–118. [CrossRef]
15. Li, J.; Yuan, H.; Zhu, Z. Improved Photoelectrochemical Performance of Z-Scheme $g\text{-}C_3N_4/Bi_2O_3/BiPO_4$ Heterostructure and Degradation Property. *Appl. Surf. Sci.* **2016**, *385*, 34–41. [CrossRef]
16. Liu, C.; Qiu, Y.; Zhang, J.; Liang, Q.; Mitsuzaki, N.; Chen, Z. Construction of CdS Quantum Dots Modified $g\text{-}C_3N_4$/ZnO Heterostructured Photoanode for Efficient Photoelectrochemical Water Splitting. *J. Photochem. Photobiol. A Chem.* **2019**, *371*, 109–117. [CrossRef]
17. Sun, Q.; Lv, K.; Zhang, Z.; Li, M.; Li, B. Effect of Contact Interface between TiO_2 and $g\text{-}C_3N_4$ on the Photoreactivity of $g\text{-}C_3N_4/TiO_2$ Photocatalyst:(0 0 1) vs (1 0 1) Facets of TiO_2. *Appl. Catal. B Environ.* **2015**, *164*, 420–427.
18. Liang, B.; Han, D.; Sun, C.; Zhang, W.; Qin, Q. Synthesis of SnO/ $g\text{-}C_3N_4$ Visible Light Driven Photocatalysts via Grinding Assisted Ultrasonic Route. *Ceram. Int.* **2018**, *44*, 7315–7318. [CrossRef]
19. Dai, L.; Chang, D.W.; Baek, J.; Lu, W. Carbon Nanomaterials for Advanced Energy Conversion and Storage. *small* **2012**, *8*, 1130–1166. [CrossRef]
20. Gong, Y.; Wang, J.; Wei, Z.; Zhang, P.; Li, H.; Wang, Y. Combination of Carbon Nitride and Carbon Nanotubes: Synergistic Catalysts for Energy Conversion. *ChemSusChem* **2014**, *7*, 2303–2309. [CrossRef]
21. Mao, Z.; Chen, J.; Yang, Y.; Wang, D.; Bie, L.; Fahlman, B.D. Novel $g\text{-}C_3N_4/CoO$ Nanocomposites with Significantly Enhanced Visible-Light Photocatalytic Activity for H_2 Evolution. *ACS Appl. Mater. Interfaces* **2017**, *9*, 12427–12435. [CrossRef]

22. Zou, Y.; Shi, J.-W.; Ma, D.; Fan, Z.; Lu, L.; Niu, C. In Situ Synthesis of C-Doped TiO_2@ g-C_3N_4 Core-Shell Hollow Nanospheres with Enhanced Visible-Light Photocatalytic Activity for H_2 Evolution. *Chem. Eng. J.* **2017**, *322*, 435–444. [CrossRef]
23. Hasanvandian, F.; Moradi, M.; Samani, S.A.; Kakavandi, B.; Setayesh, S.R.; Noorisepehr, M. Effective Promotion of g–C_3N_4 Photocatalytic Performance via Surface Oxygen Vacancy and Coupling with Bismuth-Based Semiconductors towards Antibiotics Degradation. *Chemosphere* **2022**, *287*, 132273. [CrossRef]
24. Zhang, C.; Qin, D.; Zhou, Y.; Qin, F.; Wang, H.; Wang, W.; Yang, Y.; Zeng, G. Dual Optimization Approach to Mo Single Atom Dispersed g-C_3N_4 Photocatalyst: Morphology and Defect Evolution. *Appl. Catal. B Environ.* **2022**, *303*, 120904. [CrossRef]
25. Zhang, S.; Gu, P.; Ma, R.; Luo, C.; Wen, T.; Zhao, G.; Cheng, W.; Wang, X. Recent Developments in Fabrication and Structure Regulation of Visible-Light-Driven g-C_3N_4-Based Photocatalysts towards Water Purification: A Critical Review. *Catal. Today* **2019**, *335*, 65–77. [CrossRef]
26. Thomas, A.; Fischer, A.; Goettmann, F.; Antonietti, M.; Müller, J.-O.; Schlögl, R.; Carlsson, J.M. Graphitic Carbon Nitride Materials: Variation of Structure and Morphology and Their Use as Metal-Free Catalysts. *J. Mater. Chem.* **2008**, *18*, 4893–4908. [CrossRef]
27. Ye, L.; Wang, D.; Chen, S. Fabrication and Enhanced Photoelectrochemical Performance of MoS2/S-Doped g-C_3N_4 Heterojunction Film. *ACS Appl. Mater. Interfaces* **2016**, *8*, 5280–5289. [CrossRef] [PubMed]
28. Arumugam, M.; Tahir, M.; Praserthdam, P. Effect of Nonmetals (B, O, P, and S) Doped with Porous g-C_3N_4 for Improved Electron Transfer towards Photocatalytic CO_2 Reduction with Water into CH_4. *Chemosphere* **2022**, *286*, 131765. [CrossRef] [PubMed]
29. Yang, S.; Sun, Q.; Han, W.; Shen, Y.; Ni, Z.; Zhang, S.; Chen, L.; Zhang, L.; Cao, J.; Zheng, H. A Simple and High Efficient Composite Based on g-C_3N_4 for Super Rapid Removal of Multiple Organic Dyes in Water under Sunlight. *Catal. Sci. Technol.* 2022, in press.
30. Zhang, C.; Li, Y.; Shuai, D.; Shen, Y.; Xiong, W.; Wang, L. Graphitic Carbon Nitride (g-C_3N_4)-Based Photocatalysts for Water Disinfection and Microbial Control: A Review. *Chemosphere* **2019**, *214*, 462–479. [CrossRef] [PubMed]
31. Yan, S.C.; Li, Z.S.; Zou, Z.G. Photodegradation Performance of g-C_3N_4 Fabricated by Directly Heating Melamine. *Langmuir* **2009**, *25*, 10397–10401. [CrossRef]
32. Praus, P.; Svoboda, L.; Ritz, M.; Troppová, I.; Šihor, M.; Kočí, K. Graphitic Carbon Nitride: Synthesis, Characterization and Photocatalytic Decomposition of Nitrous Oxide. *Mater. Chem. Phys.* **2017**, *193*, 438–446. [CrossRef]
33. Giannakopoulou, T.; Papailias, I.; Todorova, N.; Boukos, N.; Liu, Y.; Yu, J.; Trapalis, C. Tailoring the Energy Band Gap and Edges' Potentials of g-C_3N_4/TiO_2 Composite Photocatalysts for NOx Removal. *Chem. Eng. J.* **2017**, *310*, 571–580. [CrossRef]
34. Tay, Q.; Kanhere, P.; Ng, C.F.; Chen, S.; Chakraborty, S.; Huan, A.C.H.; Sum, T.C.; Ahuja, R.; Chen, Z. Defect Engineered g-C_3N_4 for Efficient Visible Light Photocatalytic Hydrogen Production. *Chem. Mater.* **2015**, *27*, 4930–4933. [CrossRef]
35. Mo, Z.; She, X.; Li, Y.; Liu, L.; Huang, L.; Chen, Z.; Zhang, Q.; Xu, H.; Li, H. Synthesis of g-C_3N_4 at Different Temperatures for Superior Visible/UV Photocatalytic Performance and Photoelectrochemical Sensing of MB Solution. *RSC Adv.* **2015**, *5*, 101552–101562. [CrossRef]
36. Paul, D.R.; Sharma, R.; Nehra, S.P.; Sharma, A. Effect of Calcination Temperature, PH and Catalyst Loading on Photodegradation Efficiency of Urea Derived Graphitic Carbon Nitride towards Methylene Blue Dye Solution. *RSC Adv.* **2019**, *9*, 15381–15391. [CrossRef]
37. Fan, X.; Xing, Z.; Shu, Z.; Zhang, L.; Wang, L.; Shi, J. Improved Photocatalytic Activity of g-C_3N_4 Derived from Cyanamide–Urea Solution. *RSC Adv.* **2015**, *5*, 8323–8328. [CrossRef]
38. Liu, H.; Yu, D.; Sun, T.; Du, H.; Jiang, W.; Muhammad, Y.; Huang, L. Fabrication of Surface Alkalinized g-C_3N_4 and TiO_2 Composite for the Synergistic Adsorption-Photocatalytic Degradation of Methylene Blue. *Appl. Surf. Sci.* **2019**, *473*, 855–863. [CrossRef]
39. Li, F.; Zhao, R.; Yang, B.; Wang, W.; Liu, Y.; Gao, J.; Gong, Y. Facial Synthesis of Dandelion-like g-C_3N_4/Ag with High Performance of Photocatalytic Hydrogen Production. *Int. J. Hydrogen Energy* **2019**, *44*, 30185–30195. [CrossRef]
40. Hu, C.; Hung, W.-Z.; Wang, M.-S.; Lu, P.-J. Phosphorus and Sulfur Codoped g-C_3N_4 as an Efficient Metal-Free Photocatalyst. *Carbon* **2018**, *127*, 374–383. [CrossRef]
41. Chen, Y.; Wang, B.; Lin, S.; Zhang, Y.; Wang, X. Activation of N→ ΠΠ* Transitions in Two-Dimensional Conjugated Polymers for Visible Light Photocatalysis. *J. Phys. Chem. C* **2014**, *118*, 29981–29989. [CrossRef]
42. Dias, E.M.; Christoforidis, K.C.; Francas, L.; Petit, C. Tuning Thermally Treated Graphitic Carbon Nitride for H_2 Evolution and CO_2 Photoreduction: The Effects of Material Properties and Mid-Gap States. *ACS Appl. Energy Mater.* **2018**, *1*, 6524–6534. [CrossRef]
43. Ding, Z.; Chen, X.; Antonietti, M.; Wang, X. Synthesis of Transition Metal-modified Carbon Nitride Polymers for Selective Hydrocarbon Oxidation. *ChemSusChem* **2011**, *4*, 274–281. [CrossRef]
44. Yuan, Y.; Zhang, L.; Xing, J.; Utama, M.I.B.; Lu, X.; Du, K.; Li, Y.; Hu, X.; Wang, S.; Genç, A. High-Yield Synthesis and Optical Properties of g-C_3N_4. *Nanoscale* **2015**, *7*, 12343–12350. [CrossRef] [PubMed]
45. Wang, X.; Maeda, K.; Chen, X.; Takanabe, K.; Domen, K.; Hou, Y.; Fu, X.; Antonietti, M. Polymer Semiconductors for Artificial Photosynthesis: Hydrogen Evolution by Mesoporous Graphitic Carbon Nitride with Visible Light. *J. Am. Chem. Soc.* **2009**, *131*, 1680–1681. [CrossRef] [PubMed]
46. Creighton, J.R.; Ho, P. Introduction to Chemical Vapor Deposition (CVD). *Chem. Vap. Depos.* **2001**, *2*, 1–22.

47. Xu, Z.; Guan, L.; Li, H.; Sun, J.; Ying, Z.; Wu, J.; Xu, N. Structure Transition Mechanism of Single-Crystalline Silicon, g-C_3N_4, and Diamond Nanocone Arrays Synthesized by Plasma Sputtering Reaction Deposition. *J. Phys. Chem. C* **2015**, *119*, 29062–29070. [CrossRef]
48. Zhang, J.; Wang, Y.; Jin, J.; Zhang, J.; Lin, Z.; Huang, F.; Yu, J. Efficient Visible-Light Photocatalytic Hydrogen Evolution and Enhanced Photostability of Core/Shell CdS/g-C_3N_4 Nanowires. *ACS Appl. Mater. Interfaces* **2013**, *5*, 10317–10324. [CrossRef]
49. Sano, T.; Tsutsui, S.; Koike, K.; Hirakawa, T.; Teramoto, Y.; Negishi, N.; Takeuchi, K. Activation of Graphitic Carbon Nitride (g-C_3N_4) by Alkaline Hydrothermal Treatment for Photocatalytic NO Oxidation in Gas Phase. *J. Mater. Chem. A* **2013**, *1*, 6489–6496. [CrossRef]
50. Cui, Y.; Ding, Z.; Fu, X.; Wang, X. Construction of Conjugated Carbon Nitride Nanoarchitectures in Solution at Low Temperatures for Photoredox Catalysis. *Angew. Chemie* **2012**, *124*, 11984–11988. [CrossRef]
51. Muniandy, L.; Adam, F.; Mohamed, A.R.; Iqbal, A.; Rahman, N.R.A. Cu^{2+} Coordinated Graphitic Carbon Nitride (Cu-g-C_3N_4) Nanosheets from Melamine for the Liquid Phase Hydroxylation of Benzene and VOCs. *Appl. Surf. Sci.* **2017**, *398*, 43–55. [CrossRef]
52. Hu, C.; Chu, Y.-C.; Lin, Y.-R.; Yang, H.-C.; Wang, K.-H. Photocatalytic Dye and Cr (VI) Degradation Using a Metal-Free Polymeric g-C_3N_4 Synthesized from Solvent-Treated Urea. *Polymers.* **2019**, *11*, 182. [CrossRef]
53. Liang, L.; Cong, Y.; Wang, F.; Yao, L.; Shi, L. Hydrothermal Pre-Treatment Induced Cyanamide to Prepare Porous g-C_3N_4 with Boosted Photocatalytic Performance. *Diam. Relat. Mater.* **2019**, *98*, 107499. [CrossRef]
54. Cao, J.; Fan, H.; Wang, C.; Ma, J.; Dong, G.; Zhang, M. Facile Synthesis of Carbon Self-Doped g-C_3N_4 for Enhanced Photocatalytic Hydrogen Evolution. *Ceram. Int.* **2020**, *46*, 7888–7895. [CrossRef]
55. Hong, Y.; Liu, E.; Shi, J.; Lin, X.; Sheng, L.; Zhang, M.; Wang, L.; Chen, J. A Direct One-Step Synthesis of Ultrathin g-C_3N_4 Nanosheets from Thiourea for Boosting Solar Photocatalytic H_2 Evolution. *Int. J. Hydrogen Energy* **2019**, *44*, 7194–7204. [CrossRef]
56. Wehrstedt, K.-D.; Wildner, W.; Güthner, T.; Holzrichter, K.; Mertschenk, B.; Ulrich, A. Safe Transport of Cyanamide. *J. Hazard. Mater.* **2009**, *170*, 829–835. [CrossRef] [PubMed]
57. Pham, T.-T.; Shin, E.W. Influence of g-C_3N_4 Precursors in g-C_3N_4/$NiTiO_3$ Composites on Photocatalytic Behavior and the Interconnection between g-C_3N_4 and $NiTiO_3$. *Langmuir* **2018**, *34*, 13144–13154. [CrossRef]
58. Guan, C.; Jiang, J.; Pang, S.; Chen, X.; Webster, R.D.; Lim, T.-T. Facile Synthesis of Pure g-C_3N_4 Materials for Peroxymonosulfate Activation to Degrade Bisphenol A: Effects of Precursors and Annealing Ambience on Catalytic Oxidation. *Chem. Eng. J.* **2020**, *387*, 123726. [CrossRef]
59. Jung, H.; Pham, T.-T.; Shin, E.W. Effect of g-C_3N_4 Precursors on the Morphological Structures of g-C_3N_4/ZnO Composite Photocatalysts. *J. Alloys Compd.* **2019**, *788*, 1084–1092. [CrossRef]
60. Zhang, G.; Zhang, J.; Zhang, M.; Wang, X. Polycondensation of Thiourea into Carbon Nitride Semiconductors as Visible Light Photocatalysts. *J. Mater. Chem.* **2012**, *22*, 8083–8091. [CrossRef]
61. Xue, J.; Ma, S.; Zhou, Y.; Wang, Q. Au-Loaded Porous Graphitic C_3N_4/Graphene Layered Composite as a Ternary Plasmonic Photocatalyst and Its Visible-Light Photocatalytic Performance. *Rsc Adv.* **2015**, *5*, 88249–88257. [CrossRef]
62. Edgar, I.C.; Johnstone, S.M.; Milton, M. Urea to Melamine Process. U.S. Patent 3,095,416, 25 June 1963.
63. Wen, J.; Xie, J.; Chen, X.; Li, X. A Review on g-C_3N_4 -Based Photocatalysts. *Appl. Surf. Sci.* **2017**, *391*, 72–123. [CrossRef]
64. Mishra, A.; Mehta, A.; Basu, S.; Shetti, N.P.; Reddy, K.R.; Aminabhavi, T.M. Graphitic Carbon Nitride (g-C_3N_4)–Based Metal-Free Photocatalysts for Water Splitting: A Review. *Carbon* **2019**, *149*, 693–721. [CrossRef]
65. Teixeira, I.F.; Barbosa, E.C.M.; Tsang, S.C.E.; Camargo, P.H.C. Carbon Nitrides and Metal Nanoparticles: From Controlled Synthesis to Design Principles for Improved Photocatalysis. *Chem. Soc. Rev.* **2018**, *47*, 7783–7817. [CrossRef] [PubMed]
66. Kumar, S.; Karthikeyan, S.; Lee, A.F. g-C_3N_4-Based Nanomaterials for Visible Light-Driven Photocatalysis. *Catalysts* **2018**, *8*, 74. [CrossRef]
67. Ai, Z.; Shao, Y.; Chang, B.; Zhang, L.; Shen, J.; Wu, Y.; Huang, B.; Hao, X. Rational Modulation of Pn Homojunction in P-Doped g-C_3N_4 Decorated with Ti_3C_2 for Photocatalytic Overall Water Splitting. *Appl. Catal. B Environ.* **2019**, *259*, 118077. [CrossRef]
68. Pan, Y.; Li, D.; Jiang, H. Sodium-Doped C_3N_4/MOF Heterojunction Composites with Tunable Band Structures for Photocatalysis: Interplay between Light Harvesting and Electron Transfer. *Chem. Eur. J.* **2018**, *24*, 18403–18407. [CrossRef] [PubMed]
69. Putri, L.K.; Ng, B.-J.; Er, C.-C.; Ong, W.-J.; Chang, W.S.; Mohamed, A.R.; Chai, S.-P. Insights on the Impact of Doping Levels in Oxygen-Doped GC_3N_4 and Its Effects on Photocatalytic Activity. *Appl. Surf. Sci.* **2020**, *504*, 144427. [CrossRef]
70. Sudrajat, H. A One-Pot, Solid-State Route for Realizing Highly Visible Light Active Na-Doped GC_3N_4 Photocatalysts. *J. Solid State Chem.* **2018**, *257*, 26–33. [CrossRef]
71. Wang, L.; Guo, X.; Chen, Y.; Ai, S.; Ding, H. Cobalt-Doped g-C_3N_4 as a Heterogeneous Catalyst for Photo-Assisted Activation of Peroxymonosulfate for the Degradation of Organic Contaminants. *Appl. Surf. Sci.* **2019**, *467*, 954–962. [CrossRef]
72. Li, G.; Wang, R.; Wang, B.; Zhang, J. Sm-Doped Mesoporous g-C_3N_4 as Efficient Catalyst for Degradation of Tylosin: Influencing Factors and Toxicity Assessment. *Appl. Surf. Sci.* **2020**, *517*, 146212. [CrossRef]
73. Bellardita, M.; García-López, E.I.; Marcì, G.; Krivtsov, I.; García, J.R.; Palmisano, L. Selective Photocatalytic Oxidation of Aromatic Alcohols in Water by Using P-Doped g-C_3N_4. *Appl. Catal. B Environ.* **2018**, *220*, 222–233. [CrossRef]
74. Wu, M.; Zhang, J.; He, B.; Wang, H.; Wang, R.; Gong, Y. In-Situ Construction of Coral-like Porous P-Doped g-C_3N_4 Tubes with Hybrid 1D/2D Architecture and High Efficient Photocatalytic Hydrogen Evolution. *Appl. Catal. B Environ.* **2019**, *241*, 159–166. [CrossRef]

75. Ranjbakhsh, E.; Izadyar, M.; Nakhaeipour, A.; Habibi-Yangjeh, A. P-doped g-C_3N_4 as an Efficient Photocatalyst for CO_2 Conversion into Value-added Materials: A Joint Experimental and Theoretical Study. *Int. J. Quantum Chem.* **2020**, *120*, e26388. [CrossRef]
76. Chen, P.; Chen, L.; Ge, S.; Zhang, W.; Wu, M.; Xing, P.; Rotamond, T.B.; Lin, H.; Wu, Y.; He, Y. Microwave Heating Preparation of Phosphorus Doped g-C_3N_4 and Its Enhanced Performance for Photocatalytic H_2 Evolution in the Help of Ag_3PO_4 Nanoparticles. *Int. J. Hydrogen Energy* **2020**, *45*, 14354–14367. [CrossRef]
77. Cao, S.; Fan, B.; Feng, Y.; Chen, H.; Jiang, F.; Wang, X. Sulfur-Doped g-C_3N_4 Nanosheets with Carbon Vacancies: General Synthesis and Improved Activity for Simulated Solar-Light Photocatalytic Nitrogen Fixation. *Chem. Eng. J.* **2018**, *353*, 147–156. [CrossRef]
78. Chen, Y.; Li, W.; Jiang, D.; Men, K.; Li, Z.; Li, L.; Sun, S.; Li, J.; Huang, Z.-H.; Wang, L.-N. Facile Synthesis of Bimodal Macroporous g-C_3N_4 /SnO_2 Nanohybrids with Enhanced Photocatalytic Activity. *Sci. Bull.* **2019**, *64*, 44–53. [CrossRef]
79. Long, D.; Chen, Z.; Rao, X.; Zhang, Y. Sulfur-Doped g-C_3N_4 and $BiPO_4$ Nanorod Hybrid Architectures for Enhanced Photocatalytic Hydrogen Evolution under Visible Light Irradiation. ACS Appl. *Energy Mater.* **2020**, *3*, 5024–5030.
80. Oh, W.-D.; Lok, L.-W.; Veksha, A.; Giannis, A.; Lim, T.-T. Enhanced Photocatalytic Degradation of Bisphenol A with Ag-Decorated S-Doped g-C_3N_4 under Solar Irradiation: Performance and Mechanistic Studies. *Chem. Eng. J.* **2018**, *333*, 739–749. [CrossRef]
81. Sun, C.; Zhang, H.; Liu, H.; Zheng, X.; Zou, W.; Dong, L.; Qi, L. Enhanced Activity of Visible-Light Photocatalytic H_2 Evolution of Sulfur-Doped g-C_3N_4 Photocatalyst via Nanoparticle Metal Ni as Cocatalyst. *Appl. Catal. B Environ.* **2018**, *235*, 66–74. [CrossRef]
82. Fu, J.; Zhu, B.; Jiang, C.; Cheng, B.; You, W.; Yu, J. Hierarchical Porous O-doped g-C_3N_4 with Enhanced Photocatalytic CO_2 Reduction Activity. *Small* **2017**, *13*, 1603938. [CrossRef] [PubMed]
83. Wang, H.; Guan, Y.; Hu, S.; Pei, Y.; Ma, W.; Fan, Z. Hydrothermal Synthesis of Band Gap-Tunable Oxygen-Doped g-C_3N_4 with Outstanding "Two-Channel" Photocatalytic H_2O_2 Production Ability Assisted by Dissolution–Precipitation Process. *Nano* **2019**, *14*, 1950023. [CrossRef]
84. Zeng, Y.; Liu, X.; Liu, C.; Wang, L.; Xia, Y.; Zhang, S.; Luo, S.; Pei, Y. Scalable One-Step Production of Porous Oxygen-Doped g-C_3N_4 Nanorods with Effective Electron Separation for Excellent Visible-Light Photocatalytic Activity. *Appl. Catal. B Environ.* **2018**, *224*, 1–9. [CrossRef]
85. Zhang, Y.; Chen, Z.; Li, J.; Lu, Z.; Wang, X. Self-Assembled Synthesis of Oxygen-Doped g-C_3N_4 Nanotubes in Enhancement of Visible-Light Photocatalytic Hydrogen. *J. Energy Chem.* **2021**, *54*, 36–44. [CrossRef]
86. Panneri, S.; Ganguly, P.; Mohan, M.; Nair, B.N.; Mohamed, A.A.P.; Warrier, K.G.; Hareesh, U.S. Photoregenerable, Bifunctional Granules of Carbon-Doped g-C_3N_4 as Adsorptive Photocatalyst for the Efficient Removal of Tetracycline Antibiotic. *ACS Sustain. Chem. Eng.* **2017**, *5*, 1610–1618. [CrossRef]
87. Babu, P.; Mohanty, S.; Naik, B.; Parida, K. Serendipitous Assembly of Mixed Phase $BiVO_4$ on B-Doped g-C_3N_4: An Appropriate p–n Heterojunction for Photocatalytic O_2 Evolution and Cr (VI) Reduction. *Inorg. Chem.* **2019**, *58*, 12480–12491. [CrossRef]
88. Jiang, L.; Yuan, X.; Zeng, G.; Liang, J.; Wu, Z.; Yu, H.; Mo, D.; Wang, H.; Xiao, Z.; Zhou, C. Nitrogen Self-Doped g-C_3N_4 Nanosheets with Tunable Band Structures for Enhanced Photocatalytic Tetracycline Degradation. *J. Colloid Interface Sci.* **2019**, *536*, 17–29. [CrossRef] [PubMed]
89. Zhu, D.; Zhou, Q. Nitrogen Doped g-C_3N_4 with the Extremely Narrow Band Gap for Excellent Photocatalytic Activities under Visible Light. *Appl. Catal. B Environ.* **2021**, *281*, 119474. [CrossRef]
90. Wang, S.; Zhan, J.; Chen, K.; Ali, A.; Zeng, L.; Zhao, H.; Hu, W.; Zhu, L.; Xu, X. Potassium-Doped g-C_3N_4 Achieving Efficient Visible-Light-Driven CO_2 Reduction. *ACS Sustain. Chem. Eng.* **2020**, *8*, 8214–8222. [CrossRef]
91. Zhang, R.; Niu, S.; Zhang, X.; Jiang, Z.; Zheng, J.; Guo, C. Combination of Experimental and Theoretical Investigation on Ti-Doped g-C_3N_4 with Improved Photo-Catalytic Activity. *Appl. Surf. Sci.* **2019**, *489*, 427–434. [CrossRef]
92. Wang, J.-C.; Cui, C.-X.; Kong, Q.-Q.; Ren, C.-Y.; Li, Z.; Qu, L.; Zhang, Y.; Jiang, K. Mn-Doped g-C_3N_4 Nanoribbon for Efficient Visible-Light Photocatalytic Water Splitting Coupling with Methylene Blue Degradation. *ACS Sustain. Chem. Eng.* **2018**, *6*, 8754–8761. [CrossRef]
93. Faisal, M.; Ismail, A.A.; Harraz, F.A.; Al-Sayari, S.A.; El-Toni, A.M.; Al-Assiri, M.S. Synthesis of Highly Dispersed Silver Doped g-C_3N_4 Nanocomposites with Enhanced Visible-Light Photocatalytic Activity. *Mater. Des.* **2016**, *98*, 223–230. [CrossRef]
94. Hu, J.; Zhang, P.; An, W.; Liu, L.; Liang, Y.; Cui, W. In-Situ Fe-Doped g-C_3N_4 Heterogeneous Catalyst via Photocatalysis-Fenton Reaction with Enriched Photocatalytic Performance for Removal of Complex Wastewater. *Appl. Catal. B Environ.* **2019**, *245*, 130–142. [CrossRef]
95. Babu, B.; Shim, J.; Yoo, K. Efficient Solar-Light-Driven Photoelectrochemical Water Oxidation of One-Step in-Situ Synthesized Co-Doped g-C_3N_4 Nanolayers. *Ceram. Int.* **2020**, *46*, 16422–16430. [CrossRef]
96. Huang, J.; Li, D.; Li, R.; Zhang, Q.; Chen, T.; Liu, H.; Liu, Y.; Lv, W.; Liu, G. An Efficient Metal-Free Phosphorus and Oxygen Co-Doped g-C_3N_4 Photocatalyst with Enhanced Visible Light Photocatalytic Activity for the Degradation of Fluoroquinolone Antibiotics. *Chem. Eng. J.* **2019**, *374*, 242–253. [CrossRef]
97. Zhou, P.; Meng, X.; Li, L.; Sun, T. P, S Co-Doped g-C_3N_4 Isotype Heterojunction Composites for High-Efficiency Photocatalytic H_2 Evolution. *J. Alloys Compd.* **2020**, *827*, 154259. [CrossRef]
98. Cui, Y.; Wang, H.; Yang, C.; Li, M.; Zhao, Y.; Chen, F. Post-Activation of in Situ BF Codoped g-C_3N_4 for Enhanced Photocatalytic H_2 Evolution. *Appl. Surf. Sci.* **2018**, *441*, 621–630. [CrossRef]
99. Fang, W.; Liu, J.; Yu, L.; Jiang, Z.; Shangguan, W. Novel (Na, O) Co-Doped g-C_3N_4 with Simultaneously Enhanced Absorption and Narrowed Bandgap for Highly Efficient Hydrogen Evolution. *Appl. Catal. B Environ.* **2017**, *209*, 631–636. [CrossRef]

100. Chen, C.; Xie, M.; Kong, L.; Lu, W.; Feng, Z.; Zhan, J. Mn_3O_4 Nanodots Loaded g-C_3N_4 Nanosheets for Catalytic Membrane Degradation of Organic Contaminants. *J. Hazard. Mater.* **2020**, *390*, 122146. [CrossRef] [PubMed]
101. Surikanti, G.R.; Bajaj, P.; Sunkara, M.V. g-C_3N_4-Mediated Synthesis of Cu_2O To Obtain Porous Composites with Improved Visible Light Photocatalytic Degradation of Organic Dyes. *ACS Omega* **2019**, *4*, 17301–17316. [CrossRef]
102. Yan, D.; Wu, X.; Pei, J.; Wu, C.; Wang, X.; Zhao, H. Construction of g-C_3N_4/TiO_2/Ag Composites with Enhanced Visible-Light Photocatalytic Activity and Antibacterial Properties. *Ceram. Ceram. Int.* **2020**, *46*, 696–702. [CrossRef]
103. Rabani, I.; Zafar, R.; Subalakshmi, K.; Kim, H.-S.; Bathula, C.; Seo, Y.-S. A Facile Mechanochemical Preparation of Co_3O_4@ g-C_3N_4 for Application in Supercapacitors and Degradation of Pollutants in Water. *J. Hazard. Mater.* **2021**, *407*, 124360. [CrossRef] [PubMed]
104. Mohammadi, R.; Alamgholiloo, H.; Gholipour, B.; Rostamnia, S.; Khaksar, S.; Farajzadeh, M.; Shokouhimehr, M. Visible-Light-Driven Photocatalytic Activity of ZnO/g-C_3N_4 Heterojunction for the Green Synthesis of Biologically Interest Small Molecules of Thiazolidinones. *J. Photochem. Photobiol. A Chem.* **2020**, *402*, 112786. [CrossRef]
105. Bard, A.J.; Fox, M.A. Artificial Photosynthesis: Solar Splitting of Water to Hydrogen and Oxygen. *Acc. Chem. Res.* **1995**, *28*, 141–145. [CrossRef]
106. Thompson, T.L.; Yates, J.T. Surface Science Studies of the Photoactivation of TiO_2 New Photochemical Processes. *Chem. Rev.* **2006**, *106*, 4428–4453. [CrossRef] [PubMed]
107. Fujishima, A.; Honda, K. Electrochemical Photolysis of Water at a Semiconductor Electrode. *Nature* **1972**, *238*, 37–38. [CrossRef]
108. Tan, Y.; Chen, Y.; Mahimwalla, Z.; Johnson, M.B.; Sharma, T.; Brüning, R.; Ghandi, K. Novel Synthesis of Rutile Titanium Dioxide–Polypyrrole Nano Composites and Their Application in Hydrogen Generation. *Synth. Met.* **2014**, *189*, 77–85. [CrossRef]
109. Christoforidis, K.C.; Montini, T.; Fittipaldi, M.; Jaén, J.J.D.; Fornasiero, P. Photocatalytic Hydrogen Production by Boron Modified TiO_2/Carbon Nitride Heterojunctions. *ChemCatChem* **2019**, *11*, 6408–6416. [CrossRef]
110. Crake, A.; Christoforidis, K.C.; Godin, R.; Moss, B.; Kafizas, A.; Zafeiratos, S.; Durrant, J.R.; Petit, C. Titanium Dioxide/Carbon Nitride Nanosheet Nanocomposites for Gas Phase CO_2 Photoreduction under UV-Visible Irradiation. *Appl. Catal. B Environ.* **2019**, *242*, 369–378. [CrossRef]
111. Acharya, R.; Parida, K. A Review on TiO_2/g-C_3N_4 Visible-Light-Responsive Photocatalysts for Sustainable Energy Generation and Environmental Remediation. *J. Environ. Chem. Eng.* **2020**, *8*, 103896. [CrossRef]
112. Alcudia-Ramos, M.A.; Fuentez-Torres, M.O.; Ortiz-Chi, F.; Espinosa-González, C.G.; Hernández-Como, N.; García-Zaleta, D.S.; Kesarla, M.K.; Torres-Torres, J.G.; Collins-Martínez, V.; Godavarthi, S. Fabrication of g-C_3N_4/TiO_2 Heterojunction Composite for Enhanced Photocatalytic Hydrogen Production. *Ceram. Int.* **2020**, *46*, 38–45. [CrossRef]
113. Li, G.; Nie, X.; Gao, Y.; An, T. Can Environmental Pharmaceuticals Be Photocatalytically Degraded and Completely Mineralized in Water Using g-C_3N_4/TiO_2 under Visible Light Irradiation?—Implications of Persistent Toxic Intermediates. *Appl. Catal. B Environ.* **2016**, *180*, 726–732. [CrossRef]
114. Li, G.; Nie, X.; Chen, J.; Jiang, Q.; An, T.; Wong, P.K.; Zhang, H.; Zhao, H.; Yamashita, H. Enhanced Visible-Light-Driven Photocatalytic Inactivation of Escherichia Coli Using g-C_3N_4 /TiO_2 Hybrid Photocatalyst Synthesized Using a Hydrothermal-Calcination Approach. *Water Res.* **2015**, *86*, 17–24. [CrossRef] [PubMed]
115. Elbanna, O.; Fujitsuka, M.; Majima, T. g-C_3N_4/TiO_2 Mesocrystals Composite for H_2 Evolution under Visible-Light Irradiation and Its Charge Carrier Dynamics. *ACS Appl. Mater. Interfaces* **2017**, *9*, 34844–34854. [CrossRef] [PubMed]
116. Kočí, K.; Reli, M.; Troppová, I.; Šihor, M.; Kupková, J.; Kustrowski, P.; Praus, P. Photocatalytic Decomposition of N_2O over TiO_2/g-C_3N_4 Photocatalysts Heterojunction. *Appl. Surf. Sci.* **2017**, *396*, 1685–1695. [CrossRef]
117. Jiang, G.; Yang, X.; Wu, Y.; Li, Z.; Han, Y.; Shen, X. A Study of Spherical TiO_2/g-C_3N_4 Photocatalyst: Morphology, Chemical Composition and Photocatalytic Performance in Visible Light. *Mol. Catal.* **2017**, *432*, 232–241. [CrossRef]
118. Miranda, C.; Mansilla, H.; Yáñez, J.; Obregón, S.; Colón, G. Improved Photocatalytic Activity of g-C_3N_4/TiO_2 Composites Prepared by a Simple Impregnation Method. *J. Photochem. Photobiol. A Chem.* **2013**, *253*, 16–21. [CrossRef]
119. Zhang, L.; He, X.; Xu, X.; Liu, C.; Duan, Y.; Hou, L.; Zhou, Q.; Ma, C.; Yang, X.; Liu, R. Highly Active TiO_2/g-C_3N_4/G Photocatalyst with Extended Spectral Response towards Selective Reduction of Nitrobenzene. *Appl. Catal. B Environ.* **2017**, *203*, 1–8. [CrossRef]
120. Wang, J.; Wang, G.; Wang, X.; Wu, Y.; Su, Y.; Tang, H. 3D/2D Direct Z-Scheme Heterojunctions of Hierarchical TiO_2 Microflowers/g-C_3N_4 Nanosheets with Enhanced Charge Carrier Separation for Photocatalytic H_2 Evolution. *Carbon* **2019**, *149*, 618–626. [CrossRef]
121. Boonprakob, N.; Wetchakun, N.; Phanichphant, S.; Waxler, D.; Sherrell, P.; Nattestad, A.; Chen, J.; Inceesungvorn, B. Enhanced Visible-Light Photocatalytic Activity of g-C_3N_4/TiO_2 Films. *J. Colloid Interface Sci.* **2014**, *417*, 402–409. [CrossRef]
122. Li, C.; Lou, Z.; Yang, Y.; Wang, Y.; Lu, Y.; Ye, Z.; Zhu, L. Hollowsphere Nanoheterojunction of g-C_3N_4@ TiO_2 with High Visible Light Photocatalytic Property. *Langmuir* **2019**, *35*, 779–786. [CrossRef]
123. Wei, H.; McMaster, W.A.; Tan, J.Z.Y.; Cao, L.; Chen, D.; Caruso, R.A. Mesoporous TiO_2/g-C_3N_4 Microspheres with Enhanced Visible-Light Photocatalytic Activity. *J. Phys. Chem. C* **2017**, *121*, 22114–22122. [CrossRef]
124. Zou, Y.; Yang, B.; Liu, Y.; Ren, Y.; Ma, J.; Zhou, X.; Cheng, X.; Deng, Y. Controllable Interface-Induced Co-Assembly toward Highly Ordered Mesoporous Pt@ TiO_2/g-C_3N_4 Heterojunctions with Enhanced Photocatalytic Performance. *Adv. Funct. Mater.* **2018**, *28*, 1806214. [CrossRef]

125. Li, K.; Huang, Z.; Zeng, X.; Huang, B.; Gao, S.; Lu, J. Synergetic Effect of Ti^{3+} and Oxygen Doping on Enhancing Photoelectrochemical and Photocatalytic Properties of TiO_2/ g-C_3N_4 Heterojunctions. *ACS Appl. Mater. Interfaces* **2017**, *9*, 11577–11586. [CrossRef] [PubMed]
126. Rathi, A.K.; Kmentová, H.; Naldoni, A.; Goswami, A.; Gawande, M.B.; Varma, R.S.; Kment, S.; Zbořil, R. Significant Enhancement of Photoactivity in Hybrid TiO_2/ g-C_3N_4 Nanorod Catalysts Modified with Cu–Ni-Based Nanostructures. *ACS Appl. Nano Mater.* **2018**, *1*, 2526–2535. [CrossRef]
127. Liu, C.; Raziq, F.; Li, Z.; Qu, Y.; Zada, A.; Jing, L. Synthesis of TiO_2/g-C_3N_4 Nanocomposites with Phosphate–Oxygen Functional Bridges for Improved Photocatalytic Activity. *Chin. J. Catal.* **2017**, *38*, 1072–1078. [CrossRef]
128. Li, Y.; Wang, R.; Li, H.; Wei, X.; Feng, J.; Liu, K.; Dang, Y.; Zhou, A. Efficient and Stable Photoelectrochemical Seawater Splitting with TiO_2@g-C_3N_4 Nanorod Arrays Decorated by Co-Pi. *J. Phys. Chem. C* **2015**, *119*, 20283–20292. [CrossRef]
129. Kholikov, B.; Hussain, J.; Zeng, H. Gold Modified TiO_2/ g-C_3N_4 for Enhanced Photocatalytic Activities to Evolved H_2 Fuel. *Inorg. Chem. Commun.* **2021**, *131*, 108787. [CrossRef]
130. Wang, C.; Zhao, Y.; Xu, H.; Li, Y.; Wei, Y.; Liu, J.; Zhao, Z. Efficient Z-Scheme Photocatalysts of Ultrathin g-C_3N_4-Wrapped Au/TiO_2-Nanocrystals for Enhanced Visible-Light-Driven Conversion of CO_2 with H_2O. *Appl. Catal. B Environ.* **2020**, *263*, 118314. [CrossRef]
131. Zada, A.; Qu, Y.; Ali, S.; Sun, N.; Lu, H.; Yan, R.; Zhang, X.; Jing, L. Improved Visible-Light Activities for Degrading Pollutants on TiO_2/ g-C_3N_4 Nanocomposites by Decorating SPR Au Nanoparticles and 2, 4-Dichlorophenol Decomposition Path. *J. Hazard. Mater.* **2018**, *342*, 715–723. [CrossRef] [PubMed]
132. Wang, C.; Rao, Z.; Mahmood, A.; Wang, X.; Wang, Y.; Xie, X.; Sun, J. Improved Photocatalytic Oxidation Performance of Gaseous Acetaldehyde by Ternary g-C_3N_4/Ag-TiO_2 Composites under Visible Light. *J. Colloid Interface Sci.* **2021**, *602*, 699–711. [CrossRef]
133. Wang, W.; Zhang, D.; Sun, P.; Ji, Z.; Duan, J. High Efficiency Photocatalytic Degradation of Indoor Formaldehyde by Ag/g-C_3N_4/TiO_2 Composite Catalyst with ZSM-5 as the Carrier. *Microporous Mesoporous Mater.* **2021**, *322*, 111134. [CrossRef]
134. Yu, B.; Meng, F.; Khan, M.W.; Qin, R.; Liu, X. Facile Synthesis of AgNPs Modified TiO_2@ g-C_3N_4 Heterojunction Composites with Enhanced Photocatalytic Activity under Simulated Sunlight. *Mater. Res. Bull.* **2020**, *121*, 110641. [CrossRef]
135. Chen, Y.; Huang, W.; He, D.; Situ, Y.; Huang, H. Construction of Heterostructured g-C_3N_4/Ag/TiO_2 Microspheres with Enhanced Photocatalysis Performance under Visible-Light Irradiation. *ACS Appl. Mater. Interfaces* **2014**, *6*, 14405–14414. [CrossRef] [PubMed]
136. Li, G.; Wu, Y.; Zhang, M.; Chu, B.; Huang, W.; Fan, M.; Dong, L.; Li, B. Enhanced Removal of Toxic Cr (VI) in Wastewater by Synthetic TiO_2/g-C_3N_4 Microspheres/RGO Photocatalyst under Irradiation of Visible Light. *Ind. Eng. Chem. Res.* **2019**, *58*, 8979–8989. [CrossRef]
137. Zhang, C.; Zhou, Y.; Bao, J.; Fang, J.; Zhao, S.; Zhang, Y.; Sheng, X.; Chen, W. Structure Regulation of ZnS@ g-C_3N_4/TiO_2 Nanospheres for Efficient Photocatalytic H_2 Production under Visible-Light Irradiation. *Chem. Eng. J.* **2018**, *346*, 226–237. [CrossRef]
138. Hu, M.; Xing, Z.; Cao, Y.; Li, Z.; Yan, X.; Xiu, Z.; Zhao, T.; Yang, S.; Zhou, W. Ti^{3+} Self-Doped Mesoporous Black TiO_2/SiO_2/g-C_3N_4 Sheets Heterojunctions as Remarkable Visible-Lightdriven Photocatalysts. *Appl. Catal. B Environ.* **2018**, *226*, 499–508. [CrossRef]
139. Obregón, S.; Zhang, Y.; Colón, G. Cascade Charge Separation Mechanism by Ternary Heterostructured BiPO4/TiO_2/g-C_3N_4 Photocatalyst. *Appl. Catal. B Environ.* **2016**, *184*, 96–103. [CrossRef]
140. Zhao, H.; Tian, C.; Mei, J.; Yang, S.; Wong, P.K. Faster Electron Injection and Higher Interface Reactivity in g-C_3N_4/Fe_2O_3 Nanohybrid for Efficient Photo-Fenton-like Activity toward Antibiotics Degradation. *Environ. Res.* **2021**, *195*, 110842. [CrossRef] [PubMed]
141. Sun, X.-Y.; Zhang, F.-J.; Kong, C. Porous g-C_3N_4/WO_3 Photocatalyst Prepared by Simple Calcination for Efficient Hydrogen Generation under Visible Light. Colloids Surfaces A Physicochem. *Eng. Asp.* **2020**, *594*, 124653. [CrossRef]
142. Zhang, Z.; Sun, Y.; Wang, Y.; Yang, Y.; Wang, P.; Shi, L.; Feng, L.; Fang, S.; Liu, Q.; Ma, L. Synthesis and Photocatalytic Activity of g-C_3N_4 /ZnO Composite Microspheres under Visible Light Exposure. *Ceram. Int.* **2022**, *48*, 3293–3302. [CrossRef]
143. Moradi, S.; Isari, A.A.; Hayati, F.; Kalantary, R.R.; Kakavandi, B. Co-Implanting of TiO_2 and Liquid-Phase-Delaminated g-C_3N_4 on Multi-Functional Graphene Nanobridges for Enhancing Photocatalytic Degradation of Acetaminophen. *Chem. Eng. J.* **2021**, *414*, 128618. [CrossRef]
144. Jo, W.-K.; Natarajan, T.S. Influence of TiO_2 Morphology on the Photocatalytic Efficiency of Direct Z-Scheme g-C_3N_4/TiO_2 Photocatalysts for Isoniazid Degradation. *Chem. Eng. J.* **2015**, *281*, 549–565. [CrossRef]
145. Saravanan, R.; Gupta, V.K.; Mosquera, E.; Gracia, F. Preparation and Characterization of V_2O_5/ZnO Nanocomposite System for Photocatalytic Application. *J. Mol. Liq.* **2014**, *198*, 409–412. [CrossRef]
146. Landry, C.J.; Burns, F.P.; Baerlocher, F.; Ghandi, K. Novel Solid-State Microbial Sensors Based on ZnO Nanorod Arrays. *Adv. Funct. Mater.* **2018**, *28*, 1706309. [CrossRef]
147. Kumar, S.; Baruah, A.; Tonda, S.; Kumar, B.; Shanker, V.; Sreedhar, B. Cost-Effective and Eco-Friendly Synthesis of Novel and Stable N-Doped ZnO/g-C_3N_4 Core–Shell Nanoplates with Excellent Visible-Light Responsive Photocatalysis. *Nanoscale* **2014**, *6*, 4830–4842. [CrossRef]
148. Uma, R.; Ravichandran, K.; Sriram, S.; Sakthivel, B. Cost-Effective Fabrication of ZnO/g-C_3N_4 Composite Thin Films for Enhanced Photocatalytic Activity against Three Different Dyes (MB, MG and RhB). *Mater. Chem. Phys.* **2017**, *201*, 147–155. [CrossRef]

149. Zhang, N.; Gao, J.; Huang, C.; Liu, W.; Tong, P.; Zhang, L. In Situ Hydrothermal Growth of ZnO/g-C_3N_4 Nanoflowers Coated Solid-Phase Microextraction Fibers Coupled with GC-MS for Determination of Pesticides Residues. *Anal. Chim. Acta* **2016**, *934*, 122–131. [CrossRef]
150. Mohammadi, I.; Zeraatpisheh, F.; Ashiri, E.; Abdi, K. Solvothermal Synthesis of g-C_3N_4 and ZnO Nanoparticles on TiO_2 Nanotube as Photoanode in DSSC. *Int. J. Hydrogen Energy* **2020**, *45*, 18831–18839. [CrossRef]
151. Jang, E.; Kim, D.W.; Hong, S.H.; Park, Y.M.; Park, T.J. Visible Light-Driven g-C_3N_4@ ZnO Heterojunction Photocatalyst Synthesized via Atomic Layer Deposition with a Specially Designed Rotary Reactor. *Appl. Surf. Sci.* **2019**, *487*, 206–210. [CrossRef]
152. Fageria, P.; Nazir, R.; Gangopadhyay, S.; Barshilia, H.C.; Pande, S. Graphitic-Carbon Nitride Support for the Synthesis of Shape-Dependent ZnO and Their Application in Visible Light Photocatalysts. *Rsc Adv.* **2015**, *5*, 80397–80409. [CrossRef]
153. Tan, X.; Wang, X.; Hang, H.; Zhang, D.; Zhang, N.; Xiao, Z.; Tao, H. Self-Assembly Method Assisted Synthesis of g-C_3N_4/ZnO Heterostructure Nanocomposites with Enhanced Photocatalytic Performance. *Opt. Mater.* **2019**, *96*, 109266. [CrossRef]
154. Jung, H.; Pham, T.-T.; Shin, E.W. Interactions between ZnO Nanoparticles and Amorphous g-C_3N_4 Nanosheets in Thermal Formation of g-C_3N_4/ZnO Composite Materials: The Annealing Temperature Effect. *Appl. Surf. Sci.* **2018**, *458*, 369–381. [CrossRef]
155. Liu, W.; Wang, M.; Xu, C.; Chen, S. Facile Synthesis of g-C_3N_4/ZnO Composite with Enhanced Visible Light Photooxidation and Photoreduction Properties. *Chem. Eng. J.* **2012**, *209*, 386–393. [CrossRef]
156. Zhang, X.; Ling, S.; Ji, H.; Xu, L.; Huang, Y.; Hua, M.; Xia, J.; Li, H. Metal Ion-Containing Ionic Liquid Assisted Synthesis and Enhanced Photoelectrochemical Performance of g-C_3N_4/ZnO Composites. *Mater. Technol.* **2018**, *33*, 185–192. [CrossRef]
157. Zhou, J.; Zhang, M.; Zhu, Y. Preparation of Visible Light-Driven g-C_3N_4@ ZnO Hybrid Photocatalyst via Mechanochemistry. *Phys. Chem. Chem. Phys.* **2014**, *16*, 17627–17633. [CrossRef] [PubMed]
158. Paul, D.R.; Gautam, S.; Panchal, P.; Nehra, S.P.; Choudhary, P.; Sharma, A. ZnO-Modified g-C_3N_4: A Potential Photocatalyst for Environmental Application. *ACS Omega* **2020**, *5*, 3828–3838. [CrossRef] [PubMed]
159. Kuang, P.-Y.; Su, Y.-Z.; Chen, G.-F.; Luo, Z.; Xing, S.-Y.; Li, N.; Liu, Z.-Q. g-C_3N_4 Decorated ZnO Nanorod Arrays for Enhanced Photoelectrocatalytic Performance. *Appl. Surf. Sci.* **2015**, *358*, 296–303. [CrossRef]
160. Ramachandra, M.; Devi Kalathiparambil Rajendra Pai, S.; Resnik Jaleel UC, J.; Pinheiro, D. Improved Photocatalytic Activity of g-C_3N_4/ZnO: A Potential Direct Z-Scheme Nanocomposite. *ChemistrySelect* **2020**, *5*, 11986–11995. [CrossRef]
161. Xing, H.; Ma, H.; Fu, Y.; Xue, M.; Zhang, X.; Dong, X.; Zhang, X. Preparation of g-C_3N_4/ZnO Composites and Their Enhanced Photocatalytic Activity. *Mater. Technol.* **2015**, *30*, 122–127. [CrossRef]
162. Ismael, M. The Photocatalytic Performance of the ZnO/ g-C_3N_4 Composite Photocatalyst toward Degradation of Organic Pollutants and Its Inactivity toward Hydrogen Evolution: The Influence of Light Irradiation and Charge Transfer. *Chem. Phys. Lett.* **2020**, *739*, 136992. [CrossRef]
163. Fang, Q.; Li, B.; Li, Y.-Y.; Huang, W.-Q.; Peng, W.; Fan, X.; Huang, G.-F. 0D/2D Z-Scheme Heterojunctions of g-C_3N_4 Quantum Dots/ZnO Nanosheets as a Highly Efficient Visible-Light Photocatalyst. *Adv. Powder Technol.* **2019**, *30*, 1576–1583. [CrossRef]
164. Wang, J.; Yang, Z.; Gao, X.; Yao, W.; Wei, W.; Chen, X.; Zong, R.; Zhu, Y. Core-Shell g-C_3N_4@ ZnO Composites as Photoanodes with Double Synergistic Effects for Enhanced Visible-Light Photoelectrocatalytic Activities. *Appl. Catal. B Environ.* **2017**, *217*, 169–180. [CrossRef]
165. Mathialagan, A.; Manavalan, M.; Venkatachalam, K.; Mohammad, F.; Oh, W.C.; Sagadevan, S. Fabrication and Physicochemical Characterization of g-C_3N_4/ZnO Composite with Enhanced Photocatalytic Activity under Visible Light. *Opt. Mater.* **2020**, *100*, 109643. [CrossRef]
166. Liu, W.; Wang, M.; Xu, C.; Chen, S.; Fu, X. Significantly Enhanced Visible-Light Photocatalytic Activity of g-C_3N_4 via ZnO Modification and the Mechanism Study. *J. Mol. Catal. A Chem.* **2013**, *368*, 9–15. [CrossRef]
167. Wang, L.; Ma, C.; Guo, Z.; Lv, Y.; Chen, W.; Chang, Z.; Yuan, Q.; Ming, H.; Wang, J. In-Situ Growth of g-C_3N_4 Layer on ZnO Nanoparticles with Enhanced Photocatalytic Performances under Visible Light Irradiation. *Mater. Lett.* **2017**, *188*, 347–350. [CrossRef]
168. Zhong, Q.; Lan, H.; Zhang, M.; Zhu, H.; Bu, M. Preparation of Heterostructure g-C_3N_4/ZnO Nanorods for High Photocatalytic Activity on Different Pollutants (MB, RhB, Cr (VI) and Eosin). *Ceram. Int.* **2020**, *46*, 12192–12199. [CrossRef]
169. Ahmad, I. Comparative Study of Metal (Al, Mg, Ni, Cu and Ag) Doped ZnO/g-C_3N_4 Composites: Efficient Photocatalysts for the Degradation of Organic Pollutants. *Sep. Purif. Technol.* **2020**, *251*, 117372. [CrossRef]
170. Ta, Q.T.H.; Namgung, G.; Noh, J.-S. Facile Synthesis of Porous Metal-Doped ZnO/g-C_3N_4 Composites for Highly Efficient Photocatalysts. *J. Photochem. Photobiol. A Chem.* **2019**, *368*, 110–119.
171. Jin, C.; Li, W.; Chen, Y.; Li, R.; Huo, J.; He, Q.; Wang, Y. Efficient Photocatalytic Degradation and Adsorption of Tetracycline over Type-II Heterojunctions Consisting of ZnO Nanorods and K-Doped Exfoliated g-C_3N_4 Nanosheets. *Ind. Eng. Chem. Res.* **2020**, *59*, 2860–2873. [CrossRef]
172. Qamar, M.A.; Shahid, S.; Javed, M.; Iqbal, S.; Sher, M.; Akbar, M.B. Highly Efficient g-C_3N_4 /Cr-ZnO Nanocomposites with Superior Photocatalytic and Antibacterial Activity. *J. Photochem. Photobiol. A Chem.* **2020**, *401*, 112776. [CrossRef]
173. Neena, D.; Humayun, M.; Zuo, W.; Liu, C.S.; Gao, W.; Fu, D.J. Hierarchical Hetero-Architectures of in-Situ g-C_3N_4-Coupled Fe-Doped ZnO Micro-Flowers with Enhanced Visible-Light Photocatalytic Activities. *Appl. Surf. Sci.* **2020**, *506*, 145017. [CrossRef]
174. Sun, M.; Chen, Z.; Jiang, X.; Feng, C.; Zeng, R. Optimized Preparation of Co-Pi Decorated g-C_3N_4 @ ZnO Shell-Core Nanorod Array for Its Improved Photoelectrochemical Performance and Stability. *J. Alloys Compd.* **2019**, *780*, 540–551. [CrossRef]

175. Kumar, S.; Kumar, A.; Kumar, A.; Balaji, R.; Krishnan, V. Highly Efficient Visible Light Active 2D-2D Nanocomposites of N-ZnO-g-C_3N_4 for Photocatalytic Degradation of Diverse Industrial Pollutants. *ChemistrySelect* **2018**, *3*, 1919–1932. [CrossRef]
176. Liu, X.; Liu, L.; Yao, Z.; Yang, Z.; Xu, H. Enhanced Visible-Light-Driven Photocatalytic Hydrogen Evolution and NO Photo-Oxidation Capacity of ZnO/g-C_3N_4 with N Dopant. *Colloids Surfaces A Physicochem. Eng. Asp.* **2020**, *599*, 124869. [CrossRef]
177. Mohamed, M.A.; Zain, M.F.M.; Minggu, L.J.; Kassim, M.B.; Jaafar, J.; Amin, N.A.S.; Mastuli, M.S.; Wu, H.; Wong, R.J.; Ng, Y.H. Bio-Inspired Hierarchical Hetero-Architectures of in-Situ C-Doped g-C_3N_4 Grafted on C, N Co-Doped ZnO Micro-Flowers with Booming Solar Photocatalytic Activity. *J. Ind. Eng. Chem.* **2019**, *77*, 393–407. [CrossRef]
178. Kong, J.-Z.; Zhai, H.-F.; Zhang, W.; Wang, S.-S.; Zhao, X.-R.; Li, M.; Li, H.; Li, A.-D.; Wu, D. Visible Light-Driven Photocatalytic Performance of N-Doped ZnO/g-C_3N_4 Nanocomposites. *Nanoscale Res. Lett.* **2017**, *12*, 1–10. [CrossRef] [PubMed]
179. Qin, J.; Yang, C.; Cao, M.; Zhang, X.; Rajendran, S.; Limpanart, S.; Ma, M.; Liu, R. Two-Dimensional Porous Sheet-like Carbon-Doped ZnO/ g-C_3N_4 Nanocomposite with High Visible-Light Photocatalytic Performance. *Mater. Lett.* **2017**, *189*, 156–159. [CrossRef]
180. Zhu, Y.-P.; Li, M.; Liu, Y.-L.; Ren, T.-Z.; Yuan, Z.-Y. Carbon-Doped ZnO Hybridized Homogeneously with Graphitic Carbon Nitride Nanocomposites for Photocatalysis. *J. Phys. Chem. C* **2014**, *118*, 10963–10971. [CrossRef]
181. Xing, Z.; Chen, Y.; Liu, C.; Yang, J.; Xu, J.; Situ, Y.; Huang, H. Synthesis of Core-Shell ZnO/Oxygen Doped g-C_3N_4 Visible Light Driven Photocatalyst via Hydrothermal Method. *J. Alloys Compd.* **2017**, *708*, 853–861. [CrossRef]
182. Chen, X.-Y.; Pan, Q.-J.; Guo, Y.-R. One-Pot Synthesis of the g-C_3N_4/S-Doped ZnO Composite with Assistance of Sodium Lignosulfonate and Its Enhanced Photodegradation on Organic Pollutants. *Mater. Res. Bull.* **2018**, *107*, 164–170. [CrossRef]
183. Liu, S.; Li, F.; Li, Y.; Hao, Y.; Wang, X.; Li, B.; Liu, R. Fabrication of Ternary g-C_3N_4/Al_2O_3/ZnO Heterojunctions Based on Cascade Electron Transfer toward Molecular Oxygen Activation. *Appl. Catal. B Environ.* **2017**, *212*, 115–128. [CrossRef]
184. Mohamed, N.A.; Safaei, J.; Ismail, A.F.; Khalid, M.N.; Jailani, M.F.A.M.; Noh, M.F.M.; Arzaee, N.A.; Zhou, D.; Sagu, J.S.; Teridi, M.A.M. Boosting Photocatalytic Activities of BiVO4 by Creation of g-C_3N_4/ZnO@ $BiVO_4$ Heterojunction. *Mater. Res. Bull.* **2020**, *125*, 110779. [CrossRef]
185. Patnaik, S.; Sahoo, D.P.; Mohapatra, L.; Martha, S.; Parida, K. $ZnCr_2O_4$@ ZnO/g-C_3N_4: A Triple-Junction Nanostructured Material for Effective Hydrogen and Oxygen Evolution under Visible Light. *Energy Technol.* **2017**, *5*, 1687–1701. [CrossRef]
186. Dong, Z.; Wu, Y.; Thirugnanam, N.; Li, G. Double Z-Scheme ZnO/ZnS/g-C_3N_4 Ternary Structure for Efficient Photocatalytic H_2 Production. *Appl. Surf. Sci.* **2018**, *430*, 293–300. [CrossRef]
187. Xiao, J.; Zhang, X.; Li, Y. A Ternary g-C_3N_4/Pt/ZnO Photoanode for Efficient Photoelectrochemical Water Splitting. *Int. J. Hydrogen Energy* **2015**, *40*, 9080–9087. [CrossRef]
188. Azimi, E.B.; Badiei, A.; Sadr, M.H. Dramatic Visible Photocatalytic Performance of g-C_3N_4 -Based Nanocomposite Due to the Synergistic Effect of AgBr and ZnO Semiconductors. *J. Phys. Chem. Solids* **2018**, *122*, 174–183. [CrossRef]
189. Adhikari, S.P.; Pant, H.R.; Kim, J.H.; Kim, H.J.; Park, C.H.; Kim, C.S. One Pot Synthesis and Characterization of Ag-ZnO/g-C_3N_4 Photocatalyst with Improved Photoactivity and Antibacterial Properties. Colloids Surfaces A Physicochem. *Eng. Asp.* **2015**, *482*, 477–484. [CrossRef]
190. Ma, S.; Zhan, S.; Xia, Y.; Wang, P.; Hou, Q.; Zhou, Q. Enhanced Photocatalytic Bactericidal Performance and Mechanism with Novel Ag/ZnO/g-C_3N_4 Composite under Visible Light. *Catal. Today* **2019**, *330*, 179–188. [CrossRef]
191. Panneri, S.; Ganguly, P.; Nair, B.N.; Mohamed, A.A.P.; Warrier, K.G.; Hareesh, U.N.S. Copyrolysed C_3N_4-Ag/ZnO Ternary Heterostructure Systems for Enhanced Adsorption and Photocatalytic Degradation of Tetracycline. *Eur. J. Inorg. Chem.* **2016**, *31*, 5068–5076. [CrossRef]
192. Lee, S.J.; Begildayeva, T.; Jung, H.J.; Koutavarapu, R.; Yu, Y.; Choi, M.; Choi, M.Y. Plasmonic ZnO/Au/g-C_3N_4 Nanocomposites as Solar Light Active Photocatalysts for Degradation of Organic Contaminants in Wastewater. *Chemosphere* **2021**, *263*, 128262. [CrossRef]
193. Thang, N.Q.; Sabbah, A.; Chen, L.-C.; Chen, K.-H.; Thi, C.M.; Van Viet, P. Localized Surface Plasmonic Resonance Role of Silver Nanoparticles in the Enhancement of Long-Chain Hydrocarbons of the CO_2 Reduction over Ag-GC_3N_4/ZnO Nanorods Photocatalysts. *Chem. Eng. Sci.* **2021**, *229*, 116049. [CrossRef]
194. Zhang, Z.; Li, X.; Chen, H.; Shao, G.; Zhang, R.; Lu, H. Synthesis and Properties of Ag/ZnO/g-C_3N_4 Ternary Micro/Nano Composites by Microwave-Assisted Method. *Mater. Res. Express* **2018**, *5*, 15021. [CrossRef]
195. Wei, X.; Liu, H.; Li, T.; Jiang, Z.; Hu, W.; Niu, Q.; Chen, J. Three-Dimensional Flower Heterojunction g-C_3N_4/Ag/ZnO Composed of Ultrathin Nanosheets with Enhanced Photocatalytic Performance. *J. Photochem. Photobiol. A Chem.* **2020**, *390*, 112342. [CrossRef]
196. Rong, X.; Qiu, F.; Jiang, Z.; Rong, J.; Pan, J.; Zhang, T.; Yang, D. Preparation of Ternary Combined ZnO-Ag_2O/Porous g-C_3N_4 Composite Photocatalyst and Enhanced Visible-Light Photocatalytic Activity for Degradation of Ciprofloxacin. *Chem. Eng. Res. Des.* **2016**, *111*, 253–261. [CrossRef]
197. Zhu, P.; Hu, M.; Duan, M.; Xie, L.; Zhao, M. High Visible Light Response Z-Scheme Ag_3PO_4/g-C_3N_4/ZnO Composite Photocatalyst for Efficient Degradation of Tetracycline Hydrochloride: Preparation, Properties and Mechanism. *J. Alloys Compd.* **2020**, *840*, 155714. [CrossRef]
198. Feng, Y.; Wang, Y.; Li, M.; Lv, S.; Li, W.; Li, Z. Novel Visible Light Induced Ag_2S/g-C_3N_4/ZnO Nanoarrays Heterojunction for Efficient Photocatalytic Performance. *Appl. Surf. Sci.* **2018**, *462*, 896–903. [CrossRef]

199. Kumaresan, N.; Sinthiya, M.M.A.; Kumar, M.P.; Ravichandran, S.; Babu, R.R.; Sethurman, K.; Ramamurthi, K. Investigation on the g-C_3N_4 Encapsulated ZnO Nanorods Heterojunction Coupled with GO for Effective Photocatalytic Activity under Visible Light Irradiation. *Arab. J. Chem.* **2020**, *13*, 2826–2843. [CrossRef]
200. Iqbal, S.; Bahadur, A.; Javed, M.; Hakami, O.; Irfan, R.M.; Ahmad, Z.; AlObaid, A.; Al-Anazy, M.M.; Baghdadi, H.B.; Abd-Rabboh, H.S.M. Design Ag-Doped ZnO Heterostructure Photocatalyst with Sulfurized Graphitic C_3N_4 Showing Enhanced Photocatalytic Activity. *Mater. Sci. Eng. B* **2021**, *272*, 115320. [CrossRef]
201. Xiang, Y.; Zhou, Q.; Li, Z.; Cui, Z.; Liu, X.; Liang, Y.; Zhu, S.; Zheng, Y.; Yeung, K.W.K.; Wu, S. A Z-Scheme Heterojunction of ZnO/CDots/C_3N_4 for Strengthened Photoresponsive Bacteria-Killing and Acceleration of Wound Healing. *J. Mater. Sci. Technol.* **2020**, *57*, 1–11. [CrossRef]
202. Zhao, S.-W.; Zheng, M.; Sun, H.-L.; Li, S.-J.; Pan, Q.-J.; Guo, Y.-R. Construction of Heterostructured g-C_3N_4/ZnO/Cellulose and Its Antibacterial Activity: Experimental and Theoretical Investigations. *Dalt. Trans.* **2020**, *49*, 3723–3734. [CrossRef] [PubMed]
203. Raza, W.; Faraz, M. Novel g-C_3N_4/Fe-ZnO/RGO Nanocomposites with Boosting Visible Light Photocatalytic Activity for MB, Cr (VI), and Outstanding Catalytic Activity toward Para-Nitrophenol Reduction. *Nanotechnology* **2020**, *31*, 325603. [CrossRef] [PubMed]
204. Meng, F.; Chang, Y.; Qin, W.; Yuan, Z.; Zhao, J.; Zhang, J.; Han, E.; Wang, S.; Yang, M.; Shen, Y. ZnO-Reduced Graphene Oxide Composites Sensitized with Graphitic Carbon Nitride Nanosheets for Ethanol Sensing. *ACS Appl. Nano Mater.* **2019**, *2*, 2734–2742. [CrossRef]
205. Guo, F.; Shi, W.; Guan, W.; Huang, H.; Liu, Y. Carbon Dots/g-C_3N_4/ZnO Nanocomposite as Efficient Visible-Light Driven Photocatalyst for Tetracycline Total Degradation. *Sep. Purif. Technol.* **2017**, *173*, 295–303. [CrossRef]
206. Wang, J.; Luo, Z.; Song, Y.; Zheng, X.; Qu, L.; Qian, J.; Wu, Y.; Wu, X.; Wu, Z. Remediation of Phenanthrene Contaminated Soil by g-C_3N_4/Fe_3O_4 Composites and Its Phytotoxicity Evaluation. *Chemosphere* **2019**, *221*, 554–562. [CrossRef] [PubMed]
207. Zhu, Z.; Yu, Y.; Dong, H.; Liu, Z.; Li, C.; Huo, P.; Yan, Y. Intercalation Effect of Attapulgite in G–C_3N_4 Modified with Fe_3O_4 Quantum Dots to Enhance Photocatalytic Activity for Removing 2-Mercaptobenzothiazole under Visible Light. *ACS Sustain. Chem. Eng.* **2017**, *5*, 10614–10623. [CrossRef]
208. Lima, M.J.; Sampaio, M.J.; Silva, C.G.; Silva, A.M.T.; Faria, J.L. Magnetically Recoverable Fe_3O_4/g-C_3N_4 Composite for Photocatalytic Production of Benzaldehyde under UV-Led Radiation. *Catal. Today* **2019**, *328*, 293–299. [CrossRef]
209. Wang, M.; Cui, S.; Yang, X.; Bi, W. Synthesis of g-C_3N_4/Fe_3O_4 Nanocomposites and Application as a New Sorbent for Solid Phase Extraction of Polycyclic Aromatic Hydrocarbons in Water Samples. *Talanta* **2015**, *132*, 922–928. [CrossRef]
210. Xu, Q.; Zhu, B.; Jiang, C.; Cheng, B.; Yu, J. Constructing 2D/2D Fe_2O_3/g-C_3N_4 Direct Z-scheme Photocatalysts with Enhanced H_2 Generation Performance. *Sol. Rrl* **2018**, *2*, 1800006. [CrossRef]
211. Ye, S.; Qiu, L.-G.; Yuan, Y.-P.; Zhu, Y.-J.; Xia, J.; Zhu, J.-F. Facile Fabrication of Magnetically Separable Graphitic Carbon Nitride Photocatalysts with Enhanced Photocatalytic Activity under Visible Light. *J. Mater. Chem. A* **2013**, *1*, 3008–3015. [CrossRef]
212. Kumar, S.; Jain, S.; Lamba, B.Y. A Review on Synthesis, Characterisation and Surface Modification of Magnetic Nanoparticle and Its Composite for Removal of Heavy Metals from Wastewater. *Int. J. Environ. Anal. Chem.* **2021**, 1–16. [CrossRef]
213. Ahmadi, R.; Hosseini, H.R.M. An Investigation on the Optimum Conditions of Synthesizing a Magnetite Based Ferrofluid as MRI Contrast Agent Using Taguchi Method. *Mater. Sci. Pol.* **2013**, *31*, 253–258. [CrossRef]
214. Alaghmandfard, A.; Sedighi, O.; Rezaei, N.T.; Abedini, A.A.; Khachatourian, A.M.; Toprak, M.S.; Seifalian, A. Recent Advances in the Modification of Carbon-Based Quantum Dots for Biomedical Applications. *Mater. Sci. Eng. C* **2020**, *120*, 111756. [CrossRef]
215. Alaghmandfard, A.; Madaah Hosseini, H.R. A Facile, Two-Step Synthesis and Characterization of Fe_3O_4–LCysteine–Graphene Quantum Dots as a Multifunctional Nanocomposite. *Appl. Nanosci.* **2021**, *11*, 849–860. [CrossRef]
216. Liu, S.; Wang, S.; Jiang, Y.; Zhao, Z.; Jiang, G.; Sun, Z. Synthesis of Fe_2O_3 Loaded Porous g-C_3N_4 Photocatalyst for Photocatalytic Reduction of Dinitrogen to Ammonia. *Chem. Eng. J.* **2019**, *373*, 572–579. [CrossRef]
217. Ding, Q.; Lam, F.L.Y.; Hu, X. Complete Degradation of Ciprofloxacin over g-C_3N_4 -Iron Oxide Composite via Heterogeneous Dark Fenton Reaction. *J. Environ. Manag.* **2019**, *244*, 23–32. [CrossRef] [PubMed]
218. Papich, M.G. Ciprofloxacin Pharmacokinetics in Clinical Canine Patients. *J. Vet. Intern. Med.* **2017**, *31*, 1508–1513. [CrossRef]
219. Duan, B.; Mei, L. A Z-Scheme Fe_2O_3/g-C_3N_4 Heterojunction for Carbon Dioxide to Hydrocarbon Fuel under Visible Illuminance. *J. Colloid Interface Sci.* **2020**, *575*, 265–273. [CrossRef] [PubMed]
220. Geng, Y.; Chen, D.; Li, N.; Xu, Q.; Li, H.; He, J.; Lu, J. Z-Scheme 2D/2D α-Fe_2O_3/g-C_3N_4 Heterojunction for Photocatalytic Oxidation of Nitric Oxide. *Appl. Catal. B Environ.* **2021**, *280*, 119409. [CrossRef]
221. Cheng, R.; Zhang, L.; Fan, X.; Wang, M.; Li, M.; Shi, J. One-Step Construction of FeO_x Modified g-C_3N_4 for Largely Enhanced Visible-Light Photocatalytic Hydrogen Evolution. *Carbon* **2016**, *101*, 62–70. [CrossRef]
222. Wang, J.; Qin, C.; Wang, H.; Chu, M.; Zada, A.; Zhang, X.; Li, J.; Raziq, F.; Qu, Y.; Jing, L. Exceptional Photocatalytic Activities for CO_2 Conversion on AlO Bridged g-C_3N_4/α-Fe_2O_3 z-Scheme Nanocomposites and Mechanism Insight with IsotopesZ. *Appl. Catal. B Environ.* **2018**, *221*, 459–466. [CrossRef]
223. Christoforidis, K.C.; Montini, T.; Bontempi, E.; Zafeiratos, S.; Jaén, J.J.D.; Fornasiero, P. Synthesis and Photocatalytic Application of Visible-Light Active β-Fe_2O_3/g-C_3N_4 Hybrid Nanocomposites. *Appl. Catal. B Environ.* **2016**, *187*, 171–180. [CrossRef]
224. Hassanzadeh-Tabrizi, S.A.; Nguyen, C.-C.; Do, T.-O. Synthesis of Fe_2O_3/Pt/Au Nanocomposite Immobilized on g-C_3N_4 for Localized Plasmon Photocatalytic Hydrogen Evolution. *Appl. Surf. Sci.* **2019**, *489*, 741–754. [CrossRef]

225. Ghandi, K.; Wang, F.; Landry, C.; Mostafavi, M. Naked Gold Nanoparticles and Hot Electrons in Water. *Sci. Rep.* **2018**, *8*, 1–6. [CrossRef]
226. Wei, Y.; Li, X.; Zhang, Y.; Yan, Y.; Huo, P.; Wang, H. g-C_3N_4 Quantum Dots and Au Nano Particles Co-Modified CeO_2/Fe_3O_4 Micro-Flowers Photocatalyst for Enhanced CO_2 Photoreduction. Renew. *Energy* **2021**, *179*, 756–765.
227. Liu, L.; Wang, M.; Wang, C. In-Situ Synthesis of Graphitic Carbon Nitride/Iron Oxide−Copper Composites and Their Application in the Electrochemical Detection of Glucose. Electrochim. *Acta* **2018**, *265*, 275–283. [CrossRef]
228. Zhang, M.; Huang, G.; Huang, J.; Chen, W. Three-Dimensional Multi-Walled Carbon Nanotubes@ g-C_3N_4@ Fe_3O_4nanocomposites-Based Magnetic Solid Phase Extraction for the Determination of Polycyclic Aromatic Hydrocarbons in Water Samples. *Microchem. J.* **2018**, *142*, 385–393. [CrossRef]
229. Wang, L.; Sun, Q.; Dou, Y.; Zhang, Z.; Yan, T.; Li, Y. Fabricating a Novel Ternary Recyclable Fe_3O_4/Graphene/Sulfur-Doped g-C_3N_4 Composite Catalyst for Enhanced Removal of Ranitidine under Visible-Light Irradiation and Reducing of Its N-Nitrosodimethylamine Formation Potential. *J. Hazard. Mater.* **2021**, *413*, 125288. [CrossRef]
230. Rashid, J.; Parveen, N.; Haq, T.U.; Iqbal, A.; Talib, S.H.; Awan, S.U.; Hussain, N.; Zaheer, M. g-C_3N_4/CeO_2/Fe_3O_4Ternary Composite as an Efficient Bifunctional Catalyst for Overall Water Splitting. *ChemCatChem* **2018**, *10*, 5587–5592. [CrossRef]
231. Zhu, Z.; Huo, P.; Lu, Z.; Yan, Y.; Liu, Z.; Shi, W.; Li, C.; Dong, H. Fabrication of Magnetically Recoverable Photocatalysts Using g-C_3N_4 for Effective Separation of Charge Carriers through like-Z-Scheme Mechanism with Fe_3O_4 Mediator. *Chem. Eng. J.* **2018**, *331*, 615–625. [CrossRef]
232. Mishra, P.; Behera, A.; Kandi, D.; Ratha, S.; Parida, K. Novel Magnetic Retrievable Visible-Light-Driven Ternary Fe_3O_4@ $NiFe_2O_4$/Phosphorus-Doped g-C_3N_4 Nanocomposite Photocatalyst with Significantly Enhanced Activity through a Double-Z-Scheme System. *Inorg. Chem.* **2020**, *59*, 4255–4272. [CrossRef]
233. Ji, H.; Jing, X.; Xu, Y.; Yan, J.; Li, H.; Li, Y.; Huang, L.; Zhang, Q.; Xu, H.; Li, H. Magnetic g-C_3N_4/$NiFe_2O_4$ Hybrids with Enhanced Photocatalytic Activity. *RSC Adv.* **2015**, *5*, 57960–57967. [CrossRef]
234. Palanivel, B.; Ayappan, C.; Jayaraman, V.; Chidambaram, S.; Maheswaran, R.; Mani, A. Inverse Spinel $NiFe_2O_4$ Deposited g-C_3N_4 Nanosheet for Enhanced Visible Light Photocatalytic Activity. *Mater. Sci. Semicond. Process.* **2019**, *100*, 87–97. [CrossRef]
235. Patnaik, S.; Das, K.K.; Mohanty, A.; Parida, K. Enhanced Photo Catalytic Reduction of Cr (VI) over Polymer-Sensitized g-C_3N_4 /$ZnFe_2O_4$ and Its Synergism with Phenol Oxidation under Visible Light Irradiation. *Catal. Today* **2018**, *315*, 52–66. [CrossRef]
236. Ismael, M.; Wu, Y. A Facile Synthesis Method for Fabrication of $LaFeO_3$/g-C_3N_4 Nanocomposite as Efficient Visible-Light-Driven Photocatalyst for Photodegradation of RhB and 4-CP. *New J. Chem.* **2019**, *43*, 13783–13793. [CrossRef]
237. Khasevani, S.G.; Gholami, M.R. Synthesis of BiOI/$ZnFe_2O_4$–Metal–Organic Framework and g-C_3N_4-Based Nanocomposites for Applications in Photocatalysis. *Ind. Eng. Chem. Res.* **2019**, *58*, 9806–9818. [CrossRef]
238. Yu, W.; Chen, J.; Shang, T.; Chen, L.; Gu, L.; Peng, T. Direct Z-Scheme g-C_3N_4/WO_3 Photocatalyst with Atomically Defined Junction for H_2 Production. *Appl. Catal. B Environ.* **2017**, *219*, 693–704. [CrossRef]
239. Zhang, H.; Feng, Z.; Zhu, Y.; Wu, Y.; Wu, T. Photocatalytic Selective Oxidation of Biomass-Derived 5-Hydroxymethylfurfural to 2, 5-Diformylfuran on WO_3/g-C_3N_4 Composite under Irradiation of Visible Light. *J. Photochem. Photobiol. A Chem.* **2019**, *371*, 1–9. [CrossRef]
240. Zhao, Z.; Sun, Y.; Dong, F. Graphitic Carbon Nitride Based Nanocomposites: A Review. *Nanoscale* **2015**, *7*, 15–37. [CrossRef]
241. Cheng, C.; Shi, J.; Hu, Y.; Guo, L. WO_3/g-C_3N_4 Composites: One-Pot Preparation and Enhanced Photocatalytic H_2 Production under Visible-Light Irradiation. *Nanotechnology* **2017**, *28*, 164002. [CrossRef] [PubMed]
242. Yan, H.; Zhu, Z.; Long, Y.; Li, W. Single-Source-Precursor-Assisted Synthesis of Porous WO_3/g-C_3N_4 with Enhanced Photocatalytic Property. *Colloids Surfaces A Physicochem. Eng. Asp.* **2019**, *582*, 123857. [CrossRef]
243. Huang, S.; Long, Y.; Ruan, S.; Zeng, Y.-J. Enhanced Photocatalytic CO_2 Reduction in Defect-Engineered Z-Scheme WO_{3-x}/ g-C_3N_4 Heterostructures. *ACS Omega* **2019**, *4*, 15593–15599. [CrossRef]
244. Zhang, X.; He, S. WOx/g-C_3N_4 Layered Heterostructures with Controlled Crystallinity towards Superior Photocatalytic Degradation and H_2 Generation. *Carbon* **2020**, *156*, 488–498. [CrossRef]
245. Han, X.; Xu, D.; An, L.; Hou, C.; Li, Y.; Zhang, Q.; Wang, H. WO_3/g-C_3N_4 Two-Dimensional Composites for Visible-Light Driven Photocatalytic Hydrogen Production. *Int. J. Hydrogen Energy* **2018**, *43*, 4845–4855. [CrossRef]
246. Vijayakumar, S.; Vadivel, S. Fiber Optic Ethanol Gas Sensor Based WO_3 and WO_3/GC_3N_4 Nanocomposites by a Novel Microwave Technique. *Opt. Laser Technol.* **2019**, *118*, 44–51. [CrossRef]
247. Zhao, R.; Li, X.; Su, J.; Gao, X. Preparation of WO_3/ g-C_3N_4 Composites and Their Application in Oxidative Desulfurization. *Appl. Surf. Sci.* **2017**, *392*, 810–816. [CrossRef]
248. Cadan, F.M.; Ribeiro, C.; Azevedo, E.B. Improving g-C_3N_4: WO_3 Z-Scheme Photocatalytic Performance under Visible Light by Multivariate Optimization of g-C_3N_4 Synthesis. *Appl. Surf. Sci.* **2021**, *537*, 147904. [CrossRef]
249. Singh, J.; Arora, A.; Basu, S. Synthesis of Coral like WO_3/ g-C_3N_4 Nanocomposites for the Removal of Hazardous Dyes under Visible Light. *J. Alloys Compd.* **2019**, *808*, 151734. [CrossRef]
250. Li, X.; Song, X.; Ma, C.; Cheng, Y.; Shen, D.; Zhang, S.; Liu, W.; Huo, P.; Wang, H. Direct Z-Scheme WO_3/Graphitic Carbon Nitride Nanocomposites for the Photoreduction of CO_2. *ACS Appl. Nano Mater.* **2020**, *3*, 1298–1306. [CrossRef]
251. Chang, F.; Zheng, J.; Wu, F.; Wang, X.; Deng, B. Binary Composites WO_3/g-C_3N_4 in Porous Morphology: Facile Construction, Characterization, and Reinforced Visible Light Photocatalytic Activity. *Colloids Surfaces A Physicochem. Eng. Asp.* **2019**, *563*, 11–21. [CrossRef]

252. Fu, J.; Xu, Q.; Low, J.; Jiang, C.; Yu, J. Ultrathin 2D/2D WO_3/g-C_3N_4 Step-Scheme H_2-Production Photocatalyst. *Appl. Catal. B Environ.* **2019**, *243*, 556–565. [CrossRef]
253. Karimi-Nazarabad, M.; Goharshadi, E.K. Highly Efficient Photocatalytic and Photoelectrocatalytic Activity of Solar Light Driven WO_3/g-C_3N_4 Nanocomposite. *Sol. Energy Mater. Sol. Cells* **2017**, *160*, 484–493. [CrossRef]
254. Chai, B.; Liu, C.; Yan, J.; Ren, Z.; Wang, Z. In-Situ Synthesis of WO_3 Nanoplates Anchored on g-C_3N_4 Z-Scheme Photocatalysts for Significantly Enhanced Photocatalytic Activity. *Appl. Surf. Sci.* **2018**, *448*, 1–8. [CrossRef]
255. Tahir, B.; Tahir, M.; Nawawi, M.G.M. Highly STable 3D/2D WO_3/g-C_3N_4 Z-Scheme Heterojunction for Stimulating Photocatalytic CO_2 Reduction by H_2O/H_2 to CO and $CH_4$4 under Visible Light. *J. CO_2 Util.* **2020**, *41*, 101270. [CrossRef]
256. Zhang, X.; Wang, X.; Meng, J.; Liu, Y.; Ren, M.; Guo, Y.; Yang, Y. Robust Z-Scheme g-C_3N_4/WO_3 Heterojunction Photocatalysts with Morphology Control of WO_3 for Efficient Degradation of Phenolic Pollutants. *Sep. Purif. Technol.* **2021**, *255*, 117693. [CrossRef]
257. Borthakur, S.; Basyach, P.; Kalita, L.; Sonowal, K.; Tiwari, A.; Chetia, P.; Saikia, L. Sunlight Assisted Degradation of a Pollutant Dye in Water by a WO_3@ g-C_3N_4 Nanocomposite Catalyst. *New J. Chem.* **2020**, *44*, 2947–2960. [CrossRef]
258. Jing, H.; Ou, R.; Yu, H.; Zhao, Y.; Lu, Y.; Huo, M.; Huo, H.; Wang, X. Engineering of g-C_3N_4 Nanoparticles/WO_3 Hollow Microspheres Photocatalyst with Z-Scheme Heterostructure for Boosting Tetracycline Hydrochloride Degradation. *Sep. Purif. Technol.* **2021**, *255*, 117646. [CrossRef]
259. Xiao, T.; Tang, Z.; Yang, Y.; Tang, L.; Zhou, Y.; Zou, Z. In Situ Construction of Hierarchical WO_3/g-C_3N_4 Composite Hollow Microspheres as a Z-Scheme Photocatalyst for the Degradation of Antibiotics. *Appl. Catal. B Environ.* **2018**, *220*, 417–428. [CrossRef]
260. Liu, X.; Jin, A.; Jia, Y.; Xia, T.; Deng, C.; Zhu, M.; Chen, C.; Chen, X. Synergy of Adsorption and Visible-Light Photocatalytic Degradation of Methylene Blue by a Bifunctional Z-Scheme Heterojunction of WO_3/g-C_3N_4. *Appl. Surf. Sci.* **2017**, *405*, 359–371. [CrossRef]
261. Zhuang, H.; Cai, Z.; Xu, W.; Huang, M.; Liu, X. In Situ Construction of WO_3/G-C_3N_4 Composite Photocatalyst with 2D–2D Heterostructure for Enhanced Visible Light Photocatalytic Performance. *New J. Chem.* **2019**, *43*, 17416–17422. [CrossRef]
262. Meng, J.; Pei, J.; He, Z.; Wu, S.; Lin, Q.; Wei, X.; Li, J.; Zhang, Z. Facile Synthesis of g-C_3N_4 Nanosheets Loaded with WO_3 Nanoparticles with Enhanced Photocatalytic Performance under Visible Light Irradiation. *RSC Adv.* **2017**, *7*, 24097–24104. [CrossRef]
263. Wang, P.; Lu, N.; Su, Y.; Liu, N.; Yu, H.; Li, J.; Wu, Y. Fabrication of WO_3@ g-C_3N_4 with Core@ Shell Nanostructure for Enhanced Photocatalytic Degradation Activity under Visible Light. *Appl. Surf. Sci.* **2017**, *423*, 197–204. [CrossRef]
264. Zhao, C.; Ran, F.; Dai, L.; Li, C.; Zheng, C.; Si, C. Cellulose-Assisted Construction of High Surface Area Z-Scheme C-Doped g-C_3N_4/WO_3 for Improved Tetracycline Degradation. *Carbohydr. Polym.* **2021**, *255*, 117343. [CrossRef]
265. Mallikarjuna, K.; Kumar, M.K.; Kim, H. Synthesis of Oxygen-Doped-g-C_3N_4/WO_3 Porous Structures for Visible Driven Photocatalytic H_2 Production. Phys. E Low-dimensional Syst. *Nanostructures* **2021**, *126*, 114428.
266. Sun, L.; Li, B.; Chu, X.; Sun, N.; Qu, Y.; Zhang, X.; Khan, I.; Bai, L.; Jing, L. Synthesis of Si–O-Bridged g-C_3N_4/WO_3 2D-Heterojunctional Nanocomposites as Efficient Photocatalysts for Aerobic Alcohol Oxidation and Mechanism Insight. *ACS Sustain. Chem. Eng.* **2019**, *7*, 9916–9927. [CrossRef]
267. Li, H.; Yu, H.; Quan, X.; Chen, S.; Zhang, Y. Uncovering the Key Role of the Fermi Level of the Electron Mediator in a Z-Scheme Photocatalyst by Detecting the Charge Transfer Process of WO_3-Metal-GC_3N_4 (Metal = Cu, Ag, Au). *ACS Appl. Mater. Interfaces* **2016**, *8*, 2111–2119. [CrossRef]
268. Chen, J.; Xiao, X.; Wang, Y.; Ye, Z. Ag Nanoparticles Decorated WO_3/g-C_3N_4 2D/2D Heterostructure with Enhanced Photocatalytic Activity for Organic Pollutants Degradation. *Appl. Surf. Sci.* **2019**, *467*, 1000–1010. [CrossRef]
269. Fan, G.; Ning, R.; Yan, Z.; Luo, J.; Du, B.; Zhan, J.; Liu, L.; Zhang, J. Double Photoelectron-Transfer Mechanism in Ag−AgCl/WO_3/g-C_3N_4 Photocatalyst with Enhanced Visible-Light Photocatalytic Activity for Trimethoprim Degradation. *J. Hazard. Mater.* **2021**, *403*, 123964. [CrossRef]
270. Truc, N.T.T.; Pham, T.-D.; Van Thuan, D.; Tran, D.T.; Nguyen, M.V.; Dang, N.M.; Trang, H.T. Superior Activity of Cu-$NiWO_4$/g-C_3N_4 Z Direct System for Photocatalytic Decomposition of VOCs in Aerosol under Visible Light. *J. Alloys Compd.* **2019**, *798*, 12–18. [CrossRef]
271. Ahmed, K.E.; Kuo, D.-H.; Zeleke, M.A.; Zelekew, O.A.; Abay, A.K. Synthesis of Sn-WO_3/g-C_3N_4 Composites with Surface Activated Oxygen for Visible Light Degradation of Dyes. *J. Photochem. Photobiol. A Chem.* **2019**, *369*, 133–141. [CrossRef]
272. Tahir, B.; Tahir, M.; Mohd Nawawi, M.G. Well-Designed 3D/2D/2D WO_3/Bt/g-C_3N_4 Z-Scheme Heterojunction for Tailoring Photocatalytic CO_2 Methanation with 2D-Layered Bentonite-Clay as the Electron Moderator under Visible Light. *Energy Fuels* **2020**, *34*, 14400–14418.
273. Ouyang, K.; Xu, B.; Yang, C.; Wang, H.; Zhan, P.; Xie, S. Synthesis of a Novel Z-Scheme Ag/WO_3/g-C_3N_4 Nanophotocatalyst for Degradation of Oxytetracycline Hydrochloride under Visible Light. *Mater. Sci. Semicond. Process.* **2022**, *137*, 106168. [CrossRef]
274. Qin, Y.; Lu, J.; Meng, F.; Lin, X.; Feng, Y.; Yan, Y.; Meng, M. Rationally Constructing of a Novel 2D/2D WO_3/Pt/g-C_3N_4 Schottky-Ohmic Junction towards Efficient Visible-Light-Driven Photocatalytic Hydrogen Evolution and Mechanism Insight. *J. Colloid Interface Sci.* **2021**, *586*, 576–587. [CrossRef] [PubMed]

275. Liu, F.; Feng, S.; Wu, Y.; Lv, X.; Wang, H.; Chen, S.-M.; Hao, Q.; Cao, Y.; Lei, W.; Tong, Z. Label-Free Photoelectrochemical Immunosensor for Aflatoxin B1 Detection Based on the Z-Scheme Heterojunction of g-C_3N_4/Au/WO_3. *Biosens. Bioelectron.* **2021**, *189*, 113373.
276. Li, J.; Hao, H.; Zhu, Z. Construction of g-C_3N_4-WO_3-Bi_2WO_6 Double Z-Scheme System with Enhanced Photoelectrochemical Performance. *Mater. Lett.* **2016**, *168*, 180–183. [CrossRef]
277. Sadiq, M.M.J.; Shenoy, U.S.; Bhat, D.K. Synthesis of $BaWO_4$/NRGO–g-C_3N_4 Nanocomposites with Excellent Multifunctional Catalytic Performance via Microwave Approach. *Front. Mater. Sci.* **2018**, *12*, 247–263. [CrossRef]
278. Huang, R.; Gu, X.; Sun, W.; Chen, L.; Du, Q.; Guo, X.; Li, J.; Zhang, M.; Li, C. In Situ Synthesis of Cu^+ Self-Doped $CuWO_4$/g-C_3N_4 Heterogeneous Fenton-like Catalysts: The Key Role of Cu^+ in Enhancing Catalytic Performance. *Sep. Purif. Technol.* **2020**, *250*, 117174. [CrossRef]
279. Jia, J.; Jiang, C.; Zhang, X.; Li, P.; Xiong, J.; Zhang, Z.; Wu, T.; Wang, Y. Urea-Modified Carbon Quantum Dots as Electron Mediator Decorated g-C_3N_4/WO_3 with Enhanced Visible-Light Photocatalytic Activity and Mechanism Insight. *Appl. Surf. Sci.* **2019**, *495*, 143524. [CrossRef]
280. He, K.; Xie, J.; Luo, X.; Wen, J.; Ma, S.; Li, X.; Fang, Y.; Zhang, X. Enhanced Visible Light Photocatalytic H_2 Production over Z-Scheme g-C_3N_4 Nansheets/WO_3 Nanorods Nanocomposites Loaded with Ni $(OH)_x$ Cocatalysts. *Chin. J. Catal.* **2017**, *38*, 240–252. [CrossRef]
281. Jiang, L.; Yuan, X.; Zeng, G.; Liang, J.; Chen, X.; Yu, H.; Wang, H.; Wu, Z.; Zhang, J.; Xiong, T. In-Situ Synthesis of Direct Solid-State Dual Z-Scheme WO_3/g-C_3N_4/Bi_2O_3 Photocatalyst for the Degradation of Refractory Pollutant. *Appl. Catal. B Environ.* **2018**, *227*, 376–385. [CrossRef]
282. Ali, S.; Humayun, M.; Pi, W.; Yuan, Y.; Wang, M.; Khan, A.; Yue, P.; Shu, L.; Zheng, Z.; Fu, Q. Fabrication of BiFeO3-g-C_3N_4-WO_3 Z-Scheme Heterojunction as Highly Efficient Visible-Light Photocatalyst for Water Reduction and 2, 4-Dichlorophenol Degradation: Insight Mechanism. *J. Hazard. Mater.* **2020**, *397*, 122708. [CrossRef]
283. Bilal Tahir, M.; Nadeem Riaz, K.; Asiri, A.M. Boosting the Performance of Visible Light-driven WO_3/g-C_3N_4 Anchored with $BiVO_4$ Nanoparticles for Photocatalytic Hydrogen Evolution. *Int. J. Energy Res.* **2019**, *43*, 5747–5758. [CrossRef]
284. Beyhaqi, A.; Zeng, Q.; Chang, S.; Wang, M.; Azimi, S.M.T.; Hu, C. Construction of G–C_3N_4/WO_3/MoS_2 Ternary Nanocomposite with Enhanced Charge Separation and Collection for Efficient Wastewater Treatment under Visible Light. *Chemosphere* **2020**, *247*, 125784. [CrossRef]
285. Cai, Z.; Huang, L.; Quan, X.; Zhao, Z.; Shi, Y.; Puma, G.L. Acetate Production from Inorganic Carbon (HCO3-) in Photo-Assisted Biocathode Microbial Electrosynthesis Systems Using WO_3/MoO_3/g-C_3N_4 Heterojunctions and Serratia Marcescens Species. *Appl. Catal. B Environ.* **2020**, *267*, 118611. [CrossRef]
286. Ibrahim, Y.O.; Gondal, M.A. Visible-Light-Driven Photocatalytic Performance of a Z-Scheme Based TiO_2/WO_3/g-C_3N_4 Ternary Heterojunctions. *Mol. Catal.* **2021**, *505*, 111494. [CrossRef]
287. Zou, Y.; Xie, Y.; Yu, S.; Chen, L.; Cui, W.; Dong, F.; Zhou, Y. SnO_2 Quantum Dots Anchored on g-C_3N_4 for Enhanced Visible-Light Photocatalytic Removal of NO and Toxic NO_2 Inhibition. *Appl. Surf. Sci.* **2019**, *496*, 143630. [CrossRef]
288. Wang, Q.; Tian, J.; Wei, L.; Liu, Y.; Yang, C. Z-Scheme Heterostructure of Fe-Doped SnO_2 Decorated Layered g-C_3N_4 with Enhanced Photocatalytic Activity under Simulated Solar Light Irradiation. *Opt. Mater.* **2020**, *101*, 109769. [CrossRef]
289. He, Y.; Zhang, L.; Fan, M.; Wang, X.; Walbridge, M.L.; Nong, Q.; Wu, Y.; Zhao, L. Z-Scheme SnO_{2-x}/g-C_3N_4 Composite as an Efficient Photocatalyst for Dye Degradation and Photocatalytic CO_2 Reduction. *Sol. Energy Mater. Sol. Cells* **2015**, *137*, 175–184. [CrossRef]
290. Cao, J.; Qin, C.; Wang, Y.; Zhang, H.; Zhang, B.; Gong, Y.; Wang, X.; Sun, G.; Bala, H.; Zhang, Z. Synthesis of g-C_3N_4 Nanosheet Modified SnO_2 Composites with Improved Performance for Ethanol Gas Sensing. *RSC Adv.* **2017**, *7*, 25504–25511. [CrossRef]
291. Wang, X.; He, Y.; Xu, L.; Xia, Y.; Gang, R. SnO_2 Particles as Efficient Photocatalysts for Organic Dye Degradation Grown In-Situ on g-C_3N_4 Nanosheets by Microwave-Assisted Hydrothermal Method. *Mater. Sci. Semicond. Process.* **2021**, *121*, 105298. [CrossRef]
292. Zhu, K.; Lv, Y.; Liu, J.; Wang, W.; Wang, C.; Li, S.; Wang, P.; Zhang, M.; Meng, A.; Li, Z. Facile Fabrication of g-C_3N_4/SnO_2 Composites and Ball Milling Treatment for Enhanced Photocatalytic Performance. *J. Alloys Compd.* **2019**, *802*, 13–18. [CrossRef]
293. Seza, A.; Soleimani, F.; Naseri, N.; Soltaninejad, M.; Montazeri, S.M.; Sadrnezhaad, S.K.; Mohammadi, M.R.; Moghadam, H.A.; Forouzandeh, M.; Amin, M.H. Novel Microwave-Assisted Synthesis of Porous g-C_3N_4/SnO_2 Nanocomposite for Solar Water-Splitting. *Appl. Surf. Sci.* **2018**, *440*, 153–161. [CrossRef]
294. Bian, H.; Wang, A.; Li, Z.; Li, Z.; Diao, Y.; Lu, J.; Li, Y.Y. g-C_3N_4-Modified Water-Crystallized Mesoporous SnO_2 for Enhanced Photoelectrochemical Properties. *Part. Part. Syst. Charact.* **2018**, *35*, 1800155. [CrossRef]
295. Ji, H.; Fan, Y.; Yan, J.; Xu, Y.; She, X.; Gu, J.; Fei, T.; Xu, H.; Li, H. Construction of SnO_2/Graphene-like GC_3N_4 with Enhanced Visible Light Photocatalytic Activity. *RSC Adv.* **2017**, *7*, 36101–36111. [CrossRef]
296. Zang, Y.; Li, L.; Li, X.; Lin, R.; Li, G. Synergistic Collaboration of g-C_3N_4/SnO_2 Composites for Enhanced Visible-Light Photocatalytic Activity. *Chem. Eng. J.* **2014**, *246*, 277–286. [CrossRef]
297. Zhang, T.; Chang, F.; Qi, Y.; Zhang, X.; Yang, J.; Liu, X.; Li, S. A Facile One-Pot and Alkali-Free Synthetic Procedure for Binary SnO_2/g-C_3N_4 Composites with Enhanced Photocatalytic Behavior. *Mater. Sci. Semicond. Process.* **2020**, *115*, 105112. [CrossRef]
298. Peng, F.; Ni, Y.; Zhou, Q.; Kou, J.; Lu, C.; Xu, Z. New g-C_3N_4 Based Photocatalytic Cement with Enhanced Visible-Light Photocatalytic Activity by Constructing Muscovite Sheet/SnO_2 Structures. *Constr. Build. Mater.* **2018**, *179*, 315–325. [CrossRef]

299. Babu, B.; Cho, M.; Byon, C.; Shim, J. Sunlight-Driven Photocatalytic Activity of SnO_2 QDs-g-C_3N_4 Nanolayers. *Mater. Lett.* **2018**, *212*, 327–331. [CrossRef]
300. Shen, H.; Zhao, X.; Duan, L.; Liu, R.; Li, H. Enhanced Visible Light Photocatalytic Activity in SnO_2@ g-C_3N_4 Core-Shell Structures. *Mater. Sci. Eng. B* **2017**, *218*, 23–30. [CrossRef]
301. Wang, X.; Ren, P. Flower-like SnO_2/g-C_3N_4 Heterojunctions: The Face-to-Face Contact Interface and Improved Photocatalytic Properties. *Adv. Powder Technol.* **2018**, *29*, 1153–1157. [CrossRef]
302. Singh, J.; Kumari, P.; Basu, S. Degradation of Toxic Industrial Dyes Using SnO_2/g-C_3N_4 Nanocomposites: Role of Mass Ratio on Photocatalytic Activity. *J. Photochem. Photobiol. A Chem.* **2019**, *371*, 136–143. [CrossRef]
303. Chen, X.; Zhou, B.; Yang, S.; Wu, H.; Wu, Y.; Wu, L.; Pan, J.; Xiong, X. In Situ Construction of an SnO_2/g-C_3N_4 Heterojunction for Enhanced Visible-Light Photocatalytic Activity. *Rsc Adv.* **2015**, *5*, 68953–68963. [CrossRef]
304. Yang, L.; Huang, J.; Shi, L.; Cao, L.; Liu, H.; Liu, Y.; Li, Y.; Song, H.; Jie, Y.; Ye, J. Sb Doped SnO_2-Decorated Porous g-C_3N_4 Nanosheet Heterostructures with Enhanced Photocatalytic Activities under Visible Light Irradiation. *Appl. Catal. B Environ.* **2018**, *221*, 670–680. [CrossRef]
305. Raziq, F.; Qu, Y.; Humayun, M.; Zada, A.; Yu, H.; Jing, L. Synthesis of SnO_2/BP Codoped g-C_3N_4 Nanocomposites as Efficient Cocatalyst-Free Visible-Light Photocatalysts for CO_2 Conversion and Pollutant Degradation. *Appl. Catal. B Environ.* **2017**, *201*, 486–494. [CrossRef]
306. Jourshabani, M.; Shariatinia, Z.; Badiei, A. In Situ Fabrication of SnO_2/S-Doped g-C_3N_4 Nanocomposites and Improved Visible Light Driven Photodegradation of Methylene Blue. *J. Mol. Liq.* **2017**, *248*, 688–702. [CrossRef]
307. Guo, W.; Huang, L.; Zhang, J.; He, Y.; Zeng, W. Ni-Doped SnO_2/g-C_3N_4 Nanocomposite with Enhanced Gas Sensing Performance for the Eff; Ective Detection of Acetone in Diabetes Diagnosis. *Sens. Actuators B Chem.* **2021**, *334*, 129666. [CrossRef]
308. Asaithambi, S.; Sakthivel, P.; Karuppaiah, M.; Yuvakkumar, R.; Velauthapillai, D.; Ahamad, T.; Khan, M.A.M.; Mohammed, M.K.A.; Vijayaprabhu, N.; Ravi, G. The Bifunctional Performance Analysis of Synthesized Ce Doped SnO_2/g-C_3N_4 Composites for Asymmetric Supercapacitor and Visible Light Photocatalytic Applications. *J. Alloys Compd.* **2021**, *866*, 158807. [CrossRef]
309. Zada, A.; Humayun, M.; Raziq, F.; Zhang, X.; Qu, Y.; Bai, L.; Qin, C.; Jing, L.; Fu, H. Exceptional Visible-light-driven Cocatalyst-free Photocatalytic Activity of g-C_3N_4 by Well Designed Nanocomposites with Plasmonic Au and SnO_2. *Adv. Energy Mater.* **2016**, *6*, 1601190. [CrossRef]
310. Yuan, F.; Sun, Z.; Li, C.; Tan, Y.; Zhang, X.; Zheng, S. Multi-Component Design and in-Situ Synthesis of Visible-Light-Driven SnO_2/g-C_3N_4/Diatomite Composite for High-Efficient Photoreduction of Cr (VI) with the Aid of Citric Acid. *J. Hazard. Mater.* **2020**, *396*, 122694. [CrossRef]
311. Babu, B.; Koutavarapu, R.; Shim, J.; Yoo, K. Enhanced Visible-Light-Driven Photoelectrochemical and Photocatalytic Performance of Au-SnO_2 Quantum Dot-Anchored g-C_3N_4 Nanosheets. *Sep. Purif. Technol.* **2020**, *240*, 116652. [CrossRef]
312. Peng, L.; Zheng, R.; Feng, D.; Yu, H.; Dong, X. Synthesis of Eco-Friendly Porous g-C_3N_4/SiO_2/SnO_2 Composite with Excellent Visible-Light Responsive Photocatalysis. *Arab. J. Chem.* **2020**, *13*, 4275–4285. [CrossRef]
313. Wu, J.; Zhang, Y.; Zhou, J.; Wang, K.; Zheng, Y.-Z.; Tao, X. Uniformly Assembling N-Type Metal Oxide Nanostructures (TiO_2 Nanoparticles and SnO_2 Nanowires) onto P Doped g-C_3N_4 Nanosheets for Efficient Photocatalytic Water Splitting. *Appl. Catal. B Environ.* **2020**, *278*, 119301. [CrossRef]
314. Faraji, M.; Mohaghegh, N.; Abedini, A. Ternary Composite of TiO_2 Nanotubes/Ti Plates Modified by g-C_3N_4 and SnO_2 with Enhanced Photocatalytic Activity for Enhancing Antibacterial and Photocatalytic Activity. J. Photochem. *Photobiol. B Biol.* **2018**, *178*, 124–132. [CrossRef] [PubMed]
315. Liu, X.-P.; Huang, B.; Mao, C.-J.; Chen, J.-S.; Jin, B.-K. Electrochemiluminescence Aptasensor for Lincomycin Antigen Detection by Using a SnO_2/Chitosan/g-C_3N_4 Nanocomposite. *Talanta* **2021**, *233*, 122546. [CrossRef]
316. Ali, G.; Zaidi, S.J.A.; Basit, M.A.; Park, T.J. Synergetic Performance of Systematically Designed g-C_3N_4/RGO/SnO_2 Nanocomposite for Photodegradation of Rhodamine-B Dye. *Appl. Surf. Sci.* **2021**, *570*, 151140. [CrossRef]
317. Seo, Y.J.; Das, P.K.; Arunachalam, M.; Ahn, K.-S.; Ha, J.-S.; Kang, S.H. Drawing the Distinguished Graphite Carbon Nitride (g-C_3N_4) on SnO_2 Nanoflake Film for Solar Water Oxidation. *Int. J. Hydrogen Energy* **2020**, *45*, 22567–22575. [CrossRef]
318. Wu, H.; Yu, S.; Wang, Y.; Han, J.; Wang, L.; Song, N.; Dong, H.; Li, C. A Facile One-Step Strategy to Construct 0D/2D SnO_2/g-C_3N_4 Heterojunction Photocatalyst for High-Efficiency Hydrogen Production Performance from Water Splitting. *Int. J. Hydrogen Energy* **2020**, *45*, 30142–30152. [CrossRef]
319. Versaci, D.; Amici, J.; Francia, C.; Bodoardo, S. Simple Approach Using g-C_3N_4 to Enable SnO_2 Anode High Rate Performance for Li Ion Battery. *Solid State Ionics* **2020**, *346*, 115210. [CrossRef]
320. Tran, H.H.; Nguyen, P.H.; Le, M.L.P.; Kim, S.-J.; Vo, V. SnO_2 Nanosheets/Graphite Oxide/g-C_3N_4 Composite as Enhanced Performance Anode Material for Lithium Ion Batteries. *Chem. Phys. Lett.* **2019**, *715*, 284–292. [CrossRef]
321. Cao, J.; Qin, C.; Wang, Y.; Zhang, B.; Gong, Y.; Zhang, H.; Sun, G.; Bala, H.; Zhang, Z. Calcination Method Synthesis of SnO_2/g-C_3N_4 Composites for a High-Performance Ethanol Gas Sensing Application. *Nanomaterials* **2017**, *7*, 98. [CrossRef]
322. Akhundi, A.; Habibi-Yangjeh, A. A Simple Large-Scale Method for Preparation of g-C_3N_4/SnO_2 Nanocomposite as Visible-Light-Driven Photocatalyst for Degradation of an Organic Pollutant. *Mater. Express* **2015**, *5*, 309–318. [CrossRef]
323. Liu, X.; Liu, X. SnO_2 Nanocrystallines Decorated g-C_3N_4 Composites with Enhanced Visible-Light Photocatalytic Activity. *Integr. Ferroelectr.* **2019**, *197*, 121–132. [CrossRef]

324. Li, Q.; He, Y.; Peng, R. One-Step Synthesis of SnO 2 Nanoparticles-Loaded Graphitic Carbon Nitride and Their Application in Thermal Decomposition of Ammonium Perchlorate. *New J. Chem.* **2015**, *39*, 8703–8707. [CrossRef]
325. Liu, Q.; Fan, C.; Tang, H.; Sun, X.; Yang, J.; Cheng, X. One-Pot Synthesis of g-C_3N_4/V_2O_5 Composites for Visible Light-Driven Photocatalytic Activity. *Appl. Surf. Sci.* **2015**, *358*, 188–195. [CrossRef]
326. Jayaraman, T.; Raja, S.A.; Priya, A.; Jagannathan, M.; Ashokkumar, M. Synthesis of a Visible-Light Active V_2O_5–GC_3N_4 Heterojunction as an Efficient Photocatalytic and Photoelectrochemical Material. *New J. Chem.* **2015**, *39*, 1367–1374. [CrossRef]
327. Jin, C.; Wang, M.; Li, Z.; Kang, J.; Zhao, Y.; Han, J.; Wu, Z. Two Dimensional Co_3O_4/g-C_3N_4 Z-Scheme Heterojunction: Mechanism Insight into Enhanced Peroxymonosulfate-Mediated Visible Light Photocatalytic Performance. *Chem. Eng. J.* **2020**, *398*, 125569. [CrossRef]
328. Wu, H.; Li, C.; Che, H.; Hu, H.; Hu, W.; Liu, C.; Ai, J.; Dong, H. Decoration of Mesoporous Co_3O_4 Nanospheres Assembled by Monocrystal Nanodots on g-C_3N_4 to Construct Z-Scheme System for Improving Photocatalytic Performance. *Appl. Surf. Sci.* **2018**, *440*, 308–319. [CrossRef]
329. Qiao, Q.; Yang, K.; Ma, L.-L.; Huang, W.-Q.; Zhou, B.-X.; Pan, A.; Hu, W.; Fan, X.; Huang, G.-F. Facile in Situ Construction of Mediator-Free Direct Z-Scheme g-C_3N_4/CeO_2 Heterojunctions with Highly Efficient Photocatalytic Activity. *J. Phys. D. Appl. Phys.* **2018**, *51*, 275302. [CrossRef]
330. Huang, L.; Li, Y.; Xu, H.; Xu, Y.; Xia, J.; Wang, K.; Li, H.; Cheng, X. Synthesis and Characterization of CeO_2/g-C_3N_4 Composites with Enhanced Visible-Light Photocatatalytic Activity. *Rsc Adv.* **2013**, *3*, 22269–22279. [CrossRef]
331. Zou, W.; Shao, Y.; Pu, Y.; Luo, Y.; Sun, J.; Ma, K.; Tang, C.; Gao, F.; Dong, L. Enhanced Visible Light Photocatalytic Hydrogen Evolution via Cubic CeO_2 Hybridized g-C_3N_4 Composite. *Appl. Catal. B Environ.* **2017**, *218*, 51–59. [CrossRef]
332. Li, Y.; Wu, S.; Huang, L.; Xu, H.; Zhang, R.; Qu, M.; Gao, Q.; Li, H. g-C_3N_4 Modified Bi_2O_3 Composites with Enhanced Visible-Light Photocatalytic Activity. *J. Phys. Chem. Solids* **2015**, *76*, 112–119. [CrossRef]
333. Zhang, J.; Hu, Y.; Jiang, X.; Chen, S.; Meng, S.; Fu, X. Design of a Direct Z-Scheme Photocatalyst: Preparation and Characterization of Bi_2O_3/g-C_3N_4 with High Visible Light Activity. *J. Hazard. Mater.* **2014**, *280*, 713–722. [CrossRef] [PubMed]
334. Wang, D.; Yu, X.; Feng, Q.; Lin, X.; Huang, Y.; Huang, X.; Li, X.; Chen, K.; Zhao, B.; Zhang, Z. In-Situ Growth of β-Bi_2O_3 Nanosheets on g-C_3N_4 to Construct Direct Z-Scheme Heterojunction with Enhanced Photocatalytic Activities. *J. Alloys Compd.* **2021**, *859*, 157795. [CrossRef]
335. Wang, X.; Liu, C.; Li, X.; Li, F.; Li, Y.; Zhao, J.; Liu, R. Construction of g-C_3N_4/Al_2O_3 Hybrids via in-Situ Acidification and Exfoliation with Enhanced Photocatalytic Activity. *Appl. Surf. Sci.* **2017**, *394*, 340–350. [CrossRef]
336. Yang, Z.-L.; Zhang, Z.-Y.; Fan, W.-L.; Hu, C.; Zhang, L.; Qi, J.-J. High-Performance g-C_3N_4 Added Carbon-Based Perovskite Solar Cells Insulated by Al_2O_3 Layer. Sol. *Energy* **2019**, *193*, 859–865.
337. Shi, J.-W.; Zou, Y.; Cheng, L.; Ma, D.; Sun, D.; Mao, S.; Sun, L.; He, C.; Wang, Z. In-Situ Phosphating to Synthesize Ni2P Decorated NiO/g-C_3N_4 Pn Junction for Enhanced Photocatalytic Hydrogen Production. *Chem. Eng. J.* **2019**, *378*, 122161. [CrossRef]
338. Li, F.; Zhao, Y.; Wang, Q.; Wang, X.; Hao, Y.; Liu, R.; Zhao, D. Enhanced Visible-Light Photocatalytic Activity of Active Al_2O_3/g-C_3N_4 Heterojunctions Synthesized via Surface Hydroxyl Modification. *J. Hazard. Mater.* **2015**, *283*, 371–381. [CrossRef] [PubMed]
339. Tzvetkov, G.; Tsvetkov, M.; Spassov, T. Ammonia-Evaporation-Induced Construction of Three-Dimensional NiO/g-C_3N_4 Composite with Enhanced Adsorption and Visible Light-Driven Photocatalytic Performance. *Superlattices Microstruct.* **2018**, *119*, 122–133. [CrossRef]
340. Sumathi, M.; Prakasam, A.; Anbarasan, P.M. Fabrication of Hexagonal Disc Shaped Nanoparticles g-C_3N_4 /NiO Heterostructured Nanocomposites for Efficient Visible Light Photocatalytic Performance. *J. Clust. Sci.* **2019**, *30*, 757–766. [CrossRef]
341. Huang, L.; Xu, H.; Zhang, R.; Cheng, X.; Xia, J.; Xu, Y.; Li, H. Synthesis and Characterization of g-C_3N_4/MoO_3 Photocatalyst with Improved Visible-Light Photoactivity. *Appl. Surf. Sci.* **2013**, *283*, 25–32. [CrossRef]
342. Zhang, X.; Yi, J.; Chen, H.; Mao, M.; Liu, L.; She, X.; Ji, H.; Wu, X.; Yuan, S.; Xu, H. Construction of a Few-Layer g-C_3N_4/α-MoO_3 Nanoneedles All-Solid-State Z-Scheme Photocatalytic System for Photocatalytic Degradation. *J. Energy Chem.* **2019**, *29*, 65–71. [CrossRef]
343. Liu, L.; Qi, Y.; Hu, J.; An, W.; Lin, S.; Liang, Y.; Cui, W. Stable Cu_2O@ g-C_3N_4 Core@ Shell Nanostructures: Efficient Visible-Light Photocatalytic Hydrogen Evolution. *Mater. Lett.* **2015**, *158*, 278–281. [CrossRef]
344. Han, S.; Hu, X.; Yang, W.; Qian, Q.; Fang, X.; Zhu, Y. Constructing the Band Alignment of Graphitic Carbon Nitride (g-C_3N_4)/Copper (I) Oxide (Cu_2O) Composites by Adjusting the Contact Facet for Superior Photocatalytic Activity. ACS Appl. *Energy Mater.* **2018**, *2*, 1803–1811. [CrossRef]
345. Liu, H.; Zhu, X.; Han, R.; Dai, Y.; Sun, Y.; Lin, Y.; Gao, D.; Wang, X.; Luo, C. Study on the Internal Electric Field in the Cu_2O/ g-C_3N_4 p–n Heterojunction Structure for Enhancing Visible Light Photocatalytic Activity. *New J. Chem.* **2020**, *44*, 1795–1805. [CrossRef]
346. Singh, P.K.; Bhardiya, S.R.; Asati, A.; Rai, V.K.; Singh, M.; Rai, A. Cu/Cu_2O@ g-C_3N_4: Recyclable Photocatalyst under Visible Light to Access 2-Aryl-/Benzimidazoles/Benzothiazoles in Water. *ChemistrySelect* **2020**, *5*, 14270–14275. [CrossRef]
347. Liang, S.; Zhou, Y.; Cai, Z.; She, C. Preparation of Porous g-C_3N_4/Ag/Cu_2O: A New Composite with Enhanced Visible-light Photocatalytic Activity. *Appl. Organomet. Chem.* **2016**, *30*, 932–938. [CrossRef]
348. Chaudhary, P.; Ingole, P.P. In-Situ Solid-State Synthesis of 2D/2D Interface between Ni/NiO Hexagonal Nanosheets Supported on g-C_3N_4 for Enhanced Photo-Electrochemical Water Splitting. *Int. J. Hydrogen Energy* **2020**, *45*, 16060–16070. [CrossRef]

349. Zhou, C.; Liu, Z.; Fang, L.; Guo, Y.; Feng, Y.; Yang, M. Kinetic and Mechanistic Study of Rhodamine B Degradation by H_2O_2 and $Cu/Al_2O_3/g\text{-}C_3N_4$ Composite. *Catalysts* **2020**, *10*, 317. [CrossRef]
350. Bao, Y.; Chen, K. A Novel Z-Scheme Visible Light Driven $Cu_2O/Cu/g\text{-}C_3N_4$ Photocatalyst Using Metallic Copper as a Charge Transfer Mediator. *Mol. Catal.* **2017**, *432*, 187–195. [CrossRef]
351. Zhang, P.; Wang, T.; Zeng, H. Design of Cu-$Cu_2O/g\text{-}C_3N_4$ Nanocomponent Photocatalysts for Hydrogen Evolution under Visible Light Irradiation Using Water-Soluble Erythrosin B Dye Sensitization. *Appl. Surf. Sci.* **2017**, *391*, 404–414. [CrossRef]
352. Liu, C.; Mao, D.; Pan, J.; Qian, J.; Zhang, W.; Chen, F.; Chen, Z.; Song, Y. Fabrication of Highly Efficient Heterostructured Ag-$CeO_2/g\text{-}C_3N_4$ Hybrid Photocatalyst with Enhanced Visible-Light Photocatalytic Activity. *J. Rare Earths* **2019**, *37*, 1269–1278. [CrossRef]
353. Pinheiro, D.; Devi, K.R.S.; Jose, A.; Karthik, K.; Sugunan, S.; Mohan, M.K. Experimental Design for Optimization of 4-Nitrophenol Reduction by Green Synthesized $CeO_2/g\text{-}C_3N_4/Ag$ Catalyst Using Response Surface Methodology. *J. Rare Earths* **2020**, *38*, 1171–1177. [CrossRef]
354. Yin, H.Y.; Zheng, Y.F.; Wang, L. $Au/CeO_2/g\text{-}C_3N_4$ Nanocomposite Modified Electrode as Electrochemical Sensor for the Determination of Phenol. *J. Nanosci. Nanotechnol.* **2020**, *20*, 5539–5545. [CrossRef]
355. Tian, N.; Huang, H.; Guo, Y.; He, Y.; Zhang, Y. A $g\text{-}C_3N_4/Bi_2O_2CO_3$ Composite with High Visible-Light-Driven Photocatalytic Activity for Rhodamine B Degradation. *Appl. Surf. Sci.* **2014**, *322*, 249–254. [CrossRef]
356. Mohammad, A.; Karim, M.R.; Khan, M.E.; Khan, M.M.; Cho, M.H. Biofilm-Assisted Fabrication of Ag@ SnO_2-g-C_3N_4 Nanostructures for Visible Light-Induced Photocatalysis and Photoelectrochemical Performance. *J. Phys. Chem. C* **2019**, *123*, 20936–20948. [CrossRef]
357. Saravanakumar, K.; Karthik, R.; Chen, S.-M.; Kumar, J.V.; Prakash, K.; Muthuraj, V. Construction of Novel $Pd/CeO_2/g\text{-}C_3N_4$ Nanocomposites as Efficient Visible-Light Photocatalysts for Hexavalent Chromium Detoxification. *J. Colloid Interface Sci.* **2017**, *504*, 514–526. [CrossRef] [PubMed]
358. Xie, Q.; He, W.; Liu, S.; Li, C.; Zhang, J.; Wong, P.K. Bifunctional S-Scheme $g\text{-}C_3N_4/Bi/BiVO_4$ Hybrid Photocatalysts toward Artificial Carbon Cycling. *Chin. J. Catal.* **2020**, *41*, 140–153. [CrossRef]
359. Han, C.; Zhang, R.; Ye, Y.; Wang, L.; Ma, Z.; Su, F.; Xie, H.; Zhou, Y.; Wong, P.K.; Ye, L. Chainmail Co-Catalyst of NiO Shell-Encapsulated Ni for Improving Photocatalytic CO_2 Reduction over GC_3N_4. *J. Mater. Chem. A* **2019**, *7*, 9726–9735. [CrossRef]
360. Zhao, X.; Guan, J.; Li, J.; Li, X.; Wang, H.; Huo, P.; Yan, Y. CeO_2/3D $g\text{-}C_3N_4$ Heterojunction Deposited with Pt Cocatalyst for Enhanced Photocatalytic CO_2 Reduction. *Appl. Surf. Sci.* **2021**, *537*, 147891. [CrossRef]
361. Karimi, M.A.; Atashkadi, M.; Ranjbar, M.; Habibi-Yangjeh, A. Novel Visible-Light-Driven Photocatalyst of $NiO/Cd/g\text{-}C_3N_4$ for Enhanced Degradation of Methylene Blue. *Arab. J. Chem.* **2020**, *13*, 5810–5820. [CrossRef]
362. Jia, Z.; Lyu, F.; Zhang, L.C.; Zeng, S.; Liang, S.X.; Li, Y.Y.; Lu, J. Pt Nanoparticles Decorated Heterostructured $g\text{-}C_3N_4/Bi_2$ MoO_6 Microplates with Highly Enhanced Photocatalytic Activities under Visible Light. *Sci. Rep.* **2019**, *9*, 1–13. [CrossRef]
363. Guo, Q.; Zhang, C.; Zhang, C.; Xin, S.; Zhang, P.; Shi, Q.; Zhang, D.; You, Y. Co_3O_4 Modified $Ag/g\text{-}C_3N_4$ Composite as a Bifunctional Cathode for Lithium-Oxygen Battery. *J. Energy Chem.* **2020**, *41*, 185–193. [CrossRef]
364. Xie, Z.; Feng, Y.; Wang, F.; Chen, D.; Zhang, Q.; Zeng, Y.; Lv, W.; Liu, G. Construction of Carbon Dots Modified $MoO_3/g\text{-}C_3N_4$ Z-Scheme Photocatalyst with Enhanced Visible-Light Photocatalytic Activity for the Degradation of Tetracycline. *Appl. Catal. B Environ.* **2018**, *229*, 96–104. [CrossRef]
365. Shi, W.; Wang, J.; Yang, S.; Lin, X.; Guo, F.; Shi, J. Fabrication of a Ternary Carbon Dots/$CoO/g\text{-}C_3N_4$ Nanocomposite Photocatalyst with Enhanced Visible-light-driven Photocatalytic Hydrogen Production. *J. Chem. Technol. Biotechnol.* **2020**, *95*, 2129–2138. [CrossRef]
366. Kumar, A.; Sharma, S.K.; Sharma, G.; Naushad, M.; Stadler, F.J. $CeO_2/g\text{-}C_3N_4/V_2O_5$ Ternary Nano Hetero-Structures Decorated with CQDs for Enhanced Photo-Reduction Capabilities under Different Light Sources: Dual Z-Scheme Mechanism. *J. Alloys Compd.* **2020**, *838*, 155692. [CrossRef]
367. Wang, H.; Yang, Y.; Qu, T.; Kang, Z.; Wang, D. Co_3O_4 and CDots Nanocrystals on $g\text{-}C_3N_4$ as a Synergetic Catalyst for Oxygen Reduction Reaction. *Green Process. Synth.* **2015**, *4*, 411–419. [CrossRef]
368. Shekardasht, M.B.; Givianrad, M.H.; Gharbani, P.; Mirjafary, Z.; Mehrizad, A. Preparation of a Novel Z-Scheme g-$C_3N_4/RGO/Bi_2Fe_4O_9$ Nanophotocatalyst for Degradation of Congo Red Dye under Visible Light. *Diam. Relat. Mater.* **2020**, *109*, 108008. [CrossRef]
369. Gong, L.; Li, X.; Zhang, Q.; Huang, B.; Yang, Q.; Yang, G.; Liu, Y. Ultrafast and Large-Scale Synthesis of Co_3O_4 Quantum Dots-C_3N_4/RGO as an Excellent ORR Electrocatalyst via a Controllable Deflagration Strategy. *Appl. Surf. Sci.* **2020**, *525*, 146624. [CrossRef]
370. Feng, Y.; Yan, T.; Wu, T.; Zhang, N.; Yang, Q.; Sun, M.; Yan, L.; Du, B.; Wei, Q. A Label-Free Photoelectrochemical Aptasensing Platform Base on Plasmon Au Coupling with MOF-Derived In_2O_3@ $g\text{-}C_3N_4$ Nanoarchitectures for Tetracycline Detection. *Sensors Actuators B Chem.* **2019**, *298*, 126817. [CrossRef]
371. Cui, Y.; Nengzi, L.; Gou, J.; Huang, Y.; Li, B.; Cheng, X. Fabrication of Dual Z-Scheme MIL-53 (Fe)/α-$Bi_2O_3/g\text{-}C_3N_4$ Ternary Composite with Enhanced Visible Light Photocatalytic Performance. *Sep. Purif. Technol.* **2020**, *232*, 115959. [CrossRef]
372. Jourshabani, M.; Shariatinia, Z.; Badiei, A. Synthesis and Characterization of Novel Sm_2O_3/S-Doped $g\text{-}C_3N_4$ Nanocomposites with Enhanced Photocatalytic Activities under Visible Light Irradiation. *Appl. Surf. Sci.* **2018**, *427*, 375–387. [CrossRef]

373. Lan, Y.; Li, Z.; Xie, W.; Li, D.; Yan, G.; Guo, S.; Pan, C.; Wu, J. In Situ Fabrication of I-Doped $Bi_2O_2CO_3$/g-C_3N_4 Heterojunctions for Enhanced Photodegradation Activity under Visible Light. *J. Hazard. Mater.* **2020**, *385*, 121622. [CrossRef] [PubMed]
374. Xue, S.; Hou, X.; Xie, W.; Wei, X.; He, D. Dramatic Improvement of Photocatalytic Activity for N-Doped Bi_2O_3/g-C_3N_4 Composites. *Mater. Lett.* **2015**, *161*, 640–643. [CrossRef]
375. Zhou, P.; Meng, X.; Sun, T. Facile Fabrication of In_2O_3/S-Doped g-C_3N_4 Heterojunction Hybrids for Enhanced Visible-Light Photocatalytic Hydrogen Evolution. *Mater. Lett.* **2020**, *261*, 127159. [CrossRef]
376. Jin, X.; Guan, Q.; Tian, T.; Li, H.; Han, Y.; Hao, F.; Cui, Y.; Li, W.; Zhu, Y.; Zhang, Y. In_2O_3/Boron Doped g-C_3N_4 Heterojunction Catalysts with Remarkably Enhanced Visible-Light Photocatalytic Efficiencies. *Appl. Surf. Sci.* **2020**, *504*, 144241. [CrossRef]
377. Liu, J.-L.; Jiang, J.; Zhang, J.-Q.; Chai, Y.-Q.; Xiao, Q.; Yuan, R. The Combination of Ternary Electrochemiluminescence System of g-C_3N_4 Nanosheet/TEA/Cu@ Cu_2O and G-Quadruplex-Driven Regeneration Strategy for Ultrasensitive Bioanalysis. *Biosens. Bioelectron.* **2020**, *152*, 112006. [CrossRef]
378. Li, J.; Li, Y.; Zhang, W.; Naraginti, S.; Sivakumar, A.; Zhang, C. Fabrication of Novel Tetrahedral Ag_3PO_4/g-C_3N_4/$BiVO_4$ Ternary Composite for Efficient Detoxification of Sulfamethoxazole. *Process Saf. Environ. Prot.* **2020**, *143*, 340–347. [CrossRef]
379. Hu, B.; Liu, Y.; Wang, Z.-W.; Song, Y.; Wang, M.; Zhang, Z.; Liu, C.-S. Bimetallic-Organic Framework Derived Porous Co_3O_4/Fe_3O_4/C-Loaded g-C_3N_4 Nanocomposites as Non-Enzymic Electrocatalysis Oxidization toward Ascorbic Acid, Dopamine Acid, and Uric Acid. *Appl. Surf. Sci.* **2018**, *441*, 694–707. [CrossRef]
380. Wang, Y.; Yu, D.; Wang, W.; Gao, P.; Zhong, S.; Zhang, L.; Zhao, Q.; Liu, B. Synthesizing Co_3O_4-$BiVO_4$/g-C_3N_4 Heterojunction Composites for Superior Photocatalytic Redox Activity. *Sep. Purif. Technol.* **2020**, *239*, 116562. [CrossRef]
381. Sudrajat, H.; Hartuti, S. Structural Properties and Catalytic Activity of a Novel Ternary CuO/GC_3N_4/Bi_2O_3 Photocatalyst. *J. Colloid Interface Sci.* **2018**, *524*, 227–235. [CrossRef]
382. Zhao, H.; Zhang, J.; Zheng, H. Facile Preparation of Dual Z-Scheme Bi_2O_3/g-C_3N_4/$Ag_6Si_2O_7$ Photocatalyst for Highly Efficient Visible-Light Photocatalytic Degradation of Organic Pollutants. *Appl. Surf. Sci.* **2020**, *527*, 146901. [CrossRef]
383. Vattikuti, S.V.P.; Police, A.K.R.; Shim, J.; Byon, C. In Situ Fabrication of the Bi_2O_3–V_2O_5 Hybrid Embedded with Graphitic Carbon Nitride Nanosheets: Oxygen Vacancies Mediated Enhanced Visible-Light–Driven Photocatalytic Degradation of Organic Pollutants and Hydrogen Evolution. *Appl. Surf. Sci.* **2018**, *447*, 740–756. [CrossRef]
384. Wu, S.; Guo, J.; Wang, Y. $Bi_2O_2CO_3$–$Bi_2O_2(OH)NO_3$/g-C_3N_4 Heterojunction as a Visible-Light-Driven Photocatalyst with Enhanced Photogenerated Charge Separation. *J. Alloys Compd.* **2020**, *818*, 152852. [CrossRef]
385. Zhong, S.; Zhou, H.; Shen, M.; Yao, Y.; Gao, Q. Rationally Designed a g-C_3N_4/BiOI/$Bi_2O_2CO_3$ Composite with Promoted Photocatalytic Activity. *J. Alloys Compd.* **2021**, *853*, 157307. [CrossRef]
386. Kumar, A.; Kumar, A.; Sharma, G.; Ala'a, H.; Naushad, M.; Ghfar, A.A.; Guo, C.; Stadler, F.J. Biochar-Templated g-C_3N_4/$Bi_2O_2CO_3$/$CoFe_2O_4$ Nano-Assembly for Visible and Solar Assisted Photo-Degradation of Paraquat, Nitrophenol Reduction and CO_2 Conversion. *Chem. Eng. J.* **2018**, *339*, 393–410. [CrossRef]
387. Min, Z.; Wang, X.; Li, Y.; Jiang, J.; Li, J.; Qian, D.; Li, J. A Highly Efficient Visible-Light-Responding Cu_2O-TiO_2/g-C_3N_4 Photocatalyst for Instantaneous Discolorations of Organic Dyes. *Mater. Lett.* **2017**, *193*, 18–21. [CrossRef]
388. Muñoz-Batista, M.J.; Nasalevich, M.A.; Savenije, T.J.; Kapteijn, F.; Gascon, J.; Kubacka, A.; Fernández-García, M. Enhancing Promoting Effects in g-C_3N_4-Mn^+/CeO_2-TiO_2 Ternary Composites: Photo-Handling of Charge Carriers. *Appl. Catal. B Environ.* **2015**, *176*, 687–698. [CrossRef]
389. da Silva Veras, T.; Mozer, T.S.; da Silva César, A. Hydrogen: Trends, Production and Characterization of the Main Process Worldwide. *Int. J. Hydrogen Energy* **2017**, *42*, 2018–2033. [CrossRef]
390. He, R.; Liang, H.; Li, C.; Bai, J. Enhanced Photocatalytic Hydrogen Production over Co_3O_4@ g-C_3N_4 Pn Junction Adhering on One-Dimensional Carbon Fiber. *Colloids Surfaces A Physicochem. Eng. Asp.* **2020**, *586*, 124200. [CrossRef]
391. Anandan, S.; Wu, J.J.; Bahnemann, D.; Emeline, A.; Ashokkumar, M. Crumpled Cu_2O-g-C_3N_4 Nanosheets for Hydrogen Evolution Catalysis. Colloids Surfaces A Physicochem. *Eng. Asp.* **2017**, *527*, 34–41. [CrossRef]
392. Shi, J.; Zheng, B.; Mao, L.; Cheng, C.; Hu, Y.; Wang, H.; Li, G.; Jing, D.; Liang, X. MoO_3/g-C_3N_4 Z-Scheme (S-Scheme) System Derived from MoS_2/Melamine Dual Precursors for Enhanced Photocatalytic H_2 Evolution Driven by Visible Light. *Int. J. Hydrogen Energy* **2021**, *46*, 2927–2935. [CrossRef]
393. Chebanenko, M.I.; Lobinsky, A.A.; Nevedomskiy, V.N.; Popkov, V.I. NiO-Decorated Graphitic Carbon Nitride toward Electrocatalytic Hydrogen Production from Ethanol. *Dalt. Trans.* **2020**, *49*, 12088–12097. [CrossRef] [PubMed]
394. Ma, X.; Zhang, J.; Wang, B.; Li, Q.; Chu, S. Hierarchical Cu_2O Foam/ g-C_3N_4 Photocathode for Photoelectrochemical Hydrogen Production. *Appl. Surf. Sci.* **2018**, *427*, 907–916. [CrossRef]
395. Paul, A.M.; Sajeev, A.; Nivetha, R.; Gothandapani, K.; Bhardwaj, P.; Govardhan, K.; Raghavan, V.; Jacob, G.; Sellapan, R.; Jeong, S.K. Cuprous Oxide (Cu_2O)/Graphitic Carbon Nitride (g-C_3N_4) Nanocomposites for Electrocatalytic Hydrogen Evolution Reaction. *Diam. Relat. Mater.* **2020**, *107*, 107899. [CrossRef]
396. Zhang, M.; Qin, J.; Rajendran, S.; Zhang, X.; Liu, R. Heterostructured D-Ti_3C_2/TiO_2/g-C_3N_4 Nanocomposites with Enhanced Visible-light Photocatalytic Hydrogen Production Activity. *ChemSusChem* **2018**, *11*, 4226–4236. [CrossRef] [PubMed]
397. Wen, P.; Sun, Y.; Li, H.; Liang, Z.; Wu, H.; Zhang, J.; Zeng, H.; Geyer, S.M.; Jiang, L. A Highly Active Three-Dimensional Z-Scheme ZnO/Au/g-C_3N_4 Photocathode for Efficient Photoelectrochemical Water Splitting. *Appl. Catal. B Environ.* **2020**, *263*, 118180. [CrossRef]

398. Wei, X.; Wang, X.; Pu, Y.; Liu, A.; Chen, C.; Zou, W.; Zheng, Y.; Huang, J.; Zhang, Y.; Yang, Y. Facile Ball-Milling Synthesis of CeO_2/g-C_3N_4 Z-Scheme Heterojunction for Synergistic Adsorption and Photodegradation of Methylene Blue: Characteristics, Kinetics, Models, and Mechanisms. *Chem. Eng. J.* **2020**, *470*, 127719. [CrossRef]
399. Zhang, S.; Yan, J.; Yang, S.; Xu, Y.; Cai, X.; Li, X.; Zhang, X.; Peng, F.; Fang, Y. Electrodeposition of Cu_2O/g-C_3N_4 Heterojunction Film on an FTO Substrate for Enhancing Visible Light Photoelectrochemical Water Splitting. *Chin. J. Catal.* **2017**, *38*, 365–371. [CrossRef]
400. Ji, C.; Yin, S.-N.; Sun, S.; Yang, S. An in Situ Mediator-Free Route to Fabricate Cu_2O/g-C_3N_4 Type-II Heterojunctions for Enhanced Visible-Light Photocatalytic H_2 Generation. *Appl. Surf. Sci.* **2018**, *434*, 1224–1231. [CrossRef]
401. Liu, L.; Qi, Y.; Hu, J.; Liang, Y.; Cui, W. Efficient Visible-Light Photocatalytic Hydrogen Evolution and Enhanced Photostability of Core@ Shell Cu_2O@ g-C_3N_4 Octahedra. *Appl. Surf. Sci.* **2015**, *351*, 1146–1154. [CrossRef]
402. Yan, H.; Yang, H. TiO_2–g-C_3N_4 Composite Materials for Photocatalytic H_2 Evolution under Visible Light Irradiation. *J. Alloys Compd.* **2011**, *509*, L26–L29. [CrossRef]
403. Marchal, C.; Cottineau, T.; Méndez-Medrano, M.G.; Colbeau-Justin, C.; Caps, V.; Keller, V. Au/TiO_2/GC_3N_4 Nanocomposites for Enhanced Photocatalytic H_2 Production from Water under Visible Light Irradiation with Very Low Quantities of Sacrificial Agents. *Adv. Energy Mater.* **2018**, *8*, 1702142. [CrossRef]
404. Geng, R.; Yin, J.; Zhou, J.; Jiao, T.; Feng, Y.; Zhang, L.; Chen, Y.; Bai, Z.; Peng, Q. In Situ Construction of Ag/TiO_2/g-C_3N_4 Heterojunction Nanocomposite Based on Hierarchical Co-Assembly with Sustainable Hydrogen Evolution. *Nanomaterials* **2020**, *10*, 1. [CrossRef] [PubMed]
405. Pan, J.; You, M.; Chi, C.; Dong, Z.; Wang, B.; Zhu, M.; Zhao, W.; Song, C.; Zheng, Y.; Li, C. The Two Dimension Carbon Quantum Dots Modified Porous g-C_3N_4/TiO_2 Nano-Heterojunctions for Visible Light Hydrogen Production Enhancement. *Int. J. Hydrogen Energy* **2018**, *43*, 6586–6593. [CrossRef]
406. Mahala, C.; Sharma, M.D.; Basu, M. ZnO Nanosheets Decorated with Graphite-like Carbon Nitride Quantum Dots as Photoanodes in Photoelectrochemical Water Splitting. *ACS Appl. Nano Mater.* **2020**, *3*, 1999–2007. [CrossRef]
407. Qin, H.; Zuo, Y.; Jin, J.; Wang, W.; Xu, Y.; Cui, L.; Dang, H. ZnO Nanorod Arrays Grown on g-C_3N_4 Micro-Sheets for Enhanced Visible Light Photocatalytic H_2 Evolution. *RSC Adv.* **2019**, *9*, 24483–24488. [CrossRef]
408. Zhang, Y.; He, S.; Guo, W.; Hu, Y.; Huang, J.; Mulcahy, J.R.; Wei, W.D. Surface-Plasmon-Driven Hot Electron Photochemistry. *Chem. Rev.* **2017**, *118*, 2927–2954. [CrossRef] [PubMed]
409. Saha, D.; Gismondi, P.; Kolasinski, K.W.; Shumlas, S.L.; Rangan, S.; Eslami, B.; McConnell, A.; Bui, T.; Cunfer, K. Fabrication of Electrospun Nanofiber Composite of g-C_3N_4 and Au Nanoparticles as Plasmonic Photocatalyst. *Surfaces Interfaces* **2021**, *26*, 101367. [CrossRef]
410. Zhang, X.; Chen, Y.L.; Liu, R.-S.; Tsai, D.P. Plasmonic Photocatalysis. *Reports Prog. Phys.* **2013**, *76*, 46401. [CrossRef]
411. Zhao, W.; Dong, Q.; Sun, C.; Xia, D.; Huang, H.; Yang, G.; Wang, G.; Leung, D.Y.C. A Novel Au/g-C_3N_4 Nanosheets/CeO_2 Hollow Nanospheres Plasmonic Heterojunction Photocatalysts for the Photocatalytic Reduction of Hexavalent Chromium and Oxidation of Oxytetracycline Hydrochloride. *Chem. Eng. J.* **2021**, *409*, 128185. [CrossRef]
412. Bashiri, R.; Mohamed, N.M.; Suhaimi, N.A.; Shahid, M.U.; Kait, C.F.; Sufian, S.; Khatani, M.; Mumtaz, A. Photoelectrochemical Water Splitting with Tailored TiO_2/$SrTiO_3$@ g-C_3N_4 Heterostructure Nanorod in Photoelectrochemical Cell. *Diam. Relat. Mater.* **2018**, *85*, 5–12. [CrossRef]
413. Wang, S.; Zheng, F.; Weng, Y.; Yuan, G.; Fang, L.; You, L. Enhanced Photoelectrochemical Performance by Interface Engineering in Ternary g-C_3N_4/TiO_2/$PbTiO_3$ Films. *Adv. Mater. Interfaces* **2020**, *7*, 2000185. [CrossRef]
414. Qu, A.; Xu, X.; Xie, H.; Zhang, Y.; Li, Y.; Wang, J. Effects of Calcining Temperature on Photocatalysis of g-C_3N_4 /TiO_2 Composites for Hydrogen Evolution from Water. *Mater. Res. Bull.* **2016**, *80*, 167–176. [CrossRef]
415. Jiang, Y.; Sun, Z.; Chen, Q.; Cao, C.; Zhao, Y.; Yang, W.; Zeng, L.; Huang, L. Fabrication of 0D/2D TiO_2 Nanodots/g-C_3N_4 S-Scheme Heterojunction Photocatalyst for Efficient Photocatalytic Overall Water Splitting. *Appl. Surf. Sci.* **2021**, *571*, 151287. [CrossRef]
416. Liu, J.; Yan, X.-T.; Qin, X.-S.; Wu, S.-J.; Zhao, H.; Yu, W.-B.; Chen, L.-H.; Li, Y.; Su, B.-L. Light-Assisted Preparation of Heterostructured g-C_3N_4/ZnO Nanorods Arrays for Enhanced Photocatalytic Hydrogen Performance. *Catal. Today* **2019**, *355*, 932–936. [CrossRef]
417. Liu, Y.; Liu, H.; Zhou, H.; Li, T.; Zhang, L. A Z-Scheme Mechanism of N-ZnO/g-C_3N_4 for Enhanced H_2 Evolution and Photocatalytic Degradation. *Appl. Surf. Sci.* **2019**, *466*, 133–140. [CrossRef]
418. Gu, Y.; Bao, A.; Zhang, X.; Yan, J.; Du, Q.; Zhang, M.; Qi, X. Facile Fabrication of Sulfur-Doped Cu_2O and g-C_3N_4 with Z-Scheme Structure for Enhanced Photocatalytic Water Splitting Performance. *Mater. Chem. Phys.* **2021**, *266*, 124542. [CrossRef]
419. Alhaddad, M.; Navarro, R.M.; Hussein, M.A.; Mohamed, R.M. Bi_2O_3/g-C_3N_4 Nanocomposites as Proficient Photocatalysts for Hydrogen Generation from Aqueous Glycerol Solutions beneath Visible Light. *Ceram. Int.* **2020**, *46*, 24873–24881. [CrossRef]
420. Ma, R.; Dong, L.; Li, B.; Su, T.; Luo, X.; Qin, Z.; Ji, H. g-C_3N_4/$BiYO_3$ Composite for Photocatalytic Hydrogen Evolution. *ChemistrySelect* **2018**, *3*, 5891–5899. [CrossRef]
421. Xu, J.; Yu, H.; Guo, H. Synthesis and Behaviors of g-C_3N_4 Coupled with LaxCo3-XO4 Nanocomposite for Improved Photocatalytic Activeity and Stability under Visible Light. *Mater. Res. Bull.* **2018**, *105*, 342–348. [CrossRef]
422. Li, Y.; Zhu, S.; Kong, X.; Liang, Y.; Li, Z.; Wu, S.; Chang, C.; Luo, S.; Cui, Z. In Situ Synthesis of a Novel Mn_3O_4/g-C_3N_4 Pn Heterostructure Photocatalyst for Water Splitting. *J. Colloid Interface Sci.* **2021**, *586*, 778–784. [CrossRef] [PubMed]

423. Song, T.; Zhang, X.; Yang, P. Bifunctional Nitrogen-Doped Carbon Dots in g-C_3N_4/WO_x Heterojunction for Enhanced Photocatalytic Water-Splitting Performance. *Langmuir* **2021**, *37*, 4236–4247. [CrossRef]
424. Fu, Y.; Zhu, C.; Wang, H.; Dou, Y.; Shi, W.; Shao, M.; Huang, H.; Liu, Y.; Kang, Z. High-Performance NiO/g-C_3N_4 Composites for Visible-Light-Driven Photocatalytic Overall Water Splitting. *Inorg. Chem. Front.* **2018**, *5*, 1646–1652. [CrossRef]
425. Cao, S.-W.; Liu, X.-F.; Yuan, Y.-P.; Zhang, Z.-Y.; Liao, Y.-S.; Fang, J.; Loo, S.C.J.; Sum, T.C.; Xue, C. Solar-to-Fuels Conversion over In_2O_3/g-C_3N_4 Hybrid Photocatalysts. *Appl. Catal. B Environ.* **2014**, *147*, 940–946. [CrossRef]
426. Guo, Y.; Chang, B.; Wen, T.; Zhang, S.; Zeng, M.; Hu, N.; Su, Y.; Yang, Z.; Yang, B. A Z-Scheme Photocatalyst for Enhanced Photocatalytic H_2 Evolution, Constructed by Growth of 2D Plasmonic MoO_{3-x} Nanoplates onto 2D g-C_3N_4 Nanosheets. *J. Colloid Interface Sci.* **2020**, *567*, 213–223. [CrossRef]
427. Hou, H.L.; Gao, F.; Wang, L.; Shang, M.; Yang, Z.; Zheng, J.; Yang, W. Superior Ternary Hybrid Photocatalysts of TiO_2/WO_3/GC_3N_4 Thoroughly Mesoporous Nanofibers for Visible-Lightdriven Hydrogen Evolution. *J. Mater. Chem. A* **2016**, *4*, 6276–6281. [CrossRef]
428. Hieu, V.Q.; Lam, T.C.; Khan, A.; Vo, T.-T.T.; Nguyen, T.-Q.; Doan, V.D.; Tran, V.A. TiO_2/Ti_3C_2/g-C_3N_4 Ternary Heterojunction for Photocatalytic Hydrogen Evolution. *Chemosphere* **2021**, *285*, 131429. [CrossRef]
429. Nie, N.; Zhang, L.; Fu, J.; Cheng, B.; Yu, J. Self-Assembled Hierarchical Direct Z-Scheme g-C_3N_4/ZnO Microspheres with Enhanced Photocatalytic CO_2 Reduction Performance. *Appl. Surf. Sci.* **2018**, *441*, 12–22. [CrossRef]
430. Mulik, B.B.; Bankar, B.D.; Munde, A.V.; Chavan, P.P.; Biradar, A.V.; Sathe, B.R. Electrocatalytic and Catalytic CO_2 Hydrogenation on ZnO/g-C_3N_4 Hybrid Nanoelectrodes. *Appl. Surf. Sci.* **2021**, *538*, 148120. [CrossRef]
431. Wang, H.; Li, H.; Chen, Z.; Li, J.; Li, X.; Huo, P.; Wang, Q. TiO_2 Modified g-C_3N_4 with Enhanced Photocatalytic CO_2 Reduction Performance. *Solid State Sci.* **2020**, *100*, 106099. [CrossRef]
432. Truc, N.T.T.; Bach, L.G.; Hanh, N.T.; Pham, T.-D.; Le Chi, N.T.P.; Tran, D.T.; Nguyen, M.V. The Superior Photocatalytic Activity of Nb Doped TiO_2/g-C_3N_4 Direct Z-Scheme System for Efficient Conversion of CO_2 into Valuable Fuels. *J. Colloid Interface Sci.* **2019**, *540*, 1–8. [CrossRef] [PubMed]
433. Guo, Q.; Fu, L.; Yan, T.; Tian, W.; Ma, D.; Li, J.; Jiang, Y.; Wang, X. Improved Photocatalytic Activity of Porous ZnO Nanosheets by Thermal Deposition Graphene-like g-C_3N_4 for CO_2 Reduction with H_2O Vapor. *Appl. Surf. Sci.* **2020**, *509*, 144773. [CrossRef]
434. Shen, D.; Li, X.; Ma, C.; Zhou, Y.; Sun, L.; Yin, S.; Huo, P.; Wang, H. Synthesized Z-Scheme Photocatalyst ZnO/g-C_3N_4 for Enhanced Photocatalytic Reduction of CO_2. *New J. Chem.* **2020**, *44*, 16390–16399. [CrossRef]
435. Liang, M.; Borjigin, T.; Zhang, Y.; Liu, B.; Liu, H.; Guo, H. Controlled Assemble of Hollow Heterostructured g-C_3N_4@ CeO_2 with Rich Oxygen Vacancies for Enhanced Photocatalytic CO_2 Reduction. *Appl. Catal. B Environ.* **2019**, *243*, 566–575. [CrossRef]
436. Tang, J.; Guo, R.; Zhou, W.; Huang, C.; Pan, W. Ball-Flower like NiO/g-C_3N_4 Heterojunction for Efficient Visible Light Photocatalytic CO_2 Reduction. *Appl. Catal. B Environ.* **2018**, *237*, 802–810. [CrossRef]
437. Sun, Z.; Fang, W.; Zhao, L.; Chen, H.; He, X.; Li, W.; Tian, P.; Huang, Z. g-C_3N_4 Foam/Cu_2O QDs with Excellent CO_2 Adsorption and Synergistic Catalytic Effect for Photocatalytic CO_2 Reduction. *Environ. Int.* **2019**, *130*, 104898. [CrossRef]
438. Truc, N.T.T.; Pham, T.-D.; Nguyen, M.V.; Van Thuan, D.; Thao, P.; Trang, H.T.; Tran, D.T.; Minh, D.N.; Hanh, N.T.; Ngoc, H.M. Advanced $NiMoO_4$/g-C_3N_4 Z-Scheme Heterojunction Photocatalyst for Efficient Conversion of CO_2 to Valuable Products. *J. Alloys Compd.* **2020**, *842*, 155860. [CrossRef]
439. Li, M.; Zhang, L.; Wu, M.; Du, Y.; Fan, X.; Wang, M.; Zhang, L.; Kong, Q.; Shi, J. Mesostructured CeO_2/g-C_3N_4 Nanocomposites: Remarkably Enhanced Photocatalytic Activity for CO_2 Reduction by Mutual Component Activations. *Nano Energy* **2016**, *19*, 145–155. [CrossRef]
440. Li, X.; Jiang, H.; Ma, C.; Zhu, Z.; Song, X.; Wang, H.; Huo, P.; Li, X. Local Surface Plasma Resonance Effect Enhanced Z-Scheme ZnO/Au/g-C_3N_4 Film Photocatalyst for Reduction of CO_2 to CO. *Appl. Catal. B Environ.* **2021**, *283*, 119638. [CrossRef]
441. He, Y.; Wang, Y.; Zhang, L.; Teng, B.; Fan, M. High-Efficiency Conversion of CO_2 to Fuel over ZnO/g-C_3N_4 Photocatalyst. *Appl. Catal. B Environ.* **2015**, *168*, 1–8. [CrossRef]
442. Reli, M.; Huo, P.; Šihor, M.; Ambrozova, N.; Troppová, I.; Matejova, L.; Lang, J.; Svoboda, L.; Kuśtrowski, P.; Ritz, M. Novel TiO_2/C_3N_4 Photocatalysts for Photocatalytic Reduction of CO_2 and for Photocatalytic Decomposition of N_2O. *J. Phys. Chem. A* **2016**, *120*, 8564–8573. [CrossRef]
443. Tang, Z.; Wang, C.; He, W.; Wei, Y.; Zhao, Z.; Liu, J. The Z-Scheme g-C_3N_4/3DOM-WO_3 Photocatalysts with Enhanced Activity for CO_2 Photoreduction into CO. *Chin. Chem. Lett.* 2021, in press. [CrossRef]
444. Guo, H.; Wan, S.; Wang, Y.; Ma, W.; Zhong, Q.; Ding, J. Enhanced Photocatalytic CO_2 Reduction over Direct Z-Scheme $NiTiO_3$/g-C_3N_4 Nanocomposite Promoted by Efficient Interfacial Charge Transfer. *Chem. Eng. J.* **2021**, *412*, 128646. [CrossRef]
445. Carmen, Z.; Daniela, S. *Textile Organic Dyes-Characteristics, Polluting Effects and Separation/Elimination Procedures from Industrial Effluents-a Critical Overview*; IntechOpen: Rijekta, Croatia, 2012.
446. Clarke, E.A.; Anliker, R. Organic Dyes and Pigments. In *Anthropogenic Compounds*; Springer: Berlin/Heidelberg, Germany, 1980.
447. Danish, M.S.S.; Bhattacharya, A.; Stepanova, D.; Mikhaylov, A.; Grilli, M.L.; Khosravy, M.; Senjyu, T. A Systematic Review of Metal Oxide Applications for Energy and Environmental Sustainability. *Metals.* **2020**, *10*, 1604. [CrossRef]
448. Devi, K.R.S.; Mathew, S.; Rajan, R.; Georgekutty, J.; Kasinathan, K.; Pinheiro, D.; Sugunan, S. Biogenic Synthesis of g-C_3N_4/Bi_2O_3 Heterojunction with Enhanced Photocatalytic Activity and Statistical Optimization of Reaction Parameters. *Appl. Surf. Sci.* **2019**, *494*, 465–476. [CrossRef]

449. Lan, Y.; Li, Z.; Li, D.; Xie, W.; Yan, G.; Guo, S. Visible-Light Responsive Z-Scheme Bi@ β-Bi_2O_3/g-C_3N_4 Heterojunction for Efficient Photocatalytic Degradation of 2, 3-Dihydroxynaphthalene. *Chem. Eng. J.* **2020**, *392*, 123686. [CrossRef]
450. Khan, A.A.; Tahir, M.; Bafaqeer, A. Constructing a STable 2D Layered Ti_3C_2 MXene Cocatalyst-Assisted TiO_2/g-C_3N_4/Ti_3C_2 Heterojunction for Tailoring Photocatalytic Bireforming of Methane under Visible Light. *Energy Fuels* **2020**, *34*, 9810–9828.
451. Ma, J.; Tan, X.; Yu, T.; Li, X. Fabrication of g-C_3N_4/TiO_2 Hierarchical Spheres with Reactive {001} TiO_2 Crystal Facets and Its Visible-Light Photocatalytic Activity. *Int. J. Hydrogen Energy* **2016**, *41*, 3877–3887. [CrossRef]
452. Rasheed, H.U.; Lv, X.; Wei, W.; Yaseen, W.; Ullah, N.; Xie, J.; Zhu, W. Synthesis and Studies of ZnO Doped with g-C_3N_4 Nanocomposites for the Degradation of Tetracycline Hydrochloride under the Visible Light Irradiation. *J. Environ. Chem. Eng.* **2019**, *7*, 103152. [CrossRef]
453. Zhu, W.; Sun, F.; Goei, R.; Zhou, Y. Construction of WO_3–g-C_3N_4 Composites as Efficient Photocatalysts for Pharmaceutical Degradation under Visible Light. *Catal. Sci. Technol.* **2017**, *7*, 2591–2600. [CrossRef]
454. Lu, N.; Wang, P.; Su, Y.; Yu, H.; Liu, N.; Quan, X. Construction of Z-Scheme g-C_3N_4/RGO/WO_3 with in Situ Photoreduced Graphene Oxide as Electron Mediator for Efficient Photocatalytic Degradation of Ciprofloxacin. *Chemosphere* **2019**, *215*, 444–453. [CrossRef]
455. Truong, H.B.; Huy, B.T.; Ray, S.K.; Lee, Y.-I.; Cho, J.; Hur, J. H_2O_2-Assisted Photocatalysis for Removal of Natural Organic Matter Using Nanosheet C_3N_4-WO_3 Composite under Visible Light and the Hybrid System with Ultrafiltration. *Chem. Eng. J.* **2020**, *399*, 125733. [CrossRef]
456. Shafawi, A.N.; Mahmud, R.A.; Ali, K.A.; Putri, L.K.; Rosli, N.I.M.; Mohamed, A.R. Bi_2O_3 Particles Decorated on Porous g-C_3N_4 Sheets: Enhanced Photocatalytic Activity through a Direct Z-Scheme Mechanism for Degradation of Reactive Black 5 under UV–Vis Light. J. Photochem. *Photobiol. A Chem.* **2020**, *389*, 112289. [CrossRef]
457. Ma, R.; Zhang, S.; Li, L.; Gu, P.; Wen, T.; Khan, A.; Li, S.; Li, B.; Wang, S.; Wang, X. Enhanced Visible-Light-Induced Photoactivity of Type-II CeO_2/g-C_3N_4 Nanosheet toward Organic Pollutants Degradation. ACS Sustain. *Chem. Eng.* **2019**, *7*, 9699–9708.
458. Barathi, D.; Rajalakshmi, N.; Ranjith, R.; Sangeetha, R.; Meyvel, S. Controllable Synthesis of CeO_2/g-C_3N_4 Hybrid Catalysts and Its Structural, Optical and Visible Light Photocatalytic Activity. *Diam. Relat. Mater.* **2021**, *111*, 108161. [CrossRef]
459. Cui, S.; Xie, B.; Li, R.; Pei, J.; Tian, Y.; Zhang, J.; Xing, X. g-C_3N_4/CeO_2 Binary Composite Prepared and Its Application in Automobile Exhaust Degradation. *Materials.* **2020**, *13*, 1274. [CrossRef]
460. Tan, L.; Xu, J.; Zhang, X.; Hang, Z.; Jia, Y.; Wang, S. Synthesis of g-C_3N_4/CeO_2 Nanocomposites with Improved Catalytic Activity on the Thermal Decomposition of Ammonium Perchlorate. *Appl. Surf. Sci.* **2015**, *356*, 447–453. [CrossRef]
461. Chen, G.; Bian, S.; Guo, C.-Y.; Wu, X. Insight into the Z-Scheme Heterostructure WO_3/g-C_3N_4 for Enhanced Photocatalytic Degradation of Methyl Orange. *Mater. Lett.* **2019**, *236*, 596–599. [CrossRef]
462. Guan, R.; Li, J.; Zhang, J.; Zhao, Z.; Wang, D.; Zhai, H.; Sun, D. Photocatalytic Performance and Mechanistic Research of ZnO/g-C_3N_4 on Degradation of Methyl Orange. *ACS omega* **2019**, *4*, 20742–20747. [CrossRef]
463. Si, Y.; Zhang, X.; Liang, T.; Xu, X.; Qiu, L.; Li, P.; Duo, S. Facile In-Situ Synthesis of 2D/3D g-C_3N_4/Cu_2O Heterojunction for High-Performance Photocatalytic Dye Degradation. *Mater. Res. Express* **2020**, *7*, 15524. [CrossRef]
464. Tian, Q.; Shen, X.; Wang, Z.; Zhu, B.; Osotsi, M.I.; Xie, X.; Jin, Y.; Chen, Z.; Zhang, L. Growth of Cu_2O Spherical Superstructures on g-C_3N_4 as Efficient Visible-Light-Driven p–n Heterojunction Photocatalysts for Degrading Various Organic Pollutants. *J. Nanosci. Nanotechnol.* **2018**, *18*, 7355–7363. [CrossRef]
465. Rabé, K.; Liu, L.; Nahyoon, N.A.; Zhang, Y.; Idris, A.M. Enhanced Rhodamine B and Coking Wastewater Degradation and Simultaneous Electricity Generation via Anodic g-C_3N_4/Fe0 (1%)/TiO_2 and Cathodic WO_3 in Photocatalytic Fuel Cell System under Visible Light Irradiation. *Electrochim. Acta* **2019**, *298*, 430–439. [CrossRef]
466. Yu, T.; Liu, L.; Yang, F. Heterojunction between Anodic TiO_2/g-C_3N_4 and Cathodic WO_3/W Nano-Catalysts for Coupled Pollutant Removal in a Self-Biased System. *Chin. J. Catal.* **2017**, *38*, 270–277. [CrossRef]
467. Tripathi, A.; Narayanan, S. Impact of TiO_2 and TiO_2/g-C_3N_4 Nanocomposite to Treat Industrial Wastewater. *Environ. Nanotechnology, Monit. Manag.* **2018**, *10*, 280–291. [CrossRef]
468. Pawar, R.C.; Son, Y.; Kim, J.; Ahn, S.H.; Lee, C.S. Integration of ZnO with g-C_3N_4 Structures in Core–Shell Approach via Sintering Process for Rapid Detoxification of Water under Visible Irradiation. *Curr. Appl. Phys.* **2016**, *16*, 101–108. [CrossRef]
469. Zhang, S.; Su, C.; Ren, H.; Li, M.; Zhu, L.; Ge, S.; Wang, M.; Zhang, Z.; Li, L.; Cao, X. In-Situ Fabrication of g-C_3N_4/ZnO Nanocomposites for Photocatalytic Degradation of Methylene Blue: Synthesis Procedure Does Matter. *Nanomaterials* **2019**, *9*, 215. [CrossRef]
470. Li, X.; Li, M.; Yang, J.; Li, X.; Hu, T.; Wang, J.; Sui, Y.; Wu, X.; Kong, L. Synergistic Effect of Efficient Adsorption g-C_3N_4/ZnO Composite for Photocatalytic Property. *J. Phys. Chem. Solids* **2014**, *75*, 441–446. [CrossRef]
471. Kumaresan, N.; Sinthiya, M.M.A.; Sarathbavan, M.; Ramamurthi, K.; Sethuraman, K.; Babu, R.R. Synergetic Effect of g-C_3N_4/ZnO Binary Nanocomposites Heterojunction on Improving Charge Carrier Separation through 2D/1D Nanostructures for Effective Photocatalytic Activity under the Sunlight Irradiation. *Sep. Purif. Technol.* **2020**, *244*, 116356. [CrossRef]
472. Liu, L.; Luo, X.; Li, Y.; Xu, F.; Gao, Z.; Zhang, X.; Song, Y.; Xu, H.; Li, H. Facile Synthesis of Few-Layer g-C_3N_4/ZnO Composite Photocatalyst for Enhancing Visible Light Photocatalytic Performance of Pollutants Removal. *Colloids Surfaces A Physicochem. Eng. Asp.* **2018**, *537*, 516–523. [CrossRef]
473. Chen, Q.; Hou, H.; Zhang, D.; Hu, S.; Min, T.; Liu, B.; Yang, C.; Pu, W.; Hu, J.; Yang, J. Enhanced Visible-Light Driven Photocatalytic Activity of Hybrid ZnO/g-C_3N_4 by High Performance Ball Milling. *J. Photochem. Photobiol. A Chem.* **2018**, *350*, 1–9. [CrossRef]

474. Tang, Q.; Meng, X.; Wang, Z.; Zhou, J.; Tang, H. One-Step Electrospinning Synthesis of TiO_2/g-C_3N_4 Nanofibers with Enhanced Photocatalytic Properties. *Appl. Surf. Sci.* **2018**, *430*, 253–262. [CrossRef]
475. Liu, H.; Zhang, Z.-G.; He, H.-W.; Wang, X.-X.; Zhang, J.; Zhang, Q.-Q.; Tong, Y.-F.; Liu, H.-L.; Ramakrishna, S.; Yan, S.-Y. One-Step Synthesis Heterostructured g-C_3N_4/TiO_2 Composite for Rapid Degradation of Pollutants in Utilizing Visible Light. *Nanomaterials* **2018**, *8*, 842. [CrossRef] [PubMed]
476. Li, X.; Xiong, J.; Xu, Y.; Feng, Z.; Huang, J. Defect-Assisted Surface Modification Enhances the Visible Light Photocatalytic Performance of g-C_3N_4@ C-TiO_2 Direct Z-Scheme Heterojunctions. *Chin. J. Catal.* **2019**, *40*, 424–433. [CrossRef]
477. Xia, Y.; Xu, L.; Peng, J.; Han, J.; Guo, S.; Zhang, L.; Han, Z.; Komarneni, S. TiO_2@ g-C_3N_4 Core/Shell Spheres with Uniform Mesoporous Structures for High Performance Visible-Light Photocatalytic Application. *Ceram. Int.* **2019**, *45*, 18844–18851. [CrossRef]
478. Wang, X.; Yang, W.; Li, F.; Xue, Y.; Liu, R.; Hao, Y. In Situ Microwave-Assisted Synthesis of Porous N-TiO_2/g-C_3N_4 Heterojunctions with Enhanced Visible-Light Photocatalytic Properties. *Ind. Eng. Chem. Res.* **2013**, *52*, 17140–17150. [CrossRef]
479. Song, G.; Chu, Z.; Jin, W.; Sun, H. Enhanced Performance of g-C_3N_4/TiO_2 Photocatalysts for Degradation of Organic Pollutants under Visible Light. *Chin. J. Chem. Eng.* **2015**, *23*, 1326–1334. [CrossRef]
480. Ma, L.; Wang, G.; Jiang, C.; Bao, H.; Xu, Q. Synthesis of Core-Shell TiO_2@ g-C_3N_4 Hollow Microspheres for Efficient Photocatalytic Degradation of Rhodamine B under Visible Light. *Appl. Surf. Sci.* **2018**, *430*, 263–272. [CrossRef]
481. Li, K.; Gao, S.; Wang, Q.; Xu, H.; Wang, Z.; Huang, B.; Dai, Y.; Lu, J. In-Situ-Reduced Synthesis of Ti^{3+} Self-Doped TiO_2/g-C_3N_4 Heterojunctions with High Photocatalytic Performance under LED Light Irradiation. *ACS Appl. Mater. Interfaces* **2015**, *7*, 9023–9030. [CrossRef] [PubMed]
482. Yan, X.; Gao, Q.; Qin, J.; Hui, X.; Ye, Z.; Li, J.; Ma, Z. A Facile Method for Fabricating TiO_2/g-C_3N_4 Hollow Nanotube Heterojunction and Its Visible Light Photocatalytic Performance. *Mater. Lett.* **2018**, *217*, 1–4. [CrossRef]
483. Christoforidis, K.C. g-C_3N_4/Ag_3PO_4 Based Binary and Ternary Heterojunction for Improved Photocatalytic Removal of Organic Pollutants. *Int. J. Environ. Anal. Chem.* published on line only. **2021**. [CrossRef]
484. Dutta, D.P.; Dagar, D. Efficient Selective Sorption of Cationic Organic Pollutant from Water and Its Photocatalytic Degradation by $AlVO_4$/g-C_3N_4 Nanocomposite. *J. Nanosci. Nanotechnol.* **2020**, *20*, 2179–2194. [CrossRef]
485. Hong, Y.; Jiang, Y.; Li, C.; Fan, W.; Yan, X.; Yan, M.; Shi, W. In-Situ Synthesis of Direct Solid-State Z-Scheme V_2O_5/g-C_3N_4 Heterojunctions with Enhanced Visible Light Efficiency in Photocatalytic Degradation of Pollutants. *Appl. Catal. B Environ.* **2016**, *180*, 663–673. [CrossRef]
486. Meng, J.; Wang, X.; Liu, Y.; Ren, M.; Zhang, X.; Ding, X.; Guo, Y.; Yang, Y. Acid-Induced Molecule Self-Assembly Synthesis of Z-Scheme WO_3/g-C_3N_4 Heterojunctions for Robust Photocatalysis against Phenolic Pollutants. *Chem. Eng. J.* **2021**, *403*, 126354. [CrossRef]
487. Liang, J.; Li, Y.; Zhang, J.; Li, C.; Yang, X.; Chen, X.; Wang, F.; Chen, C. Crystalline Phase Engineering in WO_3/g-C_3N_4 Composites for Improved Photocatalytic Performance under Visible Light. *Mater. Res. Express* **2020**, *7*, 65503. [CrossRef]
488. He, R.; Zhou, J.; Fu, H.; Zhang, S.; Jiang, C. Room-Temperature in Situ Fabrication of Bi_2O_3/g-C_3N_4 Direct Z-Scheme Photocatalyst with Enhanced Photocatalytic Activity. *Appl. Surf. Sci.* **2018**, *430*, 273–282. [CrossRef]
489. Chen, D.; Wu, S.; Fang, J.; Lu, S.; Zhou, G.; Feng, W.; Yang, F.; Chen, Y.; Fang, Z. A Nanosheet-like α-Bi_2O_3/g-C_3N_4 Heterostructure Modified by Plasmonic Metallic Bi and Oxygen Vacancies with High Photodegradation Activity of Organic Pollutants. *Sep. Purif. Technol.* **2018**, *193*, 232–241. [CrossRef]
490. Fan, G.; Ma, Z.; Li, X.; Deng, L. Coupling of Bi_2O_3 Nanoparticles with g-C_3N_4 for Enhanced Photocatalytic Degradation of Methylene Blue. *Ceram. Int.* **2021**, *47*, 5758–5766. [CrossRef]
491. Ghosh, U.; Pal, A. Fabrication of a Novel Bi_2O_3 Nanoparticle Impregnated Nitrogen Vacant 2D g-C_3N_4 Nanosheet Z Scheme Photocatalyst for Improved Degradation of Methylene Blue Dye under LED Light Illumination. *Appl. Surf. Sci.* **2020**, *507*, 144965. [CrossRef]
492. She, X.; Xu, H.; Wang, H.; Xia, J.; Song, Y.; Yan, J.; Xu, Y.; Zhang, Q.; Du, D.; Li, H. Controllable Synthesis of CeO $_2$/g-C_3N_4 Composites and Their Applications in the Environment. *Dalt. Trans.* **2015**, *44*, 7021–7031. [CrossRef]
493. Ghalkhani, M.; Charkhan, H.; Sabbaghan, M. Synthesis and Application of a Powerful Heterogeneous Photo-Fenton Catalyst Based on RGO/g-C_3N_4/Fe_3O_4/TiO_2 Nano-Composite for the Removal of Sewage Contaminants. *J. Electrochem. Soc.* **2020**, *167*, 67515. [CrossRef]
494. Vattikuti, S.V.P.; Reddy, P.A.K.; Shim, J.; Byon, C. Visible-Light-Driven Photocatalytic Activity of SnO_2–ZnO Quantum Dots Anchored on g-C_3N_4 Nanosheets for Photocatalytic Pollutant Degradation and H_2 Production. *ACS omega* **2018**, *3*, 7587–7602. [CrossRef] [PubMed]
495. Danish, M.; Muneer, M. Novel ZnSQDs-SnO_2/g-C_3N_4 Nanocomposite with Enhanced Photocatalytic Performance for the Degradation of Different Organic Pollutants in Aqueous Suspension under Visible Light. *J. Phys. Chem. Solids* **2021**, *149*, 109785. [CrossRef]
496. Zhang, Z.; Wu, J.; Liu, D. Co_3O_4/g-C_3N_4 Hybrids for Gas-Phase Hg0 Removal at Low Temperature. *Processes* **2019**, *7*, 279. [CrossRef]
497. Zhao, X.; Lu, Z.; Ji, R.; Zhang, M.; Yi, C.; Yan, Y. Biomass Carbon Modified Z-Scheme g-C_3N_4/Co_3O_4 Heterojunction with Enhanced Visible-Light Photocatalytic Activity. *Catal. Commun.* **2018**, *112*, 49–52. [CrossRef]

498. Yuan, X.; Duan, S.; Wu, G.; Sun, L.; Cao, G.; Li, D.; Xu, H.; Li, Q.; Xia, D. Enhanced Catalytic Ozonation Performance of Highly Stabilized Mesoporous ZnO Doped g-C_3N_4 Composite for Efficient Water Decontamination. *Appl. Catal. A Gen.* **2018**, *551*, 129–138. [CrossRef]
499. Zuo, S.; Chen, Y.; Liu, W.; Yao, C.; Li, X.; Li, Z.; Ni, C.; Liu, X. A Facile and Novel Construction of Attapulgite/Cu_2O/Cu/g-C_3N_4 with Enhanced Photocatalytic Activity for Antibiotic Degradation. *Ceram. Int.* **2017**, *43*, 3324–3329. [CrossRef]
500. Raha, S.; Ahmaruzzaman, M. Enhanced Performance of a Novel Superparamagnetic g-C_3N_4/NiO/ZnO/Fe_3O_4 Nanohybrid Photocatalyst for Removal of Esomeprazole: Effects of Reaction Parameters, Co-Existing Substances and Water Matrices. *Chem. Eng. J.* **2020**, *395*, 124969. [CrossRef]
501. Huo, R.; Yang, X.-L.; Yang, J.-Y.; Yang, S.-Y.; Xu, Y.-H. Self-Assembly Synthesis of $BiVO_4$/Polydopamine/g-C_3N_4 with Enhanced Visible Light Photocatalytic Performance. Mater. *Res. Bull.* **2018**, *98*, 225–230. [CrossRef]
502. Ding, J.; Lu, S.; Shen, L.; Yan, R.; Zhang, Y.; Zhang, H. Enhanced Photocatalytic Reduction for the Dechlorination of 2-Chlorodibenzo-p-Dioxin by High-Performance g-C_3N_4/NiO Heterojunction Composites under Ultraviolet-Visible Light Illumination. *J. Hazard. Mater.* **2020**, *384*, 121255. [CrossRef]
503. Zhao, W.; Yang, X.; Liu, C.; Qian, X.; Wen, Y.; Yang, Q.; Sun, T.; Chang, W.; Liu, X.; Chen, Z. Facile Construction of All-Solid-State Z-Scheme g-C_3N_4/TiO_2 Thin Film for the Efficient Visible-Light Degradation of Organic Pollutant. *Nanomaterials* **2020**, *10*, 600. [CrossRef]
504. Huang, J.; Li, D.; Li, R.; Chen, P.; Zhang, Q.; Liu, H.; Lv, W.; Liu, G.; Feng, Y. One-Step Synthesis of Phosphorus/Oxygen Co-Doped g-C_3N_4/Anatase TiO_2 Z-Scheme Photocatalyst for Significantly Enhanced Visible-Light Photocatalysis Degradation of Enrofloxacin. *J. Hazard. Mater.* **2020**, *386*, 121634. [CrossRef]
505. Hao, J.; Zhang, S.; Ren, F.; Wang, Z.; Lei, J.; Wang, X.; Cheng, T.; Li, L. Synthesis of TiO_2@ g-C_3N_4 Core-Shell Nanorod Arrays with Z-Scheme Enhanced Photocatalytic Activity under Visible Light. *J. Colloid Interface Sci.* **2017**, *508*, 419–425. [CrossRef]
506. Karpuraranjith, M.; Chen, Y.; Rajaboopathi, S.; Ramadoss, M.; Srinivas, K.; Yang, D.; Wang, B. Three-Dimensional Porous MoS2 Nanobox Embedded g-C_3N_4@ TiO_2 Architecture for Highly Efficient Photocatalytic Degradation of Organic Pollutant. *J. Colloid Interface Sci.* **2022**, *605*, 613–623. [CrossRef] [PubMed]
507. Zhou, Q.; Zhao, D.; Sun, Y.; Sheng, X.; Zhao, J.; Guo, J.; Zhou, B. G–C_3N_4–and Polyaniline-Co-Modified TiO_2 Nanotube Arrays for Significantly Enhanced Photocatalytic Degradation of Tetrabromobisphenol A under Visible Light. *Chemosphere* **2020**, *252*, 126468. [CrossRef] [PubMed]
508. Wang, Y.; Rao, L.; Wang, P.; Shi, Z.; Zhang, L. Photocatalytic Activity of N-TiO_2/O-Doped N Vacancy g-C_3N_4 and the Intermediates Toxicity Evaluation under Tetracycline Hydrochloride and Cr (VI) Coexistence Environment. *Appl. Catal. B Environ.* **2020**, *262*, 118308. [CrossRef]
509. Wang, W.; Fang, J.; Shao, S.; Lai, M.; Lu, C. Compact and Uniform TiO_2@ g-C_3N_4 Core-Shell Quantum Heterojunction for Photocatalytic Degradation of Tetracycline Antibiotics. *Appl. Catal. B Environ.* **2017**, *217*, 57–64. [CrossRef]
510. Du, X.; Bai, X.; Xu, L.; Yang, L.; Jin, P. Visible-Light Activation of Persulfate by TiO_2/g-C_3N_4 Photocatalyst toward Efficient Degradation of Micropollutants. *Chem. Eng. J.* **2020**, *384*, 123245. [CrossRef]
511. Yang, Z.; Yan, J.; Lian, J.; Xu, H.; She, X.; Li, H. g-C_3N_4/TiO_2 Nanocomposites for Degradation of Ciprofloxacin under Visible Light Irradiation. *ChemistrySelect* **2016**, *1*, 5679–5685. [CrossRef]
512. Ngullie, R.C.; Alaswad, S.O.; Bhuvaneswari, K.; Shanmugam, P.; Pazhanivel, T.; Arunachalam, P. Synthesis and Characterization of Efficient ZnO/g-C_3N_4 Nanocomposites Photocatalyst for Photocatalytic Degradation of Methylene Blue. *Coatings* **2020**, *10*, 500. [CrossRef]
513. Li, N.; Tian, Y.; Zhao, J.; Zhang, J.; Zuo, W.; Kong, L.; Cui, H. Z-Scheme 2D/3D g-C_3N_4@ ZnO with Enhanced Photocatalytic Activity for Cephalexin Oxidation under Solar Light. *Chem. Eng. J.* **2018**, *352*, 412–422. [CrossRef]
514. Prabhu, S.; Pudukudy, M.; Harish, S.; Navaneethan, M.; Sohila, S.; Murugesan, K.; Ramesh, R. Facile Construction of Djembe-like ZnO and Its Composite with g-C_3N_4 as a Visible-Light-Driven Heterojunction Photocatalyst for the Degradation of Organic Dyes. Mater. Sci. Semicond. *Process.* **2020**, *106*, 104754. [CrossRef]
515. Pan, T.; Chen, D.; Xu, W.; Fang, J.; Wu, S.; Liu, Z.; Wu, K.; Fang, Z. Anionic Polyacrylamide-Assisted Construction of Thin 2D-2D WO_3/g-C_3N_4 Step-Scheme Heterojunction for Enhanced Tetracycline Degradation under Visible Light Irradiation. *J. Hazard. Mater.* **2020**, *393*, 122366. [CrossRef] [PubMed]
516. Priya, A.; Senthil, R.A.; Selvi, A.; Arunachalam, P.; Kumar, C.K.S.; Madhavan, J.; Boddula, R.; Pothu, R.; Al-Mayouf, A.M. A Study of Photocatalytic and Photoelectrochemical Activity of As-Synthesized WO_3/g-C_3N_4 Composite Photocatalysts for AO7 Degradation. *Mater. Sci. Energy Technol.* **2020**, *3*, 43–50. [CrossRef]
517. Navarro-Aguilar, A.I.; Obregón, S.; Sanchez-Martinez, D.; Hernández-Uresti, D.B. An Efficient and Stable WO_3/g-C_3N_4 Photocatalyst for Ciprofloxacin and Orange G Degradation. *J. Photochem. Photobiol. A Chem.* **2019**, *384*, 112010. [CrossRef]
518. Manikandan, V.S.; Harish, S.; Archana, J.; Navaneethan, M. Fabrication of Novel Hybrid Z-Scheme WO_3@g-C_3N_4@ MWCNT Nanostructure for Photocatalytic Degradation of Tetracycline and the Evaluation of Antimicrobial Activity. *Chemosphere* **2021**, *287*, 132050. [CrossRef] [PubMed]
519. Zhou, S.; Wang, Y.; Zhou, K.; Ba, D.; Ao, Y.; Wang, P. In-Situ Construction of Z-Scheme g-C_3N_4/WO_3 Composite with Enhanced Visible-Light Responsive Performance for Nitenpyram Degradation. *Chin. Chem. Lett.* **2021**, *32*, 2179–2182. [CrossRef]
520. Zhang, L.; Wang, G.; Xiong, Z.; Tang, H.; Jiang, C. Fabrication of Flower-like Direct Z-Scheme β-Bi_2O_3/g-C_3N_4 Photocatalyst with Enhanced Visible Light Photoactivity for Rhodamine B Degradation. *Appl. Surf. Sci.* **2018**, *436*, 162–171. [CrossRef]

521. Hong, Y.; Li, C.; Yin, B.; Li, D.; Zhang, Z.; Mao, B.; Fan, W.; Gu, W.; Shi, W. Promoting Visible-Light-Induced Photocatalytic Degradation of Tetracycline by an Efficient and Stable Beta-Bi_2O_3@ g-C_3N_4 Core/Shell Nanocomposite. *Chem. Eng. J.* **2018**, *338*, 137–146. [CrossRef]
522. Liu, W.; Zhou, J.; Hu, Z. Nano-Sized g-C_3N_4 Thin Layer@ CeO_2 Sphere Core-Shell Photocatalyst Combined with H_2O_2 to Degrade Doxycycline in Water under Visible Light Irradiation. Sep. Purif. *Technol.* **2019**, *227*, 115665. [CrossRef]
523. Liu, W.; Zhou, J.; Yao, J. Shuttle-like CeO_2/g-C_3N_4 Composite Combined with Persulfate for the Enhanced Photocatalytic Degradation of Norfloxacin under Visible Light. *Ecotoxicol. Environ. Saf.* **2020**, *190*, 110062. [CrossRef] [PubMed]
524. Huang, Z.; Li, L.; Li, Z.; Li, H.; Wu, J. Synthesis of Novel Kaolin-Supported g-C_3N_4/CeO_2 Composites with Enhanced Photocatalytic Removal of Ciprofloxacin. *Materials.* **2020**, *13*, 3811. [CrossRef] [PubMed]
525. Wang, S.; Long, J.; Jiang, T.; Shao, L.; Li, D.; Xie, X.; Xu, F. Magnetic Fe_3O_4/CeO_2/g-C_3N_4 Composites with a Visible-Light Response as a High Efficiency Fenton Photocatalyst to Synergistically Degrade Tetracycline. *Sep. Purif. Technol.* **2021**, *278*, 119609. [CrossRef]
526. Han, C.; Ge, L.; Chen, C.; Li, Y.; Xiao, X.; Zhang, Y.; Guo, L. Novel Visible Light Induced Co_3O_4-g-C_3N_4 Heterojunction Photocatalysts for Efficient Degradation of Methyl Orange. *Appl. Catal. B Environ.* **2014**, *147*, 546–553. [CrossRef]
527. Chen, H.-Y.; Qiu, L.-G.; Xiao, J.-D.; Ye, S.; Jiang, X.; Yuan, Y.-P. Inorganic–Organic Hybrid NiO–g-C_3N_4 Photocatalyst for Efficient Methylene Blue Degradation Using Visible Light. *RSC Adv.* **2014**, *4*, 22491–22496. [CrossRef]
528. Balasubramanian, P.; Annalakshmi, M.; Chen, S.-M.; Chen, T.-W. Sonochemical Synthesis of Molybdenum Oxide (MoO_3) Microspheres Anchored Graphitic Carbon Nitride (g-C_3N_4) Ultrathin Sheets for Enhanced Electrochemical Sensing of Furazolidone. *Ultrason. Sonochem.* **2019**, *50*, 96–104. [CrossRef] [PubMed]
529. Adhikari, S.; Kim, D.-H. Heterojunction C_3N_4/MoO_3 Microcomposite for Highly Efficient Photocatalytic Oxidation of Rhodamine B. *Appl. Surf. Sci.* **2020**, *511*, 145595. [CrossRef]
530. Xue, S.; Wu, C.; Pu, S.; Hou, Y.; Tong, T.; Yang, G.; Qin, Z.; Wang, Z.; Bao, J. Direct Z-Scheme Charge Transfer in Heterostructured MoO_3/g-C_3N_4 Photocatalysts and the Generation of Active Radicals in Photocatalytic Dye Degradations. *Environ. Pollut.* **2019**, *250*, 338–345. [CrossRef]
531. Liu, L.; Huang, J.; Yu, H.; Wan, J.; Liu, L.; Yi, K.; Zhang, W.; Zhang, C. Construction of MoO_3 Nanopaticles/g-C_3N_4 Nanosheets 0D/2D Heterojuntion Photocatalysts for Enhanced Photocatalytic Degradation of Antibiotic Pollutant. *Chemosphere* **2021**, *282*, 131049. [CrossRef] [PubMed]
532. Adorna Jr, J.; Annadurai, T.; Bui, T.A.N.; Tran, H.L.; Lin, L.-Y.; Doong, R.-A. Indirect Z-Scheme Nitrogen-Doped Carbon Dot Decorated Bi_2MoO_6/g-C_3N_4 Photocatalyst for Enhanced Visible-Light-Driven Degradation of Ciprofloxacin. *Chem. Eng. J.* **2021**, *422*, 130103.
533. Van Pham, V.; Mai, D.-Q.; Bui, D.-P.; Van Man, T.; Zhu, B.; Zhang, L.; Sangkaworn, J.; Tantirungrotechai, J.; Reutrakul, V.; Cao, T.M. Emerging 2D/0D g-C_3N_4/SnO_2 S-Scheme Photocatalyst: New Generation Architectural Structure of Heterojunctions toward Visible-Light-Driven NO Degradation. *Environ. Pollut.* **2021**, *286*, 117510. [CrossRef]
534. Shi, Y.; Yang, Z.; Liu, Y.; Yu, J.; Wang, F.; Tong, J.; Su, B.; Wang, Q. Fabricating a g-C_3N_4/CuO_x Heterostructure with Tunable Valence Transition for Enhanced Photocatalytic Activity. *RSC Adv.* **2016**, *6*, 39774–39783. [CrossRef]
535. Yuan, X.; Zhou, C.; Jing, Q.; Tang, Q.; Mu, Y.; Du, A. Facile Synthesis of g-C_3N_4 Nanosheets/ZnO Nanocomposites with Enhanced Photocatalytic Activity in Reduction of Aqueous Chromium (VI) under Visible Light. *Nanomaterials* **2016**, *6*, 173. [CrossRef]
536. Sundaram, I.M.; Kalimuthu, S.; Ponniah, G. Highly Active ZnO Modified g-C_3N_4 Nanocomposite for Dye Degradation under UV and Visible Light with Enhanced Stability and Antimicrobial Activity. *Compos. Commun.* **2017**, *5*, 64–71. [CrossRef]
537. Vattikuti, S.V.P.; Byon, C. Hydrothermally Synthesized Ternary Heterostructured MoS_2/Al_2O_3/g-C_3N_4 Photocatalyst. *Mater. Res. Bull.* **2017**, *96*, 233–245. [CrossRef]
538. Wang, J.; Xia, Y.; Zhao, H.; Wang, G.; Xiang, L.; Xu, J.; Komarneni, S. Oxygen Defects-Mediated Z-Scheme Charge Separation in g-C_3N_4/ZnO Photocatalysts for Enhanced Visible-Light Degradation of 4-Chlorophenol and Hydrogen Evolution. *Appl. Catal. B Environ.* **2017**, *206*, 406–416. [CrossRef]
539. Zhou, Y.; Zeng, F.; Sun, C.; Wu, J.; Xie, Y.; Zhang, F.; Rao, S.; Wang, F.; Zhang, J.; Zhao, J. Gd_2O_3 Nanoparticles Modified g-C_3N_4 with Enhanced Photocatalysis Activity for the Degradation of Organic Pollutants1. *J. Rare Earths* **2021**, *39*, 1353–1361. [CrossRef]
540. Chen, D.; Xie, Z.; Zeng, Y.; Lv, W.; Zhang, Q.; Wang, F.; Liu, G.; Liu, H. Accelerated Photocatalytic Degradation of Quinolone Antibiotics over Z-Scheme MoO3/g-C_3N_4 Heterostructure by Peroxydisulfate under Visible Light Irradiation: Mechanism; Kinetic; and Products. *J. Taiwan Inst. Chem. Eng.* **2019**, *104*, 250–259. [CrossRef]
541. Devi KR, S.; Mathew, S.; Rajan, R.; Georgekutty, J.; Pinheiro, D.; Ananthapadmanabhan, U.; Sundararajan, M. Synthesis and Characterization of CeO_2/Bi_2O_3/GC_3N_4 Ternary Z-scheme Nanocomposite. *Int. J. Appl. Ceram. Technol.* **2020**, *17*, 2346–2356. [CrossRef]
542. Bajiri, M.A.; Hezam, A.; Namratha, K.; Viswanath, R.; Drmosh, Q.A.; Naik, H.S.B.; Byrappa, K. CuO/ZnO/g-C_3N_4 Heterostructures as Efficient Visible Light-Driven Photocatalysts. *J. Environ. Chem. Eng.* **2019**, *7*, 103412. [CrossRef]
543. Raha, S.; Ahmaruzzaman, M. Facile Fabrication of g-C_3N_4 Supported Fe_3O_4 Nanoparticles/ZnO Nanorods: A Superlative Visible Light Responsive Architecture for Express Degradation of Pantoprazole. *Chem. Eng. J.* **2020**, *387*, 123766. [CrossRef]
544. Raza, A.; Shen, H.; Haidry, A.A.; Cui, S. Hydrothermal Synthesis of Fe_3O_4/TiO_2/g-C_3N_4: Advanced Photocatalytic Application. *Appl. Surf. Sci.* **2019**, *488*, 887–895. [CrossRef]

545. Jiang, D.; Yu, H.; Yu, H. Modified g-C_3N_4/TiO_2 Nanosheets/ZnO Ternary Facet Coupled Heterojunction for Photocatalytic Degradation of p-Toluenesulfonic Acid (p-TSA) under Visible Light. *Phys. E Low-Dimens. Syst. Nanostruct.* **2017**, *85*, 1–6.
546. Tahir, M.B.; Sagir, M.; Shahzad, K. Removal of Acetylsalicylate and Methyl-Theobromine from Aqueous Environment Using Nano-Photocatalyst WO_3-TiO_2@g-C_3N_4 Composite. *J. Hazard. Mater.* **2019**, *363*, 205–213. [CrossRef] [PubMed]
547. Yu, B.; Meng, F.; Khan, M.W.; Qin, R.; Liu, X. Synthesis of Hollow TiO_2@ g-C_3N_4/Co_3O_4 Core-Shell Microspheres for Effective Photooxidation Degradation of Tetracycline and MO. *Ceram. Int.* **2020**, *46*, 13133–13143. [CrossRef]
548. Zhang, Y.; Lu, J.; Hoffmann, M.R.; Wang, Q.; Cong, Y.; Wang, Q.; Jin, H. Synthesis of g-C_3N_4/Bi_2O_3/TiO_2 Composite Nanotubes: Enhanced Activity under Visible Light Irradiation and Improved Photoelectrochemical Activity. *RSC Adv.* **2015**, *5*, 48983–48991. [CrossRef]
549. Wang, Y.; Zhang, R.; Zhang, Z.; Cao, J.; Ma, T. Host–Guest Recognition on 2D Graphitic Carbon Nitride for Nanosensing. Adv. Mater. *Interfaces* **2019**, *6*, 1901429.
550. Liu, J.-W.; Luo, Y.; Wang, Y.-M.; Duan, L.-Y.; Jiang, J.-H.; Yu, R.-Q. Graphitic Carbon Nitride Nanosheets-Based Ratiometric Fluorescent Probe for Highly Sensitive Detection of H_2O_2 and Glucose. *ACS Appl. Mater. Interfaces* **2016**, *8*, 33439–33445. [CrossRef]
551. Kundu, M.K.; Sadhukhan, M.; Barman, S. Ordered Assemblies of Silver Nanoparticles on Carbon Nitride Sheets and Their Application in the Non-Enzymatic Sensing of Hydrogen Peroxide and Glucose. *J. Mater. Chem. B* **2015**, *3*, 1289–1300. [CrossRef] [PubMed]
552. Jiang, T.; Jiang, G.; Huang, Q.; Zhou, H. High-Sensitive Detection of Dopamine Using Graphitic Carbon Nitride by Electrochemical Method. *Mater. Res. Bull.* **2016**, *74*, 271–277. [CrossRef]
553. Zuo, F.; Jin, L.; Fu, X.; Zhang, H.; Yuan, R.; Chen, S. An Electrochemiluminescent Sensor for Dopamine Detection Based on a Dual-Molecule Recognition Strategy and Polyaniline Quenching. *Sensors Actuators B Chem.* **2017**, *244*, 282–289. [CrossRef]
554. Zou, J.; Wu, S.; Liu, Y.; Sun, Y.; Cao, Y.; Hsu, J.-P.; Wee, A.T.S.; Jiang, J. An Ultra-Sensitive Electrochemical Sensor Based on 2D g-C_3N_4/CuO Nanocomposites for Dopamine Detection. *Carbon N. Y.* **2018**, *130*, 652–663. [CrossRef]
555. Rahman, N.; Yang, J.; Sohail, M.; Khan, R.; Iqbal, A.; Maouche, C.; Khan, A.A.; Husain, M.; Khattak, S.A.; Khan, S.N. Insight into Metallic Oxide Semiconductor (SnO_2, ZnO, CuO, α-Fe_2O_3, WO_3)-Carbon Nitride (g-C_3N_4) Heterojunction for Gas Sensing Application. *Sensors Actuators A Phys.* **2021**, *332*, 113128. [CrossRef]
556. Zhou, T.; Zhang, T. Recent Progress of Nanostructured Sensing Materials from 0D to 3D: Overview of Structure–Property-Application Relationship for Gas Sensors. *Small Methods* **2021**, *5*, 2100515. [CrossRef]
557. Li, P.-P.; Cao, Y.; Mao, C.-J.; Jin, B.-K.; Zhu, J.-J. TiO_2/g-C_3N_4/CdS Nanocomposite-Based Photoelectrochemical Biosensor for Ultrasensitive Evaluation of T4 Polynucleotide Kinase Activity. *Anal. Chem.* **2018**, *91*, 1563–1570. [CrossRef] [PubMed]
558. Li, X.; Zhu, L.; Zhou, Y.; Yin, H.; Ai, S. Enhanced Photoelectrochemical Method for Sensitive Detection of Protein Kinase A Activity Using TiO_2/g-C_3N_4, PAMAM Dendrimer, and Alkaline Phosphatase. *Anal. Chem.* **2017**, *89*, 2369–2376. [CrossRef]
559. Zhai, J.; Wang, T.; Wang, C.; Liu, D. UV-Light-Assisted Ethanol Sensing Characteristics of g-C_3N_4/ZnO Composites at Room Temperature. *Appl. Surf. Sci.* **2018**, *441*, 317–323. [CrossRef]
560. Li, X.; Li, Y.; Sun, G.; Luo, N.; Zhang, B.; Zhang, Z. Synthesis of a Flower-like g-C_3N_4/ZnO Hierarchical Structure with Improved CH4 Sensing Properties. *Nanomaterials* **2019**, *9*, 724. [CrossRef]
561. Wang, H.; Bai, J.; Dai, M.; Liu, K.; Liu, Y.; Zhou, L.; Liu, F.; Liu, F.; Gao, Y.; Yan, X. Visible Light Activated Excellent NO2 Sensing Based on 2D/2D ZnO/g-C_3N_4 Heterojunction Composites. *Sensors Actuators B Chem.* **2020**, *304*, 127287. [CrossRef]
562. Zeng, B.; Zhang, L.; Wan, X.; Song, H.; Lv, Y. Fabrication of α-Fe_2O_3/g-C_3N_4 Composites for Cataluminescence Sensing of H_2S. *Sensors Actuators B Chem.* **2015**, *211*, 370–376. [CrossRef]
563. Zhang, Y.; Liu, J.; Chu, X.; Liang, S.; Kong, L. Preparation of g–C_3N_4–SnO_2 Composites for Application as Acetic Acid Sensor. *J. Alloys Compd.* **2020**, *832*, 153355. [CrossRef]
564. Malik, R.; Tomer, V.K.; Chaudhary, V.; Dahiya, M.S.; Sharma, A.; Nehra, S.P.; Duhan, S.; Kailasam, K. An Excellent Humidity Sensor Based on In–SnO_2 Loaded Mesoporous Graphitic Carbon Nitride. *J. Mater. Chem. A* **2017**, *5*, 14134–14143. [CrossRef]
565. Sun, Y.; Jiang, J.; Liu, Y.; Wu, S.; Zou, J. A Facile One-Pot Preparation of Co_3O_4/g-C_3N_4 Heterojunctions with Excellent Electrocatalytic Activity for the Detection of Environmental Phenolic Hormones. *Appl. Surf. Sci.* **2018**, *430*, 362–370. [CrossRef]
566. Hassannezhad, M.; Hosseini, M.; Ganjali, M.R.; Arvand, M. A Graphitic Carbon Nitride (g-C_3N_4/Fe_3O_4) Nanocomposite: An Efficient Electrode Material for the Electrochemical Determination of Tramadol in Human Biological Fluids. *Anal. Methods* **2019**, *11*, 2064–2071. [CrossRef]
567. Karthika, A.; Suganthi, A.; Rajarajan, M. An In-Situ Synthesis of Novel V_2O_5/g-C_3N_4/PVA Nanocomposite for Enhanced Electrocatalytic Activity toward Sensitive and Selective Sensing of Folic Acid in Natural Samples. *Arab. J. Chem.* **2020**, *13*, 3639–3652. [CrossRef]
568. Selvarajan, S.; Suganthi, A.; Rajarajan, M. Fabrication of g-C_3N_4/NiO Heterostructured Nanocomposite Modified Glassy Carbon Electrode for Quercetin Biosensor. *Ultrason. Sonochem.* **2018**, *41*, 651–660. [CrossRef]
569. Wang, L.; Zhao, F.; Han, Q.; Hu, C.; Lv, L.; Chen, N.; Qu, L. Spontaneous Formation of Cu_2O–g-C_3N_4 Core–Shell Nanowires for Photocurrent and Humidity Responses. *Nanoscale* **2015**, *7*, 9694–9702. [CrossRef] [PubMed]
570. Liu, Y.; Jiang, J.; Sun, Y.; Wu, S.; Cao, Y.; Gong, W.; Zou, J. NiO and Co_3O_4 Co-Doped g-C_3N_4 Nanocomposites with Excellent Photoelectrochemical Properties under Visible Light for Detection of Tetrabromobisphenol-A. *RSC Adv.* **2017**, *7*, 36015–36020. [CrossRef]

571. Pang, X.; Cui, C.; Su, M.; Wang, Y.; Wei, Q.; Tan, W. Construction of Self-Powered Cytosensing Device Based on ZnO Nanodisks@ g-C_3N_4 Quantum Dots and Application in the Detection of CCRF-CEM Cells. *Nano Energy* **2018**, *46*, 101–109. [CrossRef]
572. Han, Z.; Luo, M.; Weng, Q.; Chen, L.; Chen, J.; Li, C.; Zhou, Y.; Wang, L. ZnO Flower-Rod/g-C_3N_4-Gold Nanoparticle-Based Photoelectrochemical Aptasensor for Detection of Carcinoembryonic Antigen. *Anal. Bioanal. Chem.* **2018**, *410*, 6529–6538. [CrossRef]
573. Huan, Z.; Chang, J.; Zhou, J. Low-Temperature Fabrication of Macroporous Scaffolds through Foaming and Hydration of Tricalcium Silicate Paste and Their Bioactivity. *J. Mater. Sci.* **2010**, *45*, 961–968. [CrossRef]
574. He, X.; Bai, S.; Jiang, J.; Ong, W.-J.; Peng, J.; Xiong, Z.; Liao, G.; Zou, J.; Li, N. Oxygen Vacancy Mediated Step-Scheme Heterojunction of $WO_{2.9}$/g-C_3N_4 for Efficient Electrochemical Sensing of 4-Nitrophenol. *Chem. Eng. J. Adv.* **2021**, *8*, 100175. [CrossRef]
575. Wang, H.; Liang, D.; Xu, Y.; Liang, X.; Qiu, X.; Lin, Z. A Highly Efficient Photoelectrochemical Sensor for Detection of Chlorpyrifos Based on 2D/2D β-Bi_2O_3/g-C_3N_4 Heterojunctions. Environ. Sci. *Nano* **2021**, *8*, 773–783.
576. Pu, Y.; Wu, Y.; Yu, Z.; Lu, L.; Wang, X. Simultaneous Determination of Cd^{2+} and Pb^{2+} by an Electrochemical Sensor Based on Fe_3O_4/Bi_2O_3/C_3N_4 Nanocomposites. *Talanta Open* **2021**, *3*, 100024. [CrossRef]
577. Bilal, S.; Hassan, M.M.; ur Rehman, M.F.; Nasir, M.; Sami, A.J.; Hayat, A. An Insect Acetylcholinesterase Biosensor Utilizing WO_3/g-C_3N_4 Nanocomposite Modified Pencil Graphite Electrode for Phosmet Detection in Stored Grains. *Food Chem.* **2021**, *346*, 128894. [CrossRef]
578. Peng, B.; Zhang, Z.; Tang, L.; Ouyang, X.; Zhu, X.; Chen, L.; Fan, X.; Zhou, Z.; Wang, J. Self-Powered Photoelectrochemical Aptasensor for Oxytetracycline Cathodic Detection Based on a Dual Z-Scheme WO_3/g-C_3N_4/MnO_2 Photoanode. *Anal. Chem.* **2021**, *26*, 9129–9138. [CrossRef]
579. Mao, L.; Xue, X.; Xu, X.; Wen, W.; Chen, M.-M.; Zhang, X.; Wang, S. Heterostructured CuO-g-C_3N_4 Nanocomposites as a Highly Efficient Photocathode for Photoelectrochemical Aflatoxin B1 Sensing. *Sensors Actuators B Chem.* **2021**, *329*, 129146. [CrossRef]
580. Matsunaga, T.; Tomoda, R.; Nakajima, T.; Wake, H. Photoelectrochemical Sterilization of Microbial Cells by Semiconductor Powders. *FEMS Microbiol. Lett.* **1985**, *29*, 211–214. [CrossRef]
581. Song, J.; Wang, X.; Ma, J.; Wang, X.; Wang, J.; Xia, S.; Zhao, J. Removal of Microcystis Aeruginosa and Microcystin-LR Using a Graphitic-C_3N_4/TiO_2 Floating Photocatalyst under Visible Light Irradiation. *Chem. Eng. J.* **2018**, *348*, 380–388. [CrossRef]
582. Chen, X.; Wang, Q.; Tian, J.; Liu, Y.; Wang, Y.; Yang, C. A Study on the Photocatalytic Sterilization Performance and Mechanism of Fe-SnO_2/g-C_3N_4 Heterojunction Materials. *New J. Chem.* **2020**, *44*, 9456–9465. [CrossRef]
583. Pant, B.; Park, M.; Lee, J.H.; Kim, H.-Y.; Park, S.-J. Novel Magnetically Separable Silver-Iron Oxide Nanoparticles Decorated Graphitic Carbon Nitride Nano-Sheets: A Multifunctional Photocatalyst via One-Step Hydrothermal Process. *J. Colloid Interface Sci.* **2017**, *496*, 343–352. [CrossRef]
584. Liu, B.; Wu, Y.; Zhang, J.; Han, X.; Shi, H. Visible-Light-Driven g-C_3N_4/Cu_2O Heterostructures with Efficient Photocatalytic Activities for Tetracycline Degradation and Microbial Inactivation. *J. Photochem. Photobiol. A Chem.* **2019**, *378*, 1–8. [CrossRef]
585. Vignesh, S.; Suganthi, S.; Sundar, J.K.; Raj, V. Construction of α-Fe_2O_3/CeO_2 Decorated g-C_3N_4 Nanosheets for Magnetically Separable Efficient Photocatalytic Performance under Visible Light Exposure and Bacterial Disinfection. *Appl. Surf. Sci.* **2019**, *488*, 763–777. [CrossRef]
586. Shanmugam, V.; Jeyaperumal, K.S.; Mariappan, P.; Muppudathi, A.L. Fabrication of Novel g-C_3N_4 Based MoS_2 and Bi_2O_3 Nanorod Embedded Ternary Nanocomposites for Superior Photocatalytic Performance and Destruction of Bacteria. *New J. Chem.* **2020**, *44*, 13182–13194. [CrossRef]
587. Induja, M.; Sivaprakash, K.; Karthikeyan, S. Facile Green Synthesis and Antimicrobial Performance of Cu_2O Nanospheres Decorated g-C_3N_4 Nanocomposite. *Mater. Res. Bull.* **2019**, *112*, 331–335. [CrossRef]
588. Li, C.; Sun, Z.; Zhang, W.; Yu, C.; Zheng, S. Highly Efficient g-C_3N_4/TiO_2/Kaolinite Composite with Novel Three-Dimensional Structure and Enhanced Visible Light Responding Ability towards Ciprofloxacin and S. Aureus. *Appl. Catal. B Environ.* **2018**, *220*, 272–282. [CrossRef]
589. Zhang, Q.; Quan, X.; Wang, H.; Chen, S.; Su, Y.; Li, Z. Constructing a Visible-Light-Driven Photocatalytic Membrane by g-C_3N_4 Quantum Dots and TiO_2 Nanotube Array for Enhanced Water Treatment. *Sci. Rep.* **2017**, *7*, 1–7.
590. Xu, J.; Li, Y.; Zhou, X.; Li, Y.; Gao, Z.; Song, Y.; Schmuki, P. Graphitic C_3N_4-Sensitized TiO_2 Nanotube Layers: A Visible-Light Activated Efficient Metal-Free Antimicrobial Platform. *Chem. Eur. J.* **2016**, *22*, 3947–3951. [CrossRef]
591. Adhikari, S.P.; Awasthi, G.P.; Lee, J.; Park, C.H.; Kim, C.S. Synthesis, Characterization, Organic Compound Degradation Activity and Antimicrobial Performance of g-C_3N_4 Sheets Customized with Metal Nanoparticles-Decorated TiO_2 Nanofibers. *RSC Adv.* **2016**, *6*, 55079–55091. [CrossRef]
592. Jiang, G.; Cao, J.; Chen, M.; Zhang, X.; Dong, F. Photocatalytic NO Oxidation on N-Doped TiO_2/g-C_3N_4 Heterojunction: Enhanced Efficiency, Mechanism and Reaction Pathway. *Appl. Surf. Sci.* **2018**, *458*, 77–85. [CrossRef]
593. Vo, V.; Thi, X.D.N.; Jin, Y.-S.; Thi, G.L.; Nguyen, T.T.; Duong, T.Q.; Kim, S.-J. SnO_2 Nanosheets/g-C_3N_4 Composite with Improved Lithium Storage Capabilities. *Chem. Phys. Lett.* **2017**, *674*, 42–47. [CrossRef]
594. Montazeri, S.M.; Sadrnezhaad, S.K. Kinetics of Sulfur Removal from Tehran Vehicular Gasoline by g-C_3N_4/SnO_2 Nanocomposite. *ACS omega* **2019**, *4*, 13180–13188. [CrossRef]
595. Li, X.; Feng, Y.; Li, M.; Li, W.; Wei, H.; Song, D. Smart Hybrids of Zn_2GeO_4 Nanoparticles and Ultrathin g-C_3N_4 Layers: Synergistic Lithium Storage and Excellent Electrochemical Performance. *Adv. Funct. Mater.* **2015**, *25*, 6858–6866. [CrossRef]

596. Mohamed, H.S.H.; Wu, L.; Li, C.-F.; Hu, Z.-Y.; Liu, J.; Deng, Z.; Chen, L.-H.; Li, Y.; Su, B.-L. In-Situ Growing Mesoporous CuO/O-Doped g-C_3N_4 Nanospheres for Highly Enhanced Lithium Storage. *ACS Appl. Mater. Interfaces* **2019**, *11*, 32957–32968. [CrossRef] [PubMed]
597. Zhang, Y.; Chang, L.; Chang, X.; Chen, H.; Li, Y.; Fan, Y.; Wang, J.; Cui, D.; Xue, C. Combining In-Situ Sedimentation and Carbon-Assisted Synthesis of Co_3O_4/g-C_3N_4 Nanocomposites for Improved Supercapacitor Performance. *Diam. Relat. Mater.* **2021**, *111*, 108165. [CrossRef]
598. Bai, L.; Huang, H.; Zhang, S.; Hao, L.; Zhang, Z.; Li, H.; Sun, L.; Guo, L.; Huang, H.; Zhang, Y. Photocatalysis-Assisted Co_3O_4/g-C_3N_4 p–n Junction All-Solid-State Supercapacitors: A Bridge between Energy Storage and Photocatalysis. *Adv. Sci.* **2020**, *7*, 2001939. [CrossRef] [PubMed]
599. Kavil, J.; Anjana, P.M.; Joshy, D.; Babu, A.; Raj, G.; Periyat, P.; Rakhi, R.B. g-C_3N_4/CuO and g-C_3N_4/Co_3O_4 Nanohybrid Structures as Efficient Electrode Materials in Symmetric Supercapacitors. *RSC Adv.* **2019**, *9*, 38430–38437. [CrossRef]
600. Zhou, Y.; Sun, L.; Wu, D.; Li, X.; Li, J.; Huo, P.; Wang, H.; Yan, Y. Preparation of 3D Porous g-C_3N_4@ V_2O_5 Composite Electrode via Simple Calcination and Chemical Precipitation for Supercapacitors. *J. Alloys Compd.* **2020**, *817*, 152707. [CrossRef]
601. Klose, W.; Rincón, S. Adsorption and Reaction of NO on Activated Carbon in the Presence of Oxygen and Water Vapour. *Fuel* **2007**, *86*, 203–209. [CrossRef]
602. Ou, M.; Zhong, Q.; Zhang, S.; Yu, L. Ultrasound Assisted Synthesis of Heterogeneous g-C_3N_4/$BiVO_4$ Composites and Their Visible-Light-Induced Photocatalytic Oxidation of NO in Gas Phase. *J. Alloys Compd.* **2015**, *626*, 401–409. [CrossRef]
603. Hu, S.; Chen, X.; Li, Q.; Li, F.; Fan, Z.; Wang, H.; Wang, Y.; Zheng, B.; Wu, G. Fe^{3+} Doping Promoted N_2 Photofixation Ability of Honeycombed Graphitic Carbon Nitride: The Experimental and Density Functional Theory Simulation Analysis. *Appl. Catal. B Environ.* **2017**, *201*, 58–69. [CrossRef]
604. Kong, Y.; Lv, C.; Zhang, C.; Chen, G. Cyano Group Modified g-C_3N_4: Molten Salt Method Achievement and Promoted Photocatalytic Nitrogen Fixation Activity. *Appl. Surf. Sci.* **2020**, *515*, 146009. [CrossRef]
605. Hu, X.; Zhang, W.; Yong, Y.; Xu, Y.; Wang, X.; Yao, X. One-Step Synthesis of Iodine-Doped g-C_3N_4 with Enhanced Photocatalytic Nitrogen Fixation Performance. *Appl. Surf. Sci.* **2020**, *510*, 145413. [CrossRef]
606. Zhang, K.; Deng, L.; Huang, M.; Tu, H.; Kong, Z.; Liang, Z.; Shao, Y.; Hao, X.; Wu, Y. Energy Band Matching WO_3/B-Doped g-C_3N_4 Z-Scheme Photocatalyst to Fix Nitrogen Effectively. *Colloids Surfaces A Physicochem. Eng. Asp.* **2022**, *633*, 127830. [CrossRef]
607. Liu, X.; Han, X.; Liang, Z.; Xue, Y.; Zhou, Y.; Zhang, X.; Cui, H.; Tian, J. Phosphorous-Doped 1T-MoS_2 Decorated Nitrogen-Doped g-C_3N_4 Nanosheets for Enhanced Photocatalytic Nitrogen Fixation. *J. Colloid Interface Sci.* **2022**, *605*, 320–329. [CrossRef] [PubMed]
608. Tao, R.; Li, X.; Li, X.; Shao, C.; Liu, Y. TiO_2/$SrTiO_3$/g-C_3N_4 Ternary Heterojunction Nanofibers: Gradient Energy Band, Cascade Charge Transfer, Enhanced Photocatalytic Hydrogen Evolution, and Nitrogen Fixation. *Nanoscale* **2020**, *12*, 8320–8329. [CrossRef]
609. Camussi, I.; Mannucci, B.; Speltini, A.; Profumo, A.; Milanese, C.; Malavasi, L.; Quadrelli, P. g-C_3N_4-Singlet Oxygen Made Easy for Organic Synthesis: Scope and Limitations. *ACS Sustain. Chem. Eng.* **2019**, *7*, 8176–8182. [CrossRef]
610. Ahmad, R.; Tripathy, N.; Khosla, A.; Khan, M.; Mishra, P.; Ansari, W.A.; Syed, M.A.; Hahn, Y.-B. Recent Advances in Nanostructured Graphitic Carbon Nitride as a Sensing Material for Heavy Metal Ions. *J. Electrochem. Soc.* **2019**, *167*, 37519. [CrossRef]
611. Chen, K.; Zhang, X.-M.; Yang, X.-F.; Jiao, M.-G.; Zhou, Z.; Zhang, M.-H.; Wang, D.-H.; Bu, X.-H. Electronic Structure of Heterojunction MoO_2/g-C_3N_4 Catalyst for Oxidative Desulfurization. Appl. *Catal. B Environ.* **2018**, *238*, 263–273. [CrossRef]
612. Lei, G.; Zhao, W.; Shen, L.; Liang, S.; Au, C.; Jiang, L. Isolated Iron Sites Embedded in Graphitic Carbon Nitride (g-C_3N_4) for Efficient Oxidative Desulfurization. *Appl. Catal. B Environ.* **2020**, *267*, 118663. [CrossRef]
613. Ma, R.; Guo, J.; Wang, D.; He, M.; Xun, S.; Gu, J.; Zhu, W.; Li, H. Preparation of Highly Dispersed WO_3/Few Layer g-C_3N_4 and Its Enhancement of Catalytic Oxidative Desulfurization Activity. *Colloids Surfaces A Physicochem. Eng. Asp.* **2019**, *572*, 250–258. [CrossRef]